Spatial resolution of prism-based surface plasmon resonance microscopy

Loïc Laplatine

UNIVERSITÉ DE GRENOBLE

THÈSE

Pour obtenir le grade de

DOCTEUR DE L'UNIVERSITÉ DE GRENOBLE

Spécialité: **Physique pour les Sciences du Vivant**

Arrêté ministérial: 7 août 2006

Présentée par

Loïc LAPLATINE

Thèse dirigée par **Dr. Roberto CALEMCZUK**

Préparée au sein du **Laboratoire des Structures et Propriétés des Architectures Moléculaires - CEA Grenoble/DSM/INAC/SPrAM**
et de **l'Ecole Doctorale de Physique**

Résolution Spatiale en Microscopie par Résonance de Plasmon de Surface à Couplage par Prisme

Thèse soutenue publiquement le **27/11/2014**,
devant le jury composé de:

Pr. Paul Charette
Université de Sherbooke, CRN^2 (Sherbrooke, Canada), Rapporteur
Pr. Christophe Vieu
Université de Toulouse, LAAS-CNRS (Toulouse, France), Rapporteur
Pr. Benoit Boulanger
Université Joseph Fourier, MATONLP (Grenoble, France), Examinateur
Pr. Malcolm Buckle
Ecole Normale Supérieur de Cachan, LBPA UMR 8113 (Cachan, France), Examinateur
Dr. Emmanuel Maillart
Horiba Jobin Yvon, (Palaiseau, France), Examinateur
Dr. Loïc LEROY
Université Joseph Fourier, SPrAM UMR-5819, Co-Encadrant de thèse

Dr. Roberto CALEMCZUK
CEA Grenoble, SPrAM UMR-5819 (Grenoble, France), Invité

UNIVERSITÉ DE GRENOBLE

THESIS

To obtain the degree

DOCTOR OF THE UNIVERSITY OF GRENOBLE

Speciality: **Physics for the Life Sciences**

Ministerial decree: August 7, 2006

Presented by

Loïc LAPLATINE

Thesis directed by **Dr. Roberto CALEMCZUK**

Prepared at the **Laboratory of Structures and Properties of Molecular Architectures - CEA Grenoble/DSM/INAC/SPrAM**
and the **Ecole Doctorale de Physique**

Spatial Resolution of Prism-based Surface Plasmon Resonance Microscopy

Thesis defended publicly **27/11/2014**,
Ph.D. thesis committee members:

Pr. Paul Charette
Sherbooke University, CRN^2 (Sherbrooke, Canada), Referee
Pr. Christophe Vieu
Toulouse University, LAAS-CNRS (Toulouse, France), Referee
Pr. Benoit Boulanger
Joseph Fourier University, MATONLP (Grenoble, France), Member
Pr. Malcolm Buckle
Ecole Normale Supérieur of Cachan, LBPA UMR 8113 (Cachan, France), Member
Dr. Emmanuel Maillart
Horiba Jobin Yvon, (Palaiseau, France), Member
Dr. Loïc LEROY
Joseph Fourier University, SPrAM UMR-5819, PhD Co-Advisor

Dr. Roberto CALEMCZUK
CEA Grenoble, SPrAM UMR-5819 (Grenoble, France), Guest

"Le peu que je sais, c'est à mon ignorance que je le dois."
Sacha GUITRY

À ceux qui m'ont mis au monde,
ainsi qu'à ceux qui me le font sans cesse découvrir sous un nouvel angle…

Abstract

Prism-based surface plasmon resonance microscopy is an optical imaging technique invented in the late 80s'. Its main advantage lies in its high sensitivity to optical index or thickness variations at a metal surface. Therefore, the monitoring of biological reactions can be performed in real-time without labeling agent such as fluorescence or enzymes. Over the last 25 years, SPR microscopy has become the major technique in label-free biodetection. The field of application range from the determination of affinity constant in biochemistry to the detection of pathogenic bacteria via cellular biology. Until now, the propagation length of the surface plasmons has been considered as the spatial resolution limit. However, many examples do not support this statement. In this PhD thesis, we demonstrate that the resolution is also limited by optical aberrations induced by the prism used to couple light and surface plasmons. Thus, we are able to explain why the experimental resolution was usually worse than the predicted one. The analysis of the image formation and the quantification of aberrations lead us to suggest two new optical configurations optimized for resolution. We also analyze which metal exhibits the better trade-off between propagation length and sensitivity. Experimentally, we obtain a resolution between 1.5 and 5 μm depending on the direction, on field-of-view up to several mm^2, and with a standard sensitivity for biodetection. We are then able to observe simultaneously several thousands of individual eukaryote and prokaryote cells. Finally, we develop a prototype dedicated to the real-time monitoring of protein secretion by immune cells. The limits of SPR microscopy and the solutions which could allow this kind of study are discussed. Preliminary results on adherent cells observation and improvement of bacterial detection are also presented.

Resumé

La microscopie par résonance de plasmons de surface à couplage par prisme a vu le jour à la fin des années 80. Le principal avantage de cette technique d'imagerie optique réside dans sa très grande sensibilité à de faibles variations d'indice optique ou d'épaisseurs à la surface d'un métal. De ce fait, le suivi d'interactions biologiques peut se faire en temps réel sans avoir recours à l'utilisation de marqueurs fluorescents ou enzymatiques. Depuis plus de 25 ans, la microscopie SPR s'est imposée comme la technique de référence de biodétection sans marquage. Ses champs d'application vont de la détermination de constantes d'affinité à la détection de bactéries pathogènes, en passant par la biologie cellulaire. Jusqu'à présent, on pensait la résolution spatiale limitée par la longueur de propagation des plasmons de surface. Or, de nombreux exemples ne corroborent pas cette hypothèse. Dans cette thèse, nous montrons qu'à ce phénomène de propagation se rajoute des aberrations optiques induites par l'utilisation d'un prisme pour coupler la lumière et les plasmons de surface. Nous expliquons ainsi pourquoi les résolutions expérimentales étaient souvent bien moins bonnes que celles attendues. Par l'analyse de la formation des images et la quantification des aberrations, nous aboutissons à deux nouvelles configurations optiques optimisées pour la résolution. Nous analysons ensuite quel métal offre le meilleur compromis entre longueur de propagation et sensibilité. Expérimentalement, nous obtenons une résolution comprise entre 1.5 et 5 μm suivant la direction, sur des champs de vision de plusieurs mm^2, et ce, avec une sensibilité standard en biodétection. Nous sommes ainsi en mesure d'observer simultanément plusieurs milliers de cellules individuelles, eucaryotes et procaryotes. Finalement, nous développons un prototype dédié au suivi en temps réel de sécrétions de protéines par des cellules immunitaires. Les limites de la microscopie SPR et les solutions qui permettraient de faire aboutir ce type d'étude sont examinées. Des études préliminaires sont aussi menées sur l'observation de cellules adhérentes ainsi que sur l'amélioration de la détection de bactéries.

Contents

List of Figures

List of Tables

Notations

A_b	Base angle of the prism
A_p	Apex angle of the prism
Ab	Antibody
Ag	Silver
Al	Aluminum
Au	Gold
BSW	Bloch Surface Wave
Cu	Copper
d	Distance between the object and the imaging side edge of the prism
d_m	Thickness of the metal layer
d_{lim}	Distance at which the resolution is limited by geometric aberration due to the prism
$diff_x$	Diffraction limit in the X axis, parallel to the SP
$diff_y$	Diffraction limit in the Y axis, perpendicular to the SP
DNA	Deoxyribonucleic acid
DOF	Depth-Of-Field
EW	Electromagnetic Wave
FTIR	Frustrated Total Internal Reflection
FOV	Field-Of-View
fps	Frame per second, acquisition frequency of the camera
FWHM	Full Width at Half Maximum
h_{bio}	Thickness of the biolayer adsorbed on the metal
I	Intensity measured on the camera sensor
I_w	Intensity at the working angle
ITO	Indium Tin Oxide, heating glass plate
L_x	Propagation length of the surface plasmons for a finite metal thickness
$L_{x,SIM}$	Propagation length in the semi-infinite media model
L_z	Penetration depth into the dielectric medium
$L_{z,metal}$	Penetration depth into the metal
k_{SP}	Wave vector of the surface plasmons (k_{SP} = k'_{SP}+i k''_{SP})

Δk_{SP}	Perturbation term of k_{SP}
k_{on}	Association constant
k_{off}	Dissociation constant
$k_{ph,x}$	X axis component of the wave vector of the incident electromagnetic wave
NA	Numerical Aperture of the imaging system
n_{bio}	Refractive index of biomolecules and microorganisms (= 1.41)
n_d	Refractive index of the dielectric medium
n_{eff}	Effective refractive index in the dielectric medium
n_{water}	Refractive index of water
n_p	Refractive index of the prism
OL	Objective lens
PBS	Phosphate Buffer Saline
PEG	Polyethylene Glycol, bio-anti-fooling
PDMS	Polydimethylsiloxane, soft microstructured elastomer stamp
Ppy	Polypyrrole
PSF	Point Spread Function, optical image of an ideal point source
R	Reflectivity of the interface in TM mode
R_{TM}	same as R
R_{res}	Reflectivity at the resonant angle
R_{TE}	Reflectivity of the interface in TE mode
R_w	Reflectivity at the working angle
RM	Resonant Mirror
SA	Spherical aberration component in the spatial resolution
$scat - gauss_x$	FWHM of the Gaussian component of the SP nanojet in the X axis
$scat_y$	FWHM of the SP nanojet in the Y axis
SNR	Signal-to-Noise-Ratio
SP	Surface Plasmon, quasi-particle representing the oscillation of charge density
SPR	Surface Plasmon Resonance
SPRi	Surface Plasmon Resonance imaging
TE	Transverse Electric polarization (also called s-polarization)
TL	Tube lens focal lens
TM	Transverse Magnetic polarization (also called p-polarization)
VWFOV	Very-Wide-Field-Of-View optimization
WD	Working Distance of the objective lens
α	Angle between the perpendicular of the virtual image and the principal ray direction
α'	Angle between the final image of the base and the camera sensor
β	Angle between the base and the virtual image

δx	FWHM of the Gaussian component of the PSF parallel to the SP
δy	FWHM of the PSF perpendicular to the SP
Δx	Spatial resolution parallel to the SP
Δy	Spatial resolution perpendicular to the SP
$\Delta\theta_{int}$	Angular diffusion of the secondary rays around θ_{int}
ΔR	Shift of reflectivity
ΔI	Shift of intensity
ϵ_d	Permittivity of the dielectric
ϵ_m	Permittivity of the metal ($\epsilon_m = \epsilon'_m + i\,\epsilon''_m$)
ϵ_p	Permittivity of the prism
λ	Free space wavelength of the incident light
θ_c	Critical angle of total internal reflection
θ_{CCD}	Angle of the imaging system axis
θ_{ext}	External working angle on the prism base
θ_{in}	Internal angle of incidence on the prism face
θ_{int}	Internal working angle on the prism base
θ_{out}	External angle of incidence on the prism face
θ_{res}	Angle of resonance on the prism base
θ_w	Working angle on the prism base
θ_ρ	surface coverage
Υ	Anamorphose coefficient
Φ	Wave aberration function

Introduction

Surface plasmons (SP) are waves of electron density propagating at the interface between a metal and a dielectric. Such waves can be resonantly excited by photons or electrons, resulting in a steep and strong absorption, referred to as "Surface plasmon Resonance" (SPR). The SPR effect was experimentally detected for the first time in 1902 [1], but it took more than 50 years to understand its origin [2]. In the late 60s', two groups independently showed that when a beam of light enters a prism which base has been coated with a very thin layer of metal, SP could propagate between the metal and the external medium, extending on each side by only a few tens of nm [3, 4]. The resonance being very sensitive on the refractive index above the metal surface, SPR could provide an unequaled level of contrast with respect to the adsorption of a thin film down to the nm. At the beginning of the 80s', this extraordinary sensitivity was used for the first time in biosensing to measure a antibody/antigen interaction without the use of any labeling technique, such as fluorescence of enzymatic reactions [5]. The label-free nature of SPR detection also means that surface interactions can be followed in real-time, thereby allowing the measure of kinetic constants. Since then, SPR has become one of the most famous label-free biosensing technique, and has been applied to a wide range of applications.

In the late 80s', two groups independently discovered that the light absorption resulting from the SPR effect could also be monitored by imaging the metal-coated surface [6, 7]. By replacing the light sensor by a camera sensor, and by adding an imaging system to it, the entire base of the prism can be visualized through one of its faces, and the local adsorption phenomena seen as an increase of reflected intensity (out of resonance condition, i.e. less absorption). The ability of SPR imaging (SPRi) to follow multiple bio-interactions simultaneously extended even more the performances of the SPR biodetection, and made this technique competitive with labeling technologies [8, 9].

The first optical optimization of prism-based SPRi dates back to 2004, when Maillart, in his PhD thesis, gave the conditions on prism refractive index, apex angle, imaging system, metal layer and wavelength of illumination in order to monitor biomolecules interactions on a approximately 1 cm^2 field-of-view (FOV). Such configuration, herein referred to as "Very-wide-field-of-view" (VWFOV), has been widely used for the monitoring of biomolecules interactions up to a thousand interactions [10] as well as for the detection of pathogenic bacteria [11].

However, the spatial resolution obtained in this optimization is in the order of 8 to 20 µm, and strongly limits studies on individual micro-organisms of only a few microns, such as cells or bacteria [12]. In addition, these high magnification images suffer from high distortions [13]. Although, non-optimized commercial prisms have also been used in SPRi. For some of them, the resolution is sufficient to monitor individual cells, but is restricted to a clear stripe usually smaller than the camera sensor [14]. Out of this stripe the image is strongly out of focus, thereby limiting the number of relevant cells to a few tens. Moreover, it is usually assumed that the resolution is limited in one direction by the propagation length L_x of SP, which induces an elongated spreading of the reflected intensity, and perpendicular to it, by the numerical aperture (NA) of the imaging system. Nonetheless, even when using high NA objectives, a resolution below 1.5 µm has never been obtained experimentally [15, 16]. Finally, incoherences between spatial resolution measured

in air and in water as a dielectric medium reinforced the conclusion that all the physical aspects governing the spatial resolution and image formation in prism-based SPR imaging have not been elucidated so far [17, 18].

The aim of my PhD thesis has been, first, to understand these mechanisms, then, to quantified their relative importance, and finally, to optimize a prism-based SPR imaging set-up to have the best spatial resolution on the widest FOV and at the best sensitivity. It leads me to describe a second optical optimization of prism-based SPRi (that could actually be subdivided into two configurations). This novel optical configuration has been applied to the observation and real-time monitoring of individual human cells and bacteria.

The manuscript is divided into 4 chapters:

Chapter 1 replaces this study in the bibliographic background of prism-based SPRi applied to biology. I begin to expose the theory of the SPR effect. I voluntary subdivided the theory into two approaches which I have named "plasmonic" and "optical". Both emphasizes different but complementary aspects describing the main properties of surface plasmons which are necessary for the understanding of the next chapters. Since my thesis deals with a very general concern of this microscopic technique, I have tried to give a global overview of SPR in terms of physical parameters: wavelength of illumination, metals, refractive index of the prism, as well as biological applications: biomolecules, bacteria and cells. I then focus on SPRi and its applications, mostly on the prism-based configuration, but also briefly on the objective-based configuration; the latter being known to exhibit the ultimate spatial resolution. The advantages and drawbacks of SPRi compared to other label-free as well as labeling techniques are succinctly discussed. This chapter ends by introducing the biological challenges that have guided my work, thereby justifying the problematic of the PhD thesis.

Chapter 2 describes the fundamentals of image formation and spatial resolution through, if I may say, the prism of geometrical optics and geometric aberrations. A short introduction emphasizes that the geometrical optical aspects are not only related to SPRi, but also apply to any other prism-based imaging technique, such as the ones relying on Bloch Surface Wave (BSW) [19], Frustrated Total Internal Reflection (FTIR) [20] and Resonant Mirrors (RM) [21]. After analyzing the general case of an arbitrary prism, I successively deal with the VWFOV configuration and with the resolution optimized configuration with its two imaging modes, referred to as "line-scan" and "classic". The quantification of geometric aberrations by the aberration function (wavefront error) leads to describe optimal prisms in terms of apex angle and refractive index for each configuration. Finally, the issue of an optimal metal coating presenting the best trade-off between sensitivity and propagation length is also addressed.

Chapter 3 is dedicated to the description of the experimental set-up. The SPR apparatus and its related software have been built all along the thesis. It can be seen as the assembly of connected elements which are presented according to their function: optics, fluidics, mechanics, thermics, acquisition software and image post-processing. Some of these sections are accompanied with a brief discussion on the technical issues I had to face. The material and methods for resolution measurements and biological experiments are also presented.

Chapter 4 presents the experimental results. In a first part, I illustrate the influence of geometric aberrations on spatial resolution by comparing the VWFOV and the resolution configurations. An elastomeric stamp is used as a resolution target. It exhibits micropillars which simulate the SPR signal of bacteria, cells or small functionalized areas. The ultimate spatial resolution is measured by using latex microbeads. By comparing with the theoretical point-spread-function (PSF), I point out and quantify the optical and plasmonic phenomena governing the spatial resolution. Then, I investigate the potential of an hybrid silver/gold coating in terms of trade-off between resolution and sensitivity. In the second part, I demonstrate the

capabilities of the resolution configuration for biological applications. Example of living cells images illustrate a discussion on image quality, time resolution and sensitivity requirements. Then, proofs of concept are established on three applications. The first one targets the monitoring of individual T lymphocyte secretions, the second one the study of adherent epithelial cells, and the last one the improvement of fast bacterial detection.

1 | Background in prism-based SPR imaging and biological context

Contents

Résumé du chapitre 1

Dans ce premier chapitre, je présente les aspects théoriques de la résonance de plasmon de surface (SPR) à couplage par prisme et de la technique d'imagerie qui lui est associée, la SPRi. Dans la mesure où cette thèse traite d'un aspect général de cette technique de microscopie, la résolution spatiale, je tente de couvrir un large spectre de métaux, d'indices optique de prisme et longueurs d'onde d'excitation. Ainsi, chacun devrait y trouver les grandeurs caractéristiques associées à son propre système SPRi, ou à celui qu'il souhaite concevoir. Autant que possible, j'illustre la théorie par des graphiques et des schémas.

Dans une première section, je scinde la théorie de la SPR en deux approches différentes, mais complémentaires. J'ai appelé la première "l'approche plasmonique", et la seconde "l'approche optique". Elles sont toutes deux basées sur la résolution des équations de Maxwell, mais tandis que la première traite d'un cas idéal d'une interface entre un métal et un diélectrique semi-infinis, la seconde considère le cas général d'un système multicouches.

Dans une seconde section, je présente les domaines d'applications de la SPR en tant que biocapteur largement utilisé en biologie, de par sa capacité à observer des phénomènes biologiques et biochimiques sans marquage et en temps réel. J'aborde ensuite les aspects physico-chimiques des interactions de surface par le modèle de Langmuir.

La troisième section est dédiée à la présentation de la SPRi, principalement à couplage par prisme, mais aussi à couplage par objectif de microscope. Je présente également les possibilités qu'apporte l'imagerie comparée aux capteurs SPR classiques, notamment pour l'ètude de micro-organismes.

L'avant-dernière section marque le début de mon travail de recherche à travers la mise en évidence de certaines incompréhensions et incohérences relatives à la résolution spatiale en SPRi à couplage par prisme. J'illustre mes propos par des exemples issus de la littérature qui révèlent trois aspects non élucidés : la résolution ultime est-elle limitée par l'ouverture numérique du système d'imagerie ? La longueur de propagation des plasmons de surfaces (L_x) est-elle la seule limite de résolution dans le sens de propagation ? Pourquoi les images ayant les meilleures résolutions sont-elles toujours présentées sur de faibles champs de vision (FOV), et inversement, pourquoi celles présentant de grands champs de vision ont-elles souvent une plus basse résolution ?

Enfin, j'expose les applications en biologie cellulaire et en microbiologie qui nécessitent d'avoir à la fois une excellente résolution spatiale, un grand champ de vision et une bonne sensibilité. Ce sont ces applications qui ont, entre autres, guidé mes travaux. Cela me permet de définir la problématique de cette thèse de doctorat :

- D'un point de vue théorique, aboutir à une meilleure compréhension des mécanismes qui régissent la résolution spatiale en SPRi à couplage par prisme.
- D'un point de vue expérimental, fabriquer un montage capable de répondre à nos interrogations, mais surtout capable d'étudier simultanément, et à l'échelle individuelle, jusqu'à plusieurs milliers de cellules eucaryotes et procaryotes.

This first chapter presents the physical and bibliographic background to understand the issue of spatial resolution in Surface Plasmon Resonance imaging (SPRi), as well as the biological motivations that have guided this study.

The first section introduces the theory of SPR through two approaches. Even if both are based on the resolution of the Maxwell's equations, they bring different and complementary insights to understand, study and simulate the SPR effect. The first one is an ideal case of an electromagnetic wave propagating at the boundary between two semi-infinite media, and will be called "the plasmonic approach." The second one focuses on reflectivity and electric field intensity in a stratified medium, and will be called "the optical approach." The second section introduces the use of SPR as a label-free and real-time biosensing technique. The third section is devoted to SPRi and some of its applications. The penultimate section emphasizes some apparent incoherences and misunderstandings about spatial resolution in prism-based SPRi. In the last section, we place this study in the biological context that has driven to improve the spatial resolution of prism-based SPRi, and we conclude by defining the problematic of the PhD thesis.

1.1 | Theory of the surface plasmon resonance

The surface plasmon resonance is a physical effect corresponding to the presence of electromagnetic waves (EW) which propagate at a metal/dielectric interface. This idea of surface waves was first introduced in 1941 by Fano [22] to explain the diffraction anomalies of metal-coated diffraction gratings observed by Wood in 1902 [1] (known as the first reported SPR observations). However, it is only in the late 50's that the theory was fully developed by Ritchie [2], Stern and Ferrell [23] and Kanazawa [24] to explain the loss of energy undergone by electron beams passing through thin metallic foils in contact with a dielectric medium. The authors showed that the electrons inside the foil could collectively oscillate within the plane of the interface at a frequency less than the already well-established plasma (or plasmon) frequency. As illustrated in **Figure 1.1**, these oscillations correspond to a wave of electron density that gives rise to an EW also bounded to the interface. Since the electron collective oscillations in bulk material were known as "plasmons", the 2D waves were named "surface plasmons" (SP), and the 3D waves sometimes renamed "volume plasmons" [25]. Strictly speaking, SP are quasi-particles (as phonons in acoustic or holes in semiconductors) related to the energy quantization of the electron density oscillations. Here, we will use the term "surface plasmon" to refer to the associated EW, as it is usually the case in SPR literature.

SP do not appear naturally at a metal/dielectric interface and need to be excited by an external energy source. They can be generated either by sending fast electrons, as it has been done in the earliest days of surface plasmon understanding, or by an optical coupling. Electronic

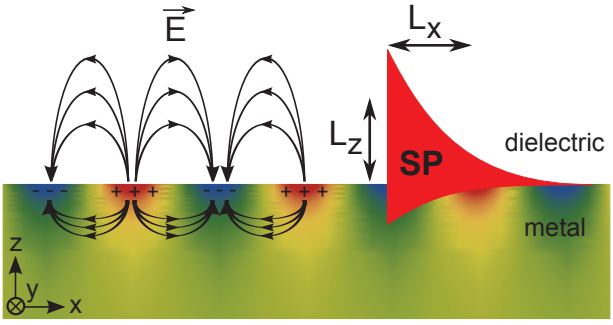

Figure 1.1: Surface Plasmon waves at the boundary of two semi-infinite media. A wave of electron density propagates at the boundary toward the X axis (depletion in red and overconcentration in blue). The local charge generates an evanescent electric field in the X and Z axis.

coupling is limited to vacuum environments, and thus, do not apply to biosensing [26]. In contrast, optical coupling can be performed in air and water environments at atmospheric pressure and room temperature. As for now, we will only focus on SP excited by light, also called surface plasmon polariton (SPP), but keeping the simple term "SP".

The term "Resonance" translates the fact that, under certain conditions, a part of the incident light is converted into SP, which rapidly dissipate into heat [27]. Hence, experimentally, this SPR effect corresponds to a peak of absorption. The conditions of resonance are very sensitive to the refractive index of the dielectric medium, but only within a subwavelength height. This localized sensitivity has been used to monitor biological interactions, the dielectric medium being in that case the aqueous solution.

Thereafter, some of the main characteristics of SPR will be illustrated by the use of curves. Unless specified, these curves are calculated with literal expressions for the refractive index of water $n_{water}(\lambda)$ from ref. [28], the refractive index of glasses $n_p(\lambda)$ from the Sellmeier equations given by the manufacturer (**Appendix A.2**) and the permittivities of metals $\epsilon_m(\lambda)$ from ref. [29] for gold, silver, aluminum and chromium, and from ref. [30] for copper (**Appendix A.1**).

1.1.1 | SPR, the plasmonic approach

The plasmonic approach considers the solution of the Maxwell's equations which describes a guided propagation mode at the plane interface between two semi-infinite media, let it be the XY plane, in contact at z = 0. When only considering non-magnetic materials, each medium is fully characterized by its complex permittivity $\epsilon = \epsilon' + i\,\epsilon''$ which is a function of the frequency f of the electric excitation: $\epsilon(f)$.

In optics, it is more convenient to express $\epsilon(\lambda)$, where λ is the free-space wavelength of an electromagnetic wave oscillating at a frequency $f = c/\lambda$, with c the speed of light in vacuum. Here, the analysis is restricted to the 400 - 1,000 nm wavelength range, with some more specific examples at λ = 632 nm, a typical wavelength used in SPR. Since only ratios of permittivities are considered, the relative permittivity $\epsilon_r = \epsilon/\epsilon_0$, where ϵ_0 is the constant vacuum permittivity, can directly be used, and the index "$_r$" omitted for the sake of clarity. In that case, the refractive index "n" is equal to $\sqrt{\epsilon}$. A detailed treatment of this approach is given by Homola in ref. [31] and Pitarke *et al.* in ref. [32].

1.1.1.1 Surface plasmon waves

By using the condition of continuity of the tangential component of the electric field $\vec{E}$, it can be shown that an EW can propagate along the interface in transverse magnetic mode (TM mode, also called p-polarization), where $\vec{E}$ lies in the XZ plane, as depicted on **Figure 1.1**. The same resolution yields no solution that would represent an EW bounded to the interface in transverse electric mode (TE mode or s-polarization) where $\vec{E}$ would only have a component along the Y axis.

The guided wave only exists if the real part of the permittivity of the two media are of opposite sign. This "plasmon condition" can be fulfilled with a metal/dielectric interface of relative permittivities $\epsilon_m = \epsilon'_m + i\,\epsilon''_m$ and $\epsilon_d = \epsilon'_d + i\,\epsilon''_d$, respectively. In biosensing applications, the dielectric is often a saline aqueous solution where the biological events take place. Its refractive index can be approximated by the one of pure water for whom $\epsilon'_d \approx 1.77$ (n_{water} ≈1.33) and $\epsilon''_d = 0$ [33]. This leads to a choice of metal with $\epsilon'_m < 0$. Several metals satisfy this condition, but in SPR mostly four of them are used [34]: gold (Au) [16], silver (Ag) [15], aluminum (Al) [17] and copper (Cu) [35].

The wavevector of surface plasmon waves is found to be:

$$k_{sp} = \frac{2\pi}{\lambda} \times \sqrt{\frac{\epsilon_d\,\epsilon_m}{\epsilon_d + \epsilon_m}} = k'_{sp} + i\,k''_{sp} \tag{1.1}$$

For the metals used in SPR, $\epsilon''_m > 0$, so k_{sp} is also complex. The electric field $\vec{E}_{sp,j}$ of the SP in each medium j have the following form:

$$\begin{aligned}\vec{E}_{sp,j}(x,z,t) &= (E_{x,j},0,E_{z,j})\,\exp(\frac{-|z|}{2\,L_{z,j}})\,\exp i(k_{sp}\,x-\omega t)\\ &= (E_{x,j},0,E_{z,j})\,\exp(\frac{-|z|}{2\,L_{z,j}})\,\exp(-x\,k''_{sp})\,\exp i(k'_{sp}\,x-\omega t)\\ &= (E_{x,j},0,E_{z,j})\,\exp(\frac{-|z|}{2\,L_{z,j}})\,\exp(\frac{-x}{2\,L_x})\,\exp i(k'_{sp}\,x-\omega t)\end{aligned} \tag{1.2}$$

In the Z axis, this wave is non-propagative and purely evanescent with a characteristic length called the penetration depth L_z. In the X axis, it is propagative, but exponentially damped due to the positive imaginary part of k_{sp} with a characteristic length called the propagation length L_x. This leads to an electric field intensity exponentially decreasing in both directions (**Figure 1.1**):

$$I_{sp,j}(x,z) \propto \vec{E}_{sp,j}\,\vec{E}^*_{sp,j} \propto \exp(\frac{-|z|}{L_{z,j}})\,\exp(\frac{-x}{L_x}) \tag{1.3}$$

where "*" means the complex conjugate.

In the literature, L_x and L_z are used to characterize the exponential decrease of either the amplitude A = $|\vec{E}|$ (V/m) or the intensity I $\propto$ A^2 (W/m^2), and are equal to the distance at which it is divided by a factor e (≈2.72). Both conventions are used, sometimes mixed. Herein, we have chosen to use the intensity convention to be consistent with the optical approach where we will only focus on light intensity. Moreover, considering the intensity is more straightforward to evaluate the experimental behaviors of such waves. Note that in the amplitude convention, these lengths would have been twice as long. As for now, except if mentioned, we will only consider the intensity of the EW.

1.1.1.2 The penetration depth L_z

The plasmonic approach gives an analytical solution of the penetration depth of the EW on each side of the interface:

$$L_{z,j} = \frac{\lambda}{4\pi} \times \left|\Im\left\{\frac{\epsilon_j}{\sqrt{\epsilon_d+\epsilon_m}}\right\}\right|^{-1} \tag{1.4}$$

where j = m for $L_{z,metal}$ and j = d for $L_{z,dielectric}$, which will be shortened by L_z. Both penetration depths for water environment are plotted in **Figure 1.2**. They emphasize the 2D character of the SP: almost 2/3 of the EW intensity is confined within the first tens of nm in the metal, and hundreds of nm in the dielectric.

L_z is then a good approximation of the height over which SP are sensitive to the refractive index in the dielectric. While $L_{z,metal}$ stays nearly constant with respect to λ, L_z increases up to a factor of 4 for all of these metals, meaning that longer λ scan deeper in the dielectric.

Refractive index changes can be induced by global variations that affect the whole dielectric refractive index n_d, such as temperature or saline concentration, as well as by the adsorption of an additional layer, such as biomolecules or microorganisms. The optical index of microorganisms and adsorbed biomolecule layers range from 1.36 to 1.55 [36]. In the present work, n_{bio} is set at a mean value of 1.41. Since the size of eukaryote cells and bacteria is at least greater than 3 times L_z, they can be considered in first approximation as a global change of n_d from n_{water} to their own refractive index n_{bio}. For biomolecules, whose typical size is in the range of the nm, the layer thickness h_{bio} will be less than L_z. In that case, it is convenient to define the effective refractive index n_{eff} "felt" by the SP. As shown by Jung *et al.* [37], the general literal expression of n_{eff}

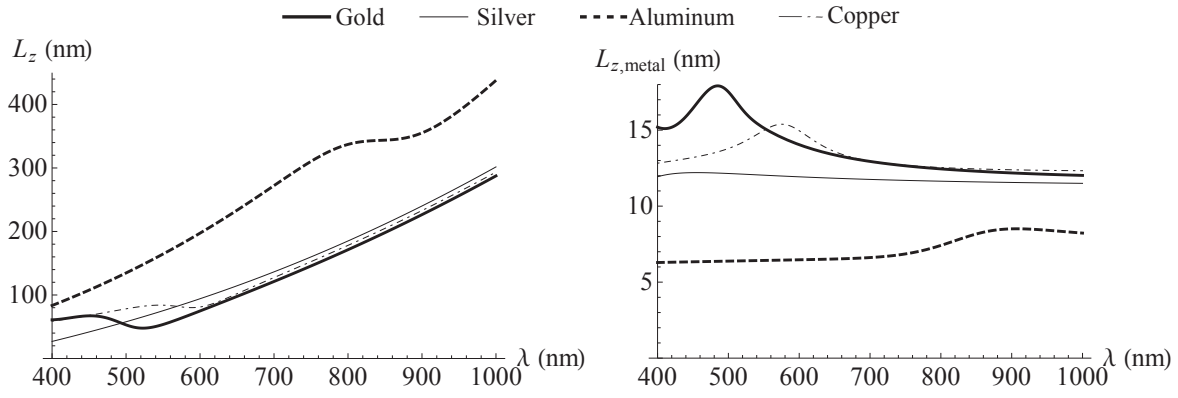

(a) dielectric **(b)** metal

Figure 1.2: Penetration depth as a function of the wavelength λ for different metals used in SPR in contact with pure water. **(a)** Penetration depth in the dielectric L_z. **(b)** Penetration depth in the metal $L_{z,metal}$.

can be found by averaging a z-dependent dielectric refractive index $n(z)$ by a weighting factor $W(z) = \exp(-z/L_z)$:

$$n_{eff} = \frac{\int_0^{+\infty} n(z)\, W(z)\, dz}{\int_0^{+\infty} W(z)\, dz} = \frac{1}{L_z} \int_0^{+\infty} n(z)\, \exp(-z/L_z)\, dz \tag{1.5}$$

In the simple case of the adsorption of a single biolayer of optical index n_{bio} and height h_{bio}, n_{eff} is then given by:

$$n_{eff} = n_d + (n_{bio} - n_d)\, [1 - \exp(-h_{bio}/L_z)] \tag{1.6}$$

For a given metal in contact with pure water, n_{eff} is a function of h_{bio} and λ. **Figure 1.3a** shows the increase of n_{eff} in refractive index unit (RIU) as a function of h_{bio} at λ = 632 nm. For $h_{bio} \ll L_z$, this increase is linear, so its derivative is constant, while for biolayer thicknesses much larger than L_z the derivative tends to zero since $n_{eff} \to n_{bio}$. Therefore, for h_{bio} = 1 nm, the increase can be considered equal to the partial derivative of n_{eff} with respect to h_{bio}, and is plotted with respect to λ in **Figure 1.3b**. As expected by comparing with **Figure 1.2a**, the smaller L_z, the higher the increase of n_{eff} with respect to h_{bio}.

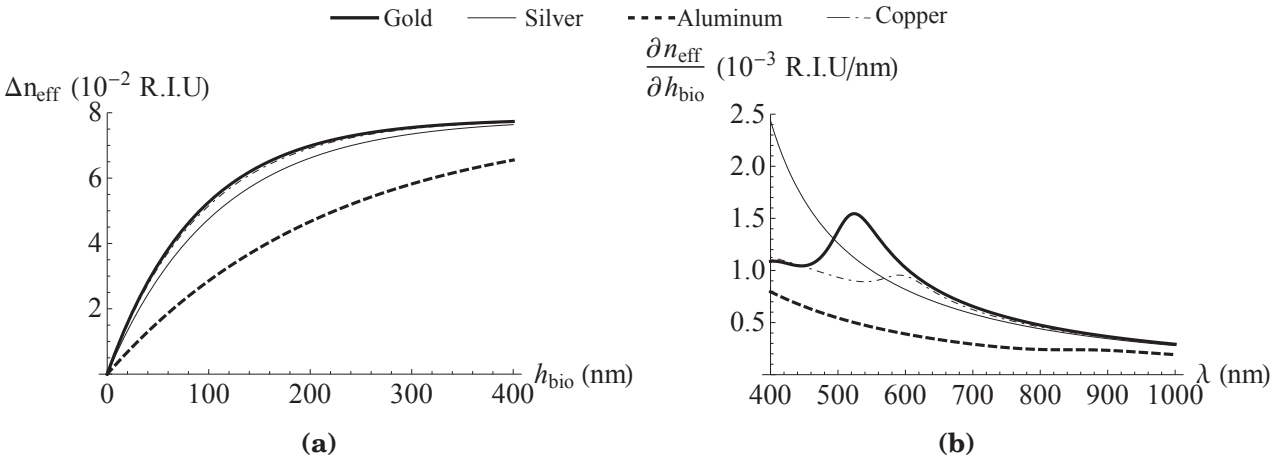

(a) **(b)**

Figure 1.3: Effective refractive index n_{eff} as a function of λ and h_{bio}. **(a)** Variation of n_{eff} with respect to h_{bio} at λ = 632 nm. **(b)** Partial derivative of n_{eff} with respect to h_{bio} as a function of λ.

1.1.1.3 The propagation length $L_{x,SIM}$ for semi-infinite media

As stated by **Equation 1.1**, the literal expression of $L_{x,SIM}$ is:

$$L_{x,SIM} = \frac{1}{2\,k''_{sp}} = \frac{\lambda}{4\pi} \times \left(\Im \left\{ \sqrt{\frac{\epsilon_d\,\epsilon_m}{\epsilon_d + \epsilon_m}} \right\} \right)^{-1} \tag{1.7}$$

For a given metal/dielectric interface, $L_{x,SIM}$ only depends on λ. The propagation lengths in water and air are plotted in **Figure 1.4**. The curves emphasize the fact that the propagation length increases with respect to λ in both water and air. Note that at the same λ, $L_{x,SIM}$ in water is more than twice smaller than $L_{x,SIM}$ in air. This length represents the fact that the SP are not localized but rather spread in the X axis. According to Berger *et al.* [16], $L_{x,SIM}$ measured for a gold/air interface is proportional to the theoretical value. In water, Wang *et al.* [38] measured $L_{x,SIM}$ at 3 µm at λ = 632 nm for a theoretical value of 3.8 µm.

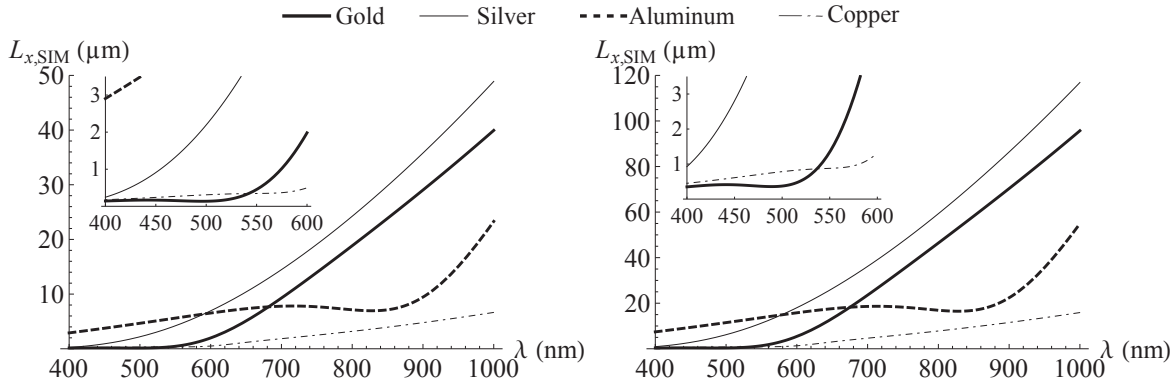

(a) water **(b)** air

Figure 1.4: Propagation length $L_{x,SIM}$ as a function of λ. Inset: magnification on shorter wavelengths.

1.1.1.4 Optical excitation of surface plasmons

The optical coupling occurs when the horizontal component (X axis) of the wavevector of the photon k_{ph} matches the real part of k_{SP}:

$$k_{ph,x} = \Re\{k_{sp}\} \tag{1.8}$$

A photon traveling in a dielectric medium of refractive index $n_d = \sqrt{\epsilon_d}$ has a wavevector of $k_{ph} = (2\pi/\lambda)\,n_d$. Unfortunately, such a photon falling on the metal/dielectric interface, even at grazing angle, cannot satisfy the coupling condition since:

$$\Re\{k_{sp}\} > \frac{2\pi}{\lambda}\sqrt{\epsilon_d}, \quad \forall\, \epsilon_d \; and \; \epsilon_m \tag{1.9}$$

As a consequence, to couple light and SP, k_{ph} needs to be increased. Two different mechanisms allow the optical coupling. The first one is based on the diffraction of a plane wave by a diffraction grating [39]. As illustrated in **Figure 1.5a**, when a plane wave impacts a diffraction grating, diffracted waves gain a multiple of the grating wavevector $k_g = 2\pi/\Lambda$ according to their diffraction order m. SP can then be excited with the correct set of θ, λ and Λ such as:

$$k'_{ph,x} = k_{ph,x} + m\,k_g = \frac{2\pi}{\lambda} n_d \sin(\theta) + m\,\frac{2\pi}{\Lambda} = \Re\{k_{sp}\} \tag{1.10}$$

The diffraction phenomenon occurs only if the length of the illuminated area is large compared to Λ. As a consequence, diffraction-coupling cannot provide true images of the surface at the micrometer scale, even when implemented in imaging mode [40].

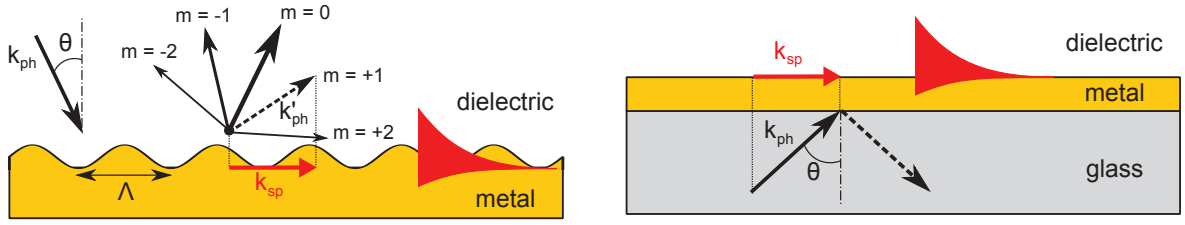

(a) diffraction coupling **(b)** glass coupling

Figure 1.5: Optical excitation of surface plasmons.

The second mechanism employed to increase k_{ph} is the glass-coupling illustrated in **Figure 1.5b**. This method was discovered independently by Otto [3], and by Kretschmann and Raether in 1968 [4]. Here, the excitation light propagates in a glass of refractive index n_p greater the n_d. In the Otto configuration, the dielectric lies between the glass and the metal, while in the Kretschmann configuration the metal is sandwiched by the glass and the dielectric. Only this latter configuration will be treated here since it is the one of the very large majority of SPRi sensors.

Hence, SP can propagate at the metal/dielectric interface by correctly choosing n_p, θ and λ such as:

$$k_{ph,x} = \frac{2\pi}{\lambda} n_p \sin(\theta) = \Re\{k_{sp}\} \tag{1.11}$$

Due to the same mechanism of unmatched wavevectors between light coming from the dielectric and SP at a plane interface, the SP cannot re-emit a photon in the dielectric. Moreover, for thicknesses of metal much larger than $L_{z,metal}$ the electric field of the SP is almost null at the glass/metal interface, so SP cannot decay into a photon in the glass either. They finally dissipate their energy into heat in the metal layer [41, 42]. As a consequence, when an incident ray of light couples to SP, the intensity of the reflected ray decreases due to absorption. This phenomenon is called Surface Plasmon Resonance (SPR). The angle of minimal reflectivity is called the angle of resonance θ_{res}, and can be deduced from **Equation 1.11** as:

$$\theta_{res} = \arcsin\left(\frac{1}{n_p} \times \Re\left\{\sqrt{\frac{\epsilon_d\,\epsilon_m}{\epsilon_d + \epsilon_m}}\right\}\right) \tag{1.12}$$

As plotted in **Figure 1.6**, for a given metal/dielectric interface, θ_{res} is a function of λ and n_p. The typical refractive index of glasses goes from 1.5 to 2 RIU in the visible range. The higher n_p, the smaller θ_{res}. Note that at a fixed angle, it is also possible to define a wavelength of resonance $\lambda_{res} = f(\theta, n_p)$.

Glass-coupling differs from electron and diffraction-coupling by the break of symmetry due to the metal layer thickness d_m, that cannot be considered infinite anymore. When a beam of light is sent above the critical angle on an uncoated prism base, it undergoes total internal reflection. Even if all the energy is back-reflected, an evanescent wave penetrates into the dielectric over a subwavelength depth. In SPR, despite of the change caused by the metal coating, this wave is responsible for the coupling: it penetrates the entire metal layer until the electric field $\vec{E}$ reaches the metal/dielectric interface and excites the SP. As $d_m \to 0$, $\vec{E}$ easily penetrates the metal layer, but the SP begin to "feel" the glass substrate, changing their wavevector, until they cannot exist anymore [31]. On the contrary, when $d_m \to +\infty$, the intensity of $\vec{E}$ at the metal/dielectric interface decreases until zero, so there is no coupling anymore, and the glass/metal interface becomes a simple mirror. This suggests an optimal metal thickness, which will be treated in the next chapter.

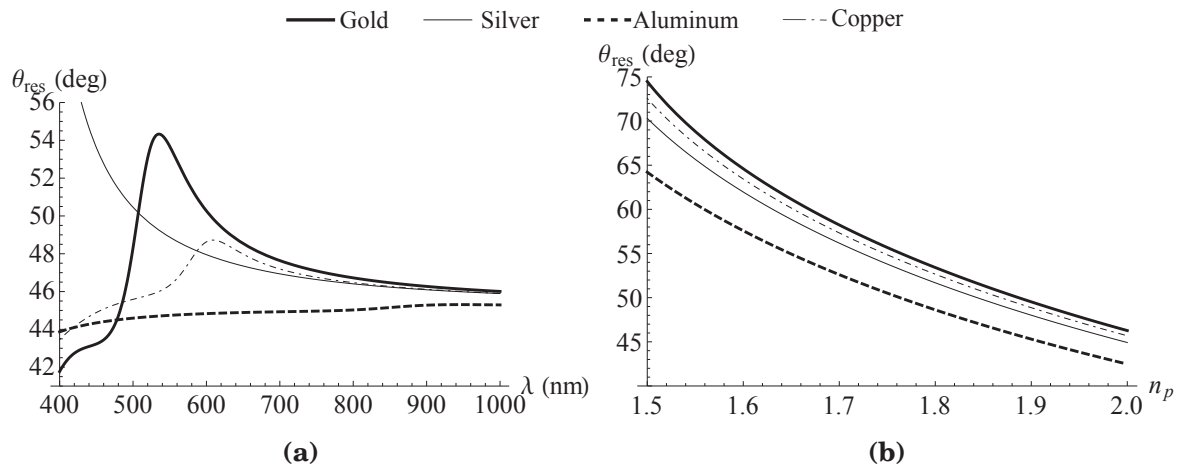

Figure 1.6: Resonant angle θ_{res} as a function of λ and n_p in water. **(a)** θ_{res} as a function of λ for N-SF66 glass ($n_p \approx$ = 1.91). **(b)** θ_{res} as a function of n_p at 632 nm.

1.1.1.5 Glass-coupling

It can be shown from **Equation 1.12** that θ_{res} is always greater than the critical angle at the glass/dielectric interface $\theta_{c,glass/dielectric} = \arcsin(n_d/n_p)$. Moreover, $\theta_{c,glass/dielectric} \geq \theta_{c,glass/air}$. As a consequence $\theta_{res} > \theta_{c,glass/air} = \arcsin(1/n_p)$. This implies that a metal-coated glass slide illuminated from the bottom cannot be used to couple light and SP as illustrated in **Figure 1.7a**. Three strategies enable having an internal angle of incidence θ_{int} that could be equal to θ_{res} [43].

The first one, called prism-based SPR, consists in using a prism so the angle of incidence of the light upon the glass can be chosen arbitrarily by changing the apex angle A_p (**Figure 1.7b**) and is at the origin of glass-coupling in 1968. Illumination and observation are performed separately on the two faces. Internal and external angles are not equal due to the refraction phenomenon at the faces, but can be express with respect to one another by:

$$\theta_{int} = \frac{\pi}{2} - \frac{A_p}{2} - \arcsin\left[\frac{\sin\left(\frac{\pi}{2} - \frac{A_p}{2} - \theta_{ext}\right)}{n_p}\right] \tag{1.13}$$

$$\theta_{ext} = \frac{\pi}{2} - \frac{A_p}{2} - \arcsin\left[n_p \sin\left(\frac{\pi}{2} - \frac{A_p}{2} - \theta_{int}\right)\right] \tag{1.14}$$

The second strategy, called objective-based SPR, works by using an oil-immersion microscope objective to get rid of the air/glass interface (**Figure 1.7c**). It has been first demonstrated by Kano *at al.* in 1998 [44]. The objective must have a numerical aperture (NA) high enough to access angles of illumination and collection greater than θ_{res} : $NA_{min} \geq n_p \sin(\theta_{res})$. Using a N-BK7 gold-coated coverslip with a matching index oil $NA_{min} \geq 1.45$. Experimentally, it is also indispensable to access angles greater than θ_{res} and objective-based SPR in water can only be performed by very-high-NA immersion-oil objectives, such as the ones used for Total Internal Reflection Fluorescence microscopy (TIRF) which only exist in high magnification ($\times$60 or $\times$100).

The use of guided mode in optical fibers represents the third strategy for glass-coupling SPR, and was demonstrated by Jorgenson and See in 1993 [45]. Several configurations are in use, but most of them are based on the etching of the cladding, of optical index n_c, and the deposition of metal on the core of the fiber, of optical index $n_f > n_c$ and $n_f > n_d$ (**Figure 1.7d**) [34]. Here, the coupling occurs for particular propagation modes rather than for an angle of incidence on the metal, so it is more convenient to determine λ_{res} instead of θ_{res}. Unlike prism or objective-coupling, fiber-based SPR does not provide images, and will not be analyzed more deeply in this study.

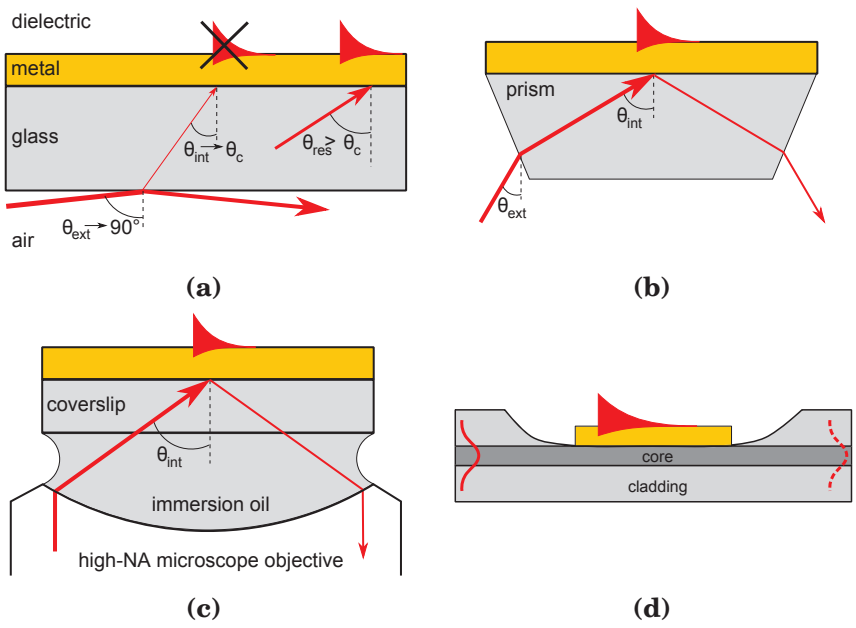

Figure 1.7: Techniques for glass coupling. **(a)** Critical angle illustration. The direct illumination of a parallel glass slide coated with metal cannot generate SP since $\theta_{res} > \theta_{c,glass/air}$. **(b)** Prism coupling. The base is coated by the metal. By adapting the apex angle A_p, θ_{int} can range from 0 to 90°. **(c)** Objective coupling. θ_{int} can be greater than $\theta_{c,glass/dielectric}$. **(a)** Fiber coupling. A part of the light propagating into the fiber couples to SP resulting in a drop of the output intensity.

1.1.1.6 Sensitivity of the angle of resonance

By replacing ϵ_d of **Equation 1.12** by n_{eff}^2 of **Equation 1.6**, θ_{res} can also be evaluated as a function of h_{bio}. **Figure 1.8** shows that the adsorption of a thin biolayer (< 50 nm) induces a proportional shift of θ_{res}, while for a thicker biolayer θ_{res} tends to $\theta_{res,bio}$, where $\theta_{res,bio}$ is the resonant angle in a dielectric of optical index n_{bio}. In other words, a biological process that induces an increase of refractive index at the interface can be converted by SPR into a measurable signal, which **Figure 1.8b** gives the "angular sensitivity". As it has been done for **Figure 1.3b**, this partial derivative is calculated as the shift of θ_{res} induced by the adsorption of a 1-nm-thick biolayer. It should be mentioned that lower n_p exhibit higher $\partial\theta_{res}/\partial h_{bio}$ (**Appendix Figure A.4**).

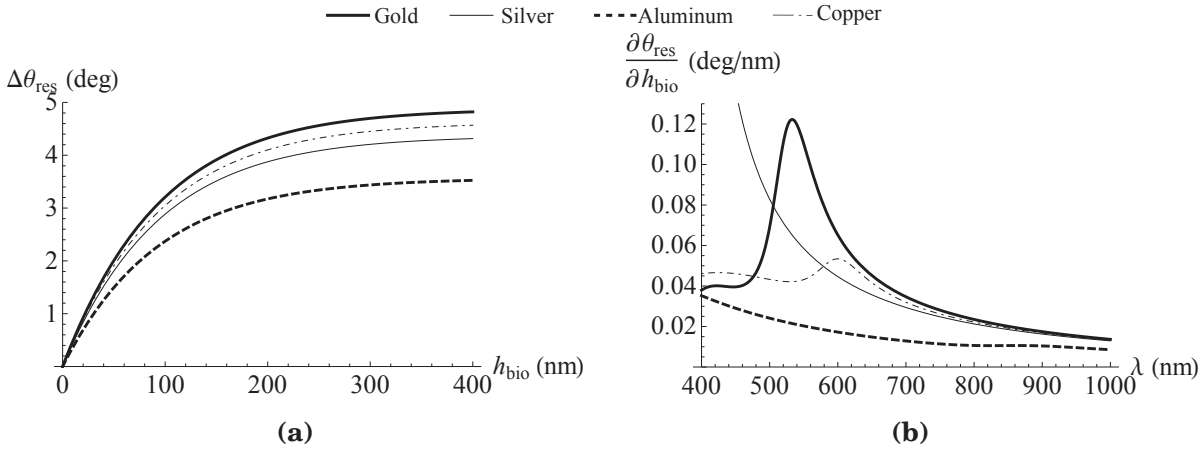

Figure 1.8: Variation of the resonant angle $\Delta\theta_{res}$ as a function of h_{bio} and λ for N-SF66 glass. **(a)** $\Delta\theta_{res}$ as a function of h_{bio} at λ = 632 nm. **(b)** Partial derivative of θ_{res} with respect to h_{bio} for $h_{bio} << L_z$. The derivative is equal to $\Delta\theta_{res}$ as a function of λ for h_{bio} = 1 nm.

Focusing on the angle of resonance at a fixed wavelength is called the "angular-modulation" while focusing on the wavelength of resonance at a fixed angle or in an optical fiber is called the "wavelength-modulation."

However, to evaluate the ability for a SPR device to detect the adsorption of a small layer, the signal to noise ratio (SNR) of the angle or wavelength measurement is also required. This SNR depends on the shape of the curve $R = f(\theta)$ or $R = f(\lambda)$, also called the "plasmon curve." The thinner the resonant peak, the better the SNR [34]. The plasmon curve is not given by the plasmonic approach, so it is crucial to use another approach to access the reflectivity as a function of the different parameters: θ, λ, n_d, d_m, h_{bio}...

1.1.2 | SPR, the optical approach

The optical approach is based on the resolution of Maxwell's equations for a plane electromagnetic wave arriving on a multilayer system. As schematically represented in **Figure 1.9**, each layer i is fully represented by three constants: its complex relative permittivity $\epsilon_i(\lambda)$, its complex relative permeability $\mu_i(\lambda)$ and its thickness h_i, except for the first and last layers which are semi-infinite. Only non-magnetic materials are treated here, so μ_i = 1. Moreover, since the first layer is the glass substrate, $\Im\{\epsilon_1\}$ = 0.

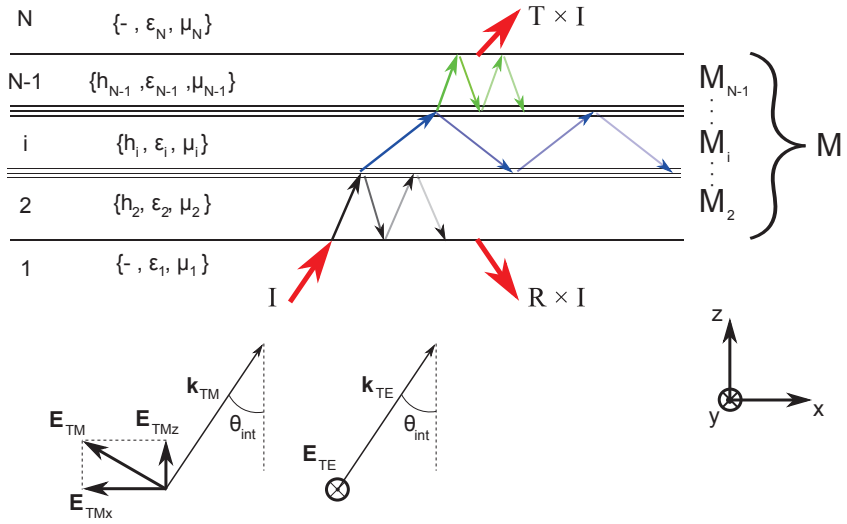

Figure 1.9: Schematic illustration of a stratified medium undergoing multiple reflections and transmissions

As in the plasmonic approach, Maxwell's equations and continuity conditions at the interface relate the electric field $\vec{E}_i$ in any layer i to $\vec{E}_{i-1}$. By propagating these relations over the entire system, $\vec{E}_N$ can be expressed as a function of $\vec{E}_1$, which enables the calculation of the reflection coefficients in amplitude r_{TM} and r_{TE}, as well as in intensity $R_{TM} = |r_{TM}|^2$ and $R_{TE} = |r_{TE}|^2$ (also called reflectivity or reflectance).

The propagation is made very practical by the use of the transfer matrix formalism, first established by Abélès in 1950 [46] , and later extended by Hansen in 1968 [47]. In this formalism, a matrix $M_i = f(h_i, \epsilon_i(\lambda), \mu_i)$ is associated with each one of the N-2 finite layers. The ratios of the tangential components E_x and E_y in successive layers are given by a function of M_i and the angle of incidence θ_i on the considered interface. The angles of incidence are just a function of the optical properties of each layer, so $\theta_i = f(\theta_1, \epsilon_1, \epsilon_2, ..., \epsilon_i)$. The beauty of this formalism lies in the fact that the global transfer matrix M of the whole system is simply obtained by multiplying the intermediate matrices: $M = M_2\ M_3\ \cdots\ M_{N-1}$. The reflectivity in both TM and TE mode can thus be calculated as a function of θ_{int} (=θ_1), λ and the list $\{h_i, \epsilon_i, \mu_i\}$ of each layer:

$$R = f(\theta_{int}, \lambda, \{\epsilon_1, \mu_1\}, ..., \{h_i, \epsilon_i, \mu_i\}, ..., \{\epsilon_N, \mu_N\}) \tag{1.15}$$

The transmission T, the adsorption A = 1-T-R and the relative electric field intensities $I_i(z)$, where i = x, y or z, can also be calculated by the same way. However, the wavevector of the EW propagating in the X axis remains strictly equal to the horizontal component of the one of the incident EW: $k_x = (2\pi/\lambda)\sqrt{\epsilon_1}\sin(\theta_{int})$. Here, k_x is purely real, so this approach does not show any intensity damping in the propagation direction, and thus, do not allow to calculate the propagation length of the SP.

1.1.2.1 The plasmon curve

It is now possible to trace the theoretical plasmon curve of a multilayer system that corresponds to the experimental sample. Most noble metals, such as gold or silver, exhibit a poor adhesion on glasses. This can be solved by inserting a very thin layer of titanium or chromium. In the following numerical simulations, a 2-nm-thick adhesion layer of chromium is taken into account. The first reported plasmon curve was obtained by Turbadar in 1959 on a silver-coated prism [48]. Unfortunately, at this time, the SPR effect was not as famous as it is nowadays, and the author did not link his observations to it.

The plasmon curves at λ = 632 nm for gold, silver, aluminum and copper coatings on a N-SF66 glass are plotted in **Figure 1.10a**. As predicted, the SPR effect only exists in TM mode, where the adsorption of a thin dielectric layer induces a positive shift of the resonant angle, so the entire curves are shifted to the right. Note that the curve shape remains almost equal, especially close to θ_{res}, so the adsorption can be seen as a simple translation. This approximation remains true for thin adsorbed layer with a purely real permittivity ($\Im\{\epsilon\}$ = 0) [49]. As a consequence, the presence of the biolayer induces a positive contrast (increase of reflectivity) for illumination angles lower than θ_{res}, and a negative contrast for angles greater than θ_{res} (**Figure 1.10b**). Here, the metal thicknesses d_m are optimized so the contrast is maximal (Au: 53 nm, Ag: 53 nm, Al: 16 nm and Cu: 30 nm). This optimization will be described and discussed in the next chapter.

Besides the angular and wavelength modulation, focusing on the shift in reflectivity at a fixed angle represents the third sensing method where ΔR characterizes the sensitivity, and is called the "intensity-modulation." As for now, we will especially focus on this last method which is widely used in SPR imaging.

1.1.2.2 Sensitivity in reflectivity

The angle where the increase of reflectivity ΔR reaches a maximum is called the working angle θ_w. In the approximation of a simple curve translation, ΔR_{max} is given by :

$$\Delta R_{max} = \Delta\theta_{res} \times -\frac{\partial R}{\partial\theta}(\theta_w) \tag{1.16}$$

As it can be seen by comparing **Figure 1.10b** with **Figure 1.10c**, for a thin biolayer, θ_w is equal to the angle where the slope $\partial R/\partial\theta$ is minimal. But as $\Delta\theta_{res}$ increases, θ_w tends to θ_{res}. Due to the difference of $\Delta\theta_{res}$ between these metals, a metal with a high absolute value of the angular slope does not necessarily exhibits a high contrast (Al for instance). The critical angle at the N-SF66/water interface is visible at 44°, but does not lead to any increase of reflectivity for adsorbed layers.

As for the angular sensitivity, the sensitivity in reflectivity is a function of both h_{bio} and λ. **Figure 1.11a** shows that ΔR_{max}, shortened by ΔR, is proportional at 95% to h_{bio} in the first 3.4 nm at λ = 632 nm. For thicker biolayers, θ_{res} continues to increase proportionally, but at a fixed working angle θ_w the derivative $\partial R/\partial\theta \to 0$ as the plasmon curve moves to the right. Consequently, ΔR for h_{bio} = 1 nm is also equal to $\partial R/\partial h_{bio}$ for a thin biolayer, and the sensitivity can be expressed in %/nm, as presented in **Figure 1.11b**. The detailed calculation of these curves is discussed in the next chapter. Let's just notice that, except for Al, the sensibility increases with λ, and a biolayer of only 1 nm can induce reflectivity shifts up to several %.

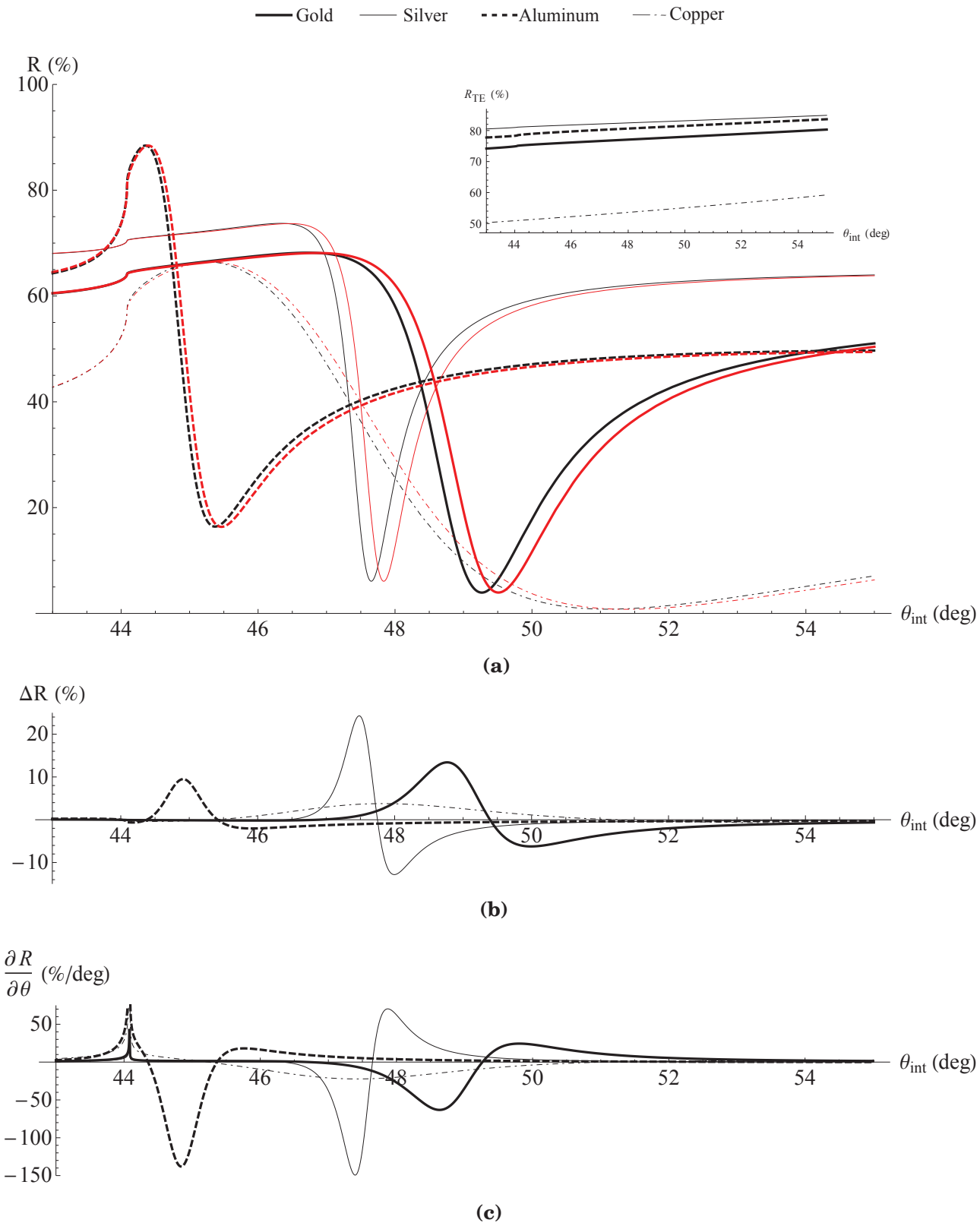

Figure 1.10: Plasmon curves at λ = 632 nm for gold, silver, aluminum and copper. **(a)** Plasmon curves for metal thicknesses optimized for sensitivity (Au: 53 nm, Ag: 53 nm, Al: 16 nm and Cu: 30 nm) in water (black) and for an additional biolayer of 5 nm (red, slightly shifted to the right) Inset: same simulation in TE polarization showing no SPR effect. **(b)** Contrast, e.g. difference between the two plasmon curves. **(c)** Angular slope of the plasmon curves in water.

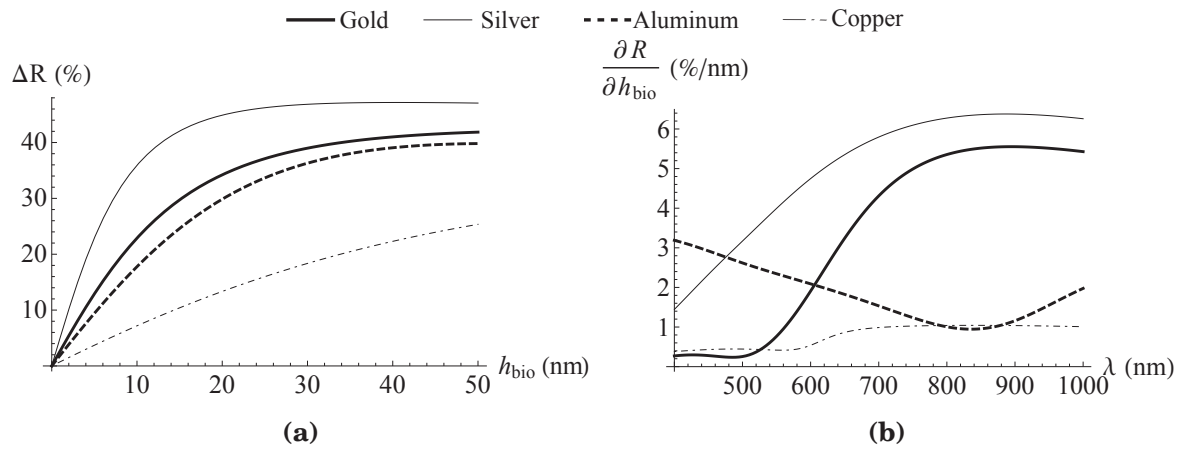

Figure 1.11: Reflectivity variation ΔR as a function of h_{bio} and λ at optimal metal thicknesses and angles. **(a)** ΔR as a function of h_{bio} at λ = 632 nm. **(b)** Variation of R as a function of λ for h_{bio} = 1 nm. This is a numerical simulation of the partial derivative of R with respect to h_{bio} calculated at a pitch of 5 nm in wavelength. The 121 points of each curve are linked by straight lines. The scatter are not shown for the sake of clarity.

1.1.2.3 The propagation length L_x for a finite metal thickness

As shown by Homola [31], the wavevector of the surface plasmon is perturbed by the presence of the coupling glass when considering a finite metal layer. The perturbed wavevector can be calculated by adding a perturbation term to k_{SP}:

$$\tilde{k}_{SP} = k_{SP} + \Delta k_{SP} \tag{1.17}$$

In the wavelength range where $|\epsilon'_m| \gg \epsilon_d$ and $|\epsilon'_m| \gg \epsilon''_m$, Δk_{SP} can be approximated by the following literal expression:

$$\Delta k_{SP} = \frac{4\pi}{\lambda} r_{pm} \exp\left(i\, 2k_{mz}\, d_m\right) \left(\frac{\epsilon_d \times \epsilon_m}{\epsilon_d + \epsilon_m}\right)^{3/2} \frac{1}{\epsilon_d - \epsilon_m} \tag{1.18}$$

where

$$r_{pm} = \frac{\epsilon_m\, k_{pz} - \epsilon_p\, k_{mz}}{\epsilon_m\, k_{pz} + \epsilon_p\, k_{mz}} \tag{1.19}$$

$$k_{mz} = \sqrt{\left(\frac{2\pi}{\lambda}\right)^2 \epsilon_m - k_{ph,x}^2} \tag{1.20}$$

$$k_{pz} = \sqrt{\left(\frac{2\pi}{\lambda}\right)^2 \epsilon_p - k_{ph,x}^2} \tag{1.21}$$

with d_m the metal thickness, and $k_{ph,x}$ the X axis component of the wavevector of the incident light wave, as defined by **Equation 1.11**. For silver and gold, the wavelength range where the condition on permittivities is valid starts at λ = 550 nm, while for aluminum and copper, $|\epsilon'_m|$ is never more than twice larger than ϵ''_m (**Appendix A.1**). We might thus expect Δk_{SP} to be less accurate for these latter metals.

The propagation length should then be recalculated to take into account the perturbation term:

$$L_x = \frac{1}{2 \times \Im\{k_{SP} + \Delta k_{SP}\}} \tag{1.22}$$

As shown in **Figure 1.12a & b**, for both gold and silver, the corrected propagation length is always smaller than the one predicted by the semi-infinite media model. Nonetheless, both models converge for thicknesses greater than ∼100 nm. For the typical thickness of ∼50 nm used for both gold and silver in SPR literature, we may then expect the propagation length to be about twice less than the one predicted by the widely used **Equation 1.7**. For the thicknesses which maximize the sensitivity, L_x is effectively half the one obtained by the semi-infinite media model (**Figure 1.12c & d**). It can be shown that Δk_{SP} is almost independent on n_p and θ_{int} close to the resonant angle. Moreover, it is principally imaginary, and thus does not perturb significantly θ_{res}, $\Delta\theta_{res}$ and L_z, especially for gold and silver above λ = 550 nm.

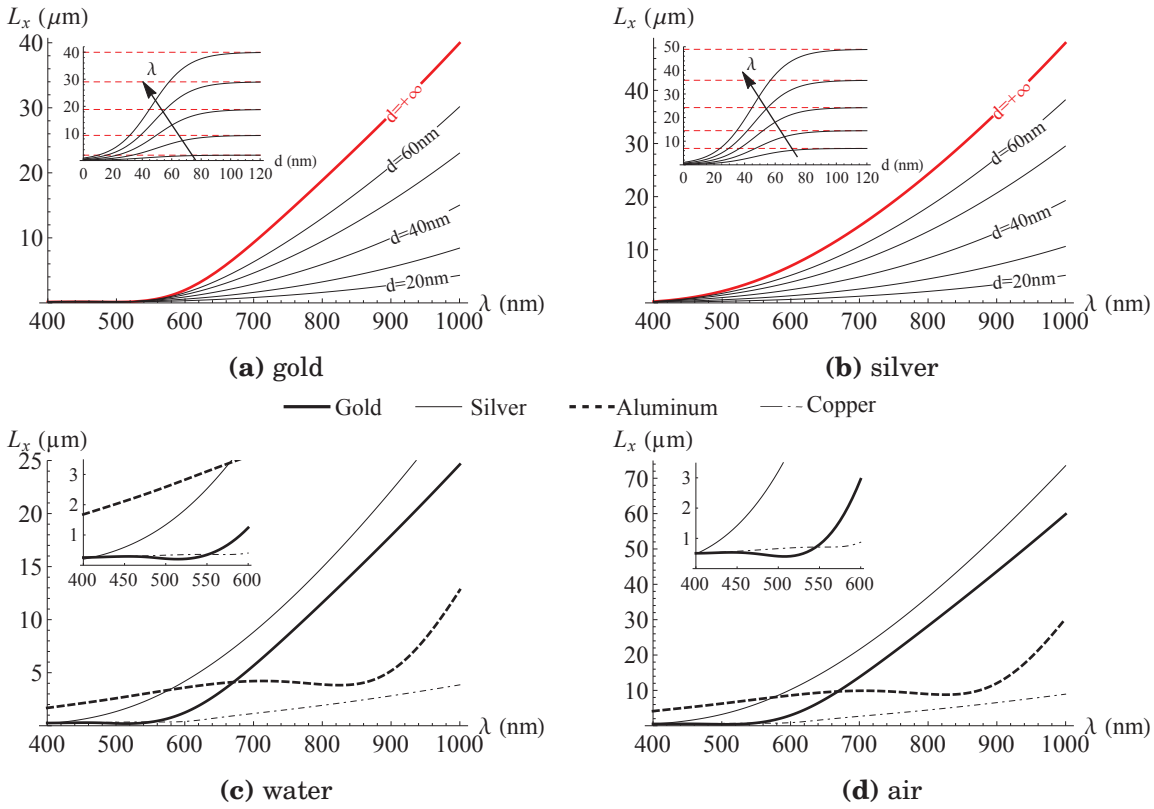

Figure 1.12: Corrected propagation length L_x as a function of λ. **(a)** N-SF66/gold/water interface for different thicknesses. The red thick line is the non-corrected $L_{x,SIM}$. **(b)** Same analysis for the N-SF66/silver/water interface. Insets: L_x with respect to d_m for λ = 600, 700, 800, 900 and 1,000 nm. The red dashed lines correspond to $L_{x,SIM}$. **(c)** N-SF66/metal/water interface with the optimal metal thicknesses used in **Figure 1.11**. **(d)** Same analysis for air. Insets: magnification on shorter wavelengths.

1.2 | Biosensing by SPR

A biosensor (or biochip) is based on the interaction between four elements [50]:

- the target (or analyte): the molecule or microorganism of interest
- the probe (or ligand): the molecule grafted on the surface of the biochip that is specific to the target. The surface is said to be "functionalized" by the probe.
- the transducer: the mechanism that converts the recognition probe/target into a measurable quantity
- the signal: the final physical signal measured by an instrument

In the case of SPR-based biosensors, the transducer is the SPR effect that converts the change of effective refractive index, resulting from the arrival of the target on the functionalized surface, into a shift of reflectivity, and the signal is a light intensity.

1.2.1 | SPR biosensors

The high sensitivity of surface plasmons to the adsorption of thin biolayers on metal surfaces have led SPR to become one of the major biosensing techniques. Unlike label-based techniques, generally relying on fluorescence, chromogenic or radioisotope detection [51], SPR does not require additional reagents and labeling steps to monitor biochemical reactions: it is a label-free technique. As a consequence, the kinetics of biological and biochemical interactions can be monitored in real-time.

The development of label-free and real-time biosensing techniques is a highly multidisciplinary field at the interface between physics, chemistry and biology. During the last decades, many technologies have emerged, generally based on electrical [52], mechanical [53] or optical transduction (SPR, diffraction [54], interferences [55, 21],...). They enable to access the kinetics of biological or biochemical processes in vivo, while label-based biodetection usually gives end-point results [56, 9]. However, most of them still remain several orders of magnitude less sensitive than labeling techniques, so both approaches should rather be seen as complementary [57].

Another advantage offered by glass-coupled-SPR is that the observation is performed in the lower half-space, so it can be simultaneously combined to other characterization techniques situated in the upper half-space, such as optical microscopy (bright-field, dark-field, differential interference contrasts, fluorescence, confocal...) [58] or Atomic Force Microscopy (AFM) [59, 60]. The enhancement and confinement of the electric field intensity at the surface can even be used to improve the sensitivity of Total Internal Reflection Fluorescence (TIRF) microscopy [61], so that both observations can be correlated [62]. The accessibility of the biochip surface is also useful to directly implement micro-devices, for example surface acoustic wave actuators [63] or microfluidic structures [64] that have demonstrated the ability to improve the SPR sensitivity and rapidity by mixing the analyte solution. Finally, the conductivity of the metal layer can be used to perform simultaneous electrochemical measurements (EC-SPR) [65, 66].

The first use of SPR for biosensing dates back to 1983 when Liedberg *et al.* detected the specific recognition between two proteins [5]. Since then, SPR has been used on a multitude of biomolecule interactions, including DNA [67], proteins [9], sugars [68], as well as small molecules such as toxins and drug residues [69].

More recently, analyses on living cells have emerged as a new challenge for SPR. SPR has been used in fundamental research to address cell biology issues [70, 71], as well as in the health and food industry where it has also demonstrated the ability to rapidly detect bacteria at low concentrations in complex and turbid media [72]. Unlike labeling methods, SPR preserves the integrity of the cells and brings results closer to the true physiological conditions [57].

1.2.2 | Surface functionalization

Metal surfaces, especially gold or silver previously activated by plasma treatment, show a relatively strong physical adsorption due to electrostatic forces when exposed to charged molecules [73]. This simple functionalization can be used to directly deposit proteins [5], as well as poly-L-lysine, known for its ability to anchor bacteria [74]. However, this technique does not apply for many probe molecules for whom a more controlled and reliable functionalization is required.

More specific surface chemistries have been developed in the last three decades. Since its first demonstration in 1983 by Nuzzo and Allara [75], the use of self-assembled monolayer (SAM) has become a well known strategy to covalently anchor organic molecules to metal surfaces [76]. A more recent technique, introduced by Livache *et al.* in 1994 [77] and widely used in our laboratory, is based on the electro-copolymerization of pyrrole monomers grafted by the probe biomolecules.

If the functionalization is localized on the surface, the active area is called a "spot." Note that a surface chemistry can be used to increase the specificity of biorecognition, but also to decrease the non-specific adsorption by "blocking" the surface [78].

Even if the four metals considered in this study have been used in SPR, gold is by far the most common and convenient in biological applications because it is stainless in aqueous solutions and biocompatible [79].

1.2.3 | Kinetics measurements by the Langmuir model

In a first approximation, the interaction between a target and a probe is governed by the Langmuir model [80]. In this simple model, the interaction leads to the temporary formation of a probe-target complex, with association and dissociation constants k_{on} and k_{off}, respectively. When the interaction takes place on a surface, the complex surface coverage ρ can be defined by:

$$target + probe \underset{k_{off}}{\overset{k_{on}}{\rightleftharpoons}} complex, \qquad \rho = \frac{complex\ surface\ density}{probe\ surface\ density} \tag{1.23}$$

If the shift in reflectivity remains small, the SPR signal is proportional to ρ which follows the differential equation [81]:

$$\frac{d\rho}{dt} = k_{on}\, c_t\, (1-\rho) - k_{off}\, \rho \tag{1.24}$$

where k_{on} is expressed in $M^{-1}\, s^{-1}$, k_{off} in s^{-1} and the concentration of target c_t in M (mol/L). The solution of **Equation 1.24** for $\rho(t=0)$ = 0 leads to the equation of association that describes the evolution of the signal when the target solution arrives on the functionalized metal surface:

$$\rho_{on}(t) = \rho_{eq}\, [1 - \exp(-t/\tau)] \tag{1.25}$$

where $\tau = (k_{on}c_t + k_{off})^{-1}$ (s) is the characteristic association time constant and $\rho_{eq} = (k_{on}c_t)/(k_{on}c_t + k_{off})$ is the equilibrium surface coverage. If the biosensor is rinsed after it has reached the equilibrium, $\rho(t)$ must satisfy **Equation 1.24** with $\rho(t=0) = \rho_{eq}$ and c_t = 0. The equation of dissociation is then given by:

$$\rho_{off}(t) = \rho_{eq}\, \exp(-k_{off}\, t) \tag{1.26}$$

The typical kinetics curve of a biodetection is plotted in **Figure 1.13**. At t=t_{on}, the target solution is injected, and the signal is driven by the association equation. At t=t_{off}, the surface is rinsed by the original buffer solution and the signal follows the dissociation equation with a characteristic dissociation time constant equal to $1/k_{off}$. k_{on} and k_{off} can be obtained by fitting both parts of the kinetics curve. Note that a more coherent fit may require a more complex model, taking into account the effect of diffusion, mass transport and non-equilibrium states [81].

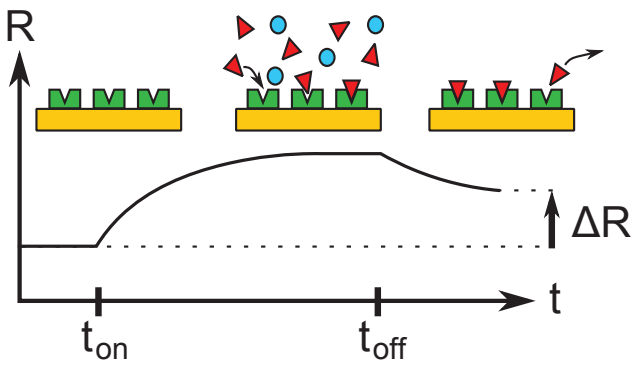

Figure 1.13: Typical kinetics curve of a biodetection monitored by SPR. Only the specific targets (red triangles) interact with the probes (green).

For protein-protein binding, and especially for cytokines, the dissociation time $1/k_{off}$ is in the order of several hours [80, 82], so the dissociation can be neglected if ΔR is measured straight away after the end of an injection. The same approximation can be done for the interaction of long DNA strands, such as the "ZIP" sequences used as standard DNA/DNA interaction models [83].

So far, only the global surface response has been envisioned. But in the view of cellular analyses, imaging the surface of the biochip is essential to be able to discriminate the signal coming from the cells, for example due to a change of position, morphology [14, 84] or inner refractive index [62], and the signal coming from outside the cells, such as a secretory activity [71].

1.3 | SPR imaging

The performances of biosensing imaging techniques, such as SPR or fluorescence, are characterized by mainly four parameters:

- sensitivity: the relative increase of signal due to a given biological events (a ratio in %)
- spatial resolution: the minimal distance between two distinguishable point source (a length)
- temporal resolution: the minimal time between two distinguishable events (a frequency, usually in frames per second, fps)
- field-of-view (FOV): the observed surface in a single image (an area, usually in mm^2)

SPR imaging was invented independently by two groups: Yeatman and Ash (London, England) in 1987 [6], and by Rothenhäusler and Knoll (Munich, Germany) in 1988 [27]. Both articles were named "Surface plasmon microscopy" and used the Kretschmann configuration with a silver-coated prism in air environment. The authors demonstrated that when the base is viewed through the exit face of the prism, the SPR effect could induce a high contrast between the bare silver and thin film coated areas. In 1990, SPRi was used for the first time in a biological application (imaging of tissues) by Okamoto and Yamaguchi [85].

The large majority of SPRi devices work in intensity-modulation, however, spectral-modulation [86], as well as angular-modulation [87], can also be implemented in imaging mode. Such hybrid modulations can improve the limit of detection and the dynamic range while being less sensitive to the bulk refractive index change or the detection area heterogeneity.

1.3.1 | Prism-based SPR imaging

The typical set-up used in prism-based SPRi is schematically represented in **Figure 1.14**. Because the reflectivity is very sensitive on the angle of incidence on the metal θ_{int}, the whole prism base has to be illuminated by a low angular divergence beam. This is usually obtained by a single lens which collimates a monochromatic point source. The beam then is passed through a linear polarizer to obtain a TM or TE polarization. The refraction occurring at the entry face of the prism modifies the angle of the rays from θ_{ext} to θ_{int} with respect to the vertical. At the exit face, the refraction also creates a virtual image of the metalized base (dashed line). A real object AB appears as A'B' from outside the prism. This virtual image becomes the object of an imaging system which forms a final image on a camera sensor (A"B"). The location of this virtual image, and thus the value of the angle α, depends on the apex angle A_p and on the refractive index n_p.

For the entire FOV to be in focus, the final image has to be coincident with the camera sensor. This issue has been deeply treated by Maillart in 2004 [88] who proposed optimal conditions on n_p and A_p that makes $\theta_{CCD} = \theta ext \Leftrightarrow \alpha = 0$, in order to obtain FOV of ~ 100 mm^2 with a simple and inexpensive imaging system. Such prisms will be referred to as "very-wide-FOV optimized." This configuration is patented [89] and is the one of Horiba Scientific SPRi devices, widely used in our laboratory. More complex imaging systems can also be envisioned [90].

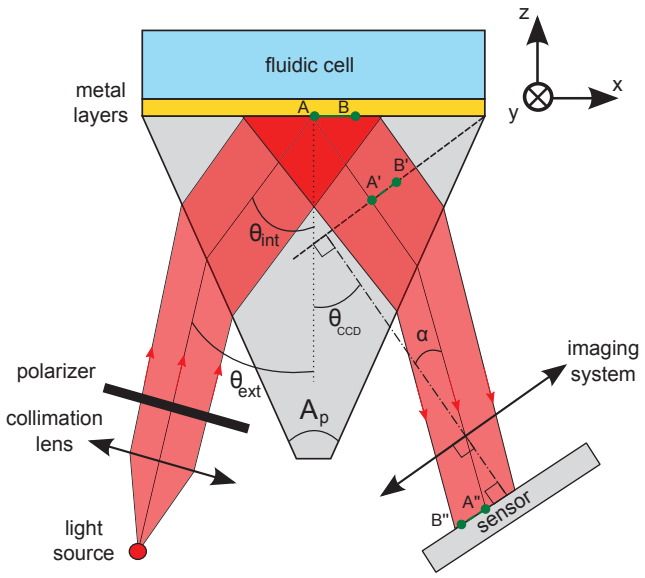

Figure 1.14: Typical prism-based SPR imaging set-up

Since the beginning of SPR imaging, L_x has been pointed out as the limiting factor for the spatial resolution [7], and widely studied, especially by de Bruijn *et al.* [15], Berger *et al.* [16, 91] and Yeatman [49]. The fact that both L_x and sensitivity increase with λ is a well-known issue of SPR imaging literature. It has been stated that high spatial resolution imaging cannot be performed with a high sensibility, and inversely, making spatial resolution the "pet hate" of prism-based SPRi [92]. This point is treated and discussed in the second part of the next chapter.

1.3.2 | Objective-based SPRi

1.3.2.1 Scanning objective-based surface plasmon microscopy

In 1998, Kano *et al.* showed that oil-immersion microscope objectives can also give SPR images of the metal/dielectric interface [44]. Contrary to prism-based imaging, the sample has to be scanned in the X and Y axis by a focused beam of light with rotation symmetry around the optical axis [93]. This can be performed either by moving the sample with a piezo-electric stage [94], or by moving the beam with acousto-optic modulators [95]. Because the angles of incidence cover a broad range around θ_{res}, the contrast between different areas is extremely small. But by imaging the back focal plane of the exit pupil of the microscope objective, the Fourier transform of the image that would have been seen by a standard inverted microscope can be obtained. This frequency domain image shows two thin dark arcs at the position k'_{sp} (nm^{-1}) corresponding to the SPR effect. The effective refractive index in the dielectric can be deduced from the radius of the arcs. In this technique, the spatial resolution is mainly governed by the size of the focused beam and by the pitch of the surface scanning. Here, the light is sent and collected in almost every direction (the polarization remains linear so the arc contrast reaches zero at two opposite angles). As a consequence, the propagation length does not induce anisotropy in spatial resolution, which can be one order of magnitude less than L_x. In 2007, Berguiga *et al.* measured a resolution better than 200 nm at λ = 632 nm in water [96], which can be considered as the ultimate resolution of all optical surface plasmon imaging techniques. The FOV is not intrinsically limited by the objective, but directly proportional to the time needed to scan the desired surface. Reported images have a FOV less than 50×50 μm^2.

1.3.2.2 Wide-field objective-based surface plasmon microscopy

In 2004, Stabler *et al.* demonstrated that objective-based SPR can also provide direct 2D images [92]. In this configuration, the illumination beam is focused at the back focal plane of the microscope objective which is conjugated with a ring-shaped mask, so that only parallel rays at θ_w or θ_{res} reach the metal surface, also with rotation symmetry around the optical axis. The surface is finally imaged as in conventional microscopy. L_x induces a small anisotropy and limits the resolution in the polarization direction, while in the perpendicular direction the resolution is limited by the NA of the objective [97]. In a second configuration, proposed by Huang *et al.* in 2007 [98], the SP are excited in only one direction (no symmetry with respect to the optical axis). As a consequence L_x induces a strong anisotropy and limits the resolution in the propagation direction [66]. Perpendicular to the SP, the resolution is limited by the effective NA corresponding to the light diffusion of the object (which is smaller than the NA of the microscope objective) and is about 0.5 µm at λ = 632 nm [38]. Here, the FOV is limited by the objective (which does not exist in magnification less than $\times$60), and is usually less than 100$\times$100 µm^2. As in prism-based SPRi, the time resolution is limited by the frame rate of the camera or the exposure time.

1.3.3 | Applications of SPRi

SPRi presents two major advantages compared to other SPR biosensing techniques. First, it can monitor simultaneously hundreds of biomolecular interactions while other SPR techniques are usually limited to a few tens. Secondly, it can directly image individual biological objects, such as microorganisms.

For multi-parallel biosensing, prism-based SPRi is preferred over objective-based SPRi because it provides a wider FOV which makes easier to functionalize multiple areas of the biochip. The very-wide-FOV optimized configuration has demonstrated the ability to monitor more than a thousand DNA hybridizations [10]. Typical applications include the study of biomolecule interactions, such as in high throughput sequencing for genomics [8] and proteomics [9], and biodetection of microorganisms, for example bacterial detection for food safety [11].

For microorganism imaging, both imaging techniques are used. Due to its very-small FOV and high resolution, objective-based SPRi is very adapted to single cell analysis [95]. Herein, "single cell" means that only one cell is imaged and analyzed, while "individual cell" means that several cells are analyzed separately on a single image. In 2011, Wang *et al.* showed that internal processes can be precisely localized within a 25-µm-wide cell by coupling objective-based SPRi and electrochemical impedance [66]. Imaging a few microorganisms at a time is also possible, but is restricted to very small objects such as viruses [38]. Prism-based SPRi has also been used to image and study the local adhesion of a single cell [17] or a few cells with diameter ranging from $\sim$100 µm [18, 84] to $\sim$15 µm [14].

1.4 | Background in spatial resolution in prism-based SPRi

In optical imaging, the ultimate resolution is limited by the diffraction that arises from the wave nature of light. However, SPRi does not only rely on pure optics, and plasmonic effects should also be considered.

1.4.1 | The diffraction limit

Let us consider a point source diffusing light in all directions (Dirac signal). In the absence of plasmonic effects, the image of this point by an ideal imaging system (i.e. free of optical aberrations) has an axi-symmetrical shape, called an airy pattern, whose intensity can be approximated by $I(x) = sinc^2(a\,x)$, where x is the space variable and a is a parameter depending on the NA and λ [99]. $I(x)$ is called the Point-Spread-Function (PSF). The standard definition of

the spatial resolution, known as the Rayleigh criterion, states that two points can be distinguished if their separation is greater than the distance Δx between the maximum and first zero of the PSF, as represented in **Figure 1.15a-c**. Δx characterizes the spatial resolution limit and is given by $\Delta x \approx 0.6\,\lambda/NA$. Note that $I(x)$ is correctly fitted by a Gaussian function (**Figure 1.15d**) and $\Delta x \approx$ FWHM (Full Width at Half Maximum). The image of a real object is the convolution of the PSF and the function that describes the geometry of this object. As shown in **Figure 1.15e** an object with dimensions smaller than Δx can be considered as a good approximation of a Dirac signal and be employed to measure the experimental spatial resolution.

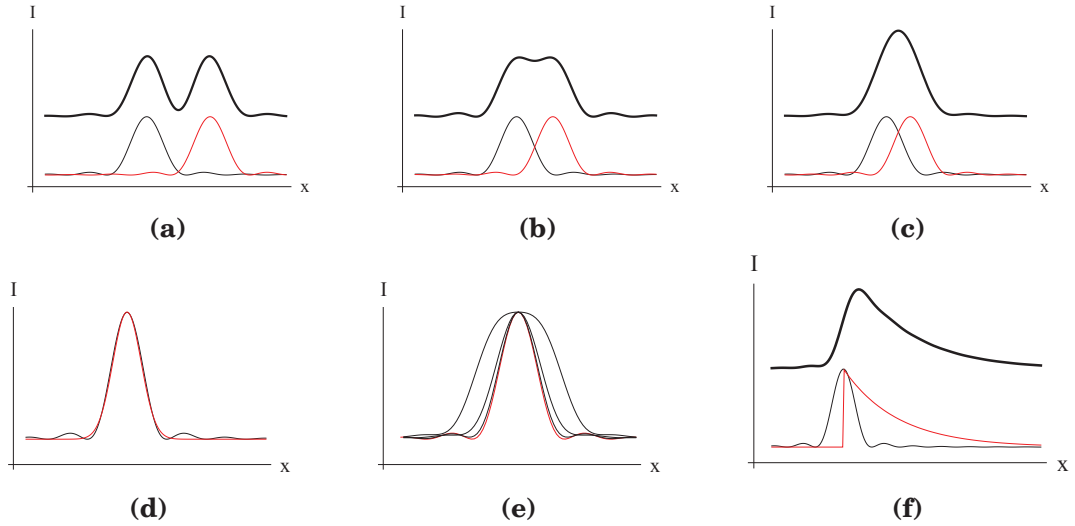

Figure 1.15: Rayleigh criterion and influence of L_x. The resultant signal is shifted for a better clarity. **(a)** Two airy patterns separated by more than the resolution limit. When summing both signals, each one of them is well distinguished from the other one. **(b)** Two airy patterns separated by the resolution limit. The final signal becomes ambiguous. **(c)** Two airy patterns separated by less than the resolution limit. The two signals are not distinguished, and the final signal is nearly equal to one signal of higher intensity. **(d)** An airy pattern fitted by a Gaussian function. **(e)** Convolution of the PSF with square functions of width 0 (red), $\Delta x/2$, Δx and $2 \times \Delta x$. **(f)** Convolution of a airy pattern and a decreasing exponential function corresponding to L_x.

1.4.2 | Additional spatial resolution limits in prism-based SPRi

In prism-based SPRi, according to literature, the main additional limitation comes from the effect of the propagation length (**Figure 1.15f**). The final signal is the convolution of the PSF and a decreasing exponential function of characteristic length L_x. The anisotropy caused by L_x is clearly visible after the Dirac signal, that is to say in the positive X direction by starting at the highest intensity point, but should remain small before (negative X direction). The volume of the prism is sometimes mentioned as another restriction for the use of high NA microscope objectives, which could also limit the spatial resolution [98, 97].

In spite of being a well-established technique, some aspects of the spatial resolution of prism-based SPRi seem to remain misunderstood. According to literature, the spatial resolution is L_x-limited in the propagation direction and diffraction-limited by the objective perpendicular to the SP [97, 100]. However, this is not the case for the very large majority of SPRi experiments. Let us comment on three aspects illustrating this misunderstanding.

1.4.2.1 Propagation length and diffraction limit

As shown by Berger *et al.* in ref. [16], the expected effect of L_x on spatial resolution in the propagation direction can be clearly seen at high magnification at the gold/air interface (**Figure**

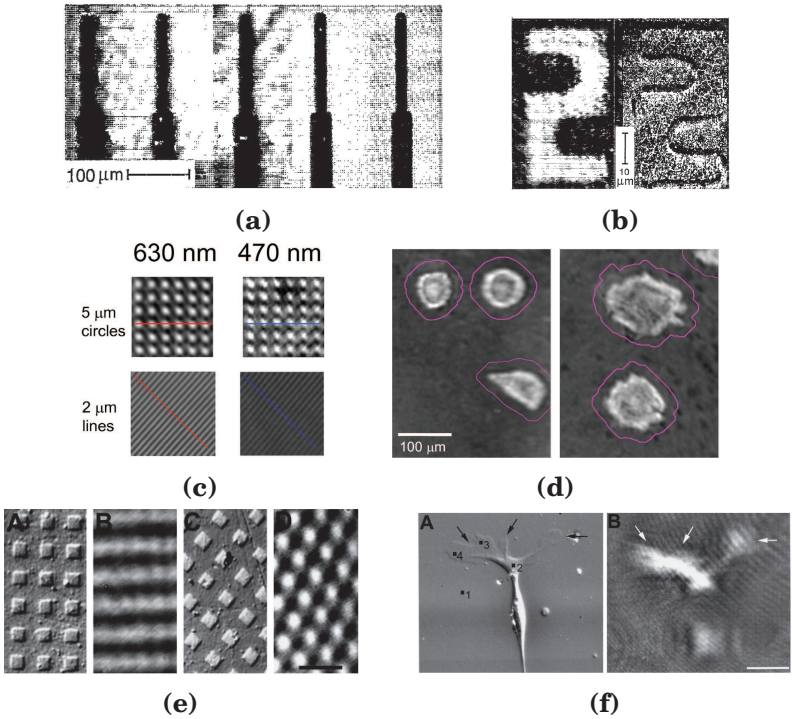

Figure 1.16: Incoherences in spatial resolution measurements: L_x and diffraction limit. **(a)** Anisotropy due to L_x at 676.4, 647.1, 632.8, 568.2 and 530.9 nm (from left to right). **(b)** Comparison between SPR (left) and AFM (right) images at λ = 530.9 nm. Scale bar: 10 µm (Figure (a) & (b) reprinted with permission from [16]. Copyright 1994, AIP Publishing LLC). **(c)** Influence of λ on spatial resolution at the Au/air interface.**(d)** SPR images at λ = 630 nm of cells deposited on a fibronectin coated gold in water (reproduced from ref. [18]). **(e)** Comparison between optical and SPR images of 6 × 6 µm metal square deposited on 53-nm-silver-coated prisms (left) and 15-nm-aluminum-coated prisms (right) at λ = 670 nm in air. SP propagate to the right. Scale bar: 20 µm. **(f)** Interference contrast (A) and corresponding SPR image (B) of a goldfish glial cell on an aluminum substrate. Scale bar: 100 µm (Figure (e) & (f) reprinted from Publication [17], Copyright (1999), with permission from Elsevier).

1.16a). However, perpendicular to the SP, the authors measure a resolution of 2 µm, which is more than 3 times larger than the diffraction limit of their imaging system (NA = 0.49, $\Delta x \sim$ 650 nm at λ = 530 nm) (**Figure 1.16b**).

Peterson *et al.* mention in ref. [18] that decreasing λ from 630 to 470 nm with a gold-coated prism in air does not induce a proportional improvement of spatial resolution in the propagation direction (**Figure 1.16c**). Moreover, giving a NA of 0.38, the diffraction limits are 990 nm and 750 nm, respectively. The experimental resolution in air is not precisely measured but seems close to these values. However, when imaging in water environment, the resolution significantly decreases, while L_x is 2.4 times smaller (**Figure 1.16d**).

In ref. [17], Giebel *et al.* measure a resolution perpendicular to the SP of 1 µm for both Al or Ag coating at λ = 670, but according to the images it is more likely close to 5 µm, while the diffraction limit should be $\sim$ 800 nm (NA = 0.5) (**Figure 1.16e**). Moreover, as for Peterson *et al*, a strong degradation of resolution is visible when switching from air to water environments (**Figure 1.16f**).

1.4.2.2 Field-of-view

In standard microscopy, it is a common habit to show successive magnifications of the same area presenting smaller and smaller FOV where the resolution is supposed to be improved respectively, since usually higher magnification objectives also have a higher NA [101]. Surprisingly, at the

best of our knowledge, there is no example of such images in SPRi.

Moreover, in a lot of SPR images, the resolution is not constant and is a function of one direction, leading to smaller effective FOV restricted to a clear stripe, with the rest of the image being blurred. This effect is clearly visible in **Figure 1.17a & b**, where both SPR images show an horizontal clear stripe. This may not be an issue when only the average intensity is monitored, such as in the first image, but when the shape of the object is also a key parameter, this effect strongly decreases the effective area of observation.

Obviously, this clear stripe effect is not visible if the images are cropped, and only display a small FOV, as it could be the case in **Figure 1.16a,b,c & e**.

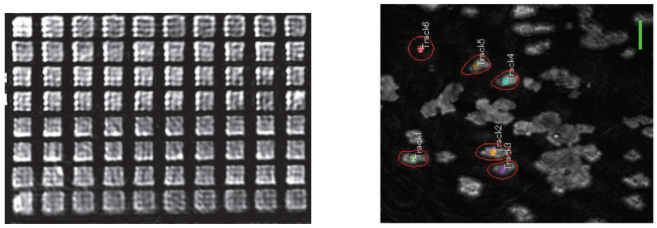

(a) **(b)**

Figure 1.17: Incoherences in spatial resolution measurements: presence of a clear stripe. **(a)** Bright rectangles correspond to areas of an SPR chip (300 × 300 µm) covered with a monolayer of albumin molecules formed on a gold surface (Reprinted with permission from [72]. Copyright (2008) American Chemical Society). **(b)** SPR image at λ = 630 nm of PAM212 cells deposited on gold in water environment. Scale bar: 20 µm (Reprinted from Publication [14], Copyright (2010), with permission from Elsevier).

1.4.2.3 Distortion

The last effect that has not been addressed so far is the distortion undergone by small objects as shown in **Figure 1.18a & b**. In the first image, as mentioned by the authors, the cells look almost 3 times larger than they are ($\sim$ 10 µm) while in the second image, they also have a star-like shape. These two distortions cannot be related to L_x since they are not anisotropic along only one direction.

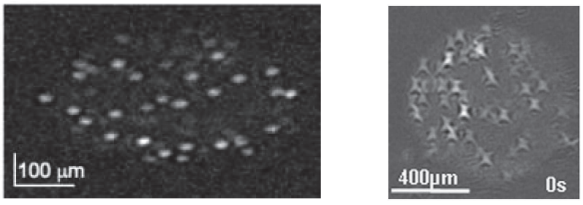

(a) **(b)**

Figure 1.18: Incoherences in spatial resolution measurements: distortion. **(a)** SPR differential image of an anti-CD19 antibody spot 20 min after binding of LS102.9 cells (Reproduced from [12] with permission of The Royal Society of Chemistry). **(b)** Individual B lymphocyte on a protein-DNA spot on gold at λ = 635 nm (Reprinted from Publication [13], Copyright (2012), with permission from Elsevier).

1.5 | Biological motivations and problematic of the PhD thesis

1.5.1 | Monitoring the secretion activity of individual eukaryote cells

Living organisms are composed of a multitude of different biomolecules (polysaccharides, lipids, proteins, nucleic acids...) in permanent interaction with each other and with the environment. But in a single cell, some of them are only present in a small amount (a few hundred or thousand). In a first approximation, we can assume that the number N of these biomolecules per cell in a genetically identical population follows a Poisson distribution law with a standard deviation equal to $\sqrt{N}$. This variability can represent up to a few %, and has been pointed out as a potential explanation for the large differences observed in terms of morphology and behaviors among homogenous populations of prokaryote [102] and eukaryote cells [103]. This intrinsic heterogeneity cannot be clearly identified by performing "bulk measurements" which only give average responses. As a consequence, the development of new devices which are able to access the individual cell level over relatively large populations have been subject to a growing interest [104].

The relevance of statistical data, and the ability to observe rare but important phenomenon at the cell scale, is crucial in the study of the immune system [105]. The main cells involved in the immune response are T and B lymphocytes. These non-adherent blood cells communicate between each other by secreting small proteins ($\sim$ 5 to 20 kDa) called cytokines. These biochemical messengers are involved in many different pathways including the activation, differentiation, secretion and proliferation of immune cells [106].

The detection of the secretory activity of individual immune cells following a specific stimulus is already a common technique used in research and clinical laboratories. It relies on label-based technologies, such as Enzyme-linked Immunosorbent Spot (ELISpot) [107], Intracellular Cytokine Staining (ICS) [108] or fluorescence [101, 82, 109, 110], which are able to measure multiple protein secretions by a population up to several thousands of cells. However, these techniques only offer single snapshots in time. By performing several experiments at increasing incubation time, the rate of secretion can be partially evaluated, but the precise kinetics of individual cells remains unknown. Moreover, the study of intercellular communications, for example the time of activation of a particular cell correlated to the secretion activity of the neighboring cells, is only accessible by real-time monitoring.

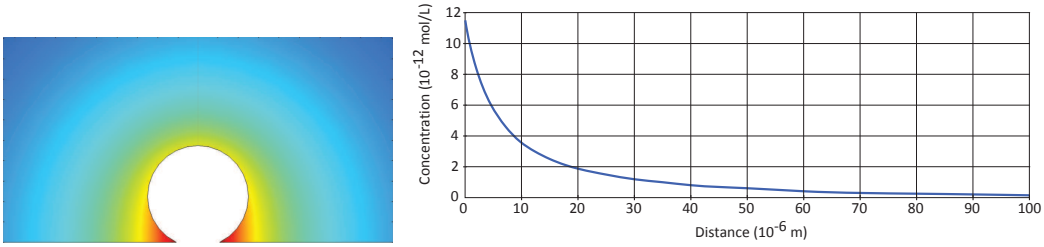

(a) **(b)**

Figure 1.19: Finite-element simulation of the protein concentration around a 10-µm-wide secreting cell by COMSOL Multiphysics. **(a)** 2D mapping at the steady-state. **(b)** Concentration at the surface with respect to the distance from the cell. The high concentration remains restricted to the close surroundings of the cell, typically in a radius of 15 µm. The simulation is performed with the following conditions: diffusion constant of 10^{-10} m^2/s, secretion rates of 10^{-13} mol·s$^{-1}\cdot$ m^{-2} (20 molecules/cells/s) [82], concentration null at a radius of 1 mm and at a height of 1 mm.

The kinetics of cellular secretion can only be answered by a label-free and real-time imaging technique that exhibits a high sensitivity to detect low amounts of secreted molecules (typical secretion rate are from 1 to 100 proteins per second and per cell [82]), a high resolution to clearly distinguish each cell from its neighbors (lymphocytes are $\sim$10 µm in diameter), and a wide-FOV

to simultaneously monitor at least a few thousand cells (secreting cells can represent less than 0,3% of a population [101]). **Figure 1.19** shows the typical profile of protein concentration in the surrounding of a 10-μm-wide secreting cell, where most of the signal is concentrated in a radius of 15 μm.

Prism-based SPRi appears as a high potential candidate. Previous works have shown that it fulfills separately each one of these requirements : high-sensitivity to cytokines secreted by primary cells (but not at the individual level) [111, 71], wide range of FOV from less than 0.1 mm^2 to a cm^2 [16, 10] and spatial resolution at the micrometer scale to access the individual cell level [18, 14, 112]. Nonetheless, in a cellular secretion experiment, all these aspects have to be combined simultaneously.

1.5.2 | Single cell adhesion studies

A high spatial resolution in SPRi at intermediate optical magnifications ($\times$10 to $\times$20) can also enable to spatially resolved the details within a multitude of individual adherent cells in contact with the biochip surface, such as the location of the focal points for instance. Studying the dynamic of cell/substrate adhesion has already been performed in SPRi [113, 84], but only on a few cells due to the restricted FOV. Once again, a wider FOV could bring more statistical data by simultaneously monitoring few tens of adherent cells.

1.5.3 | Pathogenic bacteria detection

The detection of pathogenic bacteria is another domain where high spatial resolution on wide FOV could bring new insights. Unlike conventional microscopy, SPRi only image the surface of the biochip. As a consequence it is not affected by the volume aspect of the sample, for example turbidity and color. This advantage is valuable in the monitoring of bacterial growth in complex and turbid media such as food matrices [114].

The two main specifications of bacterial detection methods are the detection-time and the detection-limit, in cfu/mL (colony forming unit). In 2013, it has been shown that the detection-limit could be significantly lower by using the so-called Culture-Capture-Measure (CCM) approach [11]. Since the concentration of bacteria varies exponentially with respect to the time passed into the reaction chamber, this detection-limit is also related to the detection-time.

In the previous experiment, only the mean intensities of each detection spot were measured as a function of the time. Then, in addition to the intensity, it may also be interesting to monitor spatial characteristics of each spot, such as the standard deviation, the skewness or the kurtosis. Such quantities could exhibit faster changes than intensity as well as bring complementary information on a bacteria strain.

Finally, the fundamental study of biofilm formation from a few bacteria and the effect of drugs on growth rate and local adhesion could also be addressed [115].

1.5.4 | Problematic of the PhD thesis: Spatial resolution in prism-based SPRi

In the two articles of **Section 1.4.2.3 Distortion**, it seems our laboratory was the first one to mention that the incoherences regarding spatial resolution could be due to optical aberrations, and pointed out the prism as being potentially responsible, but without further explanations. We also emphasized that the limitation of spatial resolution (and equivalently FOV) dramatically limits the study of microorganisms to low number of individuals, thus preventing relevant statistical data and observation of rare phenomena.

The aim of the PhD thesis is then twofold:

- Firstly, develop a new approach based on optical aberrations to address the issue of spatial resolution and image formation in prism-based SPRi. Despite the conceptual understanding

that could resolve the previous incoherences, our goal is to demonstrate the ability of prism-based SPRi to acquire images combining high resolution and high sensitivity on a wide range of FOV, that is to say make prism-based SPRi become a true microscopic technique.

- Secondly, apply the new capabilities of high resolution prism-based SPRi to the study of biological systems, such as individual secreting immune cells or bacterial growth/detection. This means build an automated set-up dedicated to biological experiments running over several hours.

2 | Spatial resolution in prism-based SPRi

Contents

Résumé du chapitre 2

Le chapitre 2 est consacré en premier lieu à l'étude de la formation des images et des aberrations géométriques dans les techniques d'imagerie à base de prisme. J'entends par là toute technique d'imagerie dont l'objet est la face interne de la base d'un prisme, et où les rayons passent par la face de sortie du prisme avant d'entrer dans le système optique d'imagerie, comme c'est le cas de la SPRi à couplage par prisme.

Après une courte introduction historique sur l'utilisation des prismes en optique, je présente les trois autres techniques d'imagerie à base de prisme connues à ce jour, et les compare à la SPRi. À travers des calculs de tracés de rayons, je donne, dans le cas d'un prisme quelconque, les expressions littérales des grandeurs importantes pour le design de systèmes optiques d'imagerie. J'analyse ensuite le cas particulier des prismes dont l'angle au sommet est optimisé pour faire des images en grand champ de vision avec un système optique simple et à faible ouverture numérique. Les aberrations géométriques inhérentes à cette optimisation sont analysées qualitativement. De cette analyse, émerge une seconde optimisation d'angle au sommet qui minimise les aberrations, et qui par conséquent, est optimisée pour offrir la meilleure résolution spatiale. De nouvelles expressions littérales des grandeurs optiques importantes sont calculées pour ces nouveaux prismes en fonction de leur indice de réfraction. Cette optimisation pour la résolution suggère l'utilisation d'un autre mode d'imagerie dit à "scan de lignes", en plus de celui dit "classique". En utilisant le modèle d'erreur du front d'onde, je quantifie les aberrations géométriques dues à la traversée de la face de sortie du prisme en fonction de l'angle au sommet pour trois verres commerciaux, et en fonction de l'indice de réfraction pour les prismes optimisés pour le grand champ de vision et pour la résolution.

La seconde partie de ce chapitre est dédiée à l'optimisation du compromis entre résolution et longueur de propagation des plasmons de surface en terme de métal, d'épaisseur de métal, et de longueur d'onde d'illumination. Cette optimisation permet aussi de mettre en lumière le fait que, pour l'or et l'argent, la sensibilité SPR en biodétection passe par un maximum pour des longueurs d'onde proches de 750 nm. Pour finir, le cas particulier d'un dépôt de métal hybride fait d'argent passivé par 5 nm d'or est analysé.

This chapter presents the physical mechanisms governing the spatial resolution in prism-based SPRi. The first part is devoted to the image formation principle and the analysis of optical aberrations induced by the prism and the imaging system. Using **Page 125** as an independent bookmark may facilitate the understanding of this first part. Specific values are given for SPRi, but the conceptual understanding can be applied to any prism-based imaging technique. The second part is dedicated to the optimization of the trade-off between sensitivity and propagation length in SPRi.

2.1 | Prisms and prism-based imaging techniques

2.1.1 | Prisms in optics

A prism is defined by the online Oxford dictionary as:

> *A solid geometric figure whose two ends are similar, equal, and parallel rectilinear figures, and whose sides are parallelograms.*

, and more specifically in optics by:

> *A glass or other transparent object in the form of a prism, especially one that is triangular with refracting surfaces at an acute angle with each other and that separates white light into a spectrum of colors.*

The first mentions of prisms date back to ancient history. They were named *vitrum trigonum*, as related by Pliny [116] and Seneca [117] who observed their ability to decompose white light (first century A.D). However, it was only in 1704 that the first scientific study on prisms, especially on their dispersion properties, was published by Newton in *Opticks* [118]. His explanation of the dispersion phenomenon was based on the law of refraction, independently established by Snell in 1621 and published by Descartes in 1637 [119], and the variation of the refractive index with respect to the wavelength.

Since then, prisms have become a major element of optical systems. A very wide variety of prisms has been designed for a lot of different applications, such as dispersing polychromatic light, deviating rays or rotating images in imaging systems. Usually they are inserted in the light path just as other elements, like lenses or mirrors. But in prism-based SPRi, the object of observation is the inner surface of the prism base. The situation where the base of a prism is imaged through one of its faces will be referred to as "prism-based imaging".

2.1.2 | Prism-based imaging techniques

In addition to SPRi, three other prism-based imaging techniques have been developed so far. They are based on the following effects: Frustrated Total Internal Reflection (FTIR) [20], Bloch Surface Wave (BSW) [19] and Resonant Mirror (RM) [21] (**Figure 2.1**).

All of them use the ability of a prism to access internal angles of incidence greater than the critical angle glass/dielectric and generate evanescent waves in the subwavelength distance above the biochip surface [120]. Historically, the first use of evanescent waves obtained with a prism and applied to biology dates back to 1956 when Ambrose studied the adhesion of a living cell deposited on a prism base illuminated in the FTIR configuration. The author imaged the cell by an optical microscope form the upper half space, thus collecting the light scattered by the area in close contact with the substrate [121].

These three prism-based imaging techniques require the same optical set-up as in SPR: a monochromatic, polarized and collimated illumination beam, and an imaging system (or a light sensor) on the other side of the glass prism (as for SPR, other configurations can be used, such as

angular or wavelength interrogation). Note that, in these works, imaging has only been performed with FTIR, but apparently there is no reason why it could not be achieved with BSW or RM.

With these techniques, unlike in SPR, the sensing surface is not a metal but a dielectric, usually a glass which can be functionalized by silane chemistry [122], and both TE and TM mode can be used for biosensing. For BSW and RM, a combination of low and high index dielectrics is required, such as SiO_2 (n≈1.4) and TiO_2 (n≈2.3).

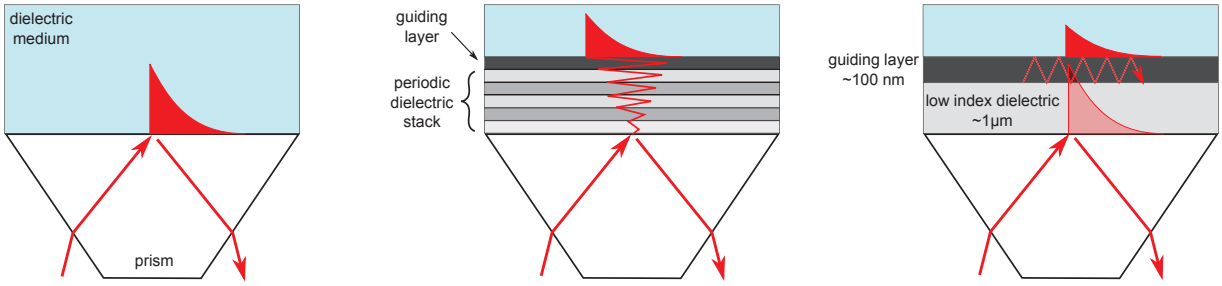

(a) FTIR **(b)** BSW **(c)** RM

Figure 2.1: Other prism-based imaging techniques used in biosensing. **(a)** Frustrated Total Internal Reflection. **(b)** Bloch Surface Wave. **(c)** Resonant Mirror.

In FTIR, there is no resonant angle. The working angle just has to be above the critical angle so the reflectivity is 100% (Total Internal Reflection) and an evanescent wave is generated at the prism/dielectric interface. Therefore, a biorecognition does not induce an increase, but a decrease of reflectivity. In the article published by Bruls *et al.* [20], when nanoparticles functionalized with the target are captured by the probe within the penetration depth, a part of the evanescent wave re-radiates in the upper half-space, and the reflected intensity decreases. Note that the use of nanoparticles in the experiment presented in ref. [20] means that FTIR cannot be considered as a label-free technique.

For BSW, the detection is very similar to SPR. The periodic dielectric stack exhibits an angle of resonance corresponding to a drop of reflectivity which is shifted to higher angles when the refractive index increases at the sensing surface.

In RM, the adsorption of a thin biolayer induces a positive shift of the resonant angle, but here, the resonance does not correspond to a drop of reflectivity, but to a 2π phase-shift of the reflected beam. This phase-shift can further be converted into a peak of reflectivity occurring when the it reaches π by using a set of crossed polarizer and analyzer [123]. As in SPR, depending on which side of the peak the working angle is chosen, a detection process can correspond to a positive or negative contrast.

Nonetheless, based on the number of published papers, SPR remains widely predominant, which can certainly be attributed to its high sensibility, ease of use and simple instrumentation, while the prism-biochips are relatively simple and inexpensive to fabricate. Hence, SPR is often used as a reference for performance comparisons [124].

Surprisingly, the issue of spatial resolution in prism-based imaging techniques (apart from plasmonic effects) have not been treated so far. The theory of image formation has been treated by Maillart in 2004 [88], but the general analytic calculation has never been presented, which has led to misunderstandings [125]. Note that the image formation can also be evaluated by a simulation software for particular cases [90]. This lack of bibliography can be attributed to the recent development of SPRi (∼25 years) and its majority use for label-free biomolecule sensing on functionalized areas in the range of several hundreds of µm, for whom spatial resolution is not a

key point. Moreover, several commercial prisms, somehow by casualty, offer images of quality sufficient to lead studies where spatial resolution and wide-FOV are not needed simultaneously. As a consequence, a wide variety of prism shapes and refractive index are in use: right-angle N-BK7 prisms [16], hemispherical N-BK7 prisms [15], S-LAL-10 prisms [126], SF10 parallelogram prisms [18] or equilateral SF-10 prisms [127], just to name a few.

2.2 | Image formation

The general calculation that gives the location of the virtual image of the base by the exit face is derived from the refraction law. As presented in **Section 1.3.1**, the entire base is illuminated by a collimated beam. However, the reflection is not purely specular, and each point of the base acts as a dispersive source which emits rays in different directions. This diffuse reflection can be attributed to the roughness of the prism base and metal layers, and to the local differences of reflectivity due to the SPR effect (discussed in chapter 4). Indeed, if the reflection were perfectly specular, the effective NA of the object/surface would be null and the formation of images impossible.

Hence, as depicted in **Figure 2.2**, the light emission from a point source O will be considered restricted to a solid angle. The solid angle is equivalent to a cone whose axis makes an angle θ_{int} with respect to the normal to the prism base (red ray = principal ray), corresponding to the angle of illumination, and of half-apex angle $\Delta\theta_{int}$ (blue rays = secondary rays).

To find the virtual image O' of O, let us first consider the principal ray emerging from the point O situated at a distance $u = d$ from the edge of an isosceles prism of refractive index n_p and apex angle A_p. This edge is taken as the origin of the frame. The base angles are equal to:

$$A_b = \frac{\pi - A_p}{2} \tag{2.1}$$

The inner and outer angles of refraction on the exit face are given by:

$$\theta_{in} = \frac{\pi}{2} - \frac{A_p}{2} - \theta_{int} \tag{2.2}$$

$$\theta_{out} = \arcsin\left[n_p \sin\left(\theta_{in}\right)\right] \tag{2.3}$$

The ray exits the prism with an external angle (equal to the external incident angle of illumination for isosceles prisms) given by:

$$\theta_{ext} = \frac{\pi}{2} - \frac{A_p}{2} - \theta_{out} \tag{2.4}$$

This external ray and its virtual extension can be mathematically represented in the frame by a line of equation $z = a \times u + b$. The slope a and the y-intercept b can be found by considering two points of the line, A and F for instance, so that $a = (z_A - z_F)/(u_A - u_F)$ and $b = z_A - a\,.\,u_A = z_F - a\,.\,u_F$. The solution for a and b is unique, but the choice of points to consider is arbitrary. Here, the point F is the intersection with the exit face, and A the intersection with the parallel to the exit face passing by O.

In the triangle AOF:

$$\frac{OA}{\sin\left(\theta_{out} - \theta_{in}\right)} = \frac{OF}{\sin\left(\frac{\pi}{2} - \theta_{out}\right)} = \frac{OF}{\cos\left(\theta_{out}\right)} \;\Rightarrow\; OA = OF\,\frac{\sin\left(\theta_{out} - \theta_{in}\right)}{\cos\left(\theta_{out}\right)} \tag{2.5}$$

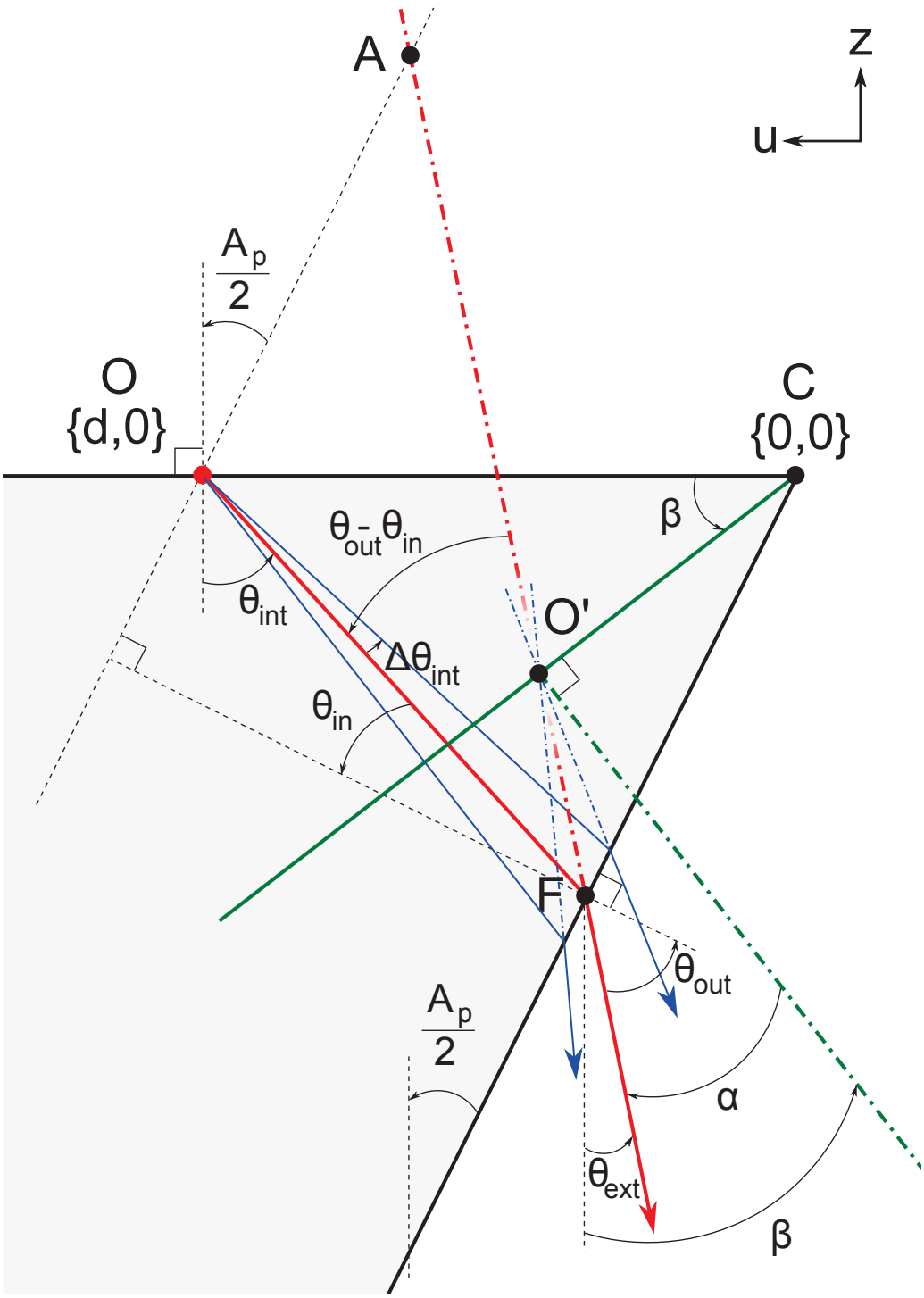

Figure 2.2: General optical scheme in prism-based imaging.

In the triangle OCF:

$$\frac{OF}{\sin\left(\frac{\pi}{2}-\frac{A_p}{2}\right)} = \frac{d}{\sin\left(\frac{\pi}{2}-\theta_{in}\right)} \Rightarrow OF = d\,\frac{\sin\left(\frac{\pi}{2}-\frac{A_p}{2}\right)}{\sin\left(\frac{\pi}{2}-\theta_{in}\right)} \tag{2.6}$$

The coordinates of F and A are then given by:

$$A\begin{cases} z_A &= OA\,\cos\left(A_p/2\right) \\ u_A &= d - OA\,\sin\left(A_p/2\right) \end{cases} \tag{2.7}$$

$$F\begin{cases} z_F &= -OF\,\cos\left(\theta_{in}\right) \\ u_F &= -z_F\,\tan\left(A_p/2\right) \end{cases} \tag{2.8}$$

To find the location of O', we need to consider at least two rays emerging from O at different angles; O' being defined by the intersection of these rays. Let us choose two rays with internal angles of $\theta_{int} - \Delta\theta_{int}$ and $\theta_{int} + \Delta\theta_{int}$. O' corresponds to the intersection of the two corresponding lines of slopes a_1 and a_2 and y-intercepts b_1 and b_2:

$$\begin{cases} z_{o'} = a_1\,.\,u_{o'} + b_1 \\ u_{o'} = \frac{z_{o'} - b_1}{a_1} \end{cases} = \begin{cases} z_{o'} = a_2\,.\,u_{o'} + b_2 \\ u_{o'} = \frac{z_{o'} - b_2}{a_2} \end{cases} \tag{2.9}$$

$$\Rightarrow \begin{cases} z_{o'} = a_1\,.\,\frac{z_{o'} - b_2}{a_2} + b_1 \\ u_{o'} = \frac{z_{o'} - b_1}{a_1} \end{cases} \Leftrightarrow \begin{cases} z_{o'}\left(1 - \frac{a_1}{a_2}\right) = -\frac{a_1\,.\,b_2}{a_2} + b_1 \\ u_{o'} = \frac{z_{o'} - b_1}{a_1} \end{cases}$$

$$\Leftrightarrow z_{o'} = \frac{-\frac{a_1\,.\,b_2}{a_2} + b_1}{\left(1 - \frac{a_1}{a_2}\right)} \quad and \quad u_{o'} = \frac{z_{o'} - b_1}{a_1} \tag{2.10}$$

Obviously, the position of O' is proportional to d, so the image plane (in green) passes by C since O'$\rightarrow$ C as $d \rightarrow 0$. The anamorphose Υ is defined by the ratio of length:

$$\Upsilon = \frac{CO'}{CO} = \frac{\sqrt{u_{o'}^2 + z_{o'}^2}}{d} \tag{2.11}$$

It is convenient to define the angle between the virtual image plane and the real object plane which is equal to the angle of the normal of the virtual image plane:

$$\beta = -\arctan\left(\frac{z_{o'}}{u_{o'}}\right) \tag{2.12}$$

The minus sign serves to compensate for the negative value of $z_{o'}$ in this frame convention, so that β is always positive and ranges from 0 to A_b. It is also practical to define the angle between the principal ray and this normal:

$$\alpha = \theta_{ext} - \beta \tag{2.13}$$

On this scheme α is negative. Note that the angles β and α are just functions of A_p, n_p, θ_{int} and $\Delta\theta_{int}$.

As a last remark, it is evident that for a ray to be able to enter and exit the prism, θ_{out} must satisfy $-\pi/2 \leq \theta_{out} \leq \pi/2 \Leftrightarrow -\theta_c \leq \theta_{in} \leq \theta_c$, where $\theta_c = \arcsin 1/n_p$ is the critical angle at the interface prism/air. As a consequence:

$$\frac{\pi}{2} - \frac{A_p}{2} - \theta_c + \Delta\theta_{int} \leq \theta_{int} \leq \frac{\pi}{2} - \frac{A_p}{2} + \theta_c - \Delta\theta_{int} \tag{2.14}$$

This means that for a given prism, the internal angle of incidence is restrained to a certain range. This is the reason why the Horiba prisms cannot perform SPR in air. Similarly, given a particular θ_{int}, for example θ_{res} or θ_w in SPR, the prism apex angle is restrained to:

$$2 \times \left(\Delta\theta_{int} - \theta_{int} + \frac{\pi}{2} - \theta_c\right) \leq A_p \leq 2 \times \left(-\Delta\theta_{int} - \theta_{int} + \frac{\pi}{2} + \theta_c\right) \tag{2.15}$$

It can also be noticed that for $|\theta_{in}| \rightarrow \theta_c$, the reflectivity at the entry and exit faces of the prism tends to one, i.e. the incident ray is almost completely externally and internally reflected, and only a low amount of light reaches the imaging system. Thus, the previous ranges should rather be calculated by replacing θ_c by $(\theta_c - \eta)$, where η is chosen to have a more "comfortable" SPR signal. For instance, at n_p = 1.5, $\eta = 3°$ limits the prism face reflectivity at 4% in TM and 30% in TE, while at n_p = 1.9, $\eta = 5°$ limits the reflectivity at 10% and 30%, respectively.

2.3 | Very-wide-FOV optimized prisms

In a standard imaging system, the final image of a plane object is also a plane that coincides with the camera sensor. The easiest way to achieve this is to place the optical axis of the imaging system normal to the object plane.

In the case of prism-based imaging, the object plane of the imaging system is not the base it-self, but the virtual image of the base, so the optical axis should have an angle β with respect to the normal of the prism base: $\theta_{CCD} = \beta$. Moreover, spherical and coma aberrations of the imaging system are minimized when rays are almost parallel to the optical axis and pass through the center part of the lenses, which corresponds to the situation where $\beta = \theta_{ext} \Leftrightarrow \alpha = 0°$ (**Figure 2.3**).

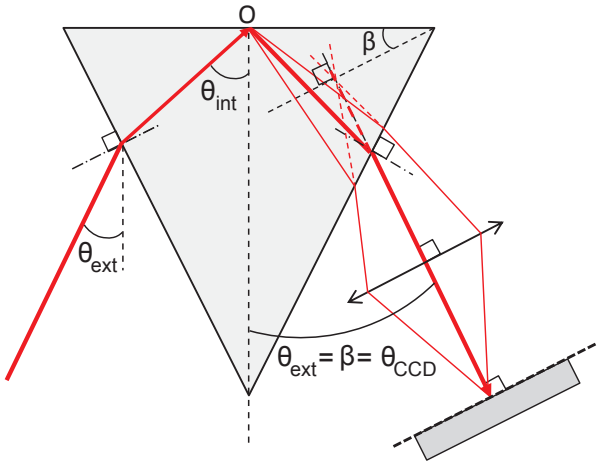

Figure 2.3: Optical scheme of a very-wide-FOV optimized prism (N-SF66 prism, A_p = 53° and θ_{int} = 48.5°).

As demonstrated by Maillart in his PhD thesis in 2004 [88], in SPRi, this condition can be fulfilled by correctly selecting the refractive index and the apex angle of the prism [88]. These prisms will be referred to as "very-wide-FOV optimized" or VWFOV.

The optimized couples $\{A_p, n_p\}$ can be determined by a numerical calculation by taking the internal angle θ_{int} equal to the SPR working angle θ_w and $\Delta\theta_{int} \rightarrow 0°$ (this choice is discussed later, and in the following curves $\Delta\theta_{int}$ = 0.1°). But unlike the resonant angle θ_{res}, θ_w has no literal expression, and has to be measured for particular values of n_p. Let us consider a gold/water interface at λ = 632 nm. As shown in **Figure 2.4a**, θ_w (from the optical approach) is only 1.5° to 0.5° smaller than θ_{res} (from the plasmonic approach) depending on n_p. Hence, using θ_{res} instead of θ_w seems a correct approximation which should not imply large errors on the final results, especially at high n_p, while allowing an easier, faster and more precise calculation. Moreover, as noticed by Maillart, θ_{res} in pure water is a good approximation of θ_w in biological media which have a slightly higher refractive index.

As shown in **Figure 2.4b**, for each refractive index n_p, there is a unique A_p that makes $\alpha = 0°$.

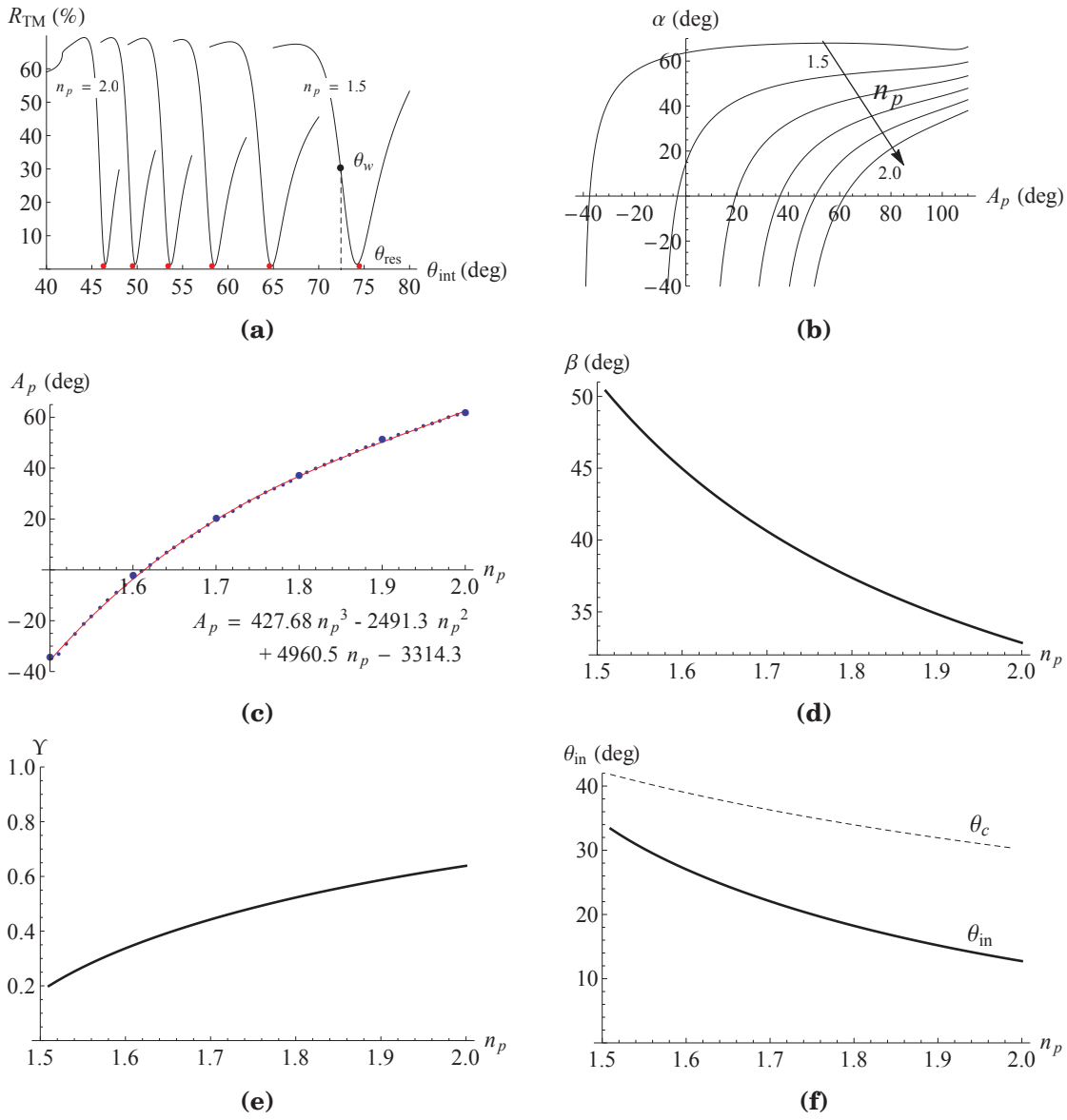

Figure 2.4: Main optical parameters of VWFOV optimized prisms at the gold/water interface. **(a)** Plasmon curves for n_p from 1.5 to 2.0 at a step of 0.1 RIU (Refractive Index Unit) at λ = 632 nm for 50-nm-gold coated prisms in water. Red dots indicate the θ_{res} calculated with the plasmonic approach. **(b)** α as a function of A_p for increasing n_p. **(c)** A_p for n_p calculated at a pitch of 0.01 RIU and corresponding polynomial fit (red line) and equation. Bigger markers correspond to the same calculation performed with θ_w as measured from the plasmon curves. **(d)** β as a function of n_p. **(e)** Anamorphose Υ as a function of n_p. **(f)** θ_{in} and $\theta_{c,prism/air}$ as a function of n_p. For the sake of clarity, the markers are not shown for β, Υ and θ_{in} and the points are linked by a straight line.

The curve $A_p = f(n_p)$ plotted in **Figure 2.4c** is obtained by solving $\alpha(A_p, n_p) = 0°$ for both A_p and n_p. The use of θ_{res} instead of θ_w is justified by an error of less than 2° on A_p at n_p = 1.5, and less than 0.5° at n_p = 2.0. A negative apex angle corresponds to a prism whose apex is truncated and facing up, and is the metal-coated surface, while for A_p = 0° the prism section is a rectangle. In this configuration, the angle of the imaging system θ_{CCD}, and thus θ_{ext}, is equal to β (**Figure 2.4d**). As n_p decreases, the effect of anamorphose becomes more important, and the virtual image length (X axis) can be up to 5 times smaller than the real base length (**Figure 2.4e**). Similarly, θ_{in} comes closer to $\theta_{c,prism/air}$, meaning that less and less light is transmitted from the illumination side to the imaging side.

2.4 | Geometric aberrations and resolution optimized prisms

In the previous simulation, we were considering two rays with a small angular difference, which of course give a single image point of O. Let us now consider a bundle of diffuse rays emerging from O. As stated by **Equation 2.10**, each pair of rays generates a single image point O', but all these points do not overlap. Hence, the image of O is not a point but a spread spot, as it is pointed out with several ray tracing in **Figure 2.5a**. These intrinsic geometric aberrations arise from the non stigmatism of the refraction law at a plane diopter, and represent a third factor that limits the spatial resolution in prism-based SPRi, in addition to the diffraction limit and the propagation length. This effect is a well-known issue in subsurface microscopy [128], but surprisingly, at the best of our knowledge, it has never been noticed in prism-based imaging so far.

For a given distance d, geometric aberrations increase with respect to θ_{in} and the angular diffusion $\Delta\theta_{int}$. In prism-based imaging, the implication is straight forward: for a given n_p, they can be minimized by changing the apex angle of the prism so that $\theta_{in} = 0°$, as illustrated in **Figure 2.5b**. Such prisms will be referred to as "resolution optimized". Note that changing the apex angle only affects the resolution in the X-axis, since the projection of the rays and the diopter in a plane perpendicular to the XZ plane is equivalent to the situation where the principal ray is perpendicular to the diopter whatever the apex angle.

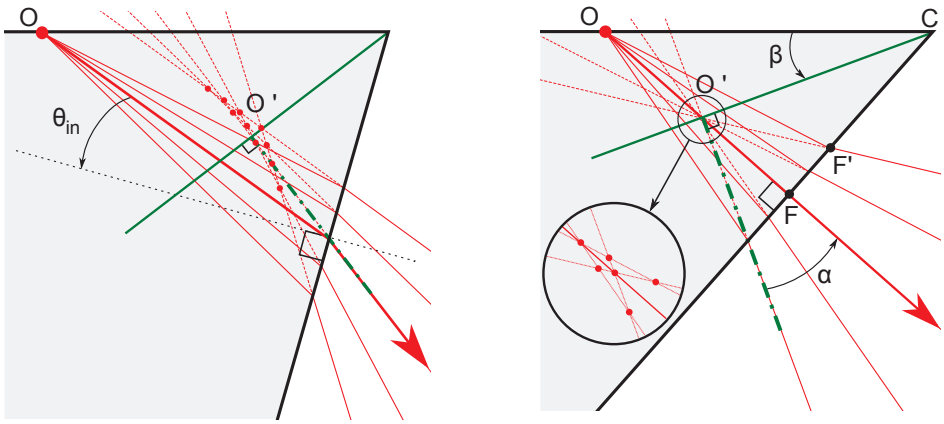

(a) **(b)**

Figure 2.5: Illustration of geometric aberrations. **(a)** VWFOV optimized prism: $\theta_{in} \neq 0$ (SF11 prism, $A_p = 32°$, $\theta_{int} = 53°$). **(b)** Prism optimized for resolution: $\theta_{in} = 0°$ (SF11 prism, $A_p = 74°$, $\theta_{int} = 53°$) with a zoom on the ray intersection points in inset. The fact that the normal to the virtual image plane is superimposed with a secondary ray is a coincidence.

In fact, everyone has surely already noticed this phenomenon in his daily life and, maybe unconsciously, got to the solution of reducing the angle of incidence on the plane diopter, for example when looking at a fish in an aquarium, as illustrated in **Figure 2.6**. Here the resolution is strongly affected in the horizontal axis, as it is visible on the white ring of its eye. Note that the non stigmatism also induces chromatic aberrations, hopefully absent in a monochromatic SPR experiment.

These aberrations cannot be minimized in the case of prisms that are optimized for very-wide-FOV since $\theta_{in} > 0°$. As shown in **Figure 2.5a**, the optical response is not of cylindrical symmetry around the principal ray, which explains the distortion undergone by cells when imaged with Horiba prisms (**Figure 1.18**). For these latter prisms, the impact of the angular diffusion can be decreased by diaphragming the imaging system. This is the reason why the apex angle of VWFOV optimized prisms have been calculated considering $\Delta\theta_{int}$ close to zero. Obviously, a trade-off must be achieved as the resolution also depends on the NA of the imaging system.

Geometric aberrations also explain the fact that, for a given prism, the spatial resolution in

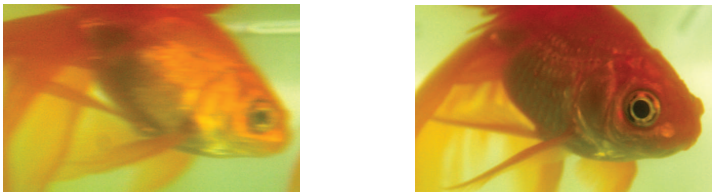

(a) **(b)**

Figure 2.6: Example of geometric aberrations in aquarium. **(a)** Bubule, the fish of our laboratory, imaged with an angle between the optical axis of the camera and the normal to the aquarium face (diopter). **(b)** Bubule imaged with the optical axis perpendicular to the aquarium face.

SPRi measured in air is not the same as the one in water, as visible in the article of Peterson *et al.* [18] and Giebel *et al.* [17] (**Figure 1.16c & d** and **Figure 1.16e & f**). The reason is that both working angles strongly differ (**Appendix Figure A.6**), and thus θ_{in}. Furthermore, for these two articles, aberrations might also explain why the changes of wavelength or metal do not necessarily induce a significant improvement on spatial resolution, meaning that the resolution is aberration-limited rather than L_x-limited. Similarly, de Bruijn *et al.* may have not noticed the presence of these aberrations since they are minimized when using hemispherical prisms imaged on a small area around the optical axis whatever n_p and θ_w [15].

2.5 | Resolution optimized prisms

For resolution optimized prisms, the optical configuration is equivalent to the one encountered in subsurface microscopy, where geometric aberrations can be approximated by spherical aberrations. Indeed, the network of ray intersections, also called caustic, has the same form as in spherical aberrations induced by lenses. Solutions such as Numerical Aperture Increasing Lens (NAIL) [128], aspheric lenses [129] or correction rings (LCPLFLN-LCD series Olympus microscope objectives) can compensate the remaining aberrations for a particular glass thickness, but restrict imaging to a narrow region of the prism. Without NAIL, the resolution is ultimately limited by the total internal reflection of the rays striking the exit face at angles $\theta_{in} > \theta_c$: $\Delta x = \frac{0.6 \times \lambda}{n_p \times \sin(\theta_c)} \approx \lambda/2$. This is true for an imaging system of NA equal to 1, otherwise the resolution is limited to $\Delta x = \frac{0.6 \times \lambda}{NA}$, and does not depend anymore on the refractive index of the prism.

Here, $\theta_{in} = 0$ implies that $\theta_{out} = 0$ and $\theta_{int} = \theta_{ext}$. But more importantly, unlike for VW-FOV optimized prisms, it also implies that, A_p, A_b, β, α and Υ have literal expressions with respect to θ_{int}, especially:

$$A_p = \pi - 2 \times \theta_{int} \quad \Leftrightarrow \quad A_b = \theta_{int} \tag{2.16}$$

Consequently, for a prism of width w, the height h from the apex angle to the base and the length c of the faces are equal to:

$$h = \frac{w}{2} \tan(\theta_{int}) \tag{2.17}$$

$$c = \frac{w}{2 \times \cos(\theta_{int})}. \tag{2.18}$$

In **Figure 2.5b**, let us consider the principal ray perpendicular to the diopter and their intersection F, as well as a secondary ray that makes an angle with the principal ray of $\Delta\theta_{int}$ before the diopter and $\Delta\theta_{ext} = \arcsin[n_p \times \sin(\Delta\theta_{int})]$ after the diopter, and of intersection point F'. In the triangle OFF', $FF' = OF \times \tan(\Delta\theta_{int})$, and in the triangle O'FF', $OF = FF'/\tan(\Delta\theta_{ext})$. As a consequence:

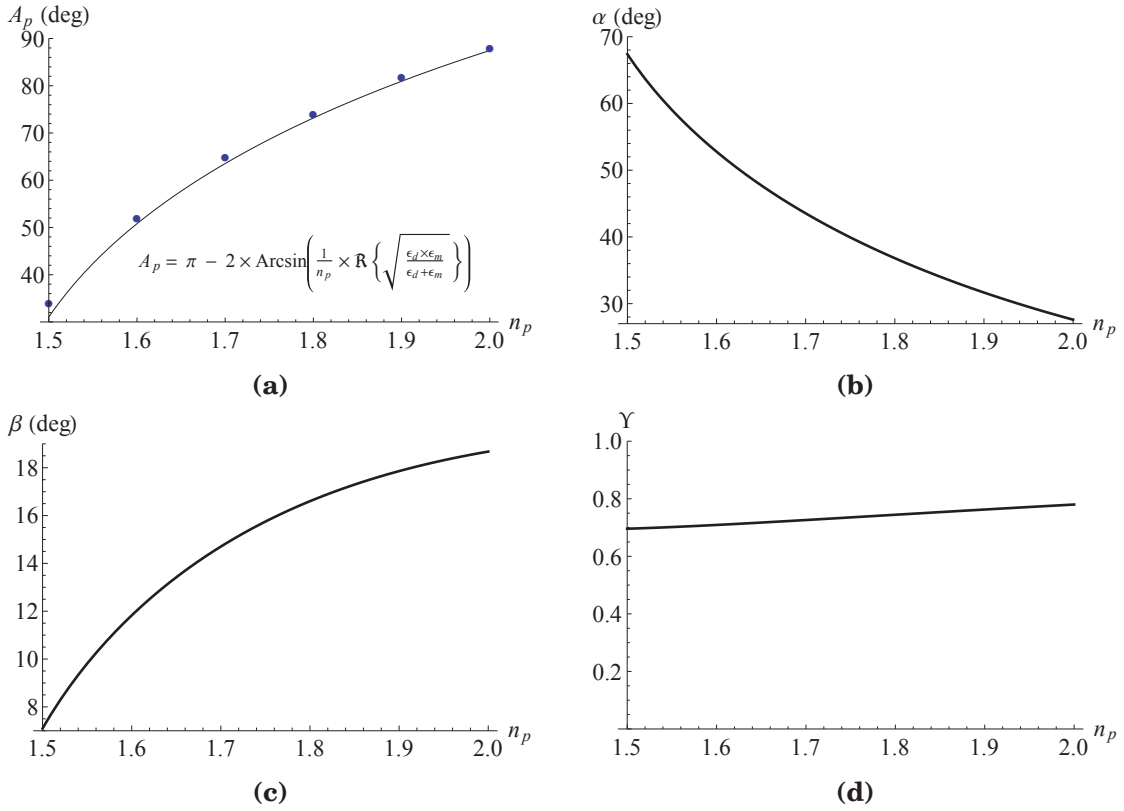

Figure 2.7: Main optical parameters of resolution optimized prisms at the gold/water interface. **(a)** A_p as a function of n_p and its literal expression. The markers correspond to A_p calculated with the θ_w measured from the plasmon curves. **(b)** α as a function of n_p. **(c)** β as a function of n_p. **(d)** Anamorphose Υ as a function of n_p.

$$O'F = \frac{\tan(\Delta\theta_{int})}{\tan(\Delta\theta_{ext})} \times OF \quad \Rightarrow \quad \lim_{\Delta\theta_{int} \to 0} O'F = \frac{OF}{n_p} \tag{2.19}$$

since the limited development in the vicinity of zero for $\sin(x)$, $\arcsin(x)$ and $\tan(x)$ is x. In this approximation of small diffusion angles, in the triangle COF:

$$OF = \sin(A_b) \times d = \sin(\theta_{int}) \times d \quad \Rightarrow \quad O'F = \frac{\sin(\theta_{int}) \times d}{n_p} \tag{2.20}$$

and

$$CF = \sin\left(\frac{\pi}{2} - \theta_{int}\right) \times d = \cos(\theta_{int}) \times d \quad \Rightarrow \quad \frac{O'F}{CF} = \frac{\tan(\theta_{int})}{n_p} \tag{2.21}$$

and in the triangle O'CF, $\tan(\alpha) = O'F/CF$. Hence:

$$\alpha = \arctan\left[\frac{\tan(\theta_{int})}{n_p}\right] \tag{2.22}$$

and β is equal to:

$$\beta = A_b - \alpha = \theta_{int} - \alpha \tag{2.23}$$

To find the anamorphose $\Upsilon = CO'/d$, we can use the triangle O'CF where $CO' = O'F/\sin(\alpha)$. Hence:

$$\Upsilon = \frac{\sin(\theta_{int})}{n_p \times \sin(\alpha)} \tag{2.24}$$

These characteristic parameters are plotted in **Figure 2.7** for the gold/water interface (for the other metals see **Appendix Figure A.5**). For such prisms, A_p is always positive and tends to 90° as $n_p \to 2$, but note that for A_p beyond a right angle, the prism base cannot be illuminated and imaged entirely. Inversely, the apex can be truncated as A_p digresses from 90°. If we neglecte $\Delta\theta_{int}$, then, the height h' and the length c' of the faces of a truncated prism can be lower down to:

$$h' = w \times \cos(\theta_{int}) \times \sin(\theta_{int}) \tag{2.25}$$

$$c' = w \times \cos(\theta_{int}) \tag{2.26}$$

For these prisms, β increases with respect to n_p and the anamorphose Υ remains close to ~0.7. Since θ_{in} = 0°, the rays undergo less internal and external reflections on the entry and exit face of the prism. Consequently, these prisms allow to collect the secondary rays even at high angular diffusion $\Delta\theta_{int}$ (ultimately < θ_c), an advantage for high resolution imaging, but also to trace the plasmon curve on a wide range of angles. However, unlike for the VWFOV optimization, α remains positive whatever n_p.

2.5.1 | Line-scan imaging mode

Two optical schemes can then be envisaged. In the first one, schematically represented in **Figure 2.8a**, the optical axis is parallel to the principal rays. This configuration leads to the theoretical highest resolution achievable in prism-based imaging because geometric aberrations due to the prism and optical aberrations due to the imaging system are minimized.

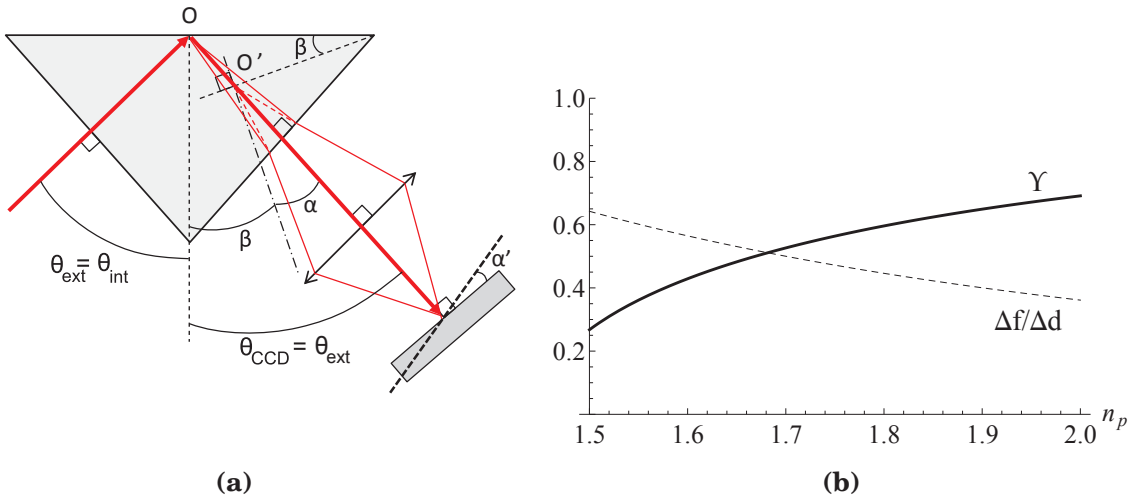

Figure 2.8: Line-scan imaging mode with resolution optimized prisms. **(a)** Optical scheme with a N-SF66 prism, A_p = 83°, θ_{int} = 48.5°. **(b)** Anamorphose and focus adjustment in line-scan imaging mode.

Here, the volume of the prism imposes a minimal working distance WD greater than O'F. For high magnification and high NA microscope objectives, whose WD is ideally as short as possible, this restricts the distance d between the object and the edge of the prism to:

$$d_{max} \leq \frac{n_p \times WD}{\sin(\theta_{int})} \quad \Leftrightarrow \quad WD_{min} \geq \frac{d \times \sin(\theta_{int})}{n_p} \tag{2.27}$$

Nonetheless, many manufacturers propose microscope objectives combining long WD and high NA. For example, the ×100 objective form the Olympus series LMPLFLN (NA = 0.8, WD = 3.3 mm, diffraction limit ≈ 350 nm) is able to image up to d = 8 mm with a N-SF66 prism at λ = 632 nm (~60 % of our prisms). Insofar as short WD is not required, there is no limitation on magnification or FOV.

In this imaging mode, the external principal ray is not perpendicular anymore to the virtual image plane. Thus, the final image is inclined by an angle α' with respect to the normal of the optical axis (Scheimpflug principle [130]): $\alpha' = \arctan\left[M \times \tan\left(\alpha\right)\right]$, where M is the magnification of the imaging system, so the higher M, the higher α'.

The non coincidence of the final image and camera sensor planes means that only a line can be in focus on the camera sensor. Due to the non-zero depth-of-field of the imaging system, this line is indeed a stripe, and the entire surface can be imaged in "line-scan imaging mode", i.e. by first sequentially adjusting the focus to scan the entire surface with this clear stripe, and secondly by juxtaposing all these clear stripes into a final image in post processing. Of course, the number of necessary stripes depends on the stripe width (where the resolution is considered sufficient), and thus on the depth-of-field of the imaging system. Note that this imaging issue is the same as the one encountered in imaging ellipsometry.

In this imaging mode, the fact that $\theta_{CCD} \neq \beta$ induces another anamorphose effect equal to $\cos(\alpha)$. The anamorphose plotted in **Figure 2.8b** is then given by:

$$\Upsilon_{line-scan} = \frac{\sin\left(\theta_{int}\right)}{n_p \times \tan\left(\alpha\right)} \tag{2.28}$$

It can also be shown that the adjustment of focus Δf to scan a distance Δd on the prism is given by:

$$\Delta f = \Delta d \frac{\tan\left(\theta_{int}\right)\cos\left(\theta_{int}\right)}{n_p} \tag{2.29}$$

For instance, using a N-SF66 prism, the imaging system has to be displaced by 390 µm to scan a real distance of 1 mm in the X axis. As shown in **Figure 2.8b**, the higher n_p, the less the focus displacement required to scan the same real distance. In conclusion, in line-can imaging mode, high refractive index prisms reduce both the anamorphose effect and the required focus adjustment.

2.5.2 | Classic imaging mode

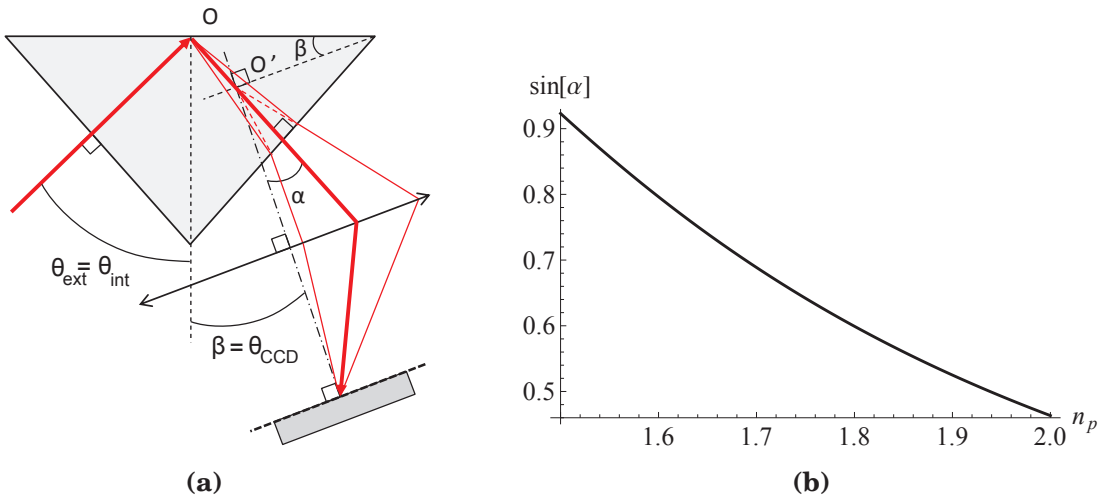

Figure 2.9: Classic imaging mode with resolution optimized prisms. **(a)** Optical scheme (N-SF66 prism, A_p = 83°, θ_{int} = 48.5°). **(b)** Minimal NA of the imaging system in order to obtain a clear image on all the sensor. NA = $\sin\left(\alpha\right)$ as a function of n_p.

In the second configuration, schematically represented in **Figure 2.9a**, the axis of the imaging system is normal to the virtual image so that the final image coincides with the camera sensor

plane. This imaging mode will be referred to as "classic imaging mode". Thus, the NA of the imaging system has to be sufficient to capture the principal ray arriving with an angle α, that is to say NA $\geq sin(\alpha)$ (**Figure 2.9b**), and ideally secondary rays with angles greater than α. However, the higher α, the higher coma and astigmatism aberrations of the imaging system [99]. It is therefore more favorable to use high refractive index prisms, which also have the benefit of offering more practical angles for imaging (the imaging systems may interfere with the illumination beam for $\theta_{CCD} = \beta$ below 15°). Of course, coma and astigmatism aberrations can also be significantly decreased by designing a corrected imaging system with a fixed magnification using a dedicated optical software [90]. In this imaging mode, the anamorphose is the one given by **Equation 2.24**.

Here, the volume of the prism imposes a minimal working distance WD greater than the distance between the virtual image plane and its parallel passing by the apex of the prism (if not truncated):

$$WD_{min} \geq c \times \sin(\alpha) \tag{2.30}$$

2.6 | Estimation of geometric aberrations

As for now, we have only addressed the issue of aberrations minimization qualitatively. But two other important questions remain: how evolve these aberrations with respect to the apex angle ? Is there an optimal refractive index ? To find the answer, these aberrations need to be evaluated quantitatively.

2.6.1 | Aberration calculation

This evaluation is performed by considering the wave aberration function Φ (also called OPD: Optical Path Difference), as proposed by Ippolito in ref. [128]. Unlike a dedicated software that would require the use of a specific imaging system, this model has the benefit of only considering the prism characteristics, while being simple and fast to code. In the article "Spatial resolution in prism-based surface plasmon resonance microscopy" [131], we have used a home made approach, thus less conventional than the wave aberration function. It is presented in details in **Appendix A.3** and leads to the same conclusions as the wave aberration model, so only the latter is presented in the present section.

The calculation of Φ is based on Optical Path Length (OPL) differences. The OPL of a ray is equal to its path lengths in each medium crossed multiplied by the corresponding optical index. Let us now consider two rays emerging from a single point O and creating a virtual image O' by crossing a single diopter, as illustrated in **Figure 2.10a**. We can also define the additional OPL, let us call it OPL', of each ray induced by the diopter by the difference of absolute OPL between the real and virtual ray. For the secondary ray, in blue, the OPL' is equal to $OF \times n_p - O'F$. The wave aberration function Φ between the principal ray (in black) and the secondary ray (in blue) can then be defined as their difference of additional OPL: $\Phi = OPL'_p - OPL'_s$ (in the article of Ippolito, $\Phi = OPL'_s - OPL'_p$, but this convention leads to a negative value for Φ if OF is positive).

The dimension of Φ is a length which represents the phase difference $\phi = \frac{2\pi\Phi}{\lambda}$ (rad) between the two rays. This is the reason why Φ is usually expressed in unit of wavelength. Practically, an optical system is considered diffraction-limited if $\Phi \leq \lambda/4$ [132], also known as the Rayleigh wavefront criterion. In that case, all the rays included between the two considered rays constructively interfere and the optical response of the imaging system (the PSF) can be considered equal to the one resulting from a perfectly spherical wavefront emerging from O'. For higher values of Φ, some rays destructively interfere and the approximation of a spherical wavefront is no longer valid.

Hence, Φ is not the resolution limit Δx, but rather a parameter to whom it is supposed to be proportional in a first approximation. Since OF and $O'F$ are proportional to d, Φ is also

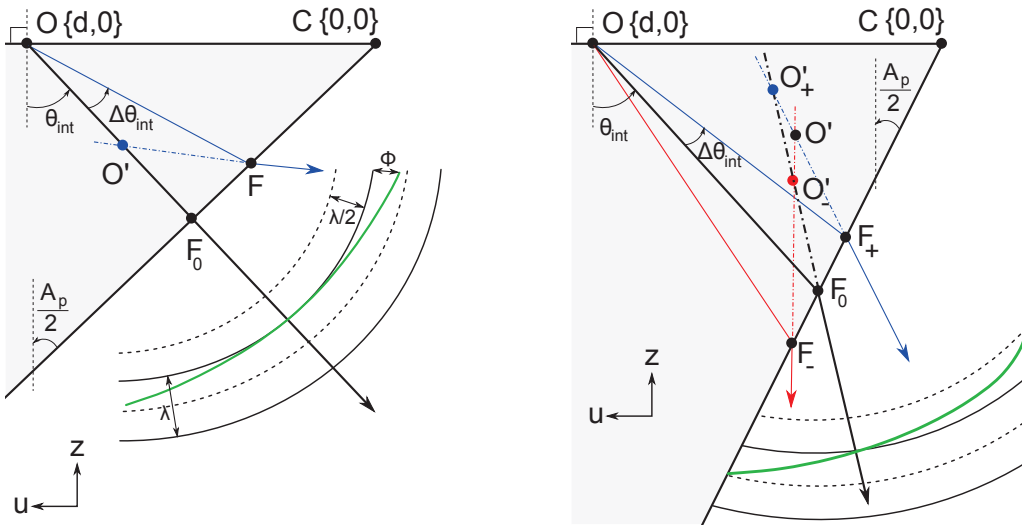

Figure 2.10: geometric aberrations estimation in prism-based imaging by the wave aberration function Φ. The wavefront in green differs from a perfectly spherical wavefront emerging from O' as $\Delta\theta_{int}$ increases. **(a)** Prism optimized for resolution. **(b)** Prism optimized for VWFOV.

proportional to d, and it is more relevant to express Φ/d. Φ in unit of λ is obtained by simply multiplying the ratio Φ/d by d, and by dividing by λ.

2.6.1.1 Resolution optimized prisms

In cylindrical coordinates, that is to say in the case of spherical aberration induced by a prism optimized for resolution, as illustrated in **Figure 2.10a**, it can be shown that Φ/d is given by [128]:

$$\frac{\Phi}{d} = -\sin(A_b) \times \left\{ n_p - \frac{1}{n_p} - \frac{1}{\cos(\Delta\theta_{int})} \left[n_p - \sqrt{\cos^2(\Delta\theta_{int}) \times \left(\frac{1}{n_p^2} - 1 \right) + 1} \right] \right\} \tag{2.31}$$

2.6.1.2 General prisms

In the general case illustrated in **Figure 2.10b**, the optical scheme is no longer of cylindrical symmetry. Nonetheless, Φ can be calculate numerically using the equations given at the beginning of this chapter in **Section 2.2**. For a principal ray of internal angle θ_{int} and a secondary ray at $+\Delta\theta_{int}$, Φ_+/d is given by :

$$\frac{\Phi_+}{d} = \frac{1}{d} \left[n_p \times (OF_0 - OF_+) + O'_+F_+ - O'_+F_0 \right] \tag{2.32}$$

The lengths OF_+ and OF_0 are directly given by **Equation 2.6**, while the lengths O'_+F_0 and O'_+F_+ need to be calculated numerically by using the position of each point given by **Equation 2.8** and **Equation 2.10**. The same method can be employed to calculate the wave aberration Φ_- of a secondary ray at $-\Delta\theta_{int}$ with respect to the principal ray.

Here, secondary rays on each side of the principal ray have different OPL and additional OPL. As a consequence, the calculation of Φ has to integrate two secondary rays with an angular diffusion of +/- $\Delta\theta_{int}$, respectively, around the principal ray at internal angle of incidence θ_{int}. Note that we could also have considered only two secondary rays with internal angles of incidence $\theta_{int} \pm \Delta\theta_{int}$ without principal ray, but in that case, at apex angles optimized for resolution, Φ would be null while spherical aberrations remain. It is then more appropriate to calculate Φ

as the average of Φ_+ and Φ_-. Depending on the angle of incidence of the principal ray on the diopter, Φ_+ and Φ_- can be of opposite sign. An arithmetic mean should then be calculated using absolute values $\Phi = \frac{|\Phi_+|+|\Phi_-|}{2}$. However, as shown in **Figure 2.11**, it leads to non physical results since Φ passes by a plateau near apex angles optimized for resolution. This can be solved by using a quadratic mean, i.e. $\Phi = \sqrt{0.5 \times \left(\Phi_+^2 + \Phi_-^2\right)}$, for whom the apex angle which minimizes Φ is unique. Note that, contrary to resolution optimized prisms, here Φ_+ and Φ_- are usually different in both sign and absolute value, and they do not follow the same evolution with respect to A_p or $\Delta\theta_{int}$. The accordingly calculated Φ should then be seen as an approximation of a more complex wave aberration function. In the plane perpendicular to the UZ plane, both Φ_+ and Φ_- are equal and described by **Equation 2.31**. Hence, the real wavefront has a 3D shape that is only symmetric by the UZ plane passing by O.

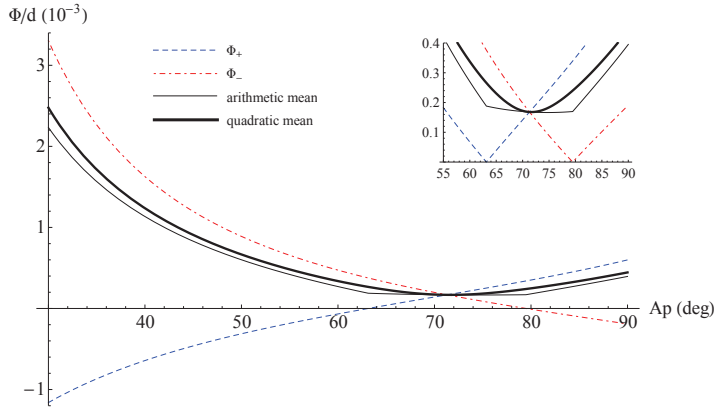

Figure 2.11: Wave aberration function Φ_+, Φ_- and Φ for a SF11 prism. In inset, a zoom on apex angles around the one optimized for resolution with Φ_+ and Φ_- in absolute values.

In the following aberration simulations, to be consistent for different n_p, $\Delta\theta_{int}$ is set in such way that it corresponds to the NA which leads to a spatial resolution by the Rayleigh criterion of Δx = 1.5 µm at λ = 632 nm, i.e. $\Delta\theta_{int} = \arcsin\left(\frac{0.6\times\lambda}{\Delta x \times n_p}\right)$. This Δx is close to the one experimentally measured in chapter 4. This makes $\Delta\theta_{int}$ vary almost linearly from 9.6° at n_p = 1.5 to 7.2° at n_p = 2.0 (9.6°, 8.2° and 7.6° for N-BK7, SF11 and N-SF66 prisms, respectively). However, at low n_p the wave aberration model diverges, even if all the rays still cross the diopter since $\theta_c - \theta_{in} > 8°$ at n_p = 1.5 for the principal ray (**Figure 2.4**). Similarly, at low A_p and low n_p, the angle α calculated by the intersection of the two secondary rays at O' also diverges. Hence, to cover the whole range of n_p and A_p, we also present the aberrations induced by secondary rays at a lower angular diffusion that corresponds to a Rayleigh criterion of Δx = 3.0 µm (4.8°, 4.1° and 3.8° for N-BK7, SF11 and N-SF66 prisms, respectively).

2.6.2 | Aberrations with respect to the apex angle

In order to estimate the aberrations with respect to the apex angle, we normalize Φ by its minimal value to express Φ_r. The first issue this model aims to answer is illustrated in **Figure 2.12** for increasing refractive index prisms: N-BK7 ($n_p \approx$1.52 at λ = 632 nm), SF11 ($n_p \approx$1.78) and N-SF66 ($n_p \approx$1.91) (**Appendix Figure A.3**). As expected, Φ_r increases as A_p digresses from its optimal value for resolution to its optimal value for VWFOV, where α = 0°. Note that taking into account an angular diffusion $\Delta\theta_{int}$ that does not tend to zero decreases the apex angle optimized for VWFOV. Experimentally, the cone of light continuously irradiates from 0 to $\Delta\theta_{int}$, so α is certainly underestimated by considering only two secondary rays (**Appendix Figure A.9**).

Secondary rays with smaller angular diffusion lead to higher Φ_r. The reason is that at apex angle optimized for resolution, where Φ_r = 1, Φ increases as $\sim \Delta\theta_{int}^4$ while for other A_p is increases

as $\sim \Delta\theta_{int}^{3.3}$ (see **Appendix Figure A.12** for a deeper discussion). Obviously, the aberrations are symmetric with respect to A_p around the optimized A_p for resolution ($\sim$36° for N-BK7 prism). It means that a gold-coated right angle N-BK7 prism working in water undergoes the same aberrations that a N-BK7 prism of A_p = 36 - (90 - 36) = -18° (but α remains close to 65° as shown in **Figure 2.4b**).

Here, the important fact is that the optimized apex angle for resolution is not confined into a narrow range, and can easily tolerate an error of +/- 3°. Consequently, resolution optimized prisms can accommodate all of the four metals, for whom θ_{res} and θ_w only vary over a few degrees, especially at longer wavelength and at high n_p (**Figure 1.6**).

This tolerance is certainly the reason why geometric aberrations were not raised by Berger *et al.* in their article on spatial resolution [16]. Indeed, commercial right-angle N-BK7 prisms are almost optimized for resolution in air ($\theta_{res} \approx 44°$ at λ = 632 nm $\Rightarrow A_p \approx 92°$).

Obviously, for an unoptimized commercial gold-coated prism, the value of α can be up to 65° depending on n_p and A_p. Hence, the NA of the imaging system will perhaps not allow to perform classic imaging mode. In this case, the imaging system angle θ_{CCD} can be set between β and θ_{ext}, which results in a clear stripe that does not necessarily cover the entire sensor. It is certainly the explanation for non homogeneity of spatial resolution on the entire FOV sometimes observed in literature, such as presented in **Figure 1.17**.

At first glance, it would be reasonable to assume that Φ_r represents the ratio of resolution between the resolution optimized A_p and any other A_p. But Φ_r depends on the angular diffusion $\Delta\theta_{int}$, as pointed out in **Figure 2.12**. Consequently, we cannot yet conclude on the absolute ratio of resolution with respect to A_p. Nonetheless, it seems coherent to assume that this ratio follows the same trend as Φ_r, and could even be equal to Φ_r for a particular value of $\Delta\theta_{int}$.

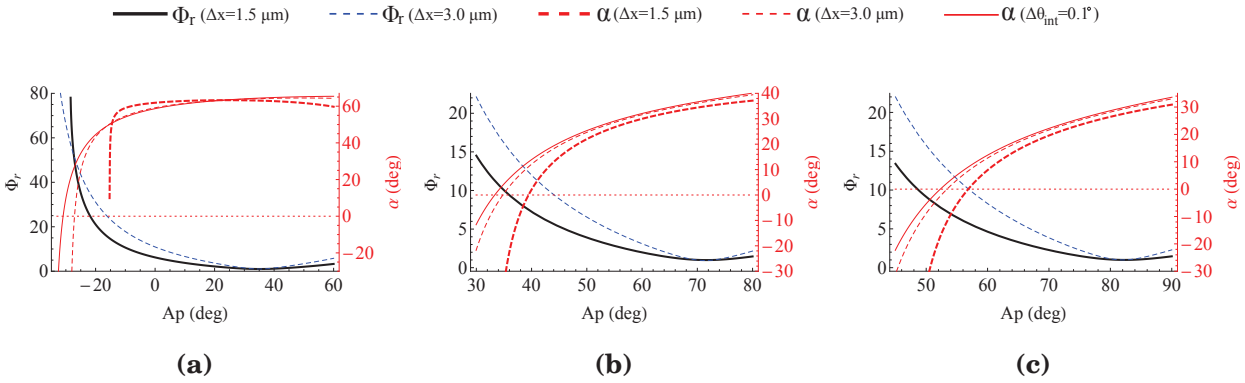

Figure 2.12: geometric aberrations as a function of A_p. **(a)** N-BK7 prisms. **(b)** SF11 prisms. **(c)** N-SF66 prisms.

2.6.3 | Aberrations with respect to the refractive index

Figure 2.13 addresses the issue of optimal n_p. For VWFOV optimized prisms, increasing the refractive index from 1.5 to 2.0 significantly decreases the aberrations, while for resolution optimized prisms Φ remains nearly constant. For a given numerical aperture $NA_{\Delta x}$ that leads to a diffraction-limit of Δx, we can calculate the distance at which the optical system is no longer diffraction-limited: $d_{lim} = \lambda/(4 \times \Phi/d)$. For $NA_{1.5\mu m}$ at λ = 632 nm, d_{lim} = 790 µm using resolution optimized prisms whatever n_p, while it is 10 times less for SF11 VWFOV optimized prisms.

Since for resolution optimized prisms high n_p makes the classic imaging mode easier, we can conclude that whatever the configuration, the higher n_p, the better for prism-based SPRi.

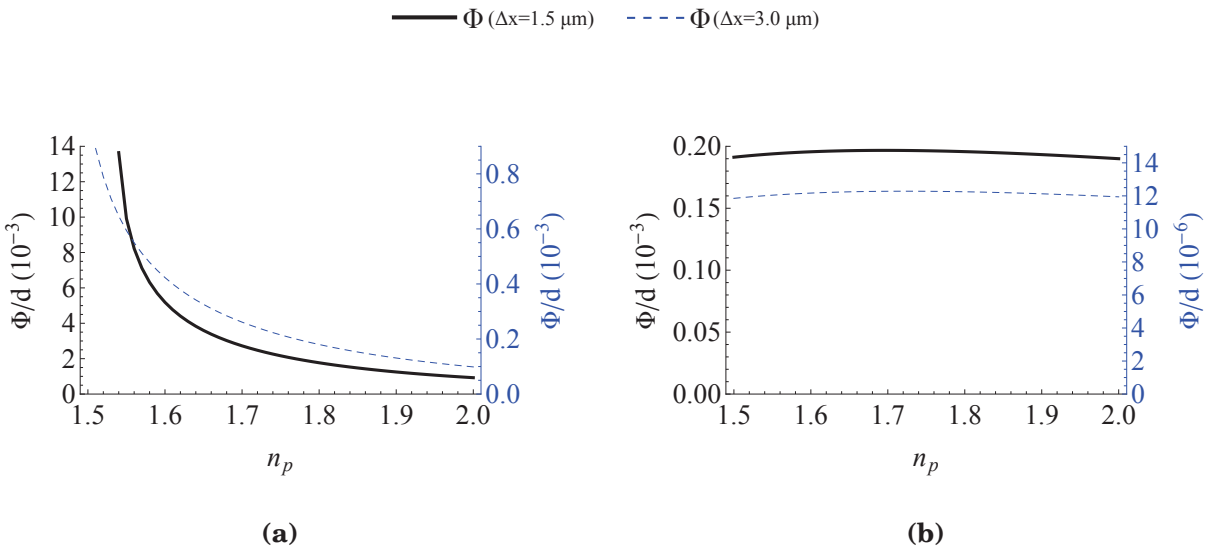

Figure 2.13: geometric aberrations as a function of n_p. The right y-axis refers to $\Phi(\Delta x$ = 3.0 μm). **(a)** VWFOV optimized prisms. **(b)** Resolution optimized prisms.

To conclude, by taking into account geometric aberrations caused by the prism, we propose explanations for several incoherences between theoretical predictions and experimental measurements of spatial resolution in prism-based SPRi. The minimization of the aberrations leads to propose a new optimized prism for resolution, in addition to the one proposed by Maillart for very-wide-FOV. The calculi and conclusions can be easily extended to any prism-based imaging technique, since there is no plasmonic consideration. Hence, the propagation length, and especially the trade-off with sensitivity, still need to be addressed.

2.7 | Trade-off between sensitivity and propagation length

In SPRi, the fact that the propagation length L_x limits the spatial resolution in the propagation direction is a well-known issue. As plotted in **Figure 1.4**, L_x increases with respect to the wavelength for these metals. The spatial resolution can then be improved by decreasing the wavelength of excitation [16], or, at a given wavelength, by choosing a metal which presents a smaller L_x [17, 98]. However, in both cases, it also influences the sensitivity. Our goal is to establish which metal exhibits the better trade-off for high resolution imaging in biosensing, that is to say which exhibits a reasonable sensitivity for biosensing at a low L_x. Obviously, this trade-off depends on the required sensitivity or resolution for a given application. Therefore, we need to plot the sensitivity as a function of L_x, and choose a couple {wavelength,metal} that satisfies our requirements.

In intensity-modulation, the SPR sensitivity is usually quantified as the increase of reflectivity with respect to an increase of the dielectric refractive index: $\partial R/\partial n_d$, and expressed in %/RIU [133, 134]. But this convention does not take into account the penetration depth L_z of the SP into the dielectric. From the optical point-of-view, a biorecognition process is equivalent to the adsorption of a homogenous biolayer of a given thickness h_{bio} on the metal. As shown by Jung *et al.* [37], the effective refractive index of the dielectric n_{eff} (the one "felt" by the SP) depends on L_z (**Equation 1.6**). Thus, the increase of effective refractive index $\Delta n_{eff} = n_{eff} - n_d$ due to a given biorecognition process also depends on λ: the higher λ, the lower Δn_{eff} (**Figure 1.3**). As a consequence, the latter convention, which considers a constant change of the refractive index whatever λ, is not the more accurate way to evaluate the SPR sensitivity in biosensing. Hence, it appears more relevant to determine the sensitivity as the increase of reflectivity ΔR (%) due to the adsorption of a biolayer of a constant thickness h_{bio} and refractive index n_{bio} = 1.41. This

sensitivity convention of constant thickness has not been studied as deeply as the standard one. Nonetheless, a few authors refer to it for discrete values [98, 16].

2.7.1 | Optimization of the metal thickness for sensitivity

As stated in the first chapter, both optical and plasmonic approaches suggest an optimal metal thickness d_m to achieved the highest sensitivity. Considering a metal/water interface undergoing the adsorption of a biolayer, d_m can be determined as the thickness for which the increase of reflectivity (or contrast) ΔR is maximal (see **Figure 1.10b**). If h_{bio} = 1 nm and if ΔR remains proportional to h_{bio} for $h_{bio} \geq 1$ nm, then, the calculated ΔR is also equal to $\partial R/\partial h_{bio}$, and the sensitivity can be expressed in %/nm. In the 400 - 1,000 nm wavelength range, ΔR is proportional to h_{bio} at 95% for $h_{bio} \leq 3.2$ nm.

Since the plasmonic approach does not integrate the metal thickness, the seek of d_m has to be performed by a numerical calculation using the optical approach. Based on the conclusion that high refractive index prisms undergo less geometric aberrations and offer more practical imaging conditions, the calculation of d_m is only presented for N-SF66 prisms, but leads to nearly the same values for other refractive index prisms (**Appendix Figure A.14**). A constant 2-nm-thick adhesion layer of chromium is taken into account for each metal.

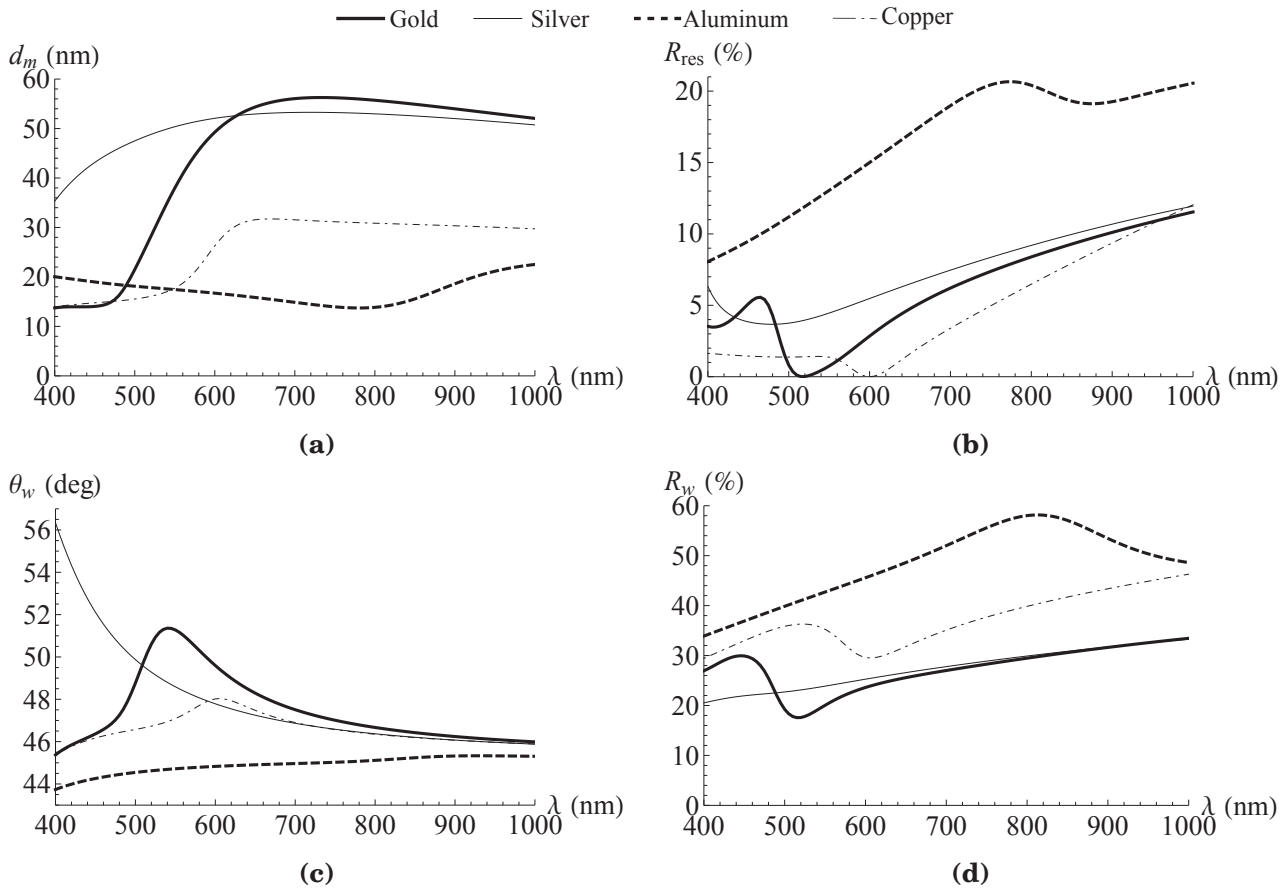

Figure 2.14: Optimal parameters for sensitivity. **(a)** Optimal metal thickness d_m as a function of λ. **(b)** Reflectivity at θ_{res}. **(c)** Working angle. **(d)** Reflectivity at θ_w.

The contrast between the bare metal and the metal plus the biolayer is a function of d_m, θ_{int} and λ: $\Delta R(d_m, \theta_{int}, \lambda)$. Hence, for each wavelength, ΔR only depends on d_m and θ_{int}. The optimization consists in searching the couple $\{d_m,\theta_{int}\}$ that maximizes ΔR at a pitch of 5 nm in wavelength from λ = 400 to 1,000 nm. This calculation is performed with the "NMaximize"

function of Mathematica[1]. For the sake of clarity the markers are not shown. As for the curves of the first chapter, we consider a perfectly monochromatic and collimated illumination, and plane interfaces.

As shown in **Figure 2.14a**, for gold, d_m is $\sim$ 55 nm at $\lambda >$ 650 nm, which is slightly higher than the standard thickness of 45-50 nm [16, 31]. The reason is that we optimize d_m for sensibility in intensity-modulation, and not to exhibit the deeper drop of reflectivity at the resonant angle [135], which is satisfied at lower thicknesses. Therefore, for the optimized thickness, the reflectivity may not necessarily reach zero at the resonant angle (**Figure 2.14b**). The decrease of the optimal gold thickness at short wavelength has been pointed out by Peterson *et al.* [18]. For silver and aluminum, d_m at λ = 632 nm are 53 and 16 nm, respectively, which is in good agreement with the thicknesses used by Huang *et al.* (50 nm for silver and 15 nm for aluminum) [98], by Giebel *et al.* (53 nm for silver and 15 nm for aluminum) [17] and by Berger *et al.* (50 nm for silver) [91]. For copper, the calculated optimal thickness is 30 nm at λ = 632 nm, equal to the thickness used by Huang *et al.* in ref. [98].

The working angle can also be determined, as shown in **Figure 2.14c**. Note that it is close to θ_{res} calculated by the plasmonic approach (**Figure 1.6**), which justifies the use of θ_{res} as an approximation of θ_w in the first part of this chapter. Since N-SF66 prisms have never been used so far, the calculated working angles cannot be compared with literature values, but are in good agreement with the experimental determination presented in chapter 4.

2.7.2 | Optimal sensitivity in SPR

The reflectivity at the working angle R_w, presented in **Figure 2.14d**, is also a key parameter to calculate the sensitivity. The sensitivity with respect to the wavelength can be given in terms of an absolute reflectivity shift [16], as plotted in **Figure 2.15a**. However, from an experimental point of view, it is more relevant to calculate the sensitivity in terms of the relative reflected intensity shift $\Delta I/I_w = \Delta R/R_w$ since the intensity at the working angle is equal to $I_w = I_0 \times R_w$ and the increase of intensity is equal $\Delta I = I_0 \times \Delta R$ where I_0 is the intensity sent to the prism. As for ΔR, $\Delta I/I_w$ is equal to $\partial(I/I_w)/\partial h_{bio}$ for very thin biolayers, and the sensitivity in intensity can be express in %/nm, as shown in **Figure 2.15b**.

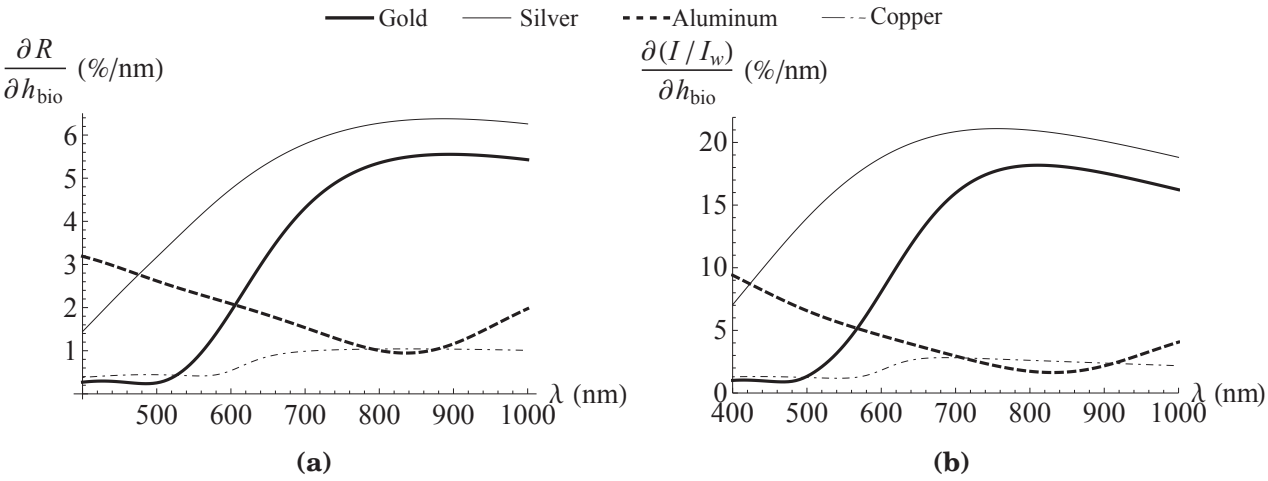

Figure 2.15: Optimal sensitivity in the visible range. **(a)** Optimal sensitivity in terms of variation of reflectivity. **(b)** Optimal sensitivity in terms of variation of intensity, i.e. the signal measured experimentally.

[1]One code line in the function which calculates the SPR reflectivity by the matrix formalism comes from a program previously coded by Jean-Bernard Fiche, during its PhD thesis (2003-2006). I have coded all the other Mathematica functions and programs presented in this thesis.

In both reflectivity or intensity representation, the sensitivity of gold, silver and copper passes by a maximum before λ = 1,000 nm. At the best of our knowledge, these optimal wavelengths for SPR sensitivity have not been pointed out so far. Indeed, in the standard convention based on a constant refractive index change ($\partial R/\partial n_d$ in %/RIU), the sensitivity monotonically increases with λ (**Appendix Figure A.15**).

Since R_w increases with λ for these three metals, in the intensity representation, the optimal wavelengths for sensitivity undergo a blue shift. The best sensitivities at $\pm$ 0.1 % and optimal wavelength ranges are 18.1 %/nm for 780 nm$\leq \lambda \leq$ 845 nm for gold, 20.1 %/nm for 705 nm$\leq \lambda \leq$ 860 nm for silver and 2.8 %/nm for 655 nm$\leq \lambda \leq$ 735 nm for copper. For gold, at λ = 632 nm, the sensitivity is about half the maximum. Note that aluminum exhibits a decrease of sensitivity with respect to λ that reaches a minimum of 1.6 %/nm for 820 nm$\leq \lambda \leq$ 840 nm. It is nonetheless better than gold at $\lambda \leq$ 560 nm. We emphasizes that this optimal sensitivities are not restricted to prism-based SPRi, but apply to all SPR sensors working in intensity-modulation. It should also be noted that the spectral and angular dispersion of the light source, and the roughness of the interfaces are not taken into account. Moreover, the calculated sensitivities obviously depend on the equations which describe the permittivities of metals, and different models may lead to different results, as discussed in **Appendix A.1**. The influence of the metal thickness on the permittivity is also neglected.

2.7.3 | Visualization of the trade-off

Since the optimization of d_m for sensitivity leads to optimal thicknesses close to $L_{z,metal}$ at short wavelengths, we can expect L_x to be more accurately described by **Equation 1.22** which takes into account the influence of the finite metal thickness and the presence of the prism. Here, we only use this latter form.

The trade-off sensitivity/L_x can now be visualized by merging the two approaches. As for the sensitivity, it can be presented in terms of reflectivity (**Figure 2.16a**) or intensity (**Figure 2.16b**). Here, the λ which corresponds to a certain point of a trade-off curve can be found so that it satisfies both the sensitivity in **Figure 2.15** and L_x in **Figure 1.4**.

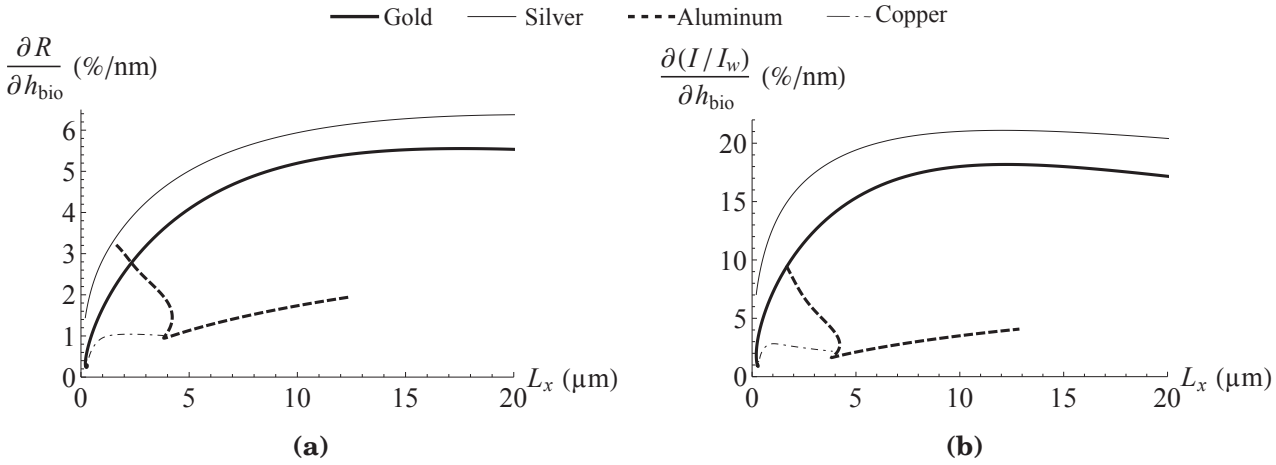

Figure 2.16: Visualization of the trade-off between sensitivity and propagation length in terms of reflectivity shift **(a)** and intensity shift **(b)**.

In the view of high spatial resolution imaging applied to 10-µm-wide cells and 1-µm-wide bacteria, we decided to work at $L_x \leq$ 3 µm. Under this condition, the trade-off is optimal first for silver and then for gold. Copper seems clearly disadvantageous for high resolution and biosensing. For these three metals, the increase of L_x is synonym to an increase of λ. For aluminum, the sensitivity decreases until λ = 830 nm while L_x slightly increases until λ = 720 nm. This correspond to the first linear decreasing part of the trade-off curve (400 nm$\leq \lambda \leq$ 720

nm). The concave part corresponds to the wavelength where both L_x and sensitivity decrease (720 nm$\leq \lambda \leq$ 830 nm) and the last linear increasing part to the wavelength for whom both quantities increases (830 nm$\leq \lambda \leq$ 1,000 nm).

Note that the use of the reflectivity shift leads to a misjudgment that aluminum is better than gold for 2 µm $\leq L_x \leq$ 3 µm. For comparison purpose, the trade-off calculated with the non-corrected L_x can be found in ref. [131]. The non-corrected L_x being proportional to the corrected one by a factor of ~2, in our article, the curves are just shifted toward higher L_x values, and both simulations lead to the same results (the trade-off curve of copper is different because the permittivity comes from different models).

2.7.4 | Hybrid silver/gold layer

To minimize the influence of L_x while conserving a good SPR sensitivity, silver appears as the optimal metal. However, insofar as the SPRi experiment is dedicated to biosensing, silver cannot be used alone due to its fast oxidation in aqueous solution [136] and needs to be protected by a second layer. Several types of stable and biocompatible protecting layers have been employed, such as oxides, widely studied by Szunerits and co-workers [136, 137], graphene [138] or gold for its stability, biocompatibility and well-known surface chemistry [79, 135]. Other strategies to reduce the influence of the propagation length have also been explored. De Bruijn *et al.* demonstrated that turning by 90° an hemispherical prism allow to have two images where the propagation length degrade the resolution in different directions [15]. The two images can then be merge in such a way as to only keep the unaffected directions. More recently, Lindquits *et al.* used an pixel-like arrays of nanoholes supporting localized SPR effect [139]. In that case the resolution in not limited by L_x but rather by the step in pixel-like micro-arrays (~ 3µm). However, each hole has to be drilled individually, thereby limiting a large scale fabrication.

Herein, we focus on an hybrid silver/gold coating (with a 2-nm-thick adhesion layer of chromium) and conduct the same optimization protocol as for the single metal layers. A similar study has been published by Ong *et al.* [135], where the authors optimized the metal thicknesses in order to obtain the deeper drop of reflectivity at the resonant angle (higher enhancement of the electric field). In contrast, our optimization targets directly the sensitivity by finding the optimal thickness of silver for a constant 5-nm-thick protecting gold layer. It can be assumed that the thinner the gold layer, the closer the sensitivity properties are to the one of silver. Here, we selected 5 nm as the minimal thickness for the gold layer to be homogenous and impermeable. The resultant sensitivity is represented in **Figure 2.17a** (see **Appendix Figure A.16** for the other optimized parameters). As expected, the hybrid coating lies between each constituent metal.

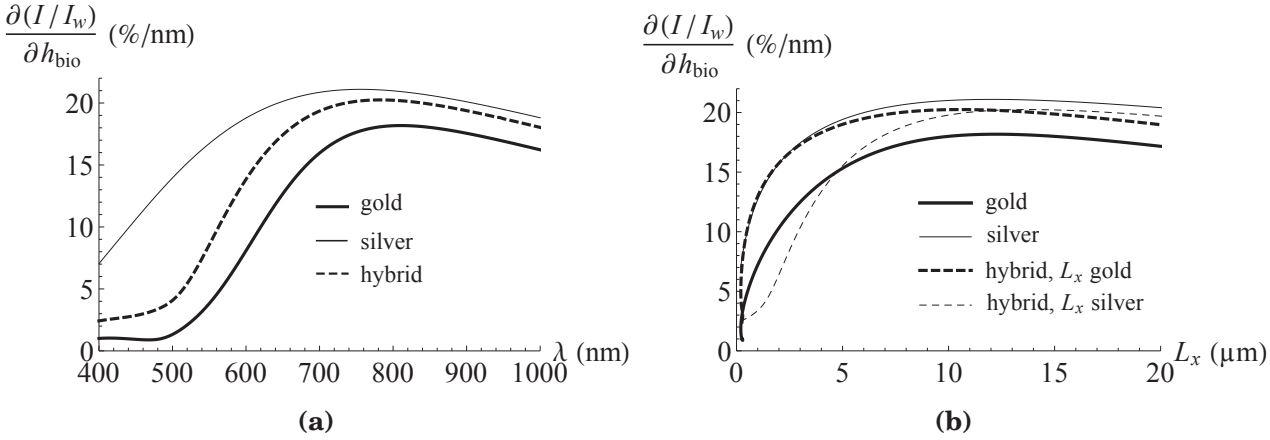

Figure 2.17: Hybrid gold/silver metal layer. **(a)** Sensitivity in intensity as a function of λ. **(b)** Boundaries of the hybrid trade-off curve and comparison with silver and gold coatings.

To characterize the trade-off sensitivity/L_x, the propagation length is required. Since the plasmonic approach only considers a unique metal of semi-infinite thickness, the propagation length of a hybrid layer cannot be calculated theoretically, and needs to be measured experimentally. It can however be assumed that the value of L_x ranges from the one of gold to the one of silver, as plotted in **Figure 2.17b**. Compared to pure gold, for L_x between 2 and 3 μm, this result suggests that the improvement will range from a factor 1.5 if L_x is the one of gold (in which case it is as good as pure silver), to 0.6 if L_x is the one of silver. Relying on this assumption, the use of a thin layer of gold on silver does not necessary lead to an improvement of the trade-off.

2.8 | Conclusion

In this chapter, in a first section, we have addressed the issue of geometric aberrations induced by the prism. Their minimization lead us to describe two novel optimized optical configurations in prism-based SPRi. Through the quantification of these aberrations, we can conclude that high refractive index prisms are optimal whatever the configuration in prism-based SPRi.

In a second section, we have theoretically determined the best SPR sensitivity in intensity modulation by optimizing the metal thickness over the 400 - 1,000 nm wavelength range. Our analysis shows that the sensitivity of gold and silver passes by a maximum at $\lambda \sim$750 nm. The visualization of the trade-off between propagation length L_x and sensitivity shows that silver, and then gold, are the best metals whatever the wavelength. The trade-off evaluation of a hybrid layer composed of silver coated with 5 nm of gold shows that the enhancement compared to bare gold lies between a factor 1.5 and 0.6 depending on L_x, which should in that case be measured experimentally.

3 | Material and Methods

Contents

Résumé du chapitre 3

Ce chapitre décrit le dispositif expérimental sur lequel ont été réalisés les expériences et mesures présentées dans le chapitre 4. Les méthodes et protocoles employés pour les expériences de biologie sont détaillés en dernière partie.

Après une présentation globale du montage, je présente successivement ses différentes grandes parties. La partie optique tout d'abord, avec notamment une discussion sur le choix d'une caméra optimale pour la SPR. La partie fluidique ensuite, avec une analyse des contraintes liées à la double observation : optique par le dessus, et SPR par le dessous. De la même façon, je décris la structure mécanique qui permet d'assembler prisme et chambre fluidique tout en permettant une observation SPR et une connexion pour les arrivées et sorties de milieu biologique. La partie régulation thermique par une technique originale de chauffage planaire et transparent est un peu plus détaillée car elle comprend des mesures de calibrage et des simulations par éléments finis.

Le pilotage automatisé du montage est assuré par un programme LabVIEW, dont je décris brièvement la philosophie. Je discute ensuite des problèmes qui se posent pour le traitement des séquences d'images intermédiaires et des séquences de séquences obtenues en imagerie par scan de lignes. Enfin, je précise le protocole de reconstruction par un programme Mathematica et par ImageJ.

Finalement, je présente les timbres de PDMS qui sont utilisés pour les mesures de résolution, ainsi que les cellules eucaryotes et procaryotes qui ont fait l'objet des dernières expériences de cette thèse.

This chapter presents the experimental set-up on which the optical and biological experiments have been performed. It focuses on the methods developed to measure the performances of high resolution prism-based SPRi in terms of spatial resolution, FOV and sensitivity. Finally, the selected microorganisms and the associated surface chemistry are introduced.

3.1 | Set-up overview

The experimental set-up brings together elements of optics, fluidics, thermics, mechanics and instrument control/automation (**Figure 3.1**).

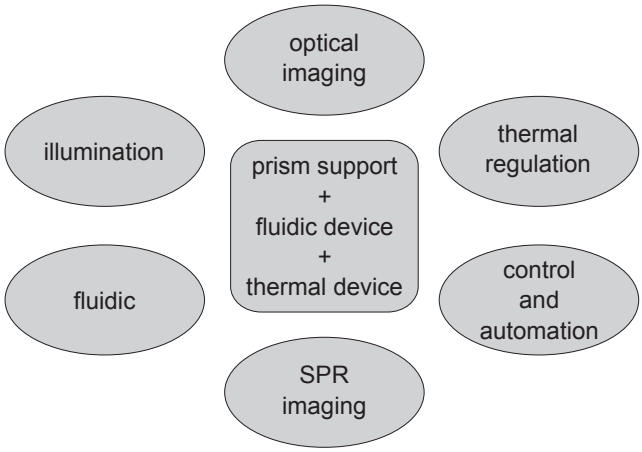

Figure 3.1: Diagram representation of the experimental set-up.

The design and fabrication of a completely new experimental set-up was one of the objectives of the PhD thesis. The idea was to build a research apparatus which is fully open and can be easily updated to accommodate to a multitude of variables, such as prism shape, air and water environments, wavelength of illumination, imaging systems and imaging modes. A more detailed schematic view can be found in **Appendix Figure A.17**.

To fulfill its function, our set-up had to respect the following specifications:

- a wide range of accessible angles of SPR illumination and imaging, typically from 15 to 80°, to accommodate air or water environments in line-scan and classic imaging mode
- imaging from above by a right optical microscope in order to correlate the SPR and optical images of microorganisms and avoid ambiguous SPR observations and interpretations
- entire biochip surface observable to experimentally measure the decrease of spatial resolution with respect to the distance from the edge of the prism, or select an area of interest
- SPR illumination:
  - angle automation at a precision less than 1° and sensitivity less than 0.05° to trace plasmon curves
  - easy change of wavelength to access several sensitivities, L_z and L_x
  - high intensity beam to image at high magnification with short aperture time in order to avoid motion blur and enable frame averaging
- SPR imaging:
  - wide range of imaging systems, from very short to very long tube lenses and working distances for the use of different optical magnifications
  - precise and automated focus adjustment to use the line-scan imaging mode
  - camera able to acquire high spatial resolution and high dynamic range images to be sensitive both inside and outside the cells

- thermal regulation from 30 to 40°C at a precision less than 1°C to maintain the microorganism in physiological conditions and prevent temperature drifts responsible for reflectivity shifts which could be confused with biodetection events
- fluidic system to inject the target, rinse the flowcell, send a biochemical stimuli or renew the culture medium for cell growth
- automated set-up to perform experiments over tens of hours

3.2 | Optics

3.2.1 | Illumination

As presented in the first chapter, the light used to generate the SP has to be monochromatic, collimated and linearly polarized. The production of such a beam is performed by 3 elements presented in **Figure 3.2a & b**.

High-power LEDs M530F1, M625F1, M660F1, M735F1, M780F2 and M850F2 (Thorlabs, $P \approx 10mW$) with Gaussian-shape spectral distributions of central wavelengths of 518, 632, 660, 721, 780 and 850 nm, respectively, and FWHM of 30 nm, are used as light sources. The effect of their non-monochromaticity is neglected [140]. Coupling these LEDs to a 400-μm-wide optical fiber is a very convenient way to bring light of different wavelengths and power to the collimation lens and polarizer. The second element is a collimation lens which forms the image of the optical fiber an infinite distance away, so the rays are parallel. In order to have the best homogeneity of light intensity within the beam at all wavelengths without readjustments, we use an achromatic aspheric glass lens (25-mm-wide, $f_{collimation}$ = 35 mm). Finally, the last element is a linear polarizer that converts the unpolarized light into TE or TM mode by a simple 90° rotation.

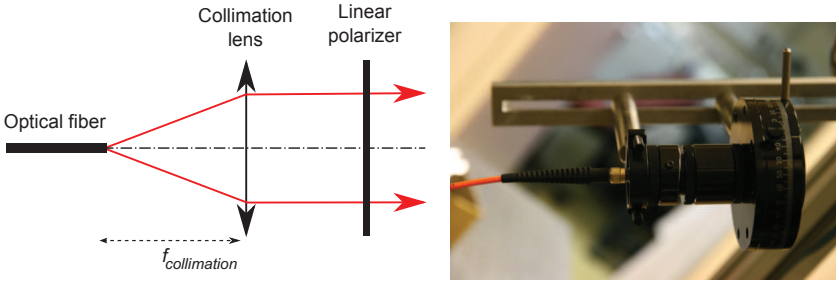

Figure 3.2: Illumination system. **(a)** Schematic view of the illumination system. A lens of focal length $f_{collimation}$ collimates the output of an optical fiber. The parallel rays then pass through a linear polarizer to obtain TE or TM polarized light. **(b)** Picture of the illumination system.

This illumination system is attached on and aligned with the illumination arm, so the light is sent toward the main axis of the set-up, where the prism lies, whatever the angle (**Figure 3.5**). Note that the distance with respect to this axis has no importance since the beam is collimated.

The angle of illumination can be manually set from 10 to 90° at a precision of 1° (measurement uncertainty of the angle read on a goniometer), and finely adjusted over a range of +/- 10° with a precision better than $10^{-3°}$ by a step motor (Oriel Encoder Mike, 0.5 inch). This motor can be controlled either by a controller box or by an homemade LabVIEW program.

3.2.2 | SPR and optical imaging systems

3.2.2.1 SPR imaging system

The SRP imaging system is based on a microscope configuration (**Figure 3.3a**): an objective lens (which can be a microscope objective) collimates the object plane situated at a distance $f_{objective}$

and a tube lens forms the image of the object plane on a camera sensor situated at a distance f_{tube}. A simple plano-convex (PCX) tube lens can be used since there are no chromatic aberrations, and for f_{tube} > 100 mm spherical aberrations can be neglected. Thus, the optical magnification ($G = f_{tube}$ / $f_{objective}$), the FOV (= Camera sensor area / G^2) and the NA (given by the objective lens) can be easily chosen. Furthermore, a diaphragm is placed just after the tube lens. It has two functions. First, it can be used to set the horizontality of the prism: when the illumination angle and the imaging system angle are equal and the diaphragm is almost closed, the prism, whatever its apex angle, is horizontal if a bright spot appears at the center of the sensor. Secondly, slightly closing the diaphragm attenuate the artifacts due to the reflections on the tube inner sides.

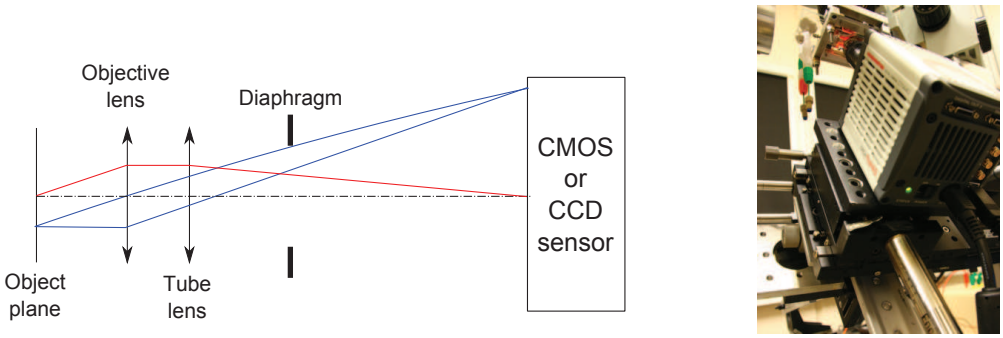

Figure 3.3: SPR imaging system. **(a)** scheme of the imaging system. **(b)** Picture of the SPR imaging system on its mechanical platform.

In line-scan imaging mode, the NA of the objective lens does not have to be especially high, but the working distance must be sufficient to image the illumination side edge of the prism. In our set-up, we use long working distance microscope objectives (Olympus, LMPLFLN series) ×50 (NA = 0.5, WD = 10.6 mm), ×20 (NA = 0.4, WD = 12.0 mm), ×10 (NA = 0.3, WD = 21.0 mm), and an Edmund Optics objective ×4 (NA = 0.1, WD = 20 mm).

In classic imaging mode with prisms optimized for resolution, the NA has to be greater than 0.51 for N-SF66 prisms and 0.62 for SF11 prisms. For small FOV images (G > 20), we use the ×50 microscope objective as objective lens, while for wide-FOV (G < 10), we use a 25-mm-wide aspheric lens of effective focal length 18.75 mm ⇔ NA=0.66 (Edmund Optics). Unlike microscope objectives composed of many lenses and corrected for the principal optical aberrations such as coma, a single lens, even aspheric, does not exhibit similar capabilities in terms of image quality. Nonetheless, at medium magnification (≈ ×5), it is a simple and inexpensive solution to achieve a resolution sufficient for individual eukaryote cells imaging on FOV up to several mm^2.

3.2.2.2 SPR imaging arm

The camera body, where the SPR imaging system is screwed, is fixed on two linear translation stages. The first one is used to move the whole imaging system within its own optical axis to control the focus, and is actuated by the same motor as the one that controls the illumination angle (range: 14 mm, accuracy: 0.1 µm, speed: from 200 to 0.5 µm/s). The second linear stage is along the Y-axis and complements the microscope displacement in the X-axis so that the same area can be visualized by both SPR and optical microscopy simultaneously.

Because the length of the imaging system can vary a lot depending on the application (long or short tube lens, eventual beam splitter cube...), these stages are mounted on a rail along the optical axis (**Figure 3.3b**). By this way, the imaging system can easily be moved and replaced while remaining aligned, and the focus can be roughly adjusted before proceeding to a finer focus with the motorized stage. For even longer imaging systems, the whole platform can be moved along the imaging arm.

3.2.2.3 SPR camera

In SPR, the two major parameters for the camera sensor are the dynamic range and the signal-to-noise ratio (SNR).

The dynamic range is the number of distinguishable intensity values, and is defined by ratio between the most and least intense possible light measurements. The largest signal achievable is equal to the maximal number of electrons that can be accumulated in a single pixel, and is known as the Full Well Capacity (FWC). The smallest signal detectable is limited by the readout noise that arises from electrons generated when pixel charges are transferred and read. At least as many gray-levels as the FWC are needed in order not to loose information. In digital cameras, gray-levels are binary coded by an even number of bits: 8-bit $\Leftrightarrow$ 256 gray-levels and 16-bit $\Leftrightarrow$ 65,536 gray-levels.

The SNR corresponds to the minimal intensity shift detectable at a certain intensity value, and can be calculated by $SNR = signal/noise$. It is also limited by noises, which can be separated into readout, dark-current and shot noises. Dark-current noise comes from electron randomly created by thermal fluctuations. This noise can be predominant for long exposure time, as in fluorescence microscopy. However, in SPRi, the dark-current and readout noises can be neglected compared to the photon noise (also called shot noise or Poisson noise).

Photon noise arises from the intrinsic nature of light. Light intensity is quantified: it is a number of individual particles (photons) that will independently interact with matter (pixels). The physical process of a photon generating an electron/hole pair in a semiconductor is governed by a statistical phenomenon described by the Poisson distribution. Let us consider several light pulses of 100 photons arriving on a pixel. The average number of electrons created per pulse is equal to a probability of interaction times the number of photons. This probability is called the quantum efficiency (QE), 70 % for instance. Once again, unlike fluorescence imaging, in SPRi, the QE does not have to be very high because the light intensity or the exposure time can be increased without suffering from additional noises. Now, because QE is a probability, we may expect the number of electrons created being close to 70, but unlikely being 70 for each single pulse. The same idea can be applied to adjacent pixels receiving the same number of photons. Poisson distribution states that the noise is equal to $\sqrt{N}$, where N is the signal. In this illustration the signal is the number of electrons per pulse and per pixel. This noise increases with respect to the signal, but since $SNR = N/\sqrt{N} = \sqrt{N}$, the higher the signal, the better the SNR. In digital camera, N_{max} corresponds to the FWC. In other words, if we work close to the full dynamic, that is to say close to the highest gray-level value, we may expect to be able to detect intensity shifts of 1/SNR per pixel ($\Leftrightarrow$ relative precision). Now, if we take into account P pixels, we will multiply the signal by P and the SNR by $\sqrt{P}$. Averaging on several pixels can be done in "space", by considering an area of P pixels on a single image, or in "time", by considering the same pixel on P successive images supposed to be identical (**Figure 3.4**). That is where the resolution and the frame rate of the camera come into play!

Our choice of camera sensor turns to the ORCA 4.0 (Hamamatsu Photonics K. K.) which specification is:

- resolution: 2048×2048 pixels (6.45-µm-wide)
- FWC: 30,000 e^-/pixel (digitally encoded in 16-bit)
- QE: 70 % at λ = 632 nm
- frame rate: 30 fps (USB 3.0) or 100 fps (cameralink)
- Temperature regulation: -10°C (air cooling)
- dark current noise: 0.06 e^-/(pixel.s) at -10°C
- readout noise: 0.9 e^-/pixel

- photon noise: $\geq$ 173 e^-/pixel $\Rightarrow$ SNR_{max}: 173
- best relative precision: $1/SNR_{max}$ = 0.58 %/pixel (measured at 0.63 %)

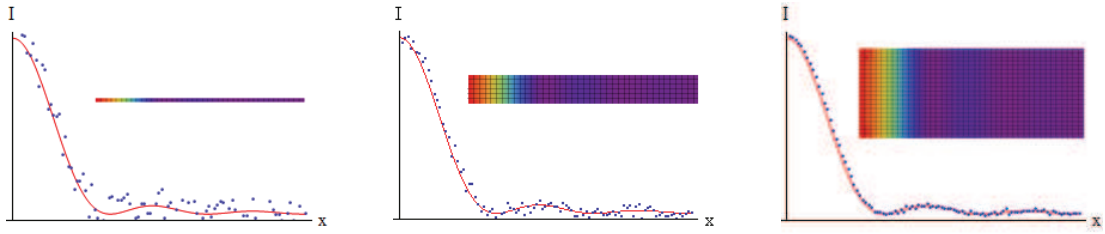

(a) P=1 **(b)** P=8 **(c)** P=64

Figure 3.4: Noise reduction illustration with increasing pixel averaging. The real signal is plotted in red, let us say it represents a light intensity as respect to a distance. The measured pixel values are the blue dots and suffer from photon noise. Inset: $I(x, y)$ with cross section line (or stripe) of increasing width **(a)** No average: a 1-pixel-wide cross-section line. **(b)** Average of P = 8 pixels. Noise reduction can be implemented by increasing the width of the cross-section line from 1 to 8 pixels, or by averaging 1-pixel-wide cross-section lines coming from 8 successive images. **(c)** P = 64. As the averaging becomes higher, the SNR is improved by a factor $\sqrt{P}$.

To give an idea of the true experimental noise, let us say we are working at 70% of the full dynamic (= mean gray-level of 45,875) so that the pixels are not saturated and can measure an increase of intensity. If we consider an area of P = 100 pixels (still allowing the observation of 40,000 different areas) or equivalently 1 pixel on P = 100 successive images, then $SNR = \sqrt{0.7 \times FWC} \times \sqrt{P} = 1450$ and the noise is about 0.07% of the absolute signal (= 32 gray-levels). Now, if we want to use the SPR reflectivity scale, we have to multiply this value by the mean value of the reflectivity when performing a classic SPR experiment, let us say 40%, which leads to a SPR reflectivity noise of approximately 0.03% and a limit of detection equal to 3 times this noise: 0.1% in reflectivity shift. According to **Figure 1.11b** of chapter 1, at λ = 632 nm at the gold/water interface, we should be able to detect the recognition of biomolecules inducing a change of refractive index equivalent to the adsorption of a 0.04-nm-thick biolayer. As a comparison, in ref. [71] the increase of reflectivity generated by the secretion of cytokines by T lymphocytes was measured at +3% for both interferon gamma (INF_γ) and Interleukin 2 (IL2).

3.2.2.4 Microscope

In order to compare optical and SPR images, an up-right Olympus microscope (BXFM-F) is placed above the SPR set-up (**Figure 3.5**). This microscope is equipped with a tube lens of focal length 160 mm and uses the same objectives as mentioned for SPR imaging. Except for the additional fluorescence filter cube between the objective and tube lens, the microscope optical scheme is equivalent to the one of SPR (**Figure 3.3a**). Images are captured in color by the 18 megapixel CMOS sensor (22.3 $\times$ 14.9 mm^2) of a Canon 600D.

This reflex camera body is relatively inexpensive compared to scientific cameras of comparable sensor resolution. However, the linearity of gray-levels as a function of light intensity, the noise and the dynamic are not as good as they are on a sensor dedicated to microscopy. A commercial software enables to adjust and automatically capture pictures at a constant rate (time-lapse). Fluorescence microscopy can also be performed. In that case, the Canon 600D is replaced by a second ORCA 4.0 presenting a low noise at low light intensity. Note that due to the multiple interfaces created by the sample environment, optical images slightly suffer from spherical aberrations, and in fluorescence imaging, artifacts are sometimes created by defects and dust at the interfaces.

The final optical set-up is shown in **Figure 3.5**. The mechanical components that have been designed during the PhD thesis have been fabricated by Philippe Montmayeul.

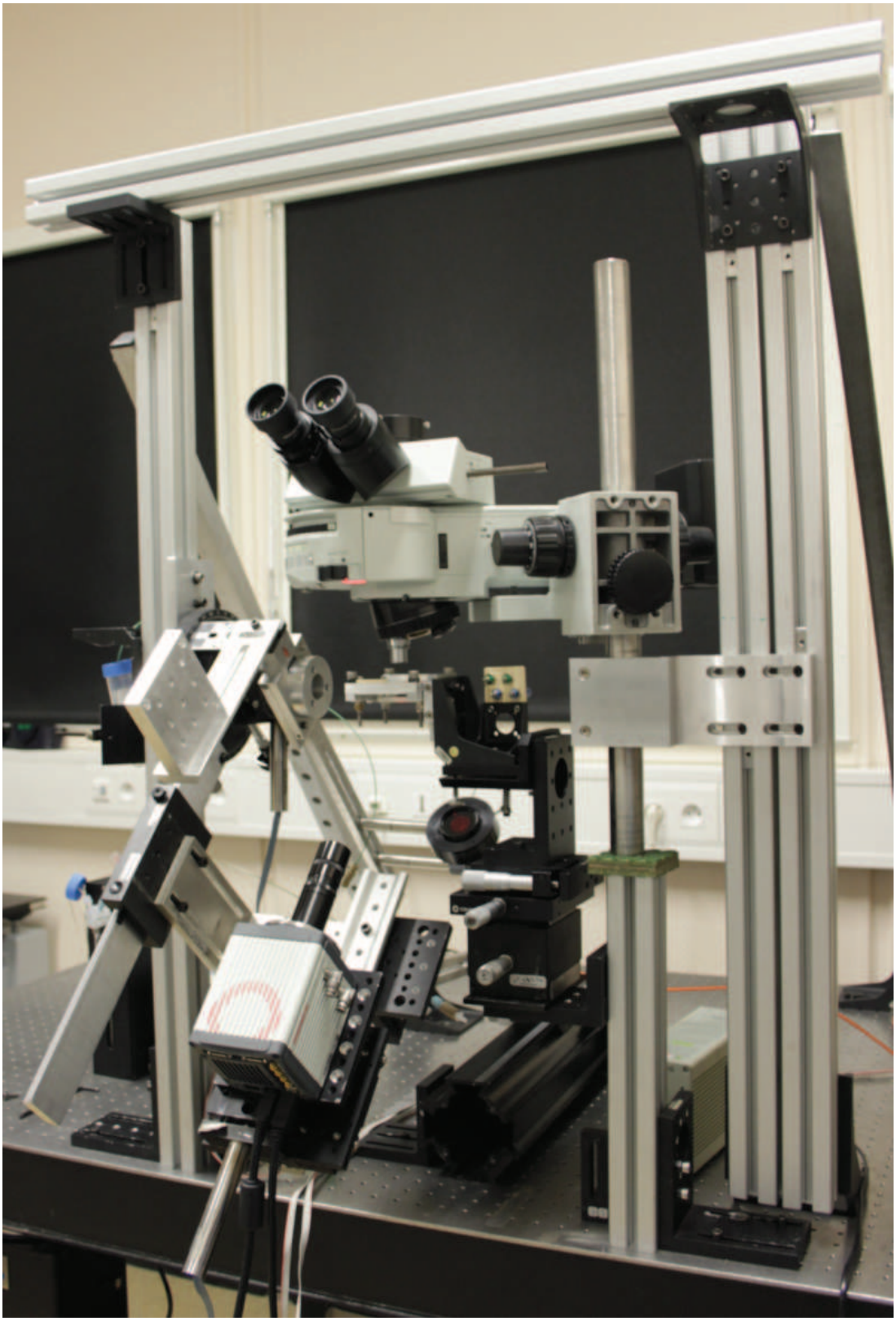

Figure 3.5: Optical set-up. A rectangular structure ensures a good mechanical stability and vibration dumping. The camera and illumination arms are fixed to the left post. The prism axis coincides with the rotation axis of the system. An optical microscope overlooks the SPR apparatus and allows simultaneous SPR and optical image acquisition.

3.3 | Fluidics

3.3.1 | Fluidic device

As previously said, an optical observation from above the prism is indispensable in most of our experiments. This constraint imposes that the flowcell must be transparent, flat, and relatively thin to allow the use of microscope objectives. As a consequence, the input and output of the fluidic device cannot be situated just above the flowcell, and need to be moved a few centimeters away. Furthermore, the channels which carry the fluids have to bypass the flowcell area in order not to deteriorate the optical microscope observation.

Another constraint is to be able to easily implement microfluidic systems instead of simple ring shape flowcells. Microfluidic systems offer the possibility to control the flow speed distribution, increase the pathway of the fluid on the biochip surface or implement some functions such as mixing or sorting. Over the years, polydimethylsiloxane (PDMS) (Sylgard 184) as become the reference material because of its physical and chemical properties. This elastomer is transparent to visible light, soft and resistant, can replicate nanometer size features, is biologically inert and porous to oxygen, and can be easily bound on glasses by oxygen plasma treatments [141].

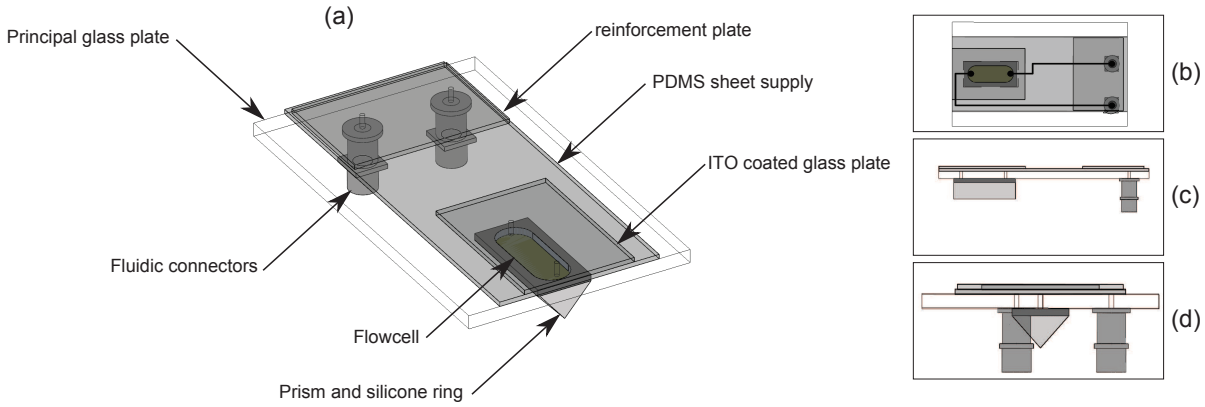

Figure 3.6: CAD views of the fluidic device. **(a)** 3D view and presentation of the different parts. **(b)** Top view. **(c)** Side view. **(d)** Front view.

These specifications led us to design the fluidic device[1] presented in **Figure 3.6**. A 3-mm-thick glass plate of 5×9 cm^2 ensures the rigidity while being transparent. A 1-mm-thick PDMS sheet patterned with 1-mm-wide and 70-µm-high channels links the fluidic connectors with the flowcell, as shown in **Figure 3.6b**. This "PDMS sheet supply" is fabricated by replicating a 4-inch silicon wafer mold microstructured by SU8 (detailed procedure in **Section 3.7**). It is then permanently bound on the top of the glass plate by exposing both elements to an oxygen plasma (30s, 12.5 W, 0.6 mbar O_2).

The fluidic connectors, where the tubes coming from the fluidic system are connected, face down below the principal glass plate which has to be drilled at 4 points. A reinforcement glass plate is also bound by oxygen plasma to the PDMS sheet supply right above the connectors in order to prevent any rupture because of too high pressures. The presence of the ITO coated glass plate is explained in **Section 3.5.1**. A flowcell made of a 1.5-mm-thick silicone ring or a PDMS microfluidic system of the same dimensions as the prism base is finally aligned with the access holes and bound to the glass plate.

[1]The first design was established and fabricated by Loïc Leroy and Sébastien Dumenil previously to the PhD thesis. I redesigned and fabricated the one presented here.

3.3.2 | Fluidic system and instrumentation

For bacterial detection, the growth medium is directly injected into the fluidic device with a syringe. The input and output connectors are then sealed.

For cellular secretion experiments, many strategies have been tested. One of them involves the following steps: fill up the fluidic device with medium, inject the cells, rinse with medium to remove uncaptured cells, and finally inject the stimuli before sealing the fluidic device. This operation requires at least two elements. The first one is a device that precisely controls the flow. In this set-up, we use a syringe pusher called "cavro pump" (**Figure 3.7a**). Depending on the syringe volume (from 0.1 to 25 ml), the flow can be set from less than 0.01 to several hundreds of µl/s. The second element is an injection system that can send a sample containing the cells or the biomolecules to the fluidic device. In our experiments, the loaded volume does not have to be precisely known. Therefore, a simple 3-entries valve connected to a syringe containing the sample is sufficient (**Figure 3.7c**).

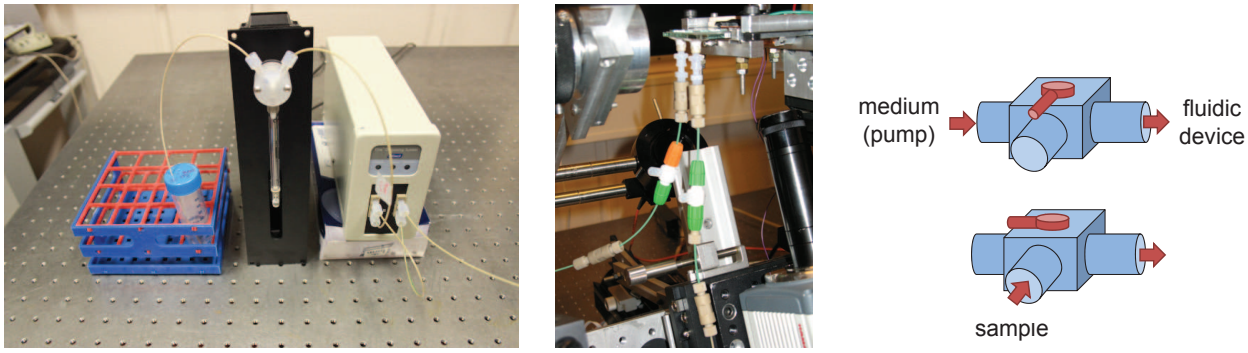

(a) **(b)** **(c)**

Figure 3.7: Fluidic system. **(a)** The medium is pumped and sent to the degasser by a control syringe pusher called cavro pump. **(b)** Two syringe connectors allow the fluidic system to easily plug the fluidic device. Each connector has a valve to avoid possible leak or flow during the experiment. **(c)** 3-entries valve used to inject an arbitrary volume of micro-organisms with a syringe.

To avoid the formation of air bubbles, or to eliminate them afterward, a degasser can be placed just after the cavro pump (**Figure 3.7a**). The principle of a degasser is to lower the air pressure around a Teflon tube where the liquid passes. Since Teflon is permeable to gas, the concentration of dissolved gas in the liquid decreases.

Living microorganisms are not adapted to degassed growth media, and need some dissolved gases to live, such as O_2, so the degasser cannot be used. Using a high flowcell can solve the problem of air bubbles without the use of a degasser because they generally stay at the upper part, in contact with the principal glass plate, and are not seen in SPR. Moreover, larger flowcells decrease the flow speed and pressure gradients that induce mechanical stresses for cells, while being closer in terms of volume to classic growth conditions (several ml). In cells and bacteria experiments, we use a 1.5-mm-high silicon ring which corresponds to a flowcell volume of ≈220 µl.

The flow rate within the fluidic device is controlled by a homemade LabVIEW program[2] that sends orders of "step frequency" to the syringe pusher (RS-232 protocol). This program enables to set constant flow rates between 0.10 to 16.6 µl/s using a 1 µl syringe. It can also "agitate" the flow by performing successive forward and backward movements. Depending on respective volumes, the average flow can be positive, null or negative. This method is used to improve the cell capture by increasing their probability of contact with the functionalized areas when they arrive into the flowcell.

[2]This program has been coded by Loïc Leroy and internship students previously to the PhD thesis.

3.4 | Prism support

The prism support, shown on **Figure 3.8**, has been designed so that the half-space beneath the prism is fully accessible by an imaging system of 25 mm in diameter (C-mount standard) having a short working distance. This is typically the case in classic imaging mode with prisms optimized for resolution. The other half-space is occupied by the fluidic and thermal devices inserted in two slides.

The prism is put in a mobile holder and reposes on 4 tiny metal parts situated at the end of each face. Once put in place, the base is horizontal and is about 1 mm higher than the rest of the holder. The prism can be further blocked by applying a pressure with a screw on one of its sides. Another mobile part, based on the same idea, has been designed for the use of Horiba SF11 prisms. This design presents the advantage to be very versatile and can apply to almost any kind of prism used in SPRi. The mobile part is guided on the fixed part by 4 threaded stems to ensure a good lateral alignment. Once the base is in contact with the flowcell, a homogeneous pressure is applied by screwing one nut on each stem. The fixed part remains mounted on a right angle bracket and can be easily dismantled from the set-up and placed on a flat surface to put the prism, the fluidic and the thermal devices.

As in standard microscopy, the sample can be laterally displaced by linear translation stages to choose the area of observation (**Figure 3.5**). However, in prism-based SPRi, moving the prism in the X direction also changes the focus adjustment. This focus can be readjusted by moving the imaging system, or by moving the prism in an oblique direction in the X/Z plane. Having a degree of freedom in the Z axis also enables to replace the prism in the illumination beam even after long displacements in the X axis. Note that when moving the prism in the Z axis, the focus on the optical microscope needs to be readjusted.

It is also necessary to be sure that the prism base is perfectly horizontal, otherwise the image of the optical microscope cannot be in focus on the entire FOV, and in line-scan imaging mode the clear line is tilted on the SPR camera sensor. The prism horizontality is controlled by a 2-axis stage allowing a angular positioning over +/- 6° (**Figure 3.5**). Experimentally, strictly fulfilling these two conditions is difficult to achieve, and small remaining tilts are sometimes corrected in image post treatment.

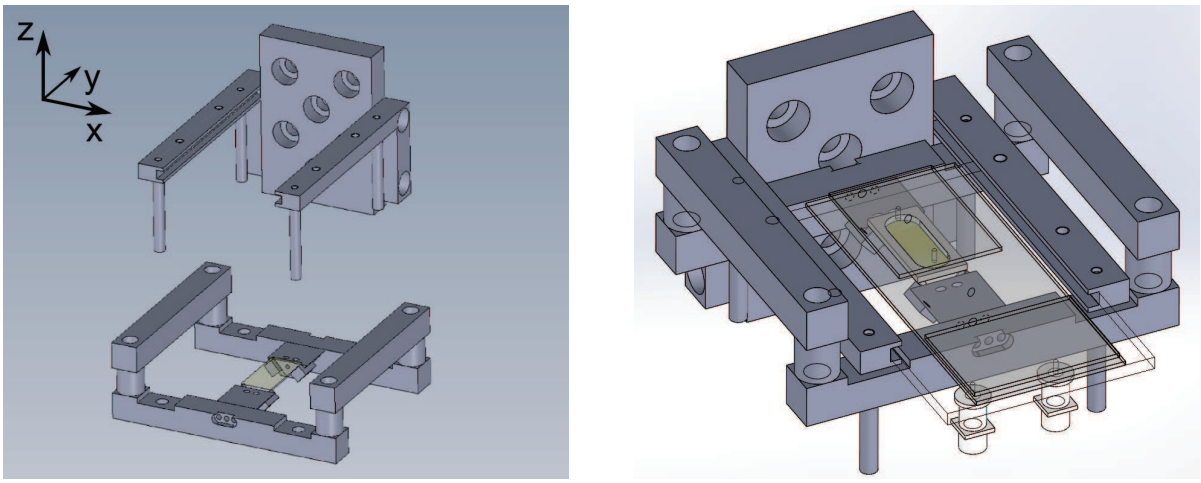

(a) **(b)**

Figure 3.8: CAD views of the prism support for SPRi. **(a)** Separate mobile and fixed parts. **(b)** Assembled prism support with fluidic device.

3.5 | Thermal regulation

3.5.1 | Thermal device

Due to the optical specifications, the entire set-up does not fit into a thermally regulated container, so only the flowcell is regulated. This solution presents the advantage to be less expensive while allowing a faster regulation over a larger range of temperatures.

As for the fluidic device, the thermal device is limited in terms of volume and transparency due to the simultaneous SPR and microscope imaging. Its function is to generate a homogenous temperature field over the center part of the flowcell ($\approx$ 1 cm^2). The temperature field should ideally be homogenous over the height of the flowcell. Nonetheless, since SPR is only sensitive in the L_z range, the homogeneity is less crucial in the Z-axis. In other words, the temperature field on the prism base should have a horizontal translational symmetry in the XY plane, but can accommodate small variations in the Z axis. These conditions suggest a heat source of the same symmetry, i.e. a plane parallel to the prism base. The closer the plane heat source is to the base, the less loss of heat by conduction in the other parts, such as the fluidic device or the prism support, and the faster the regulation. On the other hand, conduction to parts in contact with the flowcell can attenuate the temperature gradients induced by the finite size of the heat source and prism base.

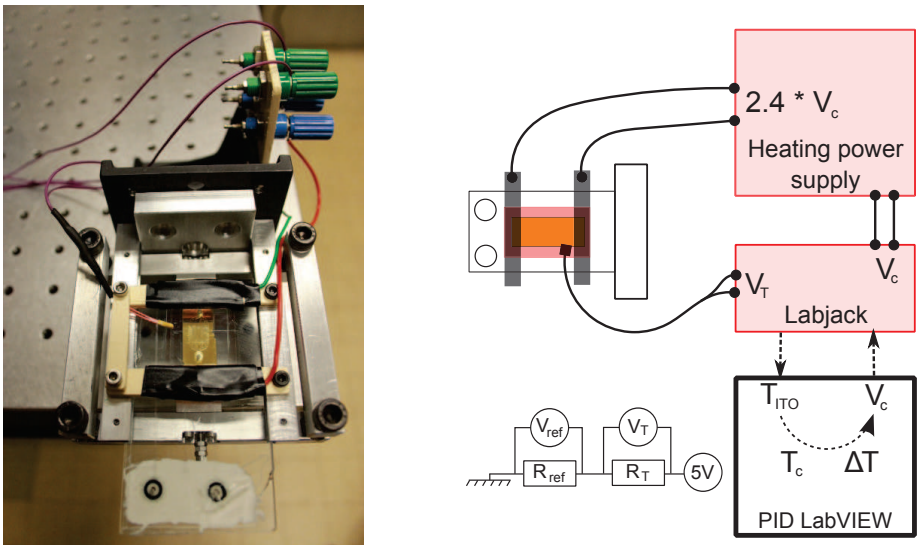

(a) **(b)**

Figure 3.9

Figure 3.10: Thermal device and system. **(a)** Picture of the thermal device mounted and connected to the prism support. **(b)** Scheme of the thermal measurement and regulation system.

This heating device can be achieved by using the joule heating effect (also called resistive or ohmic heating) with a glass slide coated with a very thin layer of Indium-Tin-Oxide (ITO)[3]. ITO is an oxide conductor composed of 90% of indium oxide (In_2O_3) and 10% of tin oxide (SnO_2) by weight and is transparent in the visible spectrum (transmittance > 85 %) (Sigma-Aldrich, ref. 576360). Since the ITO side has to face up to be in contact with the electrodes, (**Figure 3.10a**), the glass side can be bound by oxygen plasma to the PDMS sheet supply (**Figure 3.6**). The final thickness between the prism base and the ITO layer is about 6.5 mm, but since the average optical index is ~1.4, the equivalent thickness seen by the optical microscope is only 4.6 mm (=

[3]The idea to use a transparent ITO-coated glass slide as planar heat source has been proposed and demonstrated by Loïc Leroy.

thickness/refractive index). This thickness is compatible with the long working distance Olympus objectives of the LMPLFLN series, but obviously, it also induces spherical aberrations.

3.5.2 | Temperature measurements and calibration

The temperature of the flowcell $T_{flowcell}$ during an SPR experiment cannot be measured directly because of its small dimensions. It is more practical to measure and regulate the temperature of the ITO plate T_{ITO}, and correlate it to $T_{flowcell}$ by a calibration. This strategy also prevents from overheating and breaking the ITO glass slide.

T_{ITO} is monitored by a NTC thermistor (Negative Temperature Coefficient) which resistance R_T exponentially decreases when temperature increases. R_T is calculated by a LabVIEW program by simultaneously measuring the voltage V_{ref} of a reference resistor of a known resistance ($R_{ref} \approx 10\,k\Omega$) and the voltage of the thermistor V_T by a LabJack acquisition card (**Figure 3.10b**). In our electric set-up, $R_T = R_{ref}(V_T/V_{ref})$. To establish the function $R_T = f(T)$, the thermistor is immersed in a glass of water which temperature decreases from 83°C to 23°C (measured with a reference commercial thermometer) and R_T is measured every 5°C. This range makes R_T vary from 500 to 6000 Ω. The measuring points are fitted by an exponential decaying function. T_{ITO} is finally monitored by placing the thermistor head in contact with the ITO layer and by adding some thermal paste to ensure a good thermal contact.

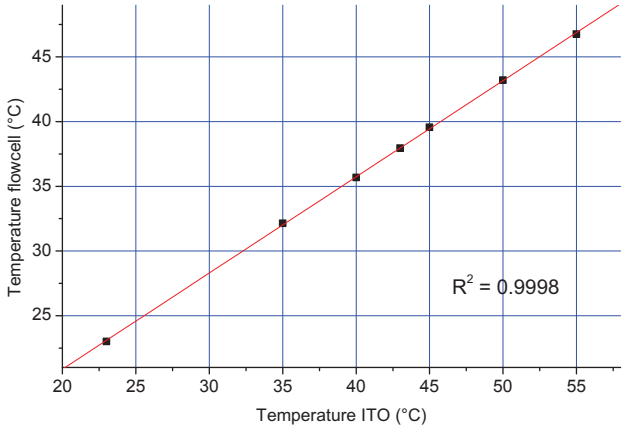

Figure 3.11: Flowcell temperature as a function of ITO temperature.

The calibration of the temperature of the flowcell $T_{flowcell} = f(T_{ITO})$ is performed by inserting and binding a second thermistor into a drilled Horiba prism, so that its head goes half a millimeter above the prism base, and is in the middle of the flowcell. Water is inserted in the fluidic device and both temperatures are monitored. While T_{ITO} stabilizes in only a few seconds, $T_{flowcell}$ needs ~10 min to asymptotically stabilize due to the thermal inertia. **Figure 3.11** shows a very linear relation over the range of desired temperatures. Note that the fit depends on the ambient temperature T_{amb} (which remains close to 23°C), but the error tends to zero as T_{ITO} becomes large compared to T_{amb}

3.5.3 | Thermal regulation and instrumentation

The LabVIEW program that drives the thermal regulation is mainly composed of a PID controller[4]. The PID aims to reduce the difference ΔT between the setpoint temperature T_c and T_{ITO} by adjusting the voltage V_c from 0 to 5 V at the output of the LabJack. Because thermal variations are relatively slow (in the order of a few seconds) due to the thermal inertia, derivative and

[4]This program has been coded by Loïc Leroy previously to the PhD thesis. I adapted it to our set-up.

integral gains are not indispensable, and only the proportional gain can be used. But in the case of a purely proportional gain, when $\Delta T \rightarrow 0°C$, V_c should also tend to zero, resulting in a decrease of $T_{ITO}(t)$ and a permanent error that makes $T_{ITO} < T_c$. Thus, to be accurate, the PID needs an additional constant term so that $V_c = K_p \times \Delta T + constant$, where K_p is the proportional gain. The constant term is in fact proportional to $T_c - T_{amb}$ in order to adjust its value with respect to the difference between the setpoint and the ambient temperature.

The feedback voltage V_c is sent to the heating power supply. The latter is made of a power operational amplifier alimented by an ATX power supply (V = +/- 12 V, DC) and generates a voltage proportional to V_c so that 5 V⇔ 12 V between the two electrodes in contact with the ITO plate. In joule heating, the dissipated heat is limited by the maximum current or voltage and by the resistance of the resistive component. In our case, I_{max} = 1.5 A, V_{max} = 12 V and R_{ITO} is $\approx 40\,\Omega$ (half a glass slide), so the maximum heat dissipated by the ITO is $Q = R \times I^2 = V^2/R$ = 3.6 W. In steady state, this power is measured at ∼1.9 W for T_{ITO} = 42°C. A part of the heat is dissipated by convection in the ambient air. Most of horizontal surfaces have a convection heat transfer coefficient in air of ∼10 W.m^{-2}.K^{-1} [142], which leads to a dissipation in the order of 0.2 W.

In the calibration experiments, $T_{flowcell}$ has been be regulated from room temperature up to 47°C at an accuracy less than 1°C and a precision less than 0.25°C, which is sufficient for the growth of the microorganisms of interest.

3.5.4 | Temperature field simulation

Before the heat generated in the ITO layer reaches the prism base, it dissipates by conduction through its own glass substrate, the PDMS sheet supply, the principal glass plate and the flowcell. The heat also dissipates by convection at all surfaces exposed to air, and by conduction to the prism support. Even if we know the real mean temperature of the flowcell through the calibration, we do not know the temperature field. It can nevertheless be estimated in first approximation by a finite element simulation where heat transfers by convection and radiation are neglected. The thermal simulation is performed by SolidWorks on the fluidic device (CAD file of **Figure 3.6**).

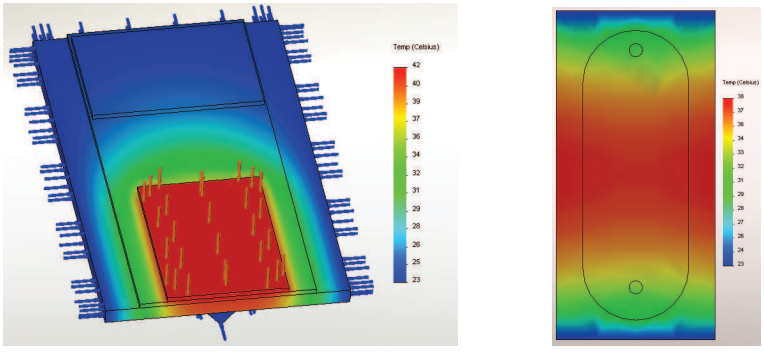

(a) **(b)**

Figure 3.12: Stationary temperature field simulation performed on SolidWorks. The ITO plate is uniformly heated-up at a temperature of 42°C (orange markers) while the surfaces in contact with the prism support are at 23°C (blue markers). **(a)** global view of the device. Temperature scale: 23 to 42°C. **(b)** Field temperature on the prism surface. Temperature scale: 23 to 38°C.

The limit conditions for the temperature are 42°C on the ITO surface and 23°C at the edges of the principal glass plate and at the 2 prism sides (not faces) which are in contact with the prism support. **Figure 3.12a** shows the global temperature field from the top of the device, and **Figure 3.12b** the temperature at the prism base. Even if these limit conditions are overestimated (the prism sides and the principal glass plate edges are surely heated up above the ambient

temperature), this simulation gives results close to the measurements: 37°C at the center of the flowcell, as measured in **Figure 3.11**. The temperature at the top of the flowcell is just 1°C higher.

As a conclusion, this heating device is effective to obtain a homogenous field temperature at +/- 1°C on the 1 cm^2 active surface of the SPR biochip.

3.6 | Optics instrumentation and image processing

3.6.1 | LabVIEW acquisition program

To perform a classic SPR experiment, the only device that needs to be automatically controlled is the camera in order to capture images at a constant rate. However, it is also practical to control the angle of illumination to automatically acquire images at different angles, and trace the plasmon curve of the areas of interest in order to choose the working angle. Moreover, in line-scan imaging mode, the focus of the SPR imaging system has to be set for each image. These three operations have been implemented in a homemade LabVIEW program divided into 4 steps, as shown in the synoptic of **Figure 3.13**.

The first step consists in setting the camera exposure time, and eventually binning (concatenation of 2×2, 4×4 or 8×8 pixels), to use the full dynamic of the sensor. At this step, the light intensity can also be adjusted. The smaller the exposure time, the less motion blur and external light perturbation, so the power of the illumination LED is usually set close to its maximum. This step precedes the plasmon curve acquisition in TM and TE mode, so these settings must be done in TE mode which exhibits a higher reflectivity.

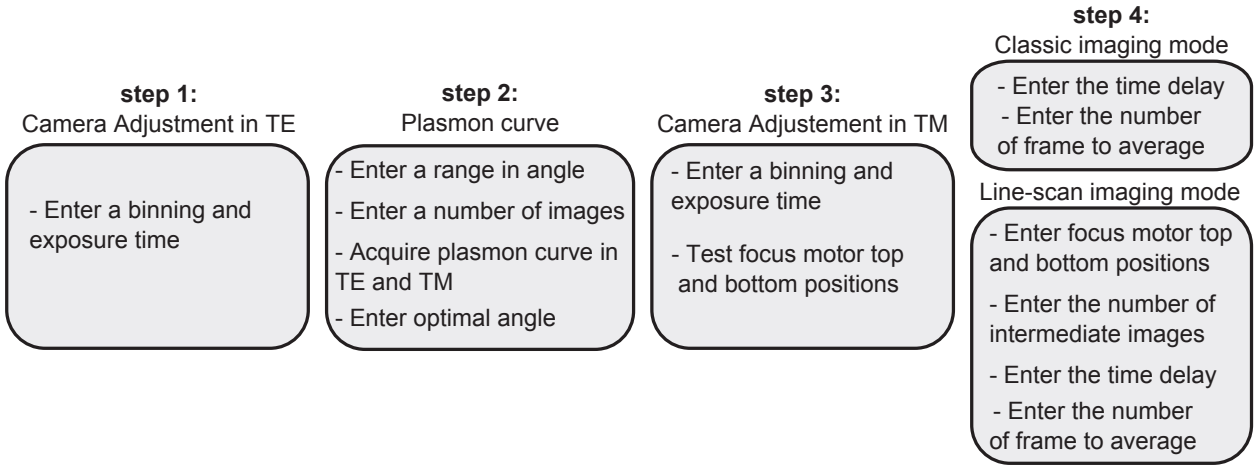

Figure 3.13: Synoptic of the optical LabVIEW program.

The second step is the plasmon curve acquisition. Here, the motor that controls the angle of illumination is moved at a chosen number of equally spaced positions over a maximum range of 20°. For each position "j" (1,2,3...), an image is captured and stored at the relative path "../plasmon-curves/sequence-1/image-j.tif". Another acquisition can then be launched in the other polarization, and will be stored in "..plasmon-curves/sequence-2". The plasmon curve is finally traced in a few seconds with the free sotfware ImageJ by using the command "File→Import→Image Sequence", choosing the region of interest (ROI) and selecting "Image→Stacks→Plot Z-axis Profile". In fact, to trace the plasmon curve and choose the working angle, a single TM acquisition is sufficient, but the TE mode enables to determinate the absolute reflectivity in TM mode $R'_{TM}(\theta_{ext})$ (the " ' "

means that the reflections at the entry and exit face of the prism are not taking into account):

$$R'_{TM}(\theta_{ext}) = R'_{TE}(\theta_{ext})\frac{I_{TM}(\theta_{ext}) - I_0}{I_{TE}(\theta_{ext}) - I_0} \tag{3.1}$$

where $R'_{TE}(\theta_{ext})$ is the reflectivity in TE mode with respect to the external angle which is used to convert the gray-levels into % of reflectivity, I_{TM} and I_{TE} are the gray-levels in the ROI in the TM and TE images, and I_0 is the gray-level in the ROI of an image without any illumination used to subtract the background signal. $R'_{TE}(\theta_{ext})$ is calculated by a homemade Mathematica program and is used as a reference since it is supposed to be independent of small refractive index changes occurring in the dielectric at angle greater than the critical angle glass/dielectric. Once the working angle is calculated, it is entered in the program which moves the illumination motor to the corresponding position.

The third step is equivalent to the first one. The camera setting is set to use the full dynamic range of the camera, but in TM mode. The area of interest is set to a mean gray-level value of $70\% \times 65,535 \approx 45,800$, so large intensity shifts can still be measured. At this step, if the experiment has to be performed in line-scan imaging mode, the position of the motor that controls the focus of the SPR imaging system, and thus the clear line position, has to be measured for both top and bottom focus of the image.

The last step is the real-time monitoring by SPRi. If it is done in classic imaging mode, then a fourth panel asks for a directory, a time-delay and a number a frame to average (to increase the SNR). If the experiment is performed in line-scan imaging mode, a fifth panel asks in addition for the camera-motor top and bottom positions, number of intermediate images and camera-motor speed. In this mode, each intermediate image "j" of a sequence "i" is stored as "../time-lapse-line-scan/sequence-i/image-j.tif". This imaging mode generates heavy data (up to several tens of GB), but the intermediate images can be erased once all final images are obtained.

Both imaging modes can be stopped and restarted, and generate a text file containing the relative time (s) and absolute time (date-time) of each image (or sequence in line-scan imaging mode).

3.6.2 | Images and sequences processing

To reconstruct a single final image from a sequence of intermediate images acquired in line-can imaging mode, first, all the intermediate images are realigned by ImageJ using the plugin Stackreg→Translation [143]. Note that this step is optional, but very useful to correct small imperfections of the optical alignment and obtain a better recomposed final image. If the clear stripe is not perfectly horizontal, the entire sequence can be tilted consequently. The final image is finally recomposed by a homemade Mathematica program which imports and crops the intermediate images before reassembling all the clear stripes together. Once the sequence imported, the program asks for the position of the clear stripe (in pixel position) on the first and the last images. All the cropped stripes are of equal width. An optional parameter allows to take into account the eventual non-linearity of the stripe position with respect to the image number.

To process an entire experiment taken in line-can imaging mode, another Mathematica program automatically performs the reconstruction on each sequence of intermediate images, and stored all the final images in a new folder. ImageJ does not provide any automatic realignment process, and the one implemented in Mathematica is too slow to be used (more than a hour for a single sequence of intermediate images). As a consequence, in the final images, small movements between stripes remain. They are barely observable at first glance, but strongly degrade the differential images. These final images are useful to observe phenomena such as cell movements, or intensity shifts on relatively large areas, but cannot be used for individual cell monitoring. To

solve this problem, another Mathematica program automatically imports and crops a specific intermediate image of interest in each sequence folder. The cropped images displaying only a few cells are then realigned with ImageJ before the analysis.

3.7 | PDMS stamp

A photomask has been designed in order to fabricate a micro-structured PDMS stamp which has been used to measure and understand the spatial resolution (a common technique in SPRi literature [18, 90, 98]). The photomask has been fabricated by the Plateforme Micro & Nanotechnologies (LAAS-CNRS, Toulouse) under the supervision of Thierry Leïchlé. It exhibits various patterns down to 2 μm repeated each mm over a total length of 3 cm, in both positive and negative contrast.

The PDMS stamp has been fabricated by replicating a silicon wafer mold [141]. The fabrication of the mold has been performed in the INAC cleanroom (Plateforme Technologique Amont, Grenoble) and consists of the following steps. First, the photomask is transferred by standard deep-UV photolithography to a silicon wafer spin-coated with the positive photoresist UV5 (Rohm and Haas). The solubility of the exposed photoresist increases. Once rinsed in an appropriate developer, only the unexposed pattern remains (opaque areas of the photomask). Then, the silicon wafer is etched by Reactive Ion Etching that digs the bare silicon areas to a depth of 4.4 μm. Finally, the remaining photoresist is rinsed and the silicon wafer is treated by oxygen plasma and silanized in vapor phase to avoid PDMS adhesion.

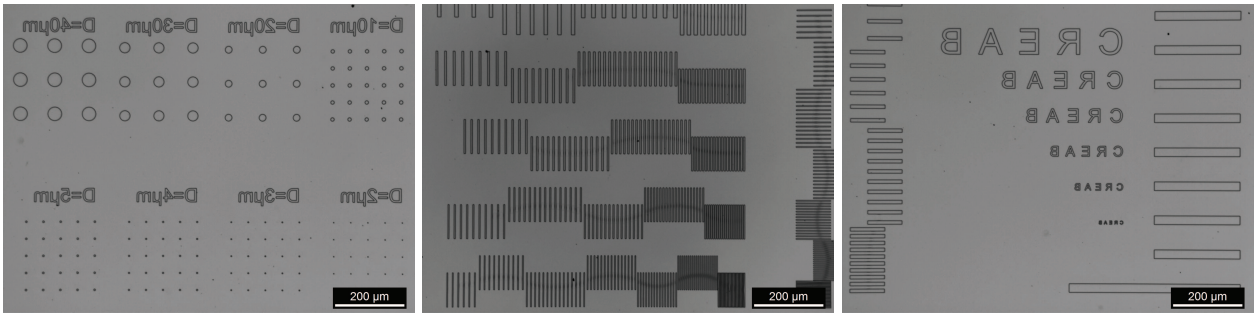

(a) **(b)** **(c)**

Figure 3.14: PDMS stamp of 4.4 μm-high patterns for resolution measurements. Since the PDMS is a replicate of the silicon wafer, it exhibits the mirror image. **(a)** Micropillars from 40 to 2 μm-wide. **(b)** Vertical lines networks. Lines width are w = 2, 3, 4, 5 and 10 μm at a pitch of 2w, 3w, 4w...etc. Vertical lines of the same pattern are also present, as seen at the right side of the image. **(c)** "CREAB" of 60 to 10 μm-high letters.

To produce higher patterns, as it is the case for the channel of the PDMS sheet supply (see **Section 3.3.1**), it is more practical to use a negative permanent photoresist (SU8-2075, Microchem). In that case, the exposed areas of the photoresist polymerize, while the unexposed areas can be dissolved, so the positive patterns correspond to the transparent parts of the photomask.

PDMS base and curing agent at a ratio of 10:1 are mixed and degassed, before being poured on the silicon wafer placed in a petri dish. It is then cured at 65° overnight. After that, the PDMS is softly peeled off. As shown in **Figure 3.14**, the PDMS stamp presents the exact same patterns as the photomask. However, Surface-Enhanced-Ellipsometric-Contrast microscopy performed with $T - SiO_2$ SURFs (Nanolane, France) reveals that the contact area of the 2-μm-wide cylindrical PDMS pillars on a the SURFs surface (and thus on the gold) is approximately 1-μm-wide. It should be mentioned that some of these smallest features are missing on the mold, and thus on the PDMS. All measurements and SPR images of PDMS stamps are performed at room temperature in deionized water.

3.8 | Prisms and metal layers

Prims optimized for very-wide-FOV in water were purchased from Horiba Scientific. They are 25-mm-long (Y axis), and the base is 12.5-mm-wide (X axis). Their apex angle is 32° and they are made of SF11 glass. The apex part of these prisms is truncated so their final height is 9 mm. Horiba prisms are already coated by a chromium adhesion layer of 1.5 nm and a gold layer of 49 nm.

2 kinds of prisms optimized for resolution were studied. For SF11 prisms, a dedicated inox support was designed in order to polish one face of Horiba prisms until an equivalent apex angle of 74° if they would be isosceles. The resultant prisms are asymmetric with base angles of 53° (exit side) and 74° (entry side). N-SF66 prisms with the same base dimensions as Horiba prisms, and an apex angle of 83°, were purchased from Schott Glaswerke AG (Switzerland/Malaysia).

The metal coatings were performed in the INAC cleanrooms PTA and BCAi. They consist in a 2-nm-thick adhesion layer of chromium and a 53-nm-thick layer of gold or a 50-nm-thick layer of silver, as calculated in **Section 2.7.1**. To test the hybrid metal coating, we directly deposit 43 nm of silver and 5 nm of gold as calculated in **Section 2.7.4**. Up to 8 prisms can be coated at a time using the support of **Figure 3.15a**.

Since N-SF66 prisms cannot be truncated, 2 prism holders have been fabricated to manipulate them and use the same apparatus as for Horiba prisms to functionalize the gold surface. The first one (**Figure 3.15b**) maintains the length at 25 mm with a final height of 13 mm, and the second one (**Figure 3.15c**) maintains the height at 9 mm with a final length of 31 mm.

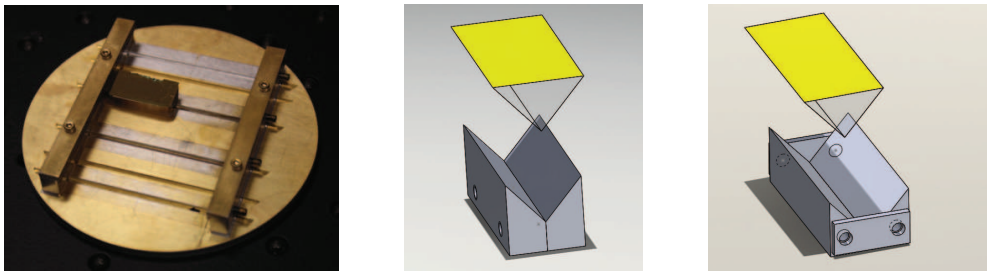

(a) **(b)** **(c)**

Figure 3.15: (a) Prism holder for metal evaporation on 8 prisms. **(b)** Prism holder that maintains the prism length at 25 mm. **(c)** Prism holder that maintains the prism height at 9 mm as Horiba prisms.

3.9 | Studied microorganisms

In this work, high resolution prism-based SPRi is applied to two eukaryote cell types and one bacterial strain. (**figure 3.16**).

3.9.1 | Eukaryote cells

The eukaryote cells we use as model in secretion experiments are known as "Jurkat cells" and come from an immortalized cell line of human T lymphocytes established in 1977 by Schneider *et al.* [144]. They are used as model cells for the study of cell secretions and immune system mechanisms [110]. Jurkat E6.1 cells grow as single-cell suspensions with an average diameter of 15 µm. They were purchased from ATCC and were cultivated at concentrations from 0.25 to 1.5×10^6/mL at 37°C and 5% CO_2 in RPMI 1640 medium, GlutaMAX^{TM} Supplement, HEPES (Gibco) supplemented by 10% FBS (PAA) and 1% penicillin-streptomycin (10,000 µg/mL) (Gibco). T lymphocytes sorted from healthy human blood samples were also used in secretion experiments,

and will be referred to as "PBMC" (Peripheral Blood Mononuclear Cell). They were purchased at the IAB (Institut Albert Bonniot - Inserm U823, Grenoble) and purified by Dieudonné Baganizi.

About ten secretion experiments have been performed at this time. All in all, each one of them represents about 2 to 3 man-days. The first steps of cultivating, sorting and activating the cells have been performed by Dieudonné Baganizi, a PhD student, and Stacie Fairley, a post-doctoral researcher. They also performed the fluorescence control after each experiment.

Human intestinal Caco-2 cells (ATCC, HTB-37) were used as model of adherent cells. The were established from gastrointestinal tumors in 1977 by Fogh *et al.*. Since then, they have become a reference for the study of cancer cells [145]. They were cultivated in AIM-V Medium, AlbuMAX Supplement (BSA) (Life Technologies) at the SCIB (Inorganic and Biological Chemistry laboratory, CEA Grenoble, INAC) and kindly provided by David Beal and Marie Dorier.

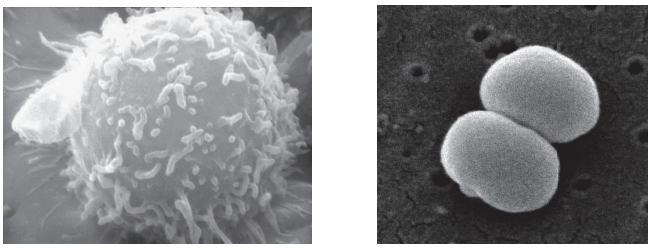

(a) **(b)**

Figure 3.16: Scanning electron microscope images of microorganisms studied by high resolution SPRi. **(a)** A T lymphocyte (source: Dr. Triche. National Cancer Institute, 1976). **(b)** Two *Staphylococcus epidermidis* (source: Janice Haney Carr, Centers for Disease Control and Prevention).

3.9.2 | Bacteria

Staphylococcus epidermidis are 1-μm-wide Gram-positive bacteria which are naturally present on human skin. They were purchased from ATCC (strain 12228) and were cultivated at 37°C in TSB medium (Sigma-Aldrich) until they reached a concentration of 1.0×10^7/mL. This bacterial strain is non-pathogenic, so it can be handled outside of our class 2 laboratory, and enables a proof of concept for pathogenic bacterial studies and detection. Before the experiment, the bacteria concentration was measured by depositing and spreading 100 μl of a diluted suspension on 3 agar plates so that the expected concentration was ∼500/ml. The plates were kept overnight in growth conditions (37°C, 5% CO_2). The next day, the number of colonies on each plate gives an estimation of the number of bacteria in the solution in terms of colony-forming unit (cfu/ml). In order to conserve the bacteria between the experiments, these agar plates, usually containing a few tens of colonies, were stored at 4°C.

3.10 | Surface functionalization and characterization

In order to recognize a target biomolecule or capture the microorganisms onto the gold surface, the biochip needs to be functionalized by probe molecules. In this work, three different functionalization techniques have been used.

3.10.1 | Electrocopolymerization of probe-grafted-pyrrole

For DNA deposition, which is a simple and standard way to measure the experimental sensitivity, the buffer is composed of acetonitrile, dimethyl sulfoxide (DMSO), lithium perchlorid, glycerol and water [77]. The solution of py-modified DNA is mixed with a higher concentrated solution of free py monomers, so the concentration ratio is 1:1,000. Prior to electropolymerization, the prisms

are cleaned and activated by a plasma treatment (40W, 0.6 mb, 75% O_2, 25% N_2, 6 min). Multiple electrodepositions (also called spotting) on a single prism are performed by using a mechanical stage which moves a micropipette containing the buffer ($\approx$ 2 µl) to several locations, and a potentiostat which applies a voltage of 2 V during 100 ms between a platinum wire immersed in the buffer and the prism surface (**Figure 3.17a**). Functionalized areas (spots) are from 300 to 1000-µm-wide depending on the gold hydrophobicity and the micropipette shape.

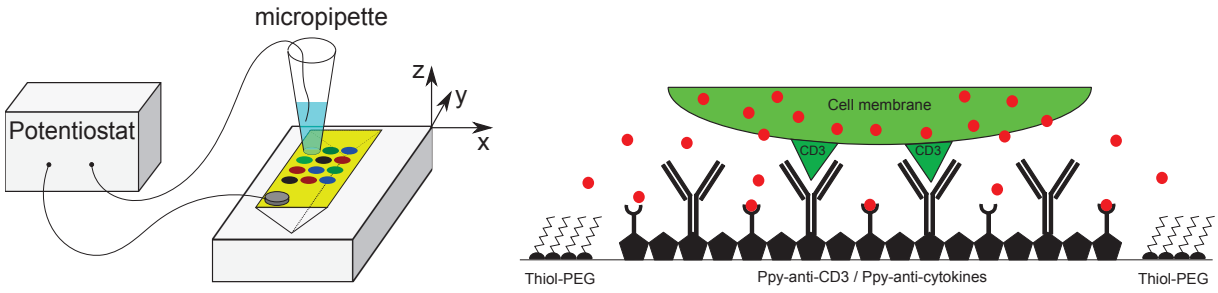

(a) **(b)**

Figure 3.17: Surface functionalization by polypyrrole for cell capture. **(a)** Electrodeposition of multiple probe molecules. **(a)** The cells are captured on the biochip surface by ppy-anti-CD3 and the cytokines detected by ppy-anti-cytokines.

Antibodies can also be grafted to pyrrole and electrodeposited. Except the buffer composition which is mostly composed of Phosphate Buffer Saline (PBS, Sigma-Aldrich) supplemented with glycerol, and a ratio of py-Ab-:free-py of 1:50,000, the method is exactly the same as for DNA spotting. It is used to anchor the secretory cells with antibodies specific for CD3 cell markers on spots named "anti-CD3" (**Figure 3.17b**). In order to detect the cytokines, these spots are co-functionalized by anti-cytokines. In this study the target secreted cytokines are interferon gamma (IFN_γ) and interleukin 2 (IL2) [71, 105].

Antibodies non specific to the Jurkat cell markers are used as negative controls, such as anti-IgG (immunoglobulin G).

3.10.2 | Self-assembled monolayer (SAM) of probe-grafted-thiols

The second functionalization technique uses self-assembled monolayer (SAM) of modified-thiols that bond to the gold surface through S-Au bounds. As for ppy, several areas can be defined on the biochip surface by simple drop deposition using the same apparatus as for electrochemistry. The drops are incubated overnight in a humid atmosphere. The entire surface can also be coated in one step by a larger drop.

In cell experiments, we use thiol-polyethylene glycol (PEG) to avoid non specific adsorption (**Figure 3.17b**). PEG-grafted-thiols (Prochimia) are diluted at a concentration of 1 mM in a phosphate buffer at 50 mM. Since electrodeposition is more aggressive than thiol binding, this step can precede or succeed the ppy-antibodies functionalization. The prism surface is finally kept in PBS 1$\times$ to prevent drying of the antibody spots.

3.10.3 | Physisorption of poly-L-lysine

The last functionalization targets bacteria capture, and consists in depositing a drop of poly-L-lysine (PLL) at a concentration of 0.01% in mass (Sigma-Aldrich, Mol. Wt. 150,000 - 300,000) onto the gold. After an incubation of $\sim$10 h, the drop is rinsed with deionized water and the bacteria solution put in contact with the gold surface.

3.10.4 | Biological recognition and surface characterization

Prior to injection of the complementary DNA (DNAc) or the target cells, a solution of Bovine Serum Albumin (BSA) at 1 % (w/w) is sent into the flowcell to decrease the non-specific absorption [78]. In a typical experiment of DNA recognition, the complementary DNA strands are coupled to biotin and injected at a concentration of 250 nM in a solution of PBS 1×. The ppy-DNA/DNAc-biotin hybridization is monitored by SPRi. A well-known method to amplify the SPR signal consists in injecting a solution of streptavidin (Sigma Aldrich S-47-62-1MG) at 200 µg/ml (in PBS) that binds to the biotin molecules [127]. The recognition can also be verified afterward by fluorescence microscopy if the streptavidin is previously conjugated to a fluorescent molecule, such as R-Phycoerythrin. This complex can be found commercially and is called SAPE (Life Technologies S-866). As pure streptavidin, it is also used at 200 µg/ml (in PBS) with an incubation time of 10 min.

3.10.5 | Experimental protocols for biological experiments

For the secretion experiment presented in chapter 4, the PBMC were incubated on the functionalized gold surface during 1 h at a concentration of 2.5×10^6/ml at 37° and 5% CO_2. The unattached cells were removed by softly rinsing the biochip surface with growth medium to reach a density where each cell is well separated from the neighboring cells. The prism was then integrated into the SPRi set-up and fresh growth medium was injected into the fluidic device to fill the flowcell, after what the inlet and outlet tubes were sealed. 15 min after the ITO temperature reached 42°C, a plasmon curve was acquired and the working angle set at the steepest point. SPR images in line-scan imaging mode were then taken every 10 min over 12 h (no frame averaging in the presented experiment).

A fluorescence observation was always performed at the end of secretion experiments. The cells were first detached form the biochip surface by a stronger rinsing with PBS, the secreted cytokines were detected through a sandwich revelation: ppy-anti-cytokines/secreted-cytokines/anti-cytokine-biotin/SAPE. Once rinsed with PBS, the prism surface was covered by a coverslip and observed by fluorescence microscopy.

For the observation of Caco-2 cells, a 500-µl-drop at a concentration of 2×10^6 cell/ml in AIM-V medium was deposited on a non functionalized gold coated N-SF66 prism. The prism was then incubated 24 h at 37°C and 5% CO_2 in a humid macro chamber to avoid evaporation. Just before the experiment, the supernatant was softly rinsed with fresh medium, and the prism placed in the SPRi set-up (no coverslip). SPR and optical images were acquired within the first hour.

For the observation of individual bacteria and the real-time monitoring of their growth, a 400 µl drop of *S.epidermidis* in TSB at a concentration of 185×10^3 cfu/ml was deposited on the PLL coated-prism and incubated during 1 h. The prism was then rinsed by TSB. For high resolution observation in line-scan imaging mode, the wet prism base was covered by a glass coverslip to allow a good bright field observation. The SPR images were taken at room temperature within the first 30 min. For the detection experiment, after the 1 h incubation and rinsing step, the prism was integrated to the SPRi set-up and fresh TSB medium was injected into the flowcell. As in secretion experiment, the inlet and outlet tubes were sealed and the flowcell heated up at 37° before acquiring the plasmon curve and setting the working angle. SPR images were then taken every 10 min in classic imaging mode (no frame averaging).

3.11 | Conclusion

In conclusion, we have achieved to design and build a prism-based SPR microscope that can work in a wide range of conditions, and which is automated to perform biological experiments over several hours.

4 | Experimental results and applications

Contents

Résumé du chapitre 4

Ce dernier chapitre expose mes résultats expérimentaux, dans un premier temps, sur l'importance des phénomènes d'aberrations géométriques dues aux prismes, ensuite, sur la mise en évidence d'une autre limite de résolution, et enfin, sur des preuves de concept en biologie cellulaire et en microbiologie.

Je commence par comparer l'influence des aberrations géométriques induites par le prisme selon qu'il est optimisé pour le grand champ de vision ou pour la résolution. Cette analyse met aussi en exergue les problématiques liées au système optique lorsqu'utilisé en mode d'imagerie classique avec des prismes optimisés pour la résolution. Je récapitule dans un tableau les avantages, inconvénients, et domaines d'applications de chacune des trois configurations optimisées en SPRi à couplage par prisme.

Dans un second volet, me concentrant uniquement sur la configuration optimale pour la résolution, je propose un modèle simple pour décrire efficacement la fonction d'étalement du point lorsque peuvent être négligées aberrations sphériques et dimensions de l'objet. Je montre alors que les deux limites ultimes de la résolution spatiale sont la longueur de propagation du plasmon, limite déjà établie depuis longtemps, mais aussi un fort phénomène de diffraction, qui n'est pas dû au système optique d'imagerie, mais plutôt à une réflexion faiblement diffuse. Ces deux derniers phénomènes font que la résolution est tout compte fait assez peu dégradée par les aberrations sphériques dues au prisme, même à un centimètre de son arrête. Je termine la partie physique expérimentale par la mesure de la longueur de propagation des plasmons de surface pour l'argent, l'or et le dépôt hybride d'argent et d'or présenté en fin de chapitre 2. Ces mesures sont en bonne adéquation avec les prédictions théoriques, sous réserve de l'utilisation d'un modèle prenant en compte la faible épaisseur de métal. Ainsi, en première analyse, ce dépôt hybride ne semble pas améliorer le compromis sensibilité et longueur de propagation comparé à l'or, que j'ai alors décidé de garder pour les applications biologiques.

La première preuve de concepts en biologie cellulaire consiste à observer par SPRi un signal de sécrétion de cytokine par des lymphocytes T individuels. Une première partie introductive traite des aspects de résolution temporelle, spatiale et de sensibilité suivant le mode d'imagerie avec des prismes optimisés pour la résolution. Des images présentant plusieurs milliers de cellules individuelles sont notamment obtenues. Même si ces expériences n'ont pas donné suite à l'observation de sécrétions à l'échelle individuelle, j'ai cependant identifié les aspects à améliorer par la suite. La deuxième preuve de concept établit la faisabilité d'imagerie à champ de vision intermédiaire pour l'étude des propriétés d'adhésion de plusieurs dizaines de cellules adhérentes simultanément, avec un niveau de détails subcellulaires. Les limites de résolution, clairement visibles aux forts grossissements optiques, sont notamment illustrées. Enfin, la dernière preuve de concept vise à rendre plus rapide la détection de bactéries par SPRi. Le suivi en temps réel de grandeurs statistiques, qui traduisent l'hétérogénéité surfacique de la croissance bactérienne, est proposé comme solution complémentaire au suivi de la simple variation d'intensité.

This chapter presents the experimental results of high resolution prism-based SPR imaging. In a first section, we demonstrate the importance of geometric aberrations by comparing the three optimized optical configurations of SPRi : very-wide-field-of-view (VWFOV) and resolution optimized prisms in line-scan and classic imaging mode. The optical aberrations arising from the prism and from the imaging system are discussed. In a second section, we focus on the ultimate spatial resolution achieved in line-scan imaging mode with resolution optimized N-SF66 prisms. We describe a method to measure the propagation length and discuss the relative importance of the diffraction-limit and SP scattering. The trend of spatial resolution with respect to the distance of the object from the imaging side edge of the prism is also addressed. In a third section, we compare the performances of gold, silver and an hybrid silver/gold coating in terms of resolution and use for biological experiments. The last part of this chapter is dedicated to biological experiments. We particularly focus on the observation of individual cells and the monitoring of their secretory activity. We also briefly demonstrate the potential and limits of SPRi for single cell analyses. Finally, we explore applications in microbiology by imaging individual bacteria and by using novel strategies to decrease the time of detection.

4.1 | Comparison between optimized optical configurations in SPRi

In addition to spatial resolution and sensitivity, field-of-view (FOV) is also a key parameter of biosensing imaging techniques. For clarity purpose, we divided the FOV into 4 categories: very-wide ($\geq$20 mm^2), wide ($\approx$6 mm^2), small ($\approx$0.7 mm^2) and very-small ($\leq$0.1 mm^2). For each SPR image, the corresponding prism and imaging system is specified in the legend. The objective and tube lens are referred to as "OL" and "TL," respectively. In the following images, the X axis is the propagation direction, and is vertical. Note that the VWFOV optimized prisms are just taken as arbitrary examples of none resolution optimized prisms, and serve to illustrate the influence of geometric aberrations in prism-based imaging.

4.1.1 | Small field-of-view

Figure 4.1 shows a comparison on small FOV between the three optimized configurations on SF11 prisms. The enhancement of spatial resolution when using the resolution optimization (A_p = 74°) is obvious compared to the VWFOV optimization (A_p = 32°). **Figure 4.1d** also reveals that geometric aberrations induced by the prism lead to the creation of artifacts, such as a sixth line of PDMS pillars at the bottom of the image. Without the understanding of geometric aberrations, the blur can easily be attributed to the effect of L_x since the spreading of the image is along the X axis. However, **Figure 4.1e** shows that L_x is barley visible at this wavelength of illumination. In line-scan imaging mode, the width of the clear stripe is proportional to the depth-of-field (DOF) of the imaging system, and can be as low as a few tens of µm (**Figure 4.1e**). Therefore, the number of necessary intermediate images is inversely proportional to the DOF.

As visible in **Figure 4.1g**, the classic imaging mode exhibits a spatial resolution similar to the one obtained in line-scan imaging mode. Nonetheless, for resolution optimized SF11 prisms, α is $\sim$37°, which means that the imaging system must have a NA close to 0.6 to perform classic imaging mode. Here, we use the $\times$50 objective with a NA of 0.5. As a consequence, the axis of the imaging system cannot be set strictly perpendicular to the virtual image, thereby extending the clear stripe width only over the central part of the sensor.

As stated in chapter 2, geometric aberrations mainly affect the resolution in the X axis. The Y axis resolution is affected by spherical aberrations, but is the same whatever the apex angle of the prism, as illustrated in **Figure 4.2**. In the VWFOV configuration, the networks of vertical PDMS lines are resolved, even the ones at a pitch of 4 µm, for which the 20 lines can be counted. The situation is clearly different for the X axis, where the horizontal lines are not resolved for

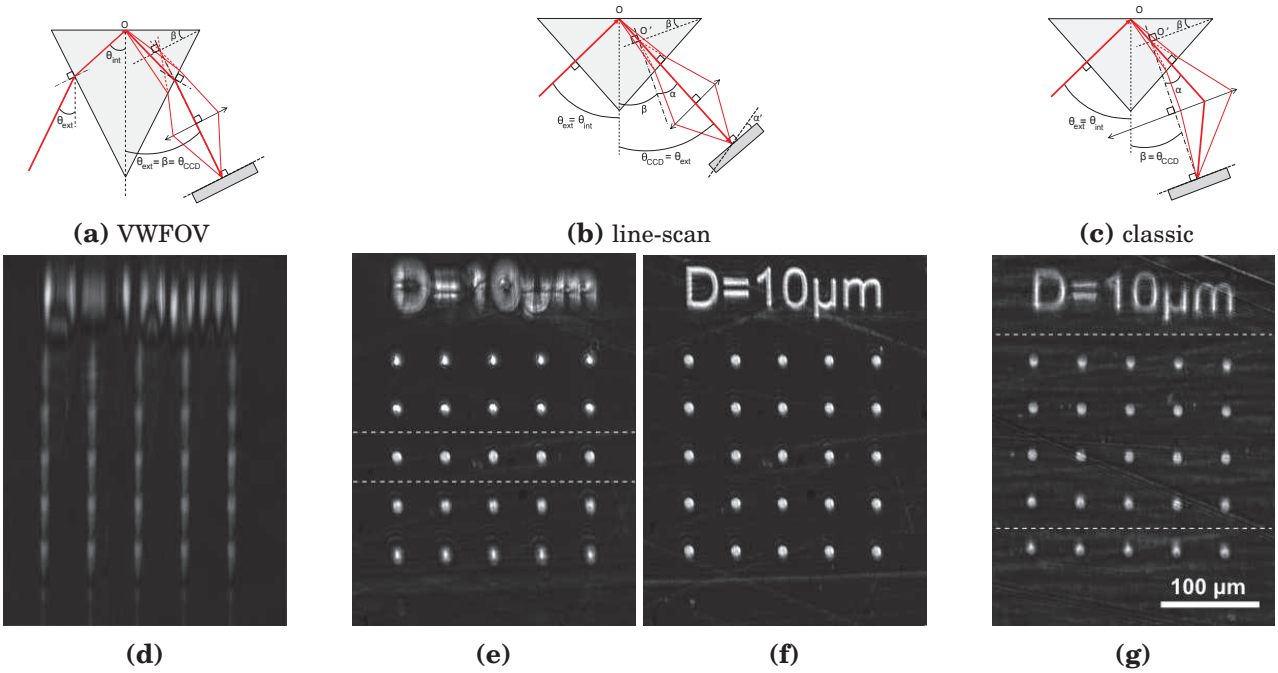

Figure 4.1: Small FOV comparison between the three optimized configurations on SF11 prisms (λ = 632 nm, water, $d \approx 5$ mm). **(a & d)** VWFOV optimized prism (SF11, OL: $\times$20, TL: 200 mm). **(b, e & f)** Resolution optimized prism in line-scan imaging mode (100 lines, SF11, OL: $\times$20, TL: 200 mm). Figure e is an example of a single intermediate image. **(c & g)** Resolution optimized prism in classic imaging mode (SF11, OL: $\times$50, TL: 65 mm).

VWFOV optimized prisms (note the presence of artifacts). In line-scan imaging mode, resolution optimized prisms exhibits a X axis resolution sufficient to resolve the horizontal PDMS lines at a pitch of 6 µm. The ones at a pitch of 4 µm are almost resolved. For N-SF66 prisms, the NA of the imaging system has to be close to 0.5 to be used in classic imaging mode. Unlike for SF11 prisms, here, the $\times$50 objective enables to observe an entirely clear FOV.

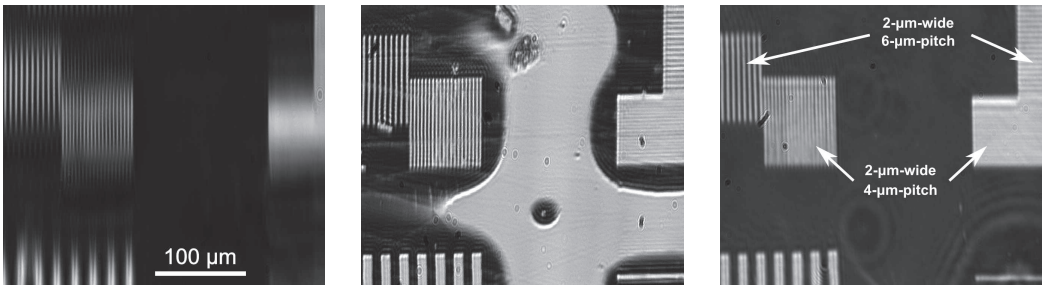

Figure 4.2: X and Y axis spatial resolution for VWFOV and resolution optimized prisms (SP propagate downward, λ = 632 nm, water, $d \approx 5$ mm). **(a)** VWFOV optimized prism (SF11, OL: $\times$20, TL: 200 mm). **(b)** Resolution optimized prism in line-scan imaging mode (125 lines). A air bubule is trapped between the PDMS and the prism (SF11, OL: $\times$20, TL: 200 mm). **(c)** Resolution optimized prism in classic imaging mode (N-SF66, OL: $\times$50, TL: 65 mm).

It should be mentioned that, in the VWFOV configuration, there are several positions of best focus (**Figure 4.3**). Here, the optical response of the 10-µm-wide PDMS pillars is close to the PSF due to the strong effect of the aberrations. Varying the distance between the imaging system and the prism affects the PSF by inducing a defocus aberration which can result in a better overall

image. For instance, in **Figure 4.3b**, all the pillars are well separated from each other, but they have a square shape, as previously reported by Bombera *et al.* [13] (**Figure 1.18b** of chapter 1). The squares measure approximately 19 × 19 μm^2. On the contrary, in **Figure 4.3d**, the pillars are correctly resolved in the Y axis, but are not separated anymore in the X axis. In addition, in this image, suppose there is another object below a PDMS pillar, and shifted in the Y axis by a few μm, as represented by the red dot. The Y axis resolution of this object is also affected on the left by the spreading of the upper pillar. As a consequence, whatever the focus adjustment, in practice, geometric aberrations also affect the lateral resolution in the Y axis.

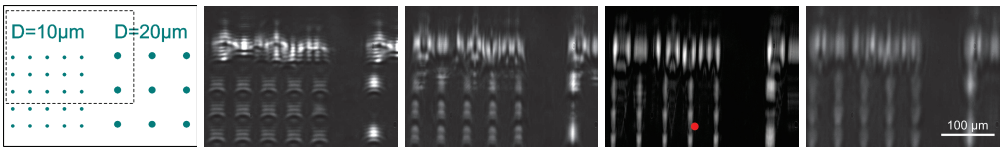

(a) **(b)** **(c)** **(d)** **(e)**

Figure 4.3: Best focus point for SF11 VWFOV optimized prisms (OL: ×20, TL: 200 mm, SP propagate downward, λ = 632 nm, water, $d \approx 5$ mm). **(a)** Patterns of the photomask. **(b - e)** SPR images at different focus adjustments.

4.1.2 | Large field-of-view

The same comparison is performed for larger FOV. Even if at first glance the image from the VWFOV configuration is similar to the ones from the resolution configurations, it suffers from the same aberrations as for small FOV, as visible on the numerical magnification (**Figure 4.4a**). Once again, the best image quality is obtained in line-scan imaging mode (**Figure 4.4b**). When using a tube lens of focal length smaller than the standard 200 mm, for which microscope objectives have been designed, optical aberrations may appear. They can induce a non linear displacement of the clear stripe with respect to the focus adjustment. Here, this effect has been corrected in the reconstruction process. In standard conditions, the clear stripe displacement on the sensor is strictly proportional to the objective lens displacement with respect to the prism.

In the case of classic imaging mode, low magnification microscope objectives cannot be used since they usually also have a small NA. Instead, we used an aspheric lens with a NA of 0.66 (f=18.75 mm). Unlike a microscope objective, such a lens is not corrected for coma, astigmatism or off-axis spherical aberrations. These aberrations degrade the spatial resolution principally in the X axis, and should not be confused with the effect of L_x or geometric aberrations caused by the prism. Moreover, the use of a short focal length tube lens in order to decrease the magnification amplifies the field curvature and distortion aberrations. In our actual optical set-up, we limit this imaging mode to wide FOV (**Figure 4.4c**). In the corresponding optical scheme shown in **Figure 4.1c**, the two secondary rays are represented with an equal angular diffusion $\pm\Delta\theta_{int}$ around the principal ray. Nonetheless, the imaging system may have a better transmission for the rays arriving closer to the optical axis, so the ray distribution might not be strictly symmetric. Consequently, this imaging mode can also suffer from small geometric aberrations due to the prism. Experimentally, we have also observed a lower contrast compared to the line-scan imaging mode (for instance when imaging PDMS micro-structures in water).

In conclusion, each configuration presents advantages and drawbacks which are summarized in **Table 4.1**. The choice is then multi-factorial: main application, range of possible applications, time-resolution, price investment, instrumentation, data post-processing (i.e. high performance computer)...

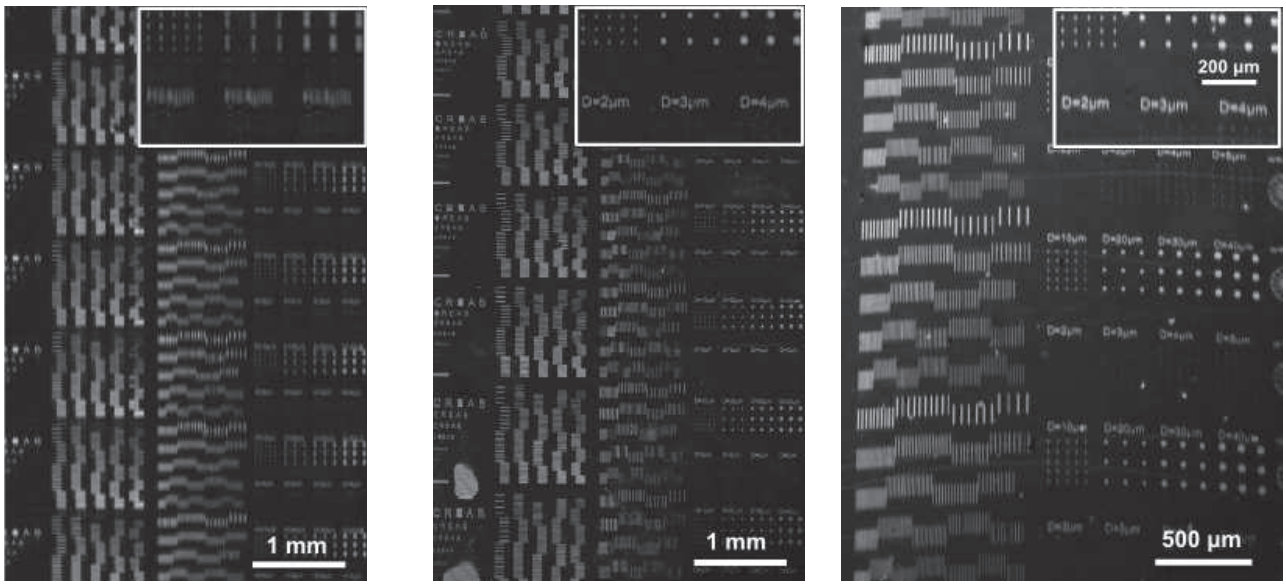

(a) VWFOV **(b)** line-scan **(c)** classic

Figure 4.4: Wide FOV comparison between the three optimized configurations (λ = 632 nm). **(a)** 20 mm^2 FOV with a VWFOV optimized prism (SF11, A_p = 32°, OL: ×4, TL: 100 mm). **(b)** 20 mm^2 FOV with a resolution optimized prism in line-scan imaging mode (N-SF66, OL: ×4, TL: 100 mm, 100 stripes). **(c)** 7 mm^2 FOV with a resolution optimized prism in classic imaging mode (N-SF66, OL: 18.75 mm (∼ ×5.3), TL: 100 mm). Inset: numerical magnification on PDMS pillars

Table 4.1: Advantages and drawbacks of prism-based SPRi configurations.

Prism optimized for *(Applications)*	**Imaging mode**	**FOV range**	**Advantage**	**Drawbacks**
very-wide-FOV *(biomolecules)*	classic	very-wide	· inexpensive, simple and long working distance imaging system with low aberrations · easy prism handling	· low resolution due to the prism · high anamorphose effect for low refractive index prisms
resolution *(biomolecules and microorganisms)*	classic	from very-small to wide	· good resolution · low anamorphose	· high NA or short working distance imaging system · aberration from the imaging system if not corrected
	line-scan	from very-small to very-wide	· ultimate resolution · simple and long working distance imaging system with low aberrations	· mechanical displacement or varifocal imaging system · image processing · lower effective frame rate · lower SNR than classic imaging mode · high anamorphose effect for low refractive index prisms

4.2 | Spatial resolution measurements

4.2.1 | Theoretical PSF perpendicular and parallel to the SP

As stated in the first chapter (**Section 1.4.1**), in conventional microscopy, the image of an object is equal to the convolution between the function describing its spatial dimensions and the function describing the diffraction phenomenon. The latter is a Airy function which can be correctly approximated by a Gaussian function. As illustrated in **Figure 4.5**, in prism-based imaging, the function representing the geometric aberrations must be added to the convolution. The effect of spherical aberrations on an ideal Dirac signal (point) can be described by an axi-symmetric function (**Appendix Figure A.7**). When considering an already diffraction-affected point source, i.e. a Airy pattern, the effect of spherical aberrations is almost the same as the one induced by the convolution with a Gaussian function [146]. Thus, a Gaussian function can be used in the convolution to approximate the effect of spherical aberrations.

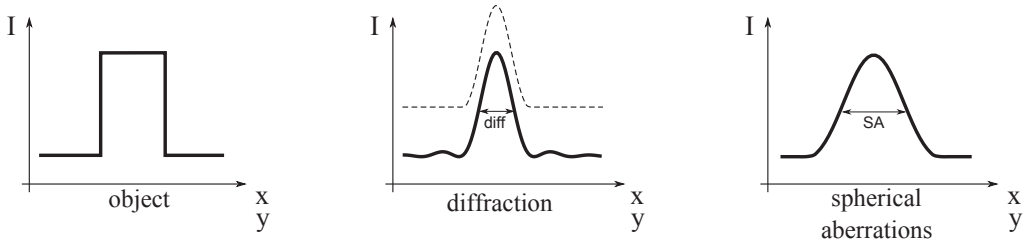

Figure 4.5: Decomposition of the theoretical PSF in prism-based imaging

In SPRi, a forth function has to be integrated to represent the surface plasmon wave scattering. SP scattering by a dielectric defects on the surface of the metal creates an asymmetric distribution of the electric field intensity, as predicted by the theory of planar SP scattering [147]. As shown in **Figure 4.6** [148], what is usually called the propagation length L_x is indeed the extension in the propagation direction of the "surface plasmon nanojet" (called "photon nanojet" in light scattering [149]). The spatial distribution of the electric field intensity exhibits mainly two aspects: first, an exponential decay after the object (L_x), and secondly, periodic oscillations before the object.

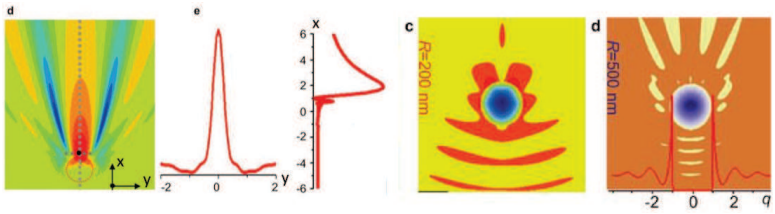

Figure 4.6: Simulation of light and surface plasmon scattering (adapted from figure 4 and 7 of ref. [148]).

The interference patterns due to SP scattering have been observed experimentally by using scanning probe microscopes which measure the intensity of the electric field [150, 151]. The SP nanojet has also been clearly observed in objective-based SPRi by Wang *et al.* [38] when imaging nanoparticles and viruses. Therefore, in prism-based SPRi, when neglecting the influence of the diffraction and the spherical aberrations, the experimental PSF should has the same shape as a SP nanojet.

As visible in **Figure 4.6**, the cross-section of the nanojet in the propagation direction can be approximated by the convolution of a Gaussian function, let us call its FWHM $scat - gauss_x$, and an exponential decaying function of characteristic length L_x. In the Y axis, the cross-section can be correctly approximated by a Gaussian function. The analytical literal expression of the

convolution between an exponential decaying function $f_{exp-decay}$ of characteristic length L_x and a Gaussian function f_{gauss} can be found using the literal solver of Mathematica:

$$f_{exp-decay}(L_x, x) = \begin{cases} 0 & -\infty < x < 0 \\ \exp\left(\frac{-x}{L_x}\right) & 0 \leq x < +\infty \end{cases} \tag{4.1}$$

$$f_{gauss}(FWHM, x) = \exp\left(-x^2 \frac{4\,ln(2)}{FWHM^2}\right) \tag{4.2}$$

where $FWHM$ is the FWHM of the Gaussian function (normalized and centered at x = 0)

$$\begin{aligned} & f_{exp-decay}(L_x, x) * f_{gauss}(FWHM, x) \\ & = \sqrt{\frac{\pi}{2}} \frac{\exp\left[\frac{-2\,x+\left(\frac{FWHM^2}{8\,\ln(2)}\right)}{2\,L_x^2}\right] erfc\left\{\frac{\sqrt{\left(\frac{FWHM^2}{8\,\ln(2)}\right)^{-1}}\left[-L_x\,x+\left(\frac{FWHM^2}{8\,\ln(2)}\right)\right]}{\sqrt{2}\,L_x}\right\}}{\sqrt{\left(\frac{FWHM^2}{8\,\ln(2)}\right)^{-1}}} \end{aligned} \tag{4.3}$$

with

$$erfc(z) = 1 - erf(z) = \frac{2}{\sqrt{\pi}} \int_z^{\infty} \exp\left(-t^2\right)\, dt \tag{4.4}$$

The two functions that describe the SP scattering in the Y and X axis are represented in **Figure 4.7**.

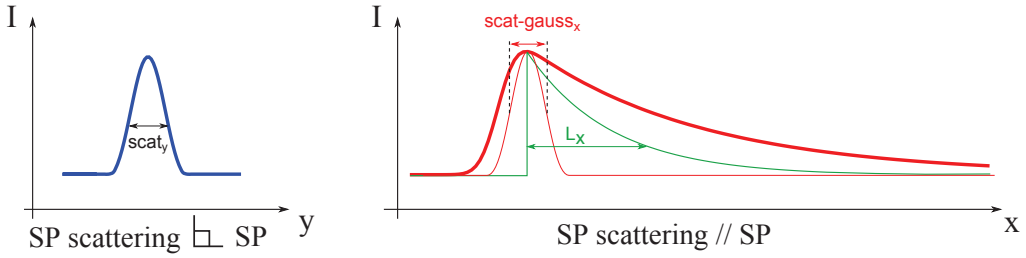

Figure 4.7: Functions describing the SP scattering effect

To measure the ultimate spatial resolution in prism-based SPRi, the object has to be smaller than the resolution limit, so that it can be approximated by a Dirac peak. Moreover, for prisms optimized for resolution, spherical aberrations can be neglected if the distance between the object and the prism edge is smaller than a critical distance d_{lim}, typically 800 µm if the resolution is 1.5 µm at λ = 632 nm for N-SF66 prisms (**Section 2.6.3**). In such case, the PSF in the Y axis is the convolution of two Gaussian functions, one representing the diffraction and the other one the SP scattering in the Y axis (**Figure 4.8a**). The convolution of two Gaussian functions is also a Gaussian function of FWHM equal to the quadratic sum of the two original ones, thereby $\delta_y = (diff_y^2 + scat_y^2)^{1/2}$. Similarly, in the X axis, the PSF is the convolution of a Gaussian function of FWHM $\delta_x = (diff_x^2 + scat - gauss_x^2)^{1/2}$ with a decaying exponential function of characteristic length L_x (**Figure 4.8b**).

4.2.2 | Resolution limit perpendicular to the SP

According to literature, the resolution perpendicular to the SP is supposed to be diffraction-limited by the NA of the imaging system. However, as discussed in **Section 1.4.2.1** of Chapter 1, such a spatial resolution is not usually obtained experimentally, especially with high NA objectives. It

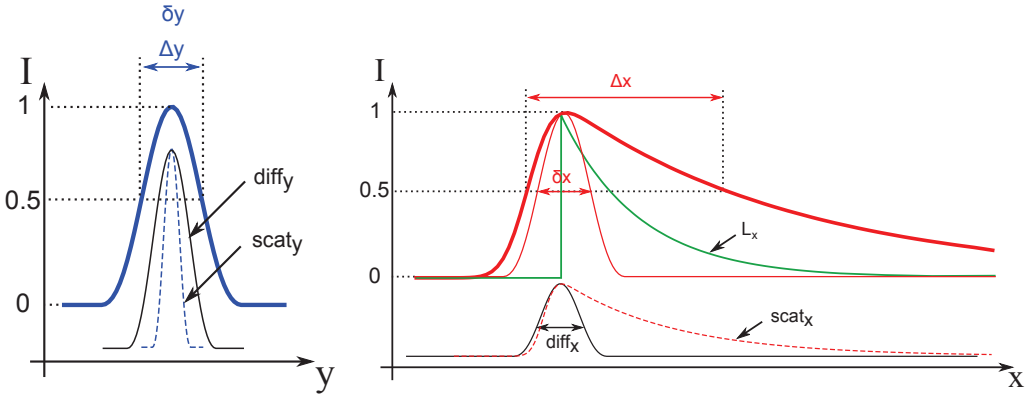

(a) perpendicular **(b)** parallel

Figure 4.8: Theoretical PSF in prism-based SPRi. **(a)** Separated signal functions. **(b)** PSF perpendicular to the SP. **(c)** PSF parallel to the SP.

can then be hypothesized that the diffuse reflection is restricted to a small solid angle due to the collimated illumination, resulting in an effective NA that can be less than the one of the imaging system. A similar hypothesis has also been proposed in objective-based SPRi by Wang *et al.* [38] to explain a δ_y measured at 0.5 µm while their objective had an NA of 1.65 ($\delta_y \approx 0.23$ µm).

To test this hypothesis, we measured the spatial resolution when imaging 1-µm-wide latex beads suspended in water at different λ and illumination conditions. For a spherical microbead of diameter D, only the part which is in the L_z range contributes to the SPR signal. The effective width is equal to $2 \times \sqrt{D \times L_z - L_z^2}$. Here, the effective widths are 570 and 680 nm at λ = 632 and 721 nm, respectively (890 and 980 nm by considering 3 L_z). The observation area is situated at a distance d less than 500 µm from the prism edge. The imaging system is composed of the 50× LMPLFLN Olympus objective (NA=0.5) and a tube lens of 200 mm, and is set at the resonant angle ($\approx 49°$). For this objective, the diffraction limits are 760 and 880 nm at λ = 632 and 721 nm, respectively, and 660 nm for white light. To further validate our hypothesis, we compare resolution measurements when using a focused and collimated illumination, as depicted in **Figure 4.9a** and **4.9b**.

With the focused illumination, we used a prism optimized for resolution but without gold (N-SF66, A_p = 83°) illuminated by a focused beam of white light from a microscope objective placed on the top (NA = 0.5). In this configuration, each bead simulates a point source emitting in all directions inside the prism. The experimental spatial resolution δ_y measured on 5 beads is 974±76 nm (**Figure 4.9c**). Note that, in the X axis, the resolution is degraded by optical aberrations arising from the cross of the base plane at grazing angles. In the Y axis, these aberrations can be neglected.

We repeated the experiment with a gold-coated prism but with the SPR illumination, i.e. a collimated beam. In that case, we obtain a δ_y of 1.42±0.18 µm at λ = 632 nm (**Figure 4.9d**) and 1.63±0.09 µm at λ = 721 nm (**Figure 4.9e**). Note that a Gaussian fit slightly overestimates the spatial resolution which is closer to 1.8 and 2.0 µm by the Rayleigh criterion.

The difference in spatial resolution between the two illuminations validate the hypothesis that the resolution perpendicular to the SP is limited not necessarily by the NA of the imaging system, but by the effective NA of the object. Here, according to the resolution determined by δ_y, the effective NA is 0.26 (0.21 when considering the period of the Airy disks). The corresponding $\Delta\theta_{int}$ is thus 7.9° for both wavelength. The hypothesis is also confirmed by the fact that 632/721 = 1.42/1.63 at ±1%. Finally, it indicates that the effect of the scattering in the Y axis can be neglected compared to the effect of diffraction: $diff_y \gg scat_y \Rightarrow \delta_y \approx diff_y$. We can assume that

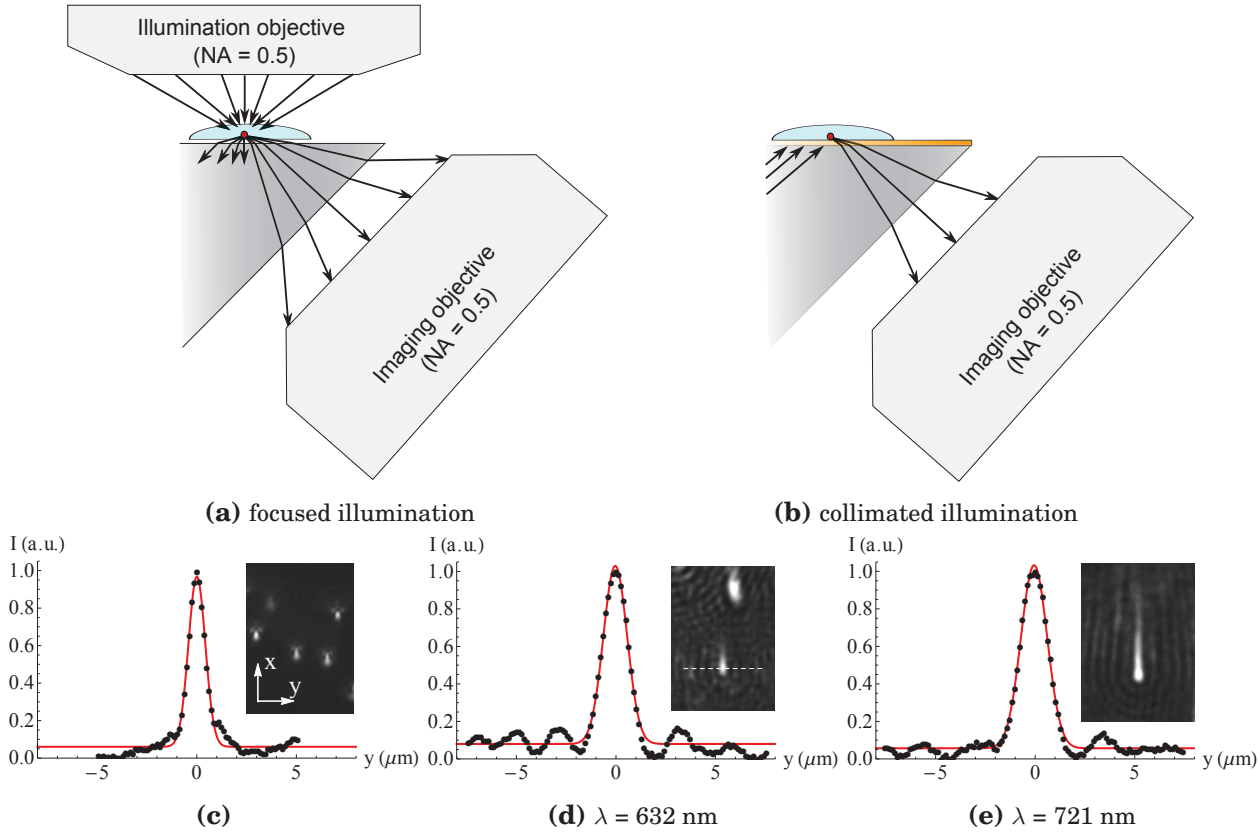

(a) focused illumination **(b)** collimated illumination

(c) **(d)** λ = 632 nm **(e)** λ = 721 nm

Figure 4.9: Experiment to measure the effective numerical aperture. **(a)** Optical scheme of a nearly perfect diffusive point source (white light). **(b)** Optical scheme of a SPR diffusive point source. **(c - e)** PSF perpendicular to the SP propagation direction and Gaussian fit (red line) for the focused white light illumination (c) and SPR illumination at λ = 632 nm (d) and 721 nm (e). In inset, 25 μm-wide-images of the microbeads (non desanamorphosed).

the small value of the light diffusion is mainly due to the collimated illumination, which has an angular divergence of $\sim$0.3°, and to the small roughness of the interfaces. Using a focused illumination could increase $\Delta\theta_{int}$, but this would also result into a complete loss of SPR contrast.

As it is visible in the images in inset of **Figure 4.9d & e**, the diffraction pattern is well defined and has a cylindrical symmetry before the bead (in these images, the anamorphose has not been corrected). After the bead, the diffraction patterns follow the shape induced by L_x. We can therefore assume that, for the imaging point-of-view, this situation is equivalent to the imaging of an asymmetric object. The cylindrical symmetry before the object indicates that the solid angle of diffusion is correctly described by a circular cone, which axis corresponds to the imaging system axis.

4.2.3 | L_x and diffraction limit parallel to the SP

In line-scan imaging mode, the anamorphose $\Upsilon_{line-scan}$ is measured at 0.66 for N-SF66 prisms, as predicted. Consequently, the diffraction limit in the X axis is supposed to be 1.5 times the one in the Y axis. This makes high refractive index prisms better for resolution in line-scan imaging mode. Therefore, considering the experiment presented in **Figure 4.9d & e**, $diff_x$ should be equal to 2.13 and 2.45 μm at λ = 632 and 721 nm, respectively.

By fitting the experimental PSF in the X axis by **Equation 4.3** (**Figure 4.10**), both δ_x and L_x can be determined. Thus, knowing, $diff_x$, we can also determine $scat - gauss_x$. The shape of the experimental curve is in very good agreement with the predicted one. Here, we found propagation lengths of 3.2 and 11.0 μm at λ = 632 and 721 nm, respectively, and δ_x of 2.7 and 2.0 μm. For the

shorter wavelength, we find a resulting $scat - gauss_x$ of 1.66 µm, but for the longer wavelength, δ_x is less than $\delta_y/\Upsilon_{line-scan}$, thereby leading to attribute an imaginary value to $scat - gauss_x$, which obviously is real. This reflects the difficulty to discriminate the importance of light diffraction and SP scattering since both have the same effect on the PSF in the X axis before the object.

However, if we neglect $scat - gauss_x$, the new curves do not differ significantly from the experimental data. The reason is that, at small propagation length, both δ_x and L_x have almost the same effect. Consequently, this makes the determination of δ_x and L_x less accurate than for longer L_x.

These results indicate that for prisms optimized for resolution, in the region where spherical aberrations can be neglected, the ultimate resolution parallel to the SP is mainly limited by L_x, but also by the diffraction weighted by the anamorphose. Under, our experimental conditions, the function that describes the SP scattering can then be approximated by a simple exponential decaying function.

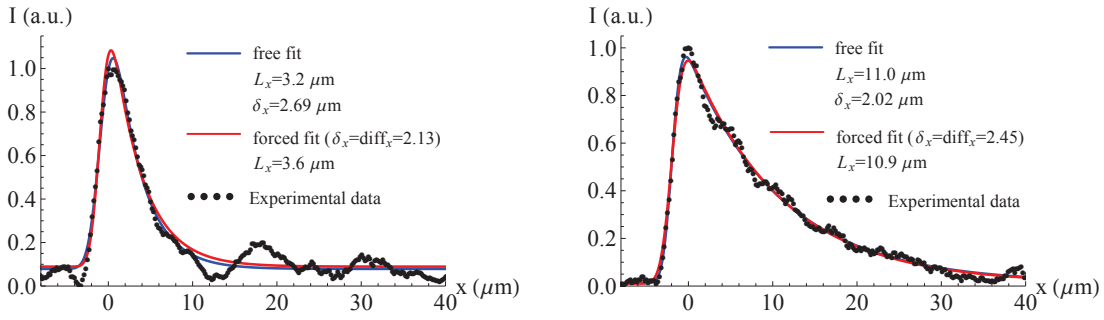

(a) λ = 632 nm **(b)** λ = 721 nm

Figure 4.10: PSF parallel to the SP and theoretical fit.

Although $\delta_y = \Delta y$ is a direct determination of the spatial resolution in the Y axis, δ_x or L_x are not good indicators of the spatial resolution in the X axis. From the experimental point-of-view, is more relevant to quantify the FWHM of the PSF: Δx. Due to the strong asymmetry of the PSF parallel to the SP, we can also distinguish the resolution before and after the maximum of intensity: Δx^- and Δx^+, respectively, as we have done in our article [131]. Δx^- can be measured as the FWHM of the Gaussian fit of the left part of the PSF. As for Δx^+, it can be determined numerically as twice the length for which the intensity is half its maximum on the right side of the PSF, as shown in **Figure 4.11**. The resolution in the X axis is then the average of these two components: $\Delta x = \frac{\Delta x^- + \Delta x^+}{2}$.

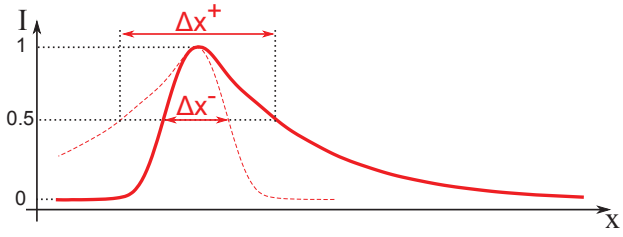

Figure 4.11: PSF parallel to the SP and resolution limits before and after the object.

It can be shown that Δx^- is almost independent on L_x but is proportional to $diff_x$, while Δx^+ follows the inverse trend (**Appendix Figure A.18**). Consequently, the resolution in the X axis before the object is strongly dependent on the diffraction limit, while after the object, the propagation length is the principal limitation. On the PSF of **Figure 4.10**, at λ = 632 and 721 nm respectively, we measured Δx^- at 3.2 and 2.8 µm, Δx^+ at 6.9 and 16.3 µm, and Δx at 5.0 and 9.6 µm.

4.2.4 | Discussion on diffraction and surface plasmon scattering

The presence of these Airy patterns could also have been attributed to the SP scattering due to the presence of an object [147]. The rings only present above the 10-µm-PDMS pillars in **Figure 4.1** (SP propagate downward) are indeed close to the simulated patterns due to scattering. But if these Airy patterns are due to SP scattering, we should not observe them in TE mode. Of course, in TE mode, the microbeads or the PDMS pillars do not produce any detectable signal since there is no SPR contrast. Therefore, we have used a small defect on the metal that gives a signal in both TM and TE mode. As shown in **Figure 4.12**, the Airy patterns are present in both modes and have a cylindrical symmetry (non desanamorphosed images). The small asymmetry in the X axis visible at 780 and 850 nm is attributed to the geometric aberrations due to the prism, which is used out of its optimal angle. Moreover, we also measured a period of oscillation in the Y axis that is proportional to the wavelength, and results in an effective NA of ∼0.21. Finally, last but not least, the intensity field oscillations visible in **Figure 4.6** are standing waves due to the interferences of the incident and reflected SP. Consequently, the spatial period should be half the wavelength of the SP ($= 2\pi/\Re\{k_{SP}\}$), that is less than 370 nm in the 400-1,000 nm wavelength range [152]. According to our spatial resolution, these patterns cannot be observed. It is however, not clear why the diffraction patterns preferentially appear before the PDMS pillars in **Figure 4.1**, even with a barely visible L_x effect. The difficulty to decorrelate the light diffraction and SP scattering comes from the fact that both phenomena rely on wave interferences, thereby presenting similar results in terms of shape. Further improvements on spatial resolution could enable to clearly distinguish these two interesting aspects of SPR microscopy.

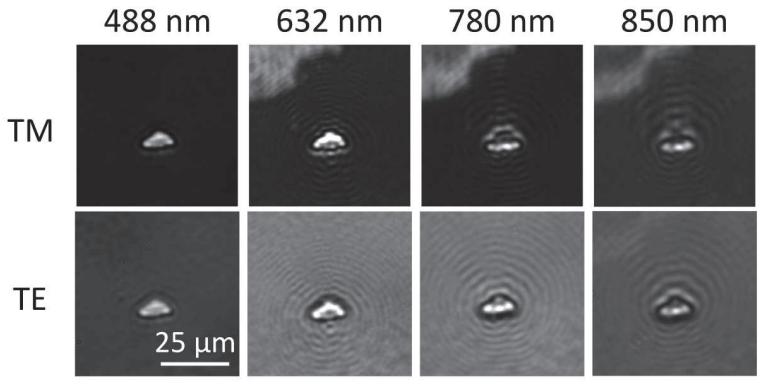

(a)

Figure 4.12: Airy patterns due to a surface defect. The surface defect appears black in bright field microscopy, and is assumed to be a lack of gold. SP propagate upward. (N-SF66, OL:×50, TL:200 mm, non desanamorphosed)

Let us finally mention that there is an ambiguity in the optical observation of the SP nanojet. On one hand, if the experimental PSF has the shape of the nanojet [38], it means that the areas of high electric field intensity appear bright. But on the other hand, the intensity enhancement is supposed to be at the resonance, where most of the light is absorbed, and corresponds to dark areas. Indeed, the farther from the resonance, the less the electric field intensity above the surface, and the higher the reflectivity. It is then not exactly clear what is observed. Does the spreading correspond to an absence of SP after the object due to the created perturbation, leading to less absorption and more reflection, or is it an increase of electric field intensity that induces more radiated losses of the SP into the prism?

4.2.5 | Resolution with respect to d

At longer distances from the prism edge, spherical aberrations cannot be neglected anymore, and the corresponding Gaussian function has to be integrated in the convolution. Thus, the PSF in the Y and X axis can still be described by the same equations by replacing $diff_y$ and $diff_x$ by $\sqrt{diff_y^2 + SA^2}$ and $\sqrt{diff_x^2 + SA^2}$, respectively, where SA is the FWHM of the Gaussian function representing the spherical aberrations. Remember that SA is proportional to d. As a consequence, the spatial resolution Δy and Δx should follow the trend depicted in **Figure 4.13a & b**.

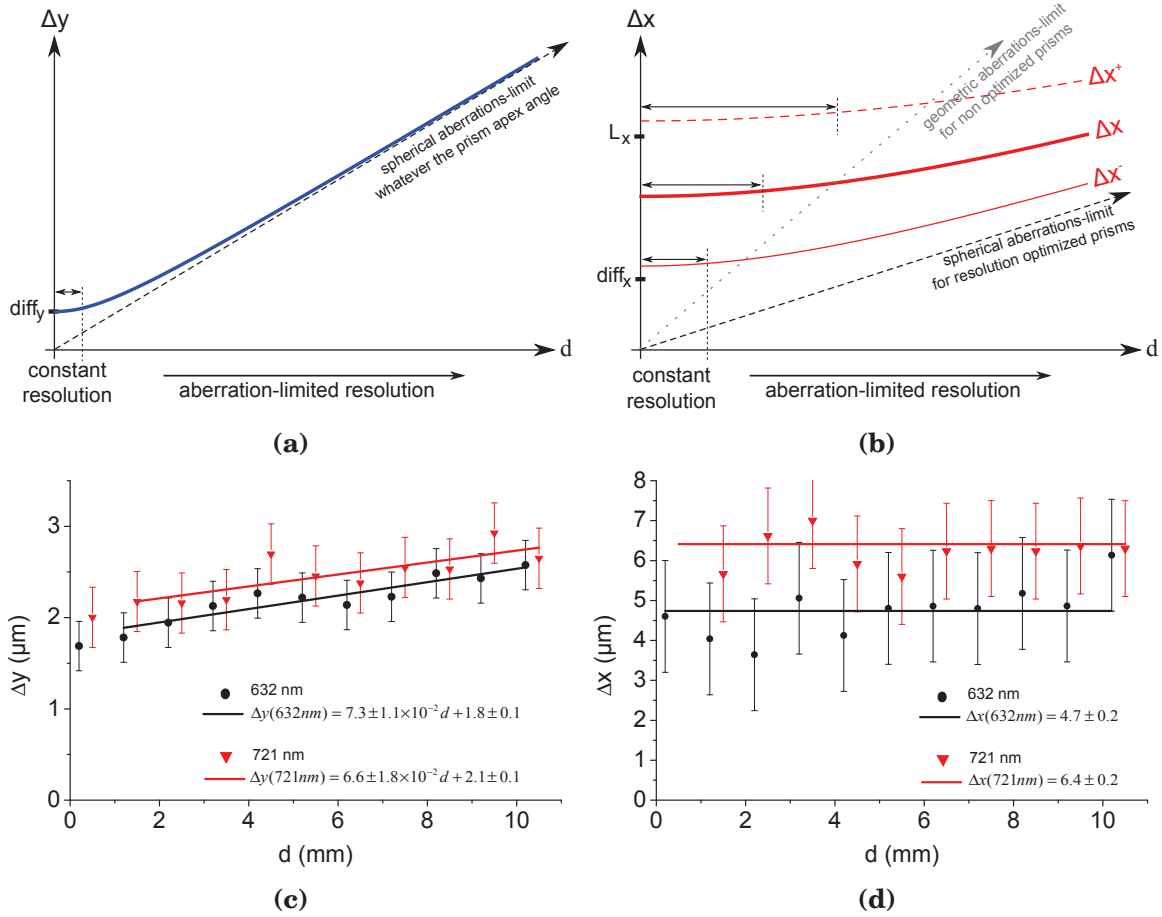

Figure 4.13: Resolution limits in prism-based SPRi with respect to the distance from the edge of the prism. **(a)** Illustration of the resolution limits perpendicular to the SP. **(b)** Illustration of the resolution limits parallel to the SP. **(c)** Experimental resolutions perpendicular to the SP in the first cm of a gold-coated N-SF66 prism. **(d)** Experimental resolutions parallel to the SP.

In the region where $diff_y$ and $diff_x$ are larger than SA, the resolution is nearly constant. These regions correspond to the critical distances d_{lim} where the aberration function Φ is less than $\lambda/4$. According to the previously measured diffraction limits, we expect d_{lim} to be ~880 µm and ~1 mm perpendicular to the SP at λ = 632 and 721 nm, respectively, while parallel to the SP, d_{lim} is a few mm.

In each cases, the spatial resolutions tend to be limited by spherical aberration as d increases. Indeed, all the curves superimpose when $SA >> diff_x$, $diff_y$ and L_x.

To test this hypothesis, we measured Δy and Δx with respect to d at λ = 632 and 721 nm. To know the exact distance d from the edge of the prism, we used the networks of 2-µm-wide PDMS pillars repeated every 1 mm over 1 cm. The contact area of the pillars on the gold has been measured by Surface Enhanced Ellipsometry Contrast (SEEC) microscopy and is ~1 µm. The results shown in **Figure 4.13c** are in good agreement with this theoretical approach. For both

wavelength, Δy increases linearly with respect to d, and the ratio of $\lim_{d\to 0} \frac{\Delta y(721nm)}{\Delta y(632nm)} = \frac{2.1}{1.8} = \frac{721}{632}$ at 2 %. The fact that Δy at $d \to 0$ is slightly higher than for the microbeads is certainly due to the width of the PDMS pillars.

The equality of the slope ($\sim$ 70 nm/mm) is coherent with the fact that the corresponding $\Delta\theta_{int}$ in the Y axis have been measured equal for both wavelengths, so they suffer from the same spherical aberrations. Due to the small value of d_{lim} ($\sim$1 mm) and the accuracy of the measurements ($\pm$300 nm), the diffraction-limited region cannot be observed.

Parallel to the SP, the dispersion of Δx makes difficult to draw precise conclusions (**Figure 4.13d**). But as expected, the resolution is nearly constant over the prism width. We believe that a larger prism should enable to observe the effect of the spherical aberrations.

As shown in **Figure 4.13b**, for prisms that are not optimized for resolution, the effect of geometric aberration is stronger, which means a steepest aberration-limit line with respect to d. Since at $d \to 0$, these aberrations can be neglected, Δx starts at the same value whatever the prism shape. Consequently, Δx for non resolution optimized prisms is more affected by aberrations, and it can be assumed that it follows the same trend as Δy in **Figure 4.13a**.

In conclusion, the resolution in high resolution prism-based SPRi is limited by the effective diffraction of the object, the propagation length and by spherical aberrations due to the prism. L_x lowers the resolution parallel to the SP, while diffraction affect both axis. Finally, spherical aberrations also slightly degrade the resolution, mainly perpendicular to the SP.

4.3 | Hybrid metal coating

In the resolution optimized configuration, the propagation length represents a strong limitation of resolution parallel to the SP. It might then be interesting to work with the metal which optimizes the trade-off between resolution and sensitivity, i.e. silver. But to ensure the stability and biocompatibility with living microorganisms, a protecting layer has to be added. Here, we deposited a 5-nm-thick protecting layer of gold on silver coated N-SF66 prisms.

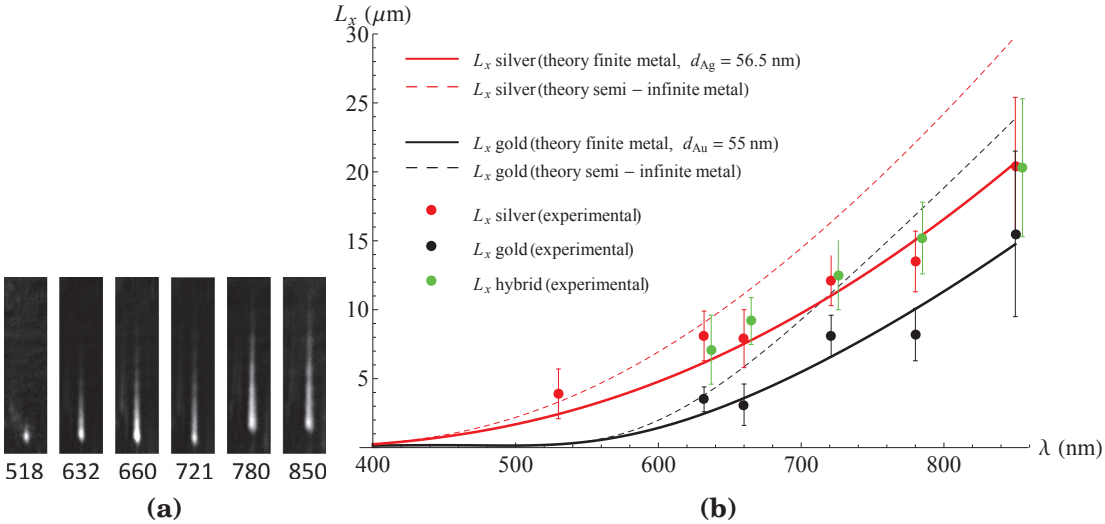

Figure 4.14: Experimental and theoretical propagation lengths for gold, silver and hybrid metal coatings. **(a)** Example of experimental PSF at increasing λ for the silver coating (15×60µm, OL: ×20, TL: 200 mm) .**(b)** L_x as a function of λ. The measured values for hybrid are shifted by +5 nm for the sake of clarity.

We restrict the analysis to the measurement of L_x in the case of gold, silver, and hybrid coating, and rely on the sensitivities theoretically calculated in chapter 2. The experimental measurements of L_x and the comparison with the theoretical values are summarized in **Figure**

4.14. As expected, we measured a clear increase of L_x with respect to the wavelength.

The best fits of the experimental data lead to thicknesses of 55.2 nm for gold, thus in good agreement with the expected values of 53 nm, and 56.4 nm for silver, i.e. 13% more than the expected 50 nm according to the quartz balance of the evaporator. This can be due to the calibration of the quartz micro-balance (which has not be evaluated) or to the inaccuracy of the model we used to calculate the permittivity of silver for very thin layers. The theoretical L_x equation only considers one metal layer, while both samples also have a chromium adhesion layer which thickness is expected to be ~2 nm. This could also explain the difference between theory and experiment. Note that $L_{x,SIM}$ significantly overestimate the propagation length, especially at high wavelength.

The accuracy of the measurement mainly depends on the imaging system focus, optical magnification and contrast. At $\lambda > 800$ nm, the L_x of silver and hybrid are longer than the width of the clear stripe when using the $\times 50$ objective. Therefore, we used the $\times 20$ objective. At short wavelength, the contrast is dramatically low, and only silver exhibits a contrast acceptable to determine a propagation length.

According to our measurements, the propagation length of the hybrid metal coating is very close to the one of silver. In consequence, based on the theoretical sensitivities, the trade-off may not be better than gold, if not worst for L_x below 5 µm, as shown in **Figure 2.17** of chapter 2.

Note that the rigorous determination of the resolution/sensitivity trade-off in the case of hybrid metal layers requires an extensive experimental study. The sensitivity and L_x must be measured for different metal thicknesses and for a multitude of wavelengths. To take into account the penetration depth L_z of the SP, the sensitivity measurement has to be performed for a constant thickness of adsorbed dielectric layer (ideally several thicknesses from 1 to 5 nm). A less rigorous alternative consists in measuring the sensitivity with respect to the bulk refractive index (**Appendix Figure A.15**), and recalculate the equivalent thickness sensitivity using **Equation 1.6**. Since there is no literal expression of L_z in the case of hybrid metal coatings, it has to be calculated numerically by the optical approach. At this time, the numerical determination of L_z by the optical approach only works for 3 layers (glass-metal-dielectric medium), so we cannot use this alternative yet. Moreover, the refractive index sensitivities of gold and silver are closer than the thickness sensitivities, thereby making the hybrid location less accurate.

The hybrid metal coating also presents a disadvantage compared to single gold coating. As shown in **Figure 4.15**, the protecting 5-nm layer of gold does not withstand the electrodeposition conditions commonly used for gold. The center part of the electropolymerized area is strongly modified, as visible in both bright field microscopy and SPRi, and leads to a complete loss of contrast and sensitivity. In addition, some parts of the hybrid layer seem to peel away from the glass surface, but this effect could perhaps be canceled by the use of a chromium adhesion layer. In practice, the use of this hybrid coating imposes to study new conditions of electrodeposition, and verify that they are compatible with the double step functionalization used in cell secretion experiments: thiol-PEG, and then Ppy-Ab.

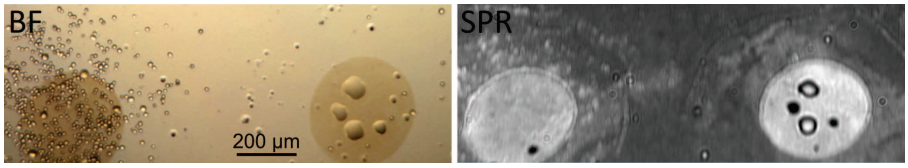

Figure 4.15: Electropolymerization damage on hybrid metal coating

Consequently, the issue of the highest spatial resolution for biological applications using a single gold layer is then changed into the issue of the sensitivity at wavelength where L_x is

significantly less than $diff_x$, that is for $\lambda < 600$ nm. In chapter 2, we have shown that thinner gold layers are optimal at short wavelength (d_m from 25 to 50 nm). In chapter 3, we have quantified the improvement of SNR by frame and pixel averaging. Optical techniques can also provide a another source of improvement. In 2011, Kim *et al.* [113] demonstrated that combining SPRi and ellipsometry (SPRiE) can significantly increase the contrast at the resonant angle. Using appropriate angles for the polarizer and the analyzer, the bare gold appears dark (null-condition) while the areas in contact with an object reflect the light (off-null condition). Under these conditions, the authors estimated the resolution at $\sim$1 µm at λ = 532 nm. Nevertheless, their measurements were restricted to cell adhesion and movements, for which the change of refractive index is large compared to biomolecules detection. In other words, their SPRiE set-up may not necessarily be suitable for experiments where individual cell imaging and biomolecules detections are performed simultaneously, and for which the working angle is not the resonant angle.

In conclusion, in a first analysis, the hybrid metal coating does not seem to bring a significant improvement on the resolution/sensitivity trade-off compared to gold. Moreover, due to its lower chemical stability in electrochemistry, we have decided to keep gold as the best metal for applications in individual cell monitoring.

4.4 | Plasmon curves of gold

According to the good agreement of L_x measurements for gold, we can expect the model used for the permittivities to be accurate, and the plasmon curves to be correctly fitted with a gold thickness of 55.2 nm. The simulated and experimental plasmon curves at λ = 632 and 721 nm are presented in **Figure 4.16**. We observe a good agreement at both wavelengths. Due to the absolute angle accuracy of the actual set-up ($\pm 1°$), the experimental points have been shifted to fit the expected plasmon curves. Experimentally, we observe a good agreement on θ_{res}, as well as shifts in θ_{res} with respect to the wavelength. For the biological experiments, we found working angles of 48 ° at λ = 632 nm and 46 ° at λ = 721 nm.

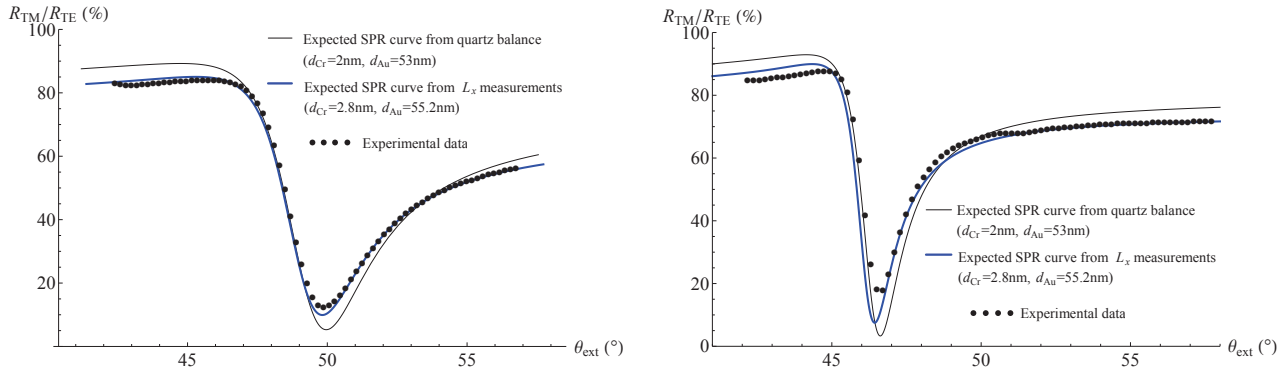

(a) λ = 632 nm **(b)** λ = 721 nm

Figure 4.16: Gold plasmon curves and corresponding expected curves based on the quartz balance of the evaporator and on the L_x measurements. d_{Cr} has been fitted to match the experimental data.

4.5 | Individual eukaryote cells monitoring

Using N-SF66 prism optimized for resolution, living eukaryote cells can be imaged at λ = 632 nm with a spatial resolution sufficient to clearly distinguish each one of them. As shown in **Figure 4.17**, in line-scan imaging mode, even a dense layer of cells leads to individual signals, where the

close surrounding of each single cell can be monitored. In **Figure 4.17a**, the number of cells is measured at more than 10,000.

If the resolution of the digital image is pixel-limited, that is to say the spatial resolution Δ_y and Δ_x are smaller than the distance encoded by 3 adjacent pixels, a higher optical magnification improves the image resolution. This is for example the case in **Figure 4.17c**. But more importantly, it also increases the number of pixels encoding for a same area, and enables to decrease the noise by averaging several pixels. For a given camera, there is then a trade-off between the number of individual cells and the SNR require for a particular application.

Recently, camera sensors with integrated piezo-actuators have been commercialized. The sensor shifts by a fraction of the pixel-width in two directions while acquiring images. For a number of displacements equal to N, the number of pixels in the final reconstructed image is proportional to N^2, or equivalently, the area encoded by each final pixel is N^2 times less.

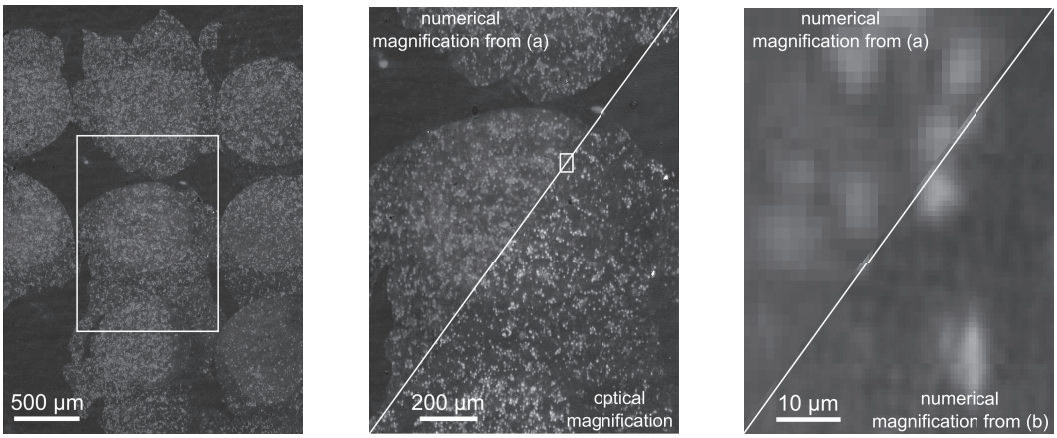

Figure 4.17: Indiviual cells imaging in line-scan imaging mode. **(a)** Jurkat cells on Ppy-grafted-anti-CD3 spots (FOV: 7.0 mm^2, OL: $\times$10, TL: 100 mm). **(b)** Optical magnification (FOV: 1.8 mm^2, OL: $\times$10, TL:200 mm) compared with the corresponding numerical magnification of (a). **(c)** numerical magnification on a few cells.

For certain applications where the number of cells is not crucial, but the expected signal is very low or the time resolution has to be high, it might be more relevant to use the classic imaging mode. In this mode, the resolution is degraded due to optical aberrations of the imaging system, but the frame rate (fps) is only limited by the exposure time, or by the camera itself if the light intensity is high enough. The ratio of SNR improvement between the two imaging modes can be calculated by considering, in line-scan imaging mode, the number of clear stripes N_{cs}, the time spent for focus adjustment t_{focus} (s), the frame rate fps (Hz) and the number of images used for frame averaging N_{fa}. The time needed to acquire an entire image and go back to the first focus position is $T = N_{cs} \times \left(\frac{N_{fa}}{fps} + t_{focus}\right)$, leading to a effective frame rate of $1/T$. Here, in the final image, the SNR is improved by $\sqrt{N_{fa}}$. If classic imaging mode is performed at the same effective frame rate, the number of frames that can be used for frame averaging is equal to $T \times fps$, improving the SNR by $\sqrt{T \times fps}$. Consequently, in classic imaging mode, the SNR is improved by $\sqrt{\frac{N_{cs} \times N_{fa} + fps \times t_{focus}}{N_{fa}}}$ compared to the line-scan imaging mode.

However, with the recent development of varifocal lenses, for which t_{focus} could be lower down to 30 ms [153], the improvement of SNR in classic imaging mode tends to $\sqrt{N_{cs}}$. For instance, averaging 100 frames at a frame rate of 100 fps and using 50 clear stripes, the improvement is 7.07. In our actual set-up, due to the slowness of the motor adjusting the focus, t_{focus} is $\sim$15s, and the maximal frame rate is limited to 15 fps due to the finite power of the light source. Therefore, when using frame averaging on 25 images and using 25 clear stripes, the improvement of SNR in classic imaging mode would be 5.8. Furthermore, external sources of noise are not taken into

account in these calculi. If these latter noises are larger than the one of the camera, increasing the number of frame to average does not improve the detection. Similarly, in practice, the effective frame rate is also governed by the time constant of the monitored bio-interaction.

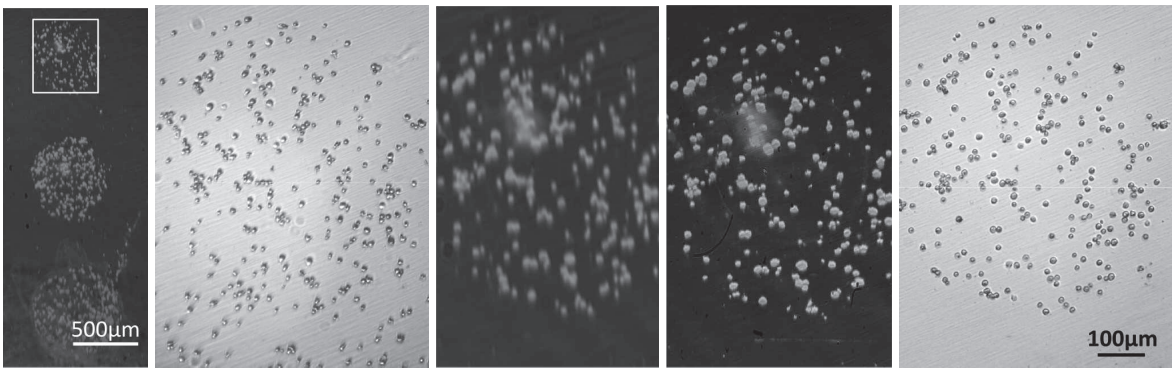

Figure 4.18: Individual cells imaging in classic and line-scan imaging mode. **(a)** cropped image of Jurkat cells on 3 Ppy-grafted-anti-CD3 spots (original FOV: 7 mm^2, OL: 18.75 mm, LT: 100 mm). **(b)** Bright field image of the upper spot. Cells are randomly distributed on the surface. **(c)** Numerical magnification on the upper spot (displayed FOV: 0.38 mm^2). **(d)** Same area acquired in line-scan imaging mode (OL: ×20, LT: 200 mm, 100 lines). **(e)** Bright field image after rinsing. Only the captured cells remain.

As shown in **Figure 4.18**, the resolution of classic imaging mode is sufficient to clearly image several hundreds of cells, even if the image quality is less than in line-scan imaging mode. This figure also demonstrates that prism-based SPR microscopy can provide information that conventional optical microscopy cannot access. Due to the small penetration depth L_z, only the cells captured on the antibody spots generate a SPR signal, while the ones just deposited on the bare gold are hardly detectable. Once rinsed, only the captured cells previously observed in SPR remain.

4.6 | Protein secretion monitoring

The real-time monitoring of protein secretion by individual cells is a typical application that could be addressed by prism-based SPR microscopy. This imaging technique exhibits both high resolution and high sensitivity on wide FOV.

4.6.1 | SPR signal estimation

The relative shift in intensity $\Delta I/I_w$ is proportional to the effective thickness h_{eff} of the protein adsorbed layer (**Figure 2.16b** of chapter 2). h_{eff} is equal to the molar volume V_M (m^3/mol) times the target concentration on the surface (mol/m^2). Assuming that we are close to an equilibrium state, this surface concentration is equal to the surface coverage ρ_{eq} multiplied by the concentration of total binding site C_0 (**Section 1.2.3**). V_M is equal to the molar mass M_m (kg/mol) of the cytokines divided by their density d (kg/m^3). Cytokines molecular weight range from 15 to 45 kDa [82] (1 kDa $\approx 1.66\times10^{-24}$kg), leading to a mean molar mass of 30 kg/mol. The typical density of proteins is usually considered close to 1,350 kg/m^3 [154], so $V_M \approx 1.5\times10^{-2}$ m^3/mol. The SPR signal in intensity can then be calculated by:

$$\frac{\Delta I}{I_w} = \frac{k_{on}\times c\times C_0}{k_{on}\times c + k_{off}} \times \frac{M_m}{d} \times \frac{\partial \Delta I/I_w}{\partial h} \tag{4.5}$$

where c (mol/m^3) is the concentration of secreted proteins at the surface, and k_{on} and k_{off} the association and dissociation constants.

The SPR signal is then a function of c. In fluorescence studies, the main strategy to increase this concentration, and thus the signal, has been to limit the diffusion by confining the cells into small volumes, such as microcubes [82] or microchannels [109]. But this configuration also limits the study of intercellular communications. Here, we do not use microstructures to confine the cells, so that they can biochemically communicate between each other. This configuration also has the benefit to be a "low-tech" strategy, which can easily be transferred to industry. It has been validated in fluorescence microscopy by Wang *et al.* [110], who measured concentrations more than 2 mg/ml of interleukin2 (IL-2) in the first micrometers around each cell ($\sim 7 \times 10^{-2}$ mol/m^3 or 70 µmol/L). The rapid decay of the concentration with respect to the distance is also pointed out by our finite-element simulation presented in **Figure 1.19** of chapter 1. However, by performing the simulation with the typical secretion rate found by Han *et al.* [82] of $\sim$ 20 molecules per cell and per second, the maximal concentration in steady state is only $\sim$10 pmol/L (300 pg/mL). Even when using a secretion rate of 100 molecules/cell/s and a diffusion constant of 10^{-9} m^2/s (instead of 10^{-10} m^2/s in our simulation), the concentration hardly reaches the nmol/L (30 ng/mL). Such a low concentration is close to the limit of detection of most SPR sensors [69].

According to Han *et al.*, k_{on} ranges from 10^5 to 10^6 L·mol$^{-1}\cdot$ s^{-1}, k_{off} from 10^{-4} to $10^{-3}\cdot$ s^{-1} and C_0 from 10^{-10} to 10^{-8} mol/m^2. In the best case, it leads to a h_{eff} of 0.1 nm and a SPR intensity shift of $\sim$1 % at λ = 632 nm. Owing a photon noise of 0.7 %/pixel when working at 2/3 of the dynamic of the CMOS censor, the limit of detection is 2.1 %. Therefore, using frame or/and pixel averaging is essential to increase the SNR. Although all the previous calculi only give an order of magnitude, we might expect to deal with very weak SPR signals.

To test the sensitivity of our set-up, we have performed a typical DNA/DNA hybridization experiment (ZIP sequences at 500 nM) where the shift of reflectivity has been measured at 0.4 % at λ = 632 nm and room temperature. This value is close to the one obtained by commercial apparatus (Horiba SPRi-Plex, 0.7% at λ = 680 nm) in the same conditions. An amplification with streptavidin lead to a further increase of 0.9% (1.2 % with SPRi-Plex). The smaller values with respect to the commercial apparatus are attributed to the use of a lower wavelength of illumination, and to the experimental differences such as gold coating quality, flowcell geometry and certainly reproducibility of the electrodeposition process.

4.6.2 | Secretion monitoring Experiments

A wide variety of configurations have been tested (imaging systems, imaging modes, frame rate, wavelength of illumination, temperature, cell capture method, cytokines...). To validate an experiment, it is essential to have both positive and negative controls. Hence, to test 3 cytokines, the biochip must ideally exhibits 9 spots. Therefore, in the latest configuration, the imaging system is chosen so that the FOV is just enough to image almost entirely 9 spots, as shown in **Figure 4.17a**. The SNR is enhanced by 5 by using a 25-images frame averaging for each intermediate image. Each final image is reconstructed from 25 intermediate images. Under these conditions, one final images takes approximately 10 min to be acquired. This low frame rate is principally due to the slowness of the camera focus motor. Nevertheless, since secretion phenomena are supposed to occur over several hours, this frame rate still enables the monitoring.

To simplify the experiment and maximize the chance to observe a secretion phenomenon, we only analyze two cytokine secretions: IFN$_\gamma$ and IL2, but keep the 9 spot configuration, as shown in the scheme of **Figure 4.19a**. Moreover, we use model cells where more than 25 % are supposed to secrete in a larger amount than real samples. As shown by **Figure 4.19b & c**, both SPR and bright field observations enable to monitor the areas of interest. For comparison purpose with other SPR prisms, in this figure, instead of correcting the anamorphose of the SPR image, we have deformed the optical image to show the small anamorphose induced by the N-SF66 prisms

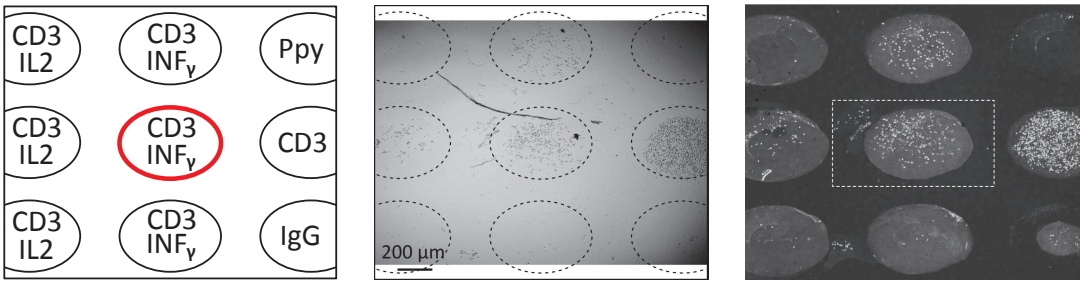

(a) **(b)** bright field **(c)** SPRi

Figure 4.19: Wide FOV bright field and SPR images of a cytokine secretion experiment on PBMC. **(a)** Scheme of the detection map. **(b)** Bright field image at the beginning of the experiment. **(c)** SPR image at the beginning of the experiment (OL: ×10, TL: 100 mm, 25 lines).

in line-scan imaging mode. In several experiments, we have observed a significant decrease of SPR signal from the cells. Indeed, the SPR and bright field images show that the majority of the cells are not perfectly fixed, and move all along the experiment. Some of them even disappear before the end of the 12 hours experiments.

During the experiment, both SPR and bright field images are acquired at the same rate. This enable to correlate both images, for instance to verify that a bright area in SPR is a cell and not a dust (**Figure 4.20a & b**). Since SPR is less sensitive than fluorescence, we perform a fluorescence revelation of the secreted cytokines at the end of the experiment to ensure that some of the cells have sufficiently secreted. In this experiment, in addition to a global detection, some brighter area may indicate a local cell secretion (**Figure 4.20c**). Both SPR and fluorescence images are merged to ensure that the fluorescence signal corresponds to the location of a cell. As shown in **Figure 4.20d**, we can distinguish several cases. On the right side of the spot, we can observe two fluorescent areas, but without any cells. This means that a fluorescence signal does not necessarily correspond to a secretion detection.

For most of the cells, there is no specific fluorescence signal, but for some of them, the fluorescence signal does correspond to a cell location. According to Wang *et al.* [110], the fluorescence must only be located just below the cells, as it is the case for the magnification 1 (Inset of **Figure 4.20d**). In that case, the SPR signal from the secretion will be completely lost in the cell signal, several order of magnitude higher (displacement or growth for instance). According to our simulations, the secretion must also extend few microns away from the cell in a cylindrical symmetry, as it is the case in the magnification 2. In the magnification 3, the fluorescence signal is strong, very localized and strongly asymmetric. It can come from a cell apoptosis, thereby releasing its highly concentrated secretory vesicles. Note that the bright field image shows several cells for this single SPR signal. In the magnification 4, the fluorescence signal spreads over several cells. Once again, due to the cell movements, the decorrelation between the secretion and cell SPR signal is very difficult, if not impossible.

Consequently, we only perform a local SPR analysis for the cases 2 and 3. These two cells were almost perfectly immobile all over the 12 h experiment. For the cell of case 2, the analyzed area has a donuts-shape of 30-µm-outer-diameter around the cell (**Figure 4.20b**), while for the case 3, the monitored area is located in the space separating several cells (**Figure 4.20b**). The results presented in **Figure 4.21** show a clear decrease of the global intensity of approximately 7 %.

This drift corresponds to a global decrease of refractive index that can be attributed to the evolution of the biological medium resulting from the cell activity, or to an unexpected increase of temperature from 3 to 5°. However, the temperature measured on the ITO plate was stable all over the experiment, and such decrease of reflected intensity has not been observed during bacterial growth experiments.

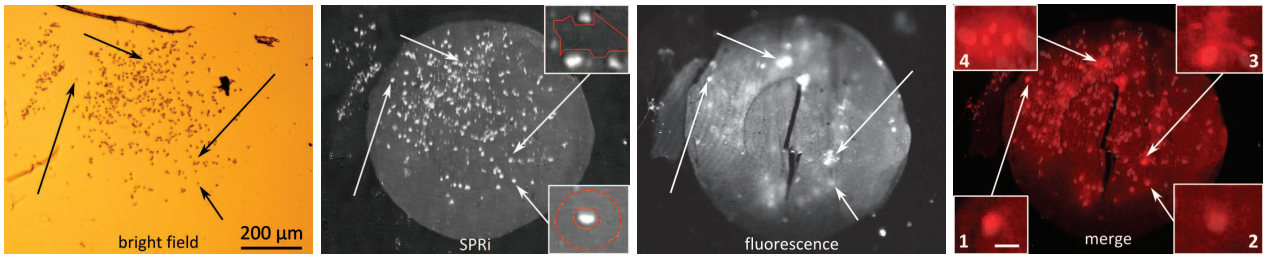

(a) **(b)** **(c)** **(d)**

Figure 4.20: IFN$_\gamma$ secretion analysis on one spot. **(a)** Bright field image cropped from figure 4.19b. **(b)** SPR image cropped from figure 4.19c. Inset: monitored areas of ∼ 500 pixels. **(c)** Fluorescence image after the experiment. **(d)** Merged SPR and fluorescence image. Inset: magnification on different cases of SPR and fluorescence signals correlation. Scale bar: 20 µm

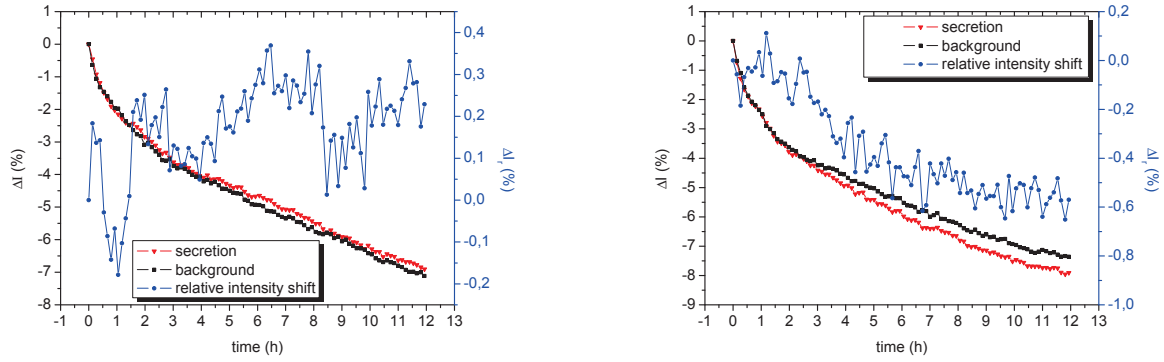

(a) **(b)**

Figure 4.21: IFN$_\gamma$ secretion analysis on individual cells. **(a)** Cell of case 2. **(b)** Cell of case 3.

Nonetheless, we can use a reference situated few tens of µm away, where no fluorescence was observed, to analyze the data. For the two cells, the corrected intensity shifts do not show any significant increases that could come from a secretion phenomenon. The corrected signals are indeed close to the noise of the measurement. This noise comes from the low amount of pixels to average (and to the absence of frame-averaging in this experiment), but also to experimental noise, that is for example, cell movements or local variation of the bulk concentration in nutriment, salt, or even cell parts from the apoptosis of the neighboring cells.

We should also mention that for such long experiments, the mechanical stability is also crucial to ensure that each clear stripe position on the sensor remain strictly equal over the time. For instance, in our actual set-up, we have noticed a clear stripe shift by ∼25 µm after 12 h. Therefore, by using the same image reconstruction parameters for each sequence, a small defocus effect can be observed between the first and the last final images, as well as in single stripes from intermediate images. Note that this small focus shift does not induce a lateral shift of the cells on the image. Therefore, it does not strongly perturb the time monitoring, at least for monitored areas greater than few hundreds of pixels.

The fluorescence microscopy experiments recently performed by Dieudonné Baganizi show that secretion signals are very localized under the cells, and do not extend more than a few µm away (**Figure 4.22**). In SPR microscopy, cell movements, even of a few µm, dramatically decrease the chance to observe a low secretion signal in a donuts-shape region of interest of only a few µm-wide around each cell.

In conclusion, the monitoring of individual cell secretions by SPR is a very challenging project, in both biology and physics, and still needs to be developed. Herein, we have however paved the way to success by analyzing the main issue to be solve: cell movements, spatial resolution and FOV, image processing and analysis, SNR improvement and instrumentation. Solutions could come from a new strategy currently under development in our laboratory which allows the distinction between the cell and secretion SPR signals. For confidentiality reasons, it cannot be further discussed here.

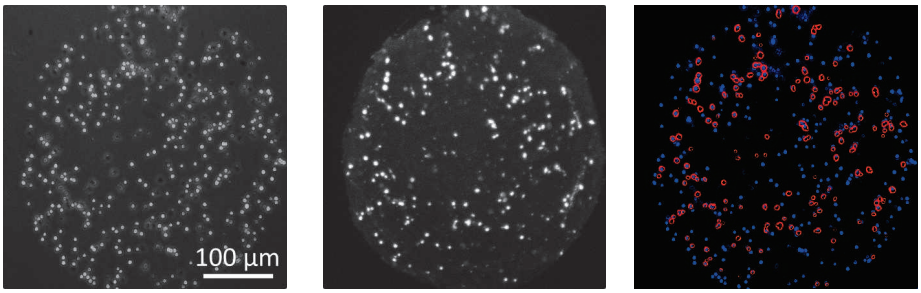

(a) bright field **(b)** fluorescence **(c)** merge

Figure 4.22: Fluorescence detection of IL2 secretions by individual PBMC.

4.7 | Single eukaryote cells observation

The ability to observe a large number of cells at the individual level is valuable in biology because it brings statistical data. However, for some applications, it is more relevant to only focus on a few cells, and imaged them in more details. In this view, the sensitivity of SPRi to variations of refractive index occurring in the L_z range has been used to study the adhesion properties between adherent cells and the substrate [18, 155, 113]. Internal changes of refractive index with respect to a biochemical stimuli have also been addressed [66, 14]. In these previous works, according to their spatial resolution, the authors have used commercial prisms for which the apex angle was only a few degrees from the optimized apex angle for resolution (A_p is not specified usually, but was certainly 60° for SF-10 [14] or S-LAL-10 prisms [113]). Therefore, they have a lateral resolution in the order of 2 µm, but usually in a clear stripe smaller than the sensor (**Figure 1.17** of chapter 1). Hence, there effective FOV is usually restricted to a few cells. In line-scan imaging mode, the spatial resolution is the same over the entire FOV, so more cells can be monitored.

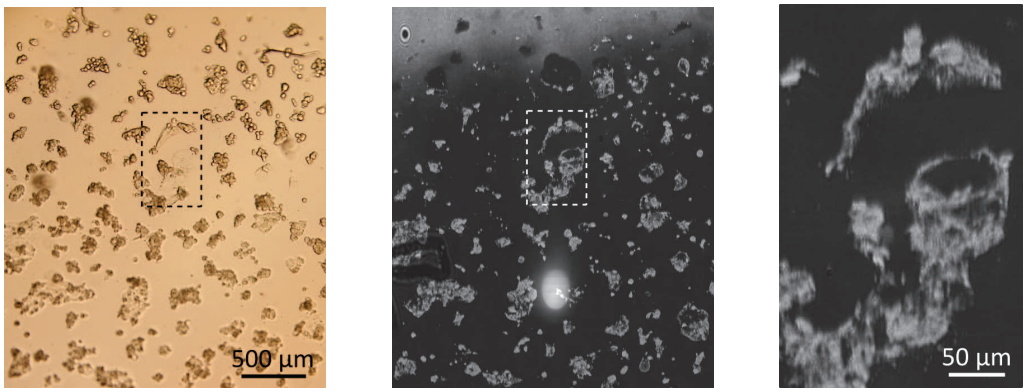

(a) **(b)** **(c)**

Figure 4.23: Wide FOV of individual adherent cells in classic imaging mode. **(a)** Bright field microscopy. **(b)** SPR image at λ = 632 nm (N-SF66, OL: ×10, TL: 200 mm, 57 stripes). **(c)** Numerical magnification of the SPR image.

According to the intrinsic spatial resolution of SPR images, using a microscope objective with a NA greater than 0.26 does not significantly improve the resolution. By using the ×10 objective (NA=0.3), each pixel of our CMOS sensor (ORCA 4.0) encodes 650 nm, that is approximately a third of the best spatial resolution. It is therefore the optimal configuration to have the best spatial resolution on the widest FOV. **Figure 4.23** shows a bright field and a SPR image of human epithelial cells (Caco-2, colon tissue) that have grown 24h on the gold surface. Note that only ∼30 cells have grown and adhered over several µm or tens of µm, while the majority of them only aggregate and are about 8 µm-wide. The numerical magnification of **Figure 4.23c** illustrates the ability to observe details within a single adherent cell over a population that can reach more than 50 separated cells.

In order to have a higher SNR, it may also be advantageous to image only a single cell at high magnification. As shown in **Figure 4.24**, using the ×50 objective does not lead to a strong improvement of spatial resolution. Indeed, at such high magnification, the main limitation comes from the propagation length, especially at high wavelengths. These images also illustrate the ability of SPR microscopy to scan different thicknesses above the surface. The penetration depths at these wavelengths of illumination are 48, 90, 131, 161 and 198 nm, respectively. Thus, at short wavelength, only the parts that have strongly adhered to the gold are visible. The SPR images show that these points are not homogeneously distributed, which cannot be seen in bright field microscopy. At λ = 518 nm, the contrast is dramatically low, but could be improved by using a thinner gold layer. For longer wavelengths, the SP are also sensitive to the inner part of the cell, thereby loosing the surface details, but accessing the volume of the cell. Using high wavelengths of excitation also generate intensity oscillations just after the SP strike the membrane, another effect which degrades the image quality. These oscillations are proportional to λ and have been studied by Berger *et al.* [91]. They arise from the interferences between the incident, transmitted and reflected SP at a perpendicular index step, such as a cell membrane.

To conclude on single cell SPR imaging, the shorter the wavelength of illumination, the smaller the influence of L_x and interferences at the index step created by the membrane. Moreover, it makes the penetration depth smaller, which is also the key advantage of SPRi compared to conventional microscopy.

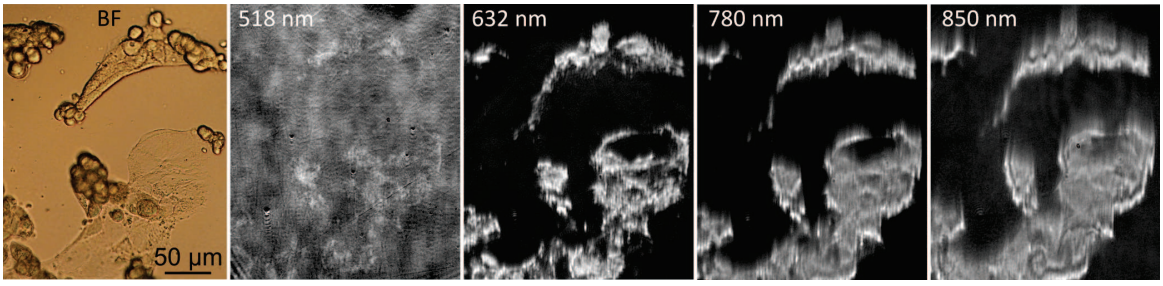

(a)

Figure 4.24: Bright field and SPR images of two adherent cells at different wavelengths (N-SF66, d ≈ 3 mm, OL: ×50, TL: 200 mm, 100 stripes)

4.8 | Individual bacteria observation

The ability to observe wide FOV with a resolution of a few µm has also been applied to the observation of individual living bacteria. Since the diameter of *Staphylococcus epidermidis* is less than the spatial resolution, their SPR signal corresponds exactly to the PSF. In **Figure 4.25**, we demonstrate the potential of high resolution prism-based SPRi in bacterial detection and study. Giving a mean density of ∼1,900 bacteria/mm^2, up to 8,000 bacteria can be simultaneously monitor at the individual level.

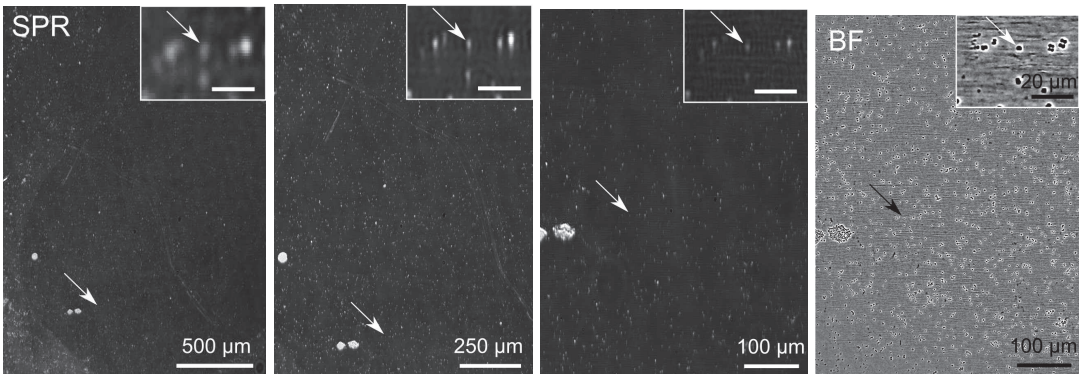

Figure 4.25: Individual bacteria observation by SPR at λ = 632 nm on a gold-coated N-SF66 prism (line-scan imaging mode). **(a)** OL: ×4, TL: 200 mm, FOV = 4.3 mm^2. **(b)** OL: ×10, TL: 200 mm, FOV = 1.6 mm^2. **(c)** OL: ×20, TL: 200 mm, FOV = 0.31 mm^2. **(d)** Bright field microscopy.

In terms of bacterial detection, this implies that the intensity increase due to the growth of micro-colonies may not be the quantity that leads to the fastest detection signal. Instead, spatial properties which reflect the heterogeneity of the bacterial growth could be used, such as standard deviation, skewness and kurtosis [156].

These statistical quantities quantify the distribution of the intensity on the SPR images, i.e. the number of pixels per gray-levels, usually represented in histogram. They can also be seen as parameters that describe the shape of the histograms. **Figure 4.26a** shows the histogram of a differential image obtained 770 min after the beginning of a detection experiment of *S.epidermidis*. Differential images are obtained by subtracting the first image of the monitoring (reference image, here taken at t = 120 min) to each following image. Here, 3,000 gray-levels have previously been subtracted to the reference image to ensure that differential images exhibit a full histogram. The corresponding image is shown in **Figure 4.26b** and is normalized for clarity purpose.

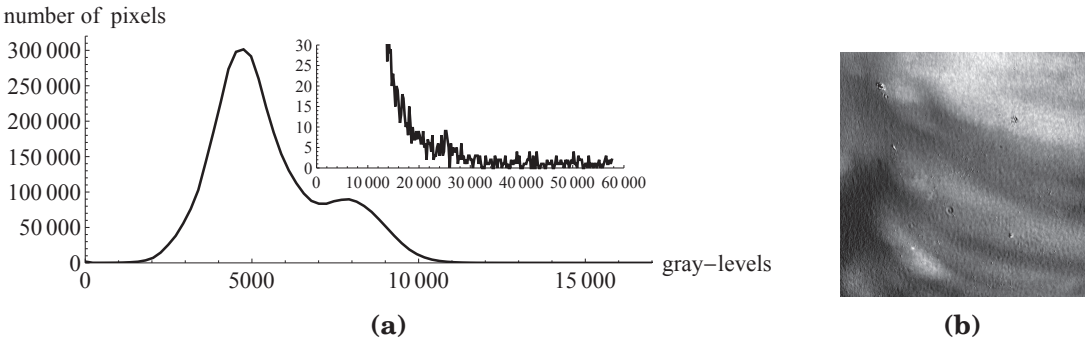

Figure 4.26: Intensity histogram of a single differential SPR image of bacterial growth monitoring. **(a)** Number of pixels with respect to the gray-level segmented into 256 over 57,650. **(b)** Normalized differential image at t = 770 min.

The standard deviation is a good indicator of the spreading of the distribution, but the skewness and kurtosis interpretations are more ambiguous and less intuitive. Skewness is sometimes interpreted as the asymmetry of the distribution, and is positive if the distribution is elongated to the right (right-tailed) and negative in the it is elongated to the left. For instance, on **Figure 4.26a** the skewness is positive. Kurtosis represents the "peakedness" of histogram (the fact that the distribution exhibits several peaks) or sharpness of the peaks (online oxford dictionary). Both parameters are indicators of the spatial heterogeneity of the intensity, which could come from the growth of micro-colonies.

Theoretically, the heterogeneity of a negative control should be constant, while the intensity

just undergo a linear drift of intensity [11]. Therefore, these other parameters should remains low compared to a positive signal.

Note that there is no reason why an homogenous system could induce an heterogeneous signal. But in practice, several parameters may break the symmetry, such as temperature gradients or heterogeneity of the surface functionalization. In this view, it might even be interesting to voluntary design non symmetric detection areas and flowcells. Experimentally, such heterogeneity of growth has been observed in SPR for several strains of bacteria.

Figure 4.27a shows the evolution of different quantities as a function of the times. For comparison purpose, each curve represents the relative and normalized quantity over the experiment. Note that standard deviation has been normalized by starting at t = 300 min since the first differential images intrinsically show very high level of standard deviation.

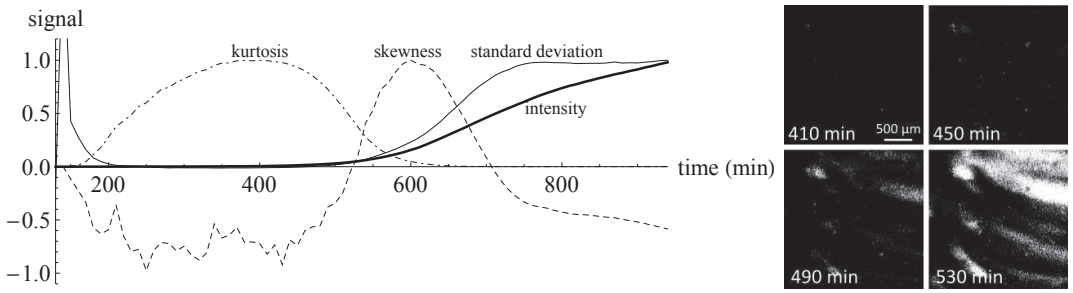

Figure 4.27: Monitoring of *S.epidermidis* micro-colonies growth at λ = 632 nm on a gold-coated N-SF66 prism functionalized with poly-L-lysine. **(a)** Normalized relative signals. **(b)** Example of normalized differential images at the critical time of growth (classic imaging mode, OL: 18,75 mm, TL: 100 mm, FOV = 7 mm^2).

Compared to intensity, which has the shape of an exponential growth, the other parameters undergo a slightly faster evolution. The two parameters that present the fastest variation are the skewness and the kurtosis. However, their interpretation needs further experiments and analyses. **Figure 4.27b** shows a set of images corresponding to this critical period where micro-colonies start to grow. On these images, individual bacteria cannot be observed due to wide field-of-view and use of classic imaging mode. We believe that having the individual resolution may improve the pertinence of these statistical parameters.

These results, even being at the preliminary stage, highlight the potential offered by high resolution prism-based SPRi for bacterial detection, both in terms of detection limit and time of detection. However, more experiments are necessary to validate and quantify an improvement of detection (comparison with negative controls, other bacterial strains, specific surface chemistry...).

4.9 | Conclusion

In this chapter, we have experimentally demonstrated the improvement of spatial resolution and FOV bring by the understanding of geometric aberrations caused by the prism. Using optimized prisms, we have also shown that the other limiting factors are the propagation length L_x and the diffraction. By analyzing the theoretical PSF, we obtain an analytical expression that can fit the experimental data and determine L_x with a good agreement with the theoretical prediction. The measurement of the influence of spherical aberrations on resolution is also in good agreement with the theoretical prediction. High resolution prism-based SPRi has then be applied to the monitoring of protein secretion by individual immune cells. We discuss several points that could explain why secretion SPR signals have not been obtained so far, and discuss the main issues that need to be solved. The new capabilities of SPRi are also applied to the observation of single adherent cells from wide to very-small FOV. We demonstrate the ability to simultaneously monitor

several tens of adherent cells presenting details related to their adhesion properties. The use of higher wavelengths of illumination allows to scan deeper in the cell, but also strongly degrades the resolution. Finally, we are able to observe up to several thousand individual bacterial signals. Therefore, by monitoring the spatial properties of the image instead of the mean intensity, we prove that the time of detection can be decreased while making the detection signal clearer and stronger.

Conclusion

In this PhD thesis, we have addressed the issue of spatial resolution in prism-based surface plasmon resonance microscopy. Our approach has been equally balanced between theoretical calculations and experimental demonstrations. The result of our work is twofold. First, we have improved the fundamental understanding of the physical mechanisms governing the lateral resolution. Secondly, we have experimentally demonstrated that optimizing the optical system leads to a significant improvement on both resolution and field-of-view, thereby opening new horizons in cellular biology and microbiology applications.

Aside from a bibliographic study which gives an overview of the main properties of prism-based SPR microscopy and its use in biosensing, the main results of this doctoral project can be segmented into four contributions.

Geometric aberrations and prism design

Giving the prism apex angle, refractive index and the incident angle of illumination, we have derived literal expressions that allow to calculate the main optical parameters of prism-based imaging: virtual image angle with respect to the base, angle between the external reflected ray and the perpendicular to the virtual image, or anamorphose to name a few.

Through the understanding that the prism exit face behaves as a plane diopter, intrinsically non stigmatic, we have demonstrated the presence of geometric aberrations which can strongly degrade the resolution. The minimization of these aberrations is satisfied when the reflected ray is perpendicular to the prism exit face, thereby defining a novel optimal prism shape for which the main optical parameters have also been derived as analytical expressions. We have shown that this resolution optimized configuration exhibits less anamorphose and more practical characteristics with high refractive index prisms. These new prisms also suggest the use of a "line-scan imaging mode", in addition to the standard "classic imaging mode".

By quantifying the geometric aberrations by the wave aberration model, we were also able to demonstrate that high refractive index prisms induce less aberrations in the very-wide-field-of-view optimization, while for resolution optimized prisms, the aberrations are almost independent on the refractive index. These results corroborate the ones we had previously obtained by an homemade ray tracing method.

From the experimental point of view, first, we have shown that a resolution of a few μm could be achieved on field-of-views up to 20 mm^2 at a typical wavelength for biosensing (632 nm). Secondly, we have demonstrated that for resolution optimized prisms, the resolution perpendicular to the propagation direction slightly depends on the distance of the object with respect to the prism edge, while in the propagation direction, geometric aberrations are not the main limiting factor.

Resolutions limits: propagation length and light diffraction

By using the matrix formalism on a SPR chip undergoing the adsorption of a 1 nm-thick biolayer, we have proven that, contrary to what has been thought so far, the sensitivity of SPR biosensors

does not necessarily increase with respect to the wavelength. This approach has allowed us to determine the optimal wavelength of illumination ($\sim$750 nm) and metal thickness ($\sim$55 nm), showing that silver, and then gold, were the most sensitive metals, while aluminum and copper exhibits lower performances.

In the view of spatial resolution, we have also addressed the trade-off between propagation length and sensitivity, showing that once again silver slightly overpasses gold. We have thus analyzed the trade-off offered by an hybrid metal coating made of silver with an additional 5-nm-thick protecting and biocompatible layer of gold. Sensitivity can be calculated theoretically, but the propagation length of hybrid structures has to be experimentally determined.

Therefore, we have defined a rigorous method to measure the propagation length based on the fit of the experimental point-spread-function that takes into account the light diffraction and the surface plasmon scattering. We have then been able to demonstrate a good agreement between the theoretical predictions and the measurements for gold and silver, thereby emphasizing the importance to use the corrected propagation length equation which considers the metal thickness. The propagation lengths measured for the hybrid metal coating are very similar to the ones of silver, which suggests that the bi-metallic structure may exhibits a worst trade-off than a simple gold coating. By analyzing the PSF, we have also clarified a long standing issue of SPRi: the object light diffusion is restricted to a narrow cone which results in an effective diffraction-limited resolution that can be worst than the one offered by the imaging system. Here, we have measured a diffraction limit at 1.5 μm, which corresponds to the one given by an objective of numerical aperture equal to 0.26 ($\sim\times$10 objective in conventional microscopy).

Biological proofs-of-concept on individual micro-organisms

The ability to combined high resolution, wide field-of-view and good sensitivity, has been applied to the monitoring of cytokine secretions by individual T lymphocytes. Such project faces with many challenges in physics, biology and biochemistry. Herein, even if secretion signals have not been observed by SPR, we have paved the way to success by pointing out the critical issues that need to be addressed: strong surface attachment of the secreting cells, improvement of the signal-to-noise ratio of the SPR detection by pixel and frame averaging (pixel-shift camera sensor, varifocal lens), mechanical and thermal stabilization of the set-up, and novel surface chemistry and functionalization.

We have also demonstrated the ability to simultaneously observe few tens of adherent cells presenting sub-cellular details allowing the study of local adhesion properties. Finally, we have reported, at the best of our knowledge, the first observation of individual bacteria by SPRi. A novel approach based on spatial properties of SPR images that could improve the rapidity of bacterial detection is finally explored.

Technical achievements in SPR microscopy

At last but not least, this work has also led to a significant improvement on the design of prism-based SPR microscopes, as well as on their instrumentation and the required image processing when using the line-scan imaging mode.

A program coded in Mathematica has been developed to calculate and optimize the most important properties of prism-based SPR microscopy, such as the optimized apex angles of the prisms, the anamorphose, the geometric aberrations, the propagation length and the optimal metal thicknesses and wavelengths for sensitivity or resolution. It is also able to fit experimental plasmon curves and point-spread-functions.

A entirely new SPR microscope has been fabricated and automated in order to perform biological experiments over several hours. Its coupling with a conventional optical microscope has been made possible by designing a thermally regulated transparent and thin fluidic device. Its

thermal properties have been evaluated both experimentally and by finite-element simulations. Moreover, all the homemade mechanical components of the final set-up, as well as the structure necessary to integrate the prism SPR chip, have been designed by a CAD software, which allows fast and efficient future improvements. Furthermore, the optimal parameters that have guided our choice of camera sensor have been identified.

Finally, the image processing steps by the use of both ImageJ and homemade Mathematica programs have been validated and give fast and efficient results.

As the author of the manuscript, and main contributor to this work, I emphasize that a PhD thesis, despite its inherent individual aspect, is never a one man work, but rather a team project, especially for this one at the interface between physics and biology. Although, I have duly cited all my collaborators in the body of the manuscript, I should also mentioned Roberto Calemczuk and Loïc Leroy, my advisor and co-advisor, as they significantly contributed to the achievement of this research project, as well as all the biologists, chemists and physicists of our laboratory.

Perspectives

The fact that several fundamental and technical issues of prism-based SPR microscopy have been identified, and some of them solved, opens up new horizons in terms of applications, but also in terms of new issues to investigate!

optical design

Since for resolution optimized prisms, the remaining aberrations are restricted to spherical aberrations, they can be compensated using an aspheric lens or a compensation plate. Indeed, the correction of spherical aberrations benefits from the background of conventional optical microscopy. However, because they are proportional to the distance between the object and the prism edge, the optical correction will also have to adapt to the location on the observed area.

The creation of an imaging system corrected for the observation of very-wide-field-of-views in classic imaging mode is also a very interesting issue of optical design. In that case, the optical scheme does not have an axial symmetry, and aberrations vary with respect to the object position both in the X and Y axes.

Owing that the geometric aberrations are shared by all prism-based imaging techniques, it would be interesting to implement our results on SPR-like effects: Bloch surface waves, frustrated total internal reflection and resonant mirrors.

Lowering the resolution limits

The understanding that the diffraction limit is due to the poor light diffusion at a mirror-like interface suggests new illumination systems that could increase this diffusion while preserving the SPR sensitivity. Obviously, as the diffusion is increased, the critical distance at which spherical aberrations limit the resolution becomes smaller and smaller. Such improvement is therefore intrinsically coupled to the design of a corrected imaging system.

As for the propagation length, SPR surface passivation with graphene may be a route to make silver films biocompatible while not strongly degrading their resolution/sensitivity trade-off [138]. Although, many promising investigations are held on surface plasmon propagation in planar geometries made of metamaterials [157, 158], magneto-optics stacks [159, 160] or polarization controlled 2D structures [161]. The ability to control the effective optical properties of the guiding layer may enable to engineer an optimal plasmonic layer in the view of the best resolution/sensitivity trade-off.

Applications

The fact that prism-based SPR microscopy is getting closer to conventional optical microscopy in terms of resolution and field-of-view, but with a vertical resolution in the order of 100 nm can be used in a wide range of applications.

In the short term, this enables statistical studies on thousands of individual eukaryote and prokaryote cells, that can for instance target the dynamic of extracellular matrix adhesion,

internal variation of refractive index, secretory activities, division or motility. For bacterial detection, image analyses can be extended to higher levels of complexity, such as the 2D dispersion of intensity (instead of the 1D histogram), the analysis of the noise frequency, or even a particle counting detection, thereby directly quantifying the number of bacteria and micro-colonies. Since the resolution limit when imaging is also the resolution limit when focusing a light beam, resolution optimized prisms could be used to perform individual cell sorting by inducing a very localized photo-thermal effect [42].

At the medium term, the enhancement of both field-of-view and resolution is synonym to high throughput screening in biochemistry, which in that case is label-free and allows the determination of affinity constants.

Finally, in the long term, prism-based SPR microscopy could also be used in studies addressing the fundamental properties of surface plasmons and their interactions with plasmonic elements, such as couplers, interferometers or mirrors [162, 163].

A | Appendix

Contents

A.1 | Permittivities of metals

In this manuscript, all the calculations of plasmonic and optical properties of metals are performed using the literal expression for the permittivity given by Vial and Laroche in ref. [29] (2007) for gold, silver, aluminum and chromium, and given by Ren, Chen and Zhang in ref. [30] (2011) for copper. The authors derived the expression of $\epsilon_m(\omega)$ using a combination of the Drude and Critical Point (DCP) models:

$$\epsilon_m(\omega) = \epsilon_\infty - \frac{\omega_D^2}{\omega^2 + i\gamma\omega} + \sum_{p=1}^{N} G_p(\omega) \tag{A.1}$$

where

$$G_p(\omega) = A_p \Omega_p \left(\frac{e^{i\phi_p}}{\Omega_p - \omega - i\Gamma_p} + \frac{e^{-i\phi_p}}{\Omega_p + \omega + i\Gamma_p} \right)$$

parameter	unit	gold	silver	chromium	aluminum	copper
ϵ_∞		1.0300	3.7325	1.1297	1.0000	3.686
ω_D	rad/s	1.3064×10^{14}	1.3354×10^{16}	8.8128×10^{15}	2.0598×10^{16}	1.34×10^{16}
γ	rad/s	1.1274×10^{14}	9.6875×10^{13}	3.8828×10^{14}	2.2876×10^{14}	6.2831×10^{14}
A_1		0.86822	2.0297	33.086	5.2306	0.562
ϕ_1	rad	−0.60756	−0.70952	−0.25722	−0.51202	−8.185
Ω_1	rad/s	4.0812×10^{15}	4.5932×10^{17}	1.7398×10^{15}	2.2694×10^{15}	3.205×10^{15}
Γ_1	rad/s	7.3277×10^{14}	1.0524×10^{18}	1.6329×10^{15}	3.2867×10^{14}	0.404×10^{15}
A_2		1.3700	−2.8925	1.6592	5.2704	27.36
ϕ_2	rad	−0.087341	−1.4459	0.83533	0.42503	0.226
Ω_2	rad/s	6.4269×10^{15}	4.7711×10^{16}	3.7925×10^{15}	2.4668×10^{15}	3.43×10^{15}
Γ_2	rad/s	6.7371×10^{14}	3.0719×10^{15}	7.3567×10^{14}	1.7731×10^{15}	0.77×10^{16}
A_3		-	-	-	-	0.242
ϕ_3	rad	-	-	-	-	−0.516
Ω_3	rad/s	-	-	-	-	7.33×10^{15}
Γ_3	rad/s	-	-	-	-	1.12×10^{15}

Table A.1: Optimized parameters of the Drude-CP model. For gold, silver, chromium and aluminum: Reproduced from [29] by permission of IOP Publishing. All rights reserved.

In order to express $\epsilon_m(\lambda)$, ω is replaced by $\frac{2\pi c}{\lambda}$, where c is the speed of light in vacuum: c = 299,792,458 m/s. These parameters are valid over the 400 – 1,000 nm wavelength range.

The real and imaginary parts of the resultant permittivities are plotted in **Figure A.1**. For the sake of clarity, we plotted -Re$\{\epsilon_m(\lambda)\}$. Note that the real part is always negative, and thus satisfies the plasmon condition.

For copper, other literal expressions of the permittivity are given by Rakic *et al.* in ref. [164] (1998). The authors derived the expression of $\epsilon_m(\omega)$ by using the Brendel-Bormann (BB) model and the Lorentz-Drude (LD) model. In the article "Spatial resolution in prism-based surface plasmon resonance microscopy" [131], we have used the BB model because at this time we did not know the existence of a DCP model for copper. In the present manuscript we use the DCP model for copper, apparently more accurate than the BB model in the 400-1,000 nm wavelength range according to the authors. As a consequence, the sensitivity curves are significantly different from our article. This emphasizes that these simulations are very dependent on the permittivity model used for the metal. The permittivity of copper by the three models is plotted in **Figure A.2**. Note that for the BB model, ϵ'_m undergone a change of sign at 0.4 eV while it remains positive in the original article (as it should be, based on the well-known LD model).

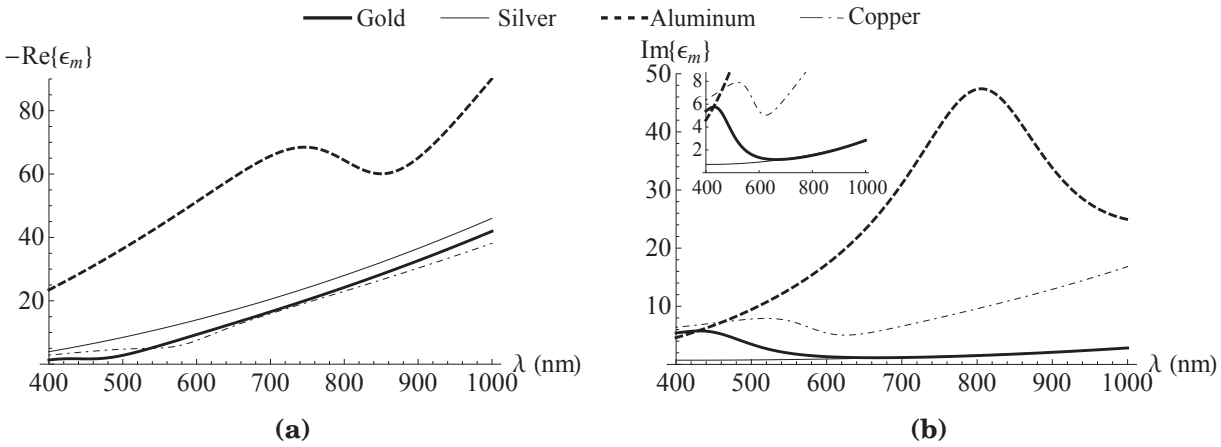

Figure A.1: Complexe permittivities of gold, silver, aluminum and copper: $\epsilon_m = \epsilon'_m + i\,\epsilon''_m$.

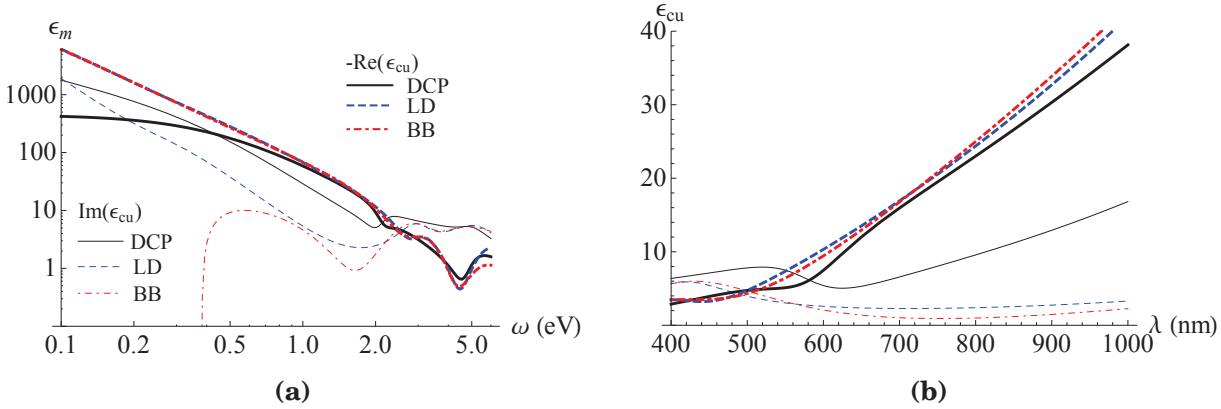

Figure A.2: Complexe permittivities of copper. **(a)** ϵ_{Cu} as a function of the energy of the excitation light in electron Volt (eV). Note that the DCP model has been established only in the 1.24 - 6 eV range ($\Leftrightarrow$ 1,000 - 200 nm wavelength range). **(b)** ϵ_{Cu} as a function of the wavelength of excitation.

A.2 | Refractive index of glasses and water

In 1871, Sellmeier demonstrated that the refractive index of glasses could be described by the following equation [165]:

$$n(\lambda) = \sqrt{1 + \sum_{j=1}^{N} \frac{B_j \lambda^2}{\lambda^2 - C_j}} \tag{A.2}$$

For typical glasses in the visible range, N = 3 and the coefficients B_j and C_j can be found in the datasheets given by the provider, Schott Glaswerke AG in our case. **Table A.2** gives the Sellmeier coefficients for N-BK7, SF11 and N-SF66 glasses valid over the 250 - 2,320 nm wavelength range, and **Figure A.3** depicts the resultant refractive index over the visible spectrum.

glass	B_1	B_2	B_3	C_1	C_2	C_3
N-BK7	1.03961212	0.231792344	1.01046945	0.00600069867	0.0200179144	103.560653
SF11	1.73848403	0.311168974	1.17490871	0.0136068604	0.0615960463	121.922711
N-SF66	2.0245976	0.470187196	2.59970433	0.0147053225	0.0692998276	161.817601

Table A.2: Sellmeier coefficient for N-BK7, SF11 and N-SF66 glasses.

For the refractive index of pure water, we use the literal expression with respect to the wavelength, salinity and temperature obtained by Quan and fry [166], and derived for pure water over the 200 - 1,100 nm wavelength range by Huibers [167]:

$$n_{water}(T, \lambda) = n_0 + n_4 T^2 + \frac{n_5 + n_7 T}{\lambda} + \frac{n_8}{\lambda^2} + \frac{n_9}{\lambda^3} \tag{A.3}$$

where $n_0 = 1.31405$, $n_4 = -2.02 \times 10^{-6}$, $n_5 = 15.868$, $n_7 = -0.00423$, $n_8 = -4382$, $n_9 = 1.1455 \times 10^6$.

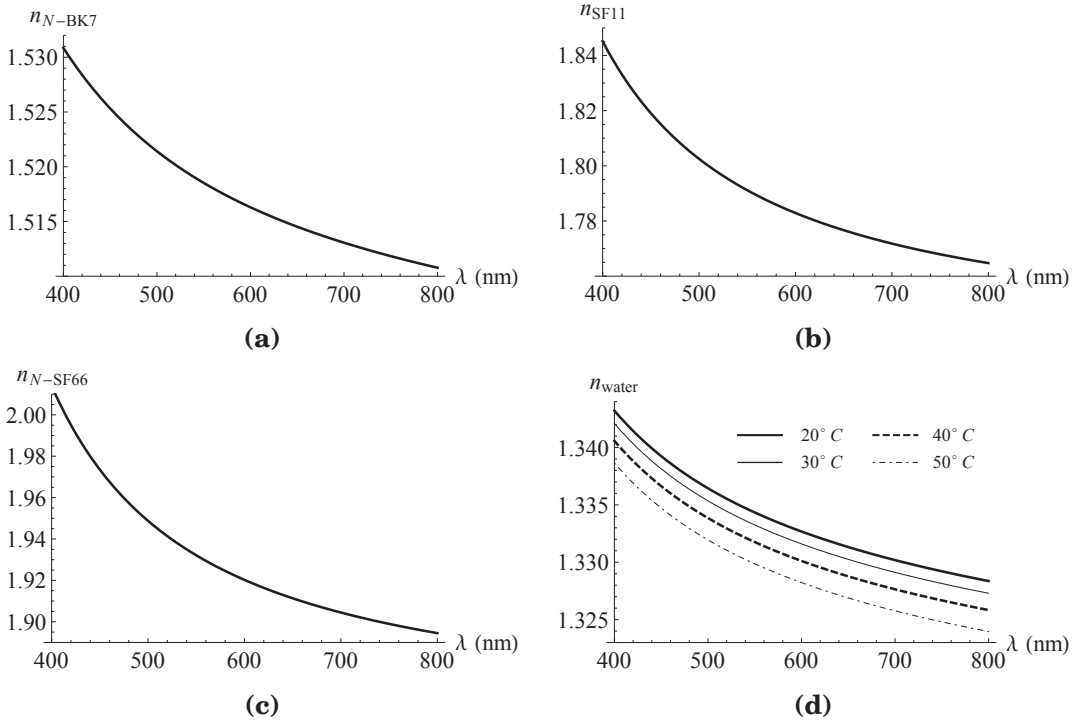

Figure A.3: Refractive index of three typical glasses covering the range 1.5 to 2 RIU and pure water at different temperatures. **(a)** $n_{N-BK7}(\lambda)$. **(b)** $n_{SF11}(\lambda)$. **(c)** $n_{N-SF66}(\lambda)$. **(d)** $n_{water}(\lambda)$

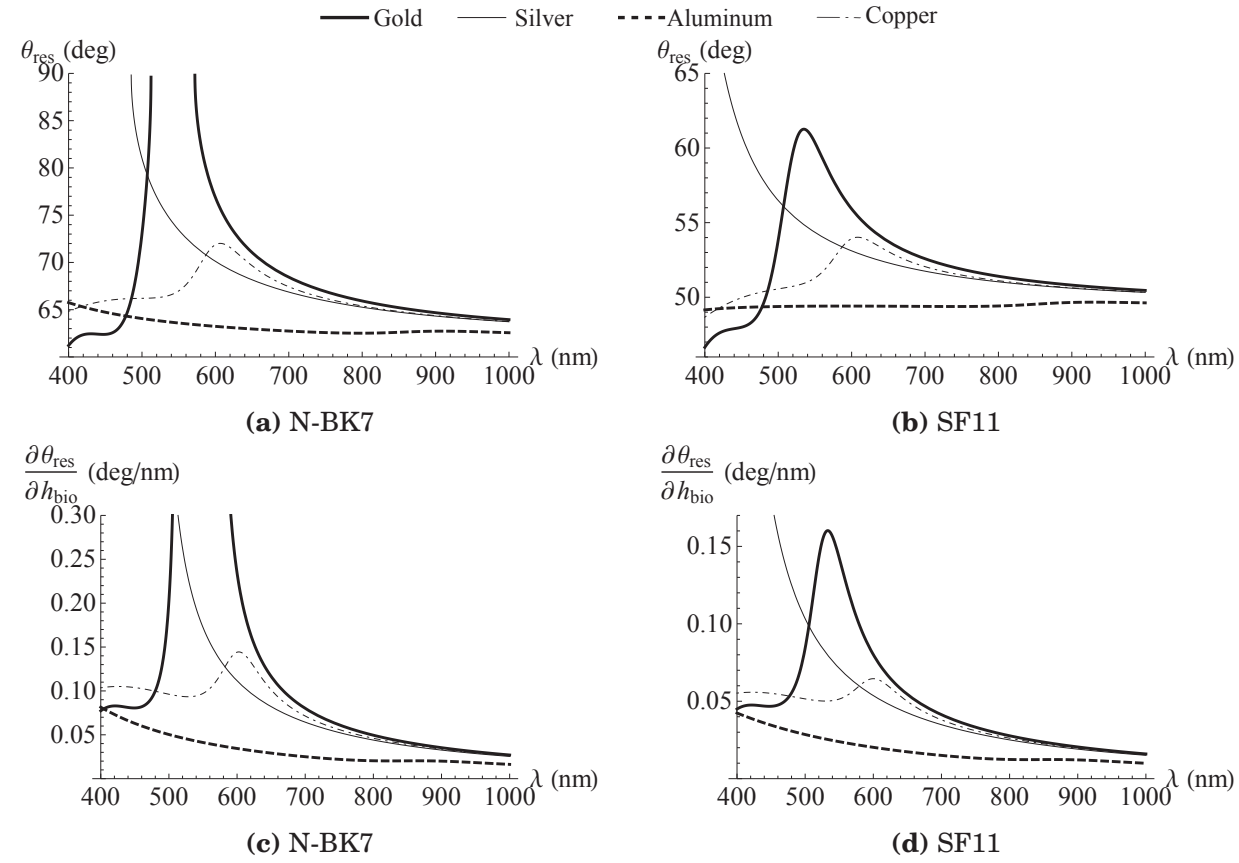

Figure A.4: Resonant angle as a function of λ and its variation with respect to h_{bio} in water for N-BK7 and SF11 glasses.

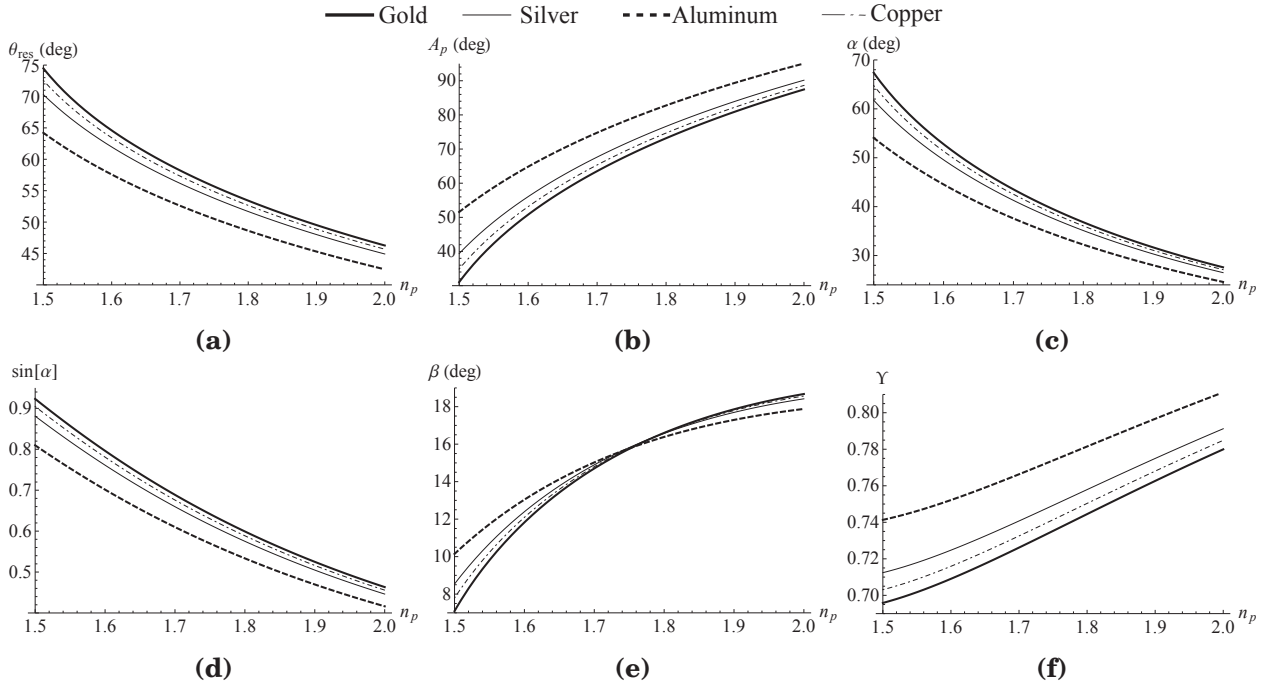

Figure A.5: Main optical parameters of resolution optimized prisms at the metal/water interface as a function of n_p at λ = 632 nm.

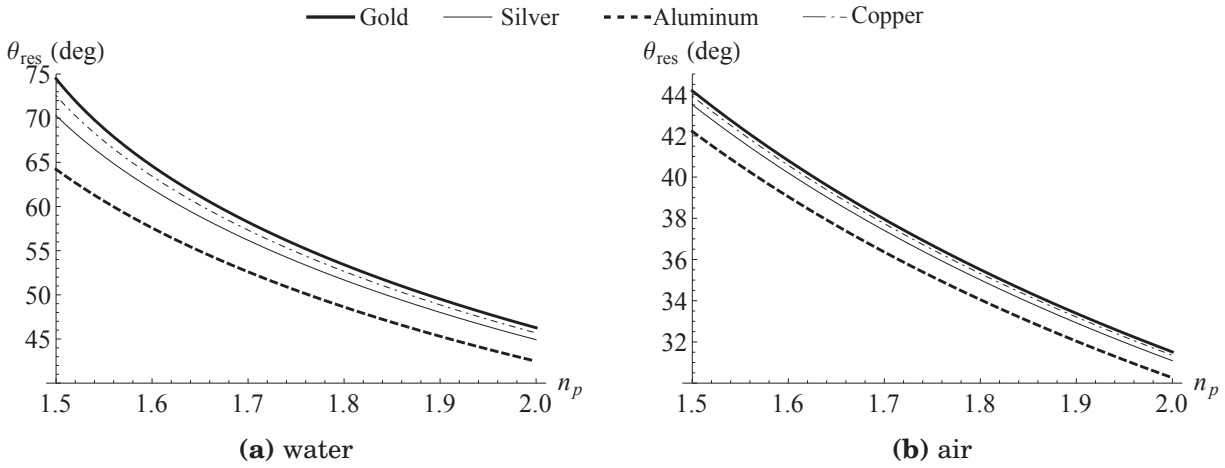

Figure A.6: Resonant angle as a function of n_p at λ = 632 nm.

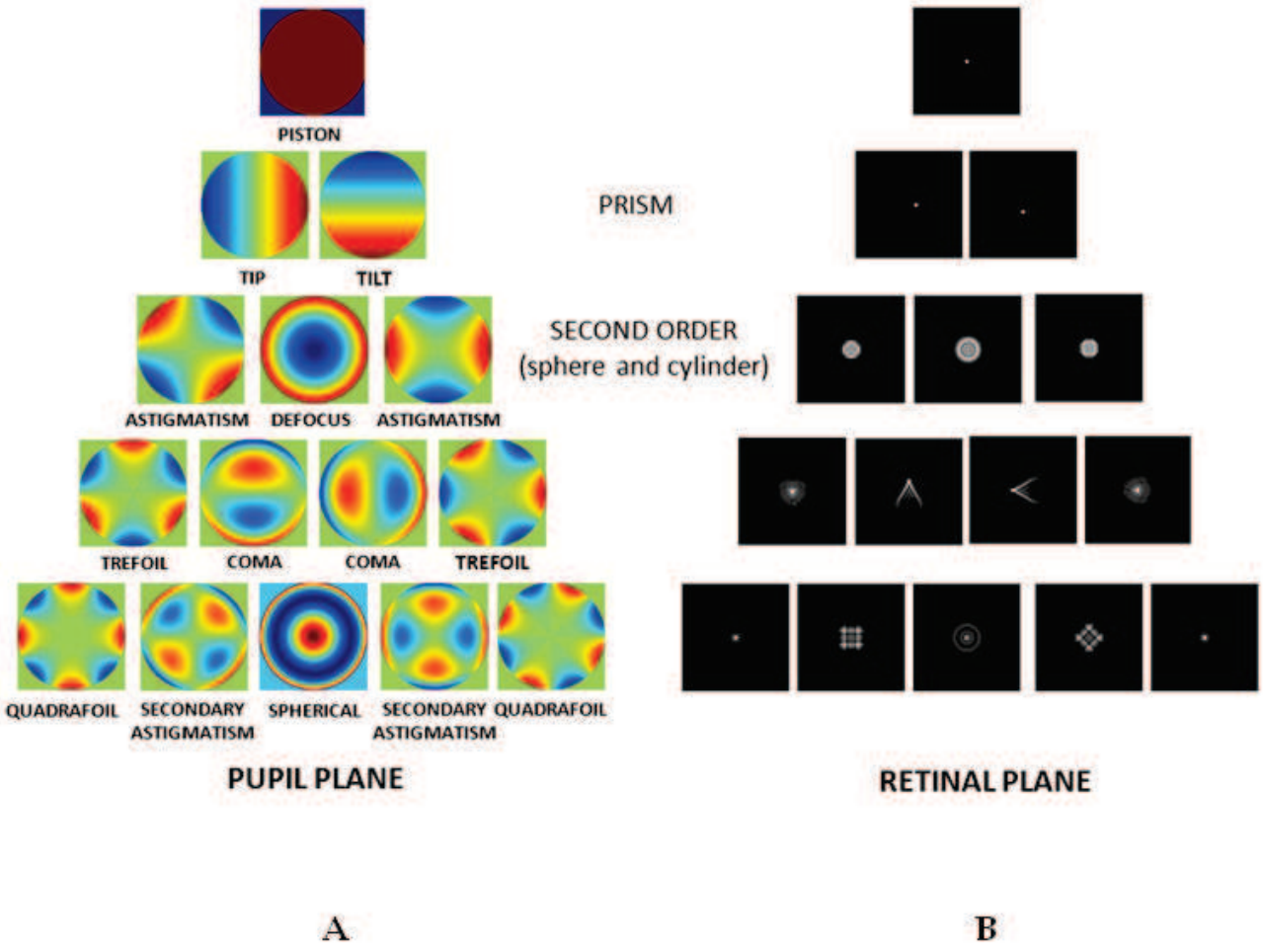

Figure A.7: Aberrations function at the exit pupil plane (A) and aberrated PSF (B) from ref. [168]. In our case, the retinal plane corresponds to the camera sensor plane.

A.3 | Aberrations calculation by the standard deviation method

In this section, we compare the estimation of geometrical aberrations by the wave aberration (Φ) model and by an homemade ray tracing model coded in Mathematica, that has been used in the article "Spatial resolution in prism-based surface plasmon resonance microscopy" [131]. This program measures the spreading of the virtual spot O' within the virtual image plane $\sigma_{//}$ (transverse aberrations) and its perpendicular σ_Γ (longitudinal aberrations). As for the wave aberration model, our model has the benefit to only consider the prism characteristics, while being simple and fast to code. But it also presents the same divergence at low refractive index and low apex angles for high angular diffusion $\Delta\theta_{int}$. Therefore, only $\Delta\theta_{int}$ that corresponds to an effective NA which leads to a spatial resolution by the Rayleigh criterion of Δx = 3 µm at λ = 632 nm is presented (4.8°, 4.1° and 3.8° for N-BK7, SF11 and N-SF66 prisms, respectively). The

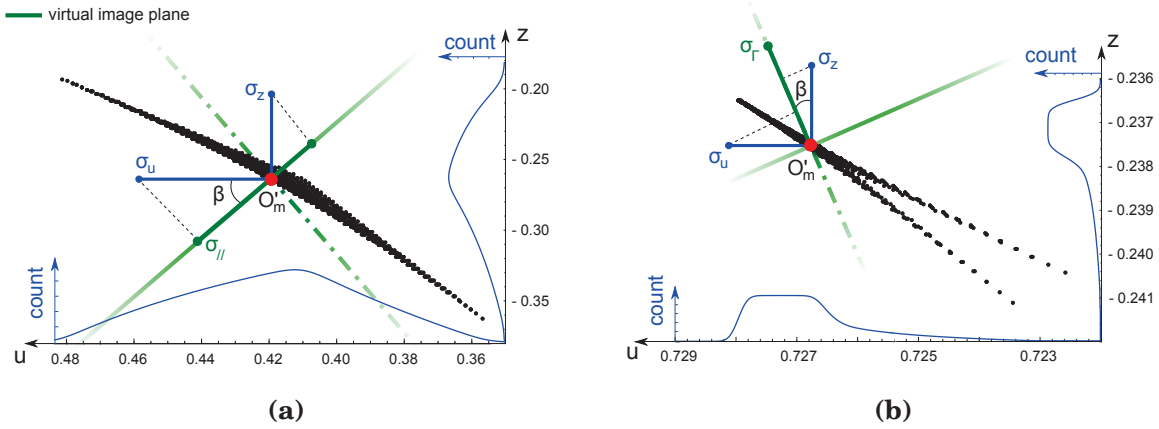

(a) **(b)**

Figure A.8: Geometrical aberrations estimation in prism-based imaging (d = 1). **(a)** calculation on a VWFOV optimized prism (Horiba prism, SF11, n_p = 1.78 at λ = 632 nm, A_p = 32°). The O' points are in black and the virtual image plane and its perpendicular are in green. For each axis, the spreading of O' points is represented by a smooth histogram (in blue) which simulates the situation where the number of points tends to infinity. The corresponding standard deviations σ_u and σ_z, as well as their projection on the virtual image plane and its perpendicular, are represented from the mean virtual point. **(b)** Same calculation on a resolution optimized prism (N-SF66, n_p = 1.91 at λ = 632 nm, A_p = 82°) and projection on the perpendicular to the virtual image plane. Note that O'_m is approximately half the way between the intersection point of secondary rays of $\Delta\theta_{int} \to 0°$ and $\Delta\theta_{int} = 4.1°$

spot corresponds to the virtual points O', which number is equal to the combination of 2 among N rays : $C_N^2 = \frac{N!}{2!\times(N-2)!}$. However, in the previous equations established for VWFOV and resolution optimized prisms, only two rays were considered to determine the coordinate of O', and thus the location of the virtual image plane. Moreover, in both cases, the calculi were done for $\Delta\theta_{int} \to 0°$. Here, several rays need to be taking into account, with obviously $\Delta\theta_{int} \neq 0°$. Therefore, the virtual image plane location has to be redefined. In this simulations, all the rays have the same weight. Then, it seems coherent to define a mean virtual point O'_m, which coordinates are the mean values of $u_{o'}$ and $z_{o'}$, whereby passes the virtual image plane.

The O' points distribution has a standard deviation in the U and Z axis: σ_u and σ_z respectively, which projection onto the virtual image plane and its perpendicular is given by $\sigma_{//} = \cos(\beta) \times \sigma_u + \sin(\beta) \times \sigma_z$ and $\sigma_\Gamma = \sin(\beta) \times \sigma_u + \cos(\beta) \times \sigma_z$ respectively, as depicted in **Figure A.8**. Note that, unlike a vector, a standard deviation has no direction, so their projections can only be added. The plane perpendicular to the external principal ray could also have been taken as reference for the projection. In that case, β has to be replaced by θ_{ext} and $\sigma_{//}$ describes the standard deviation within a plane perpendicular to the principal ray, while σ_Γ states for the standard deviation on the principal ray. This second convention seems more appropriated for

line-scan imaging mode, while the first one is more pertinent for classic imaging mode. However, both lead to nearly the same results (**Figure A.11**) so only the first one will be used hereafter.

Herein, we consider 41 equally angular spaced rays ($\rightarrow$ 820 points) within an angular diffusion of +/- $\Delta\theta_{int}$. The dimension of $\sigma_{//}$ and σ_{Γ} is a length which is proportional to d. Hence, they can be express relatively to d. It must be emphasized that these two quantities, especially $\sigma_{//}$, are not the resolution limit in itself, but rather parameters to whom it is supposed to be proportional in a first approximation, just as for the wave aberration model.

A.3.1 | Aberrations with respect to the apex angle

In order to estimate the aberrations with respect to the apex angle, we normalize the standard deviations by their minimal values to express $\sigma_{r//}$ and $\sigma_{r\Gamma}$. The results shown in **Figure A.9** for N-BK7, SF11 and N-SF66 prisms are very close to the ones obtained by the wave aberration model, reinforcing the relevance of this novel approach. As expected, both $\sigma_{//}$ and σ_{Γ} increase as A_p digresses from its optimal value for resolution to its optimal value for VWFOV, where α = 0°.

The standard deviation method also shows that the optimized apex angle for resolution is not confined into a narrow range, and can easily tolerates an error of +/- 3°. Consequently, resolution optimized prisms can accommodate all of the four metals, for whom θ_{res} and θ_w only range on a few degrees, especially at longer wavelength and at high n_p (**Figure 1.6**).

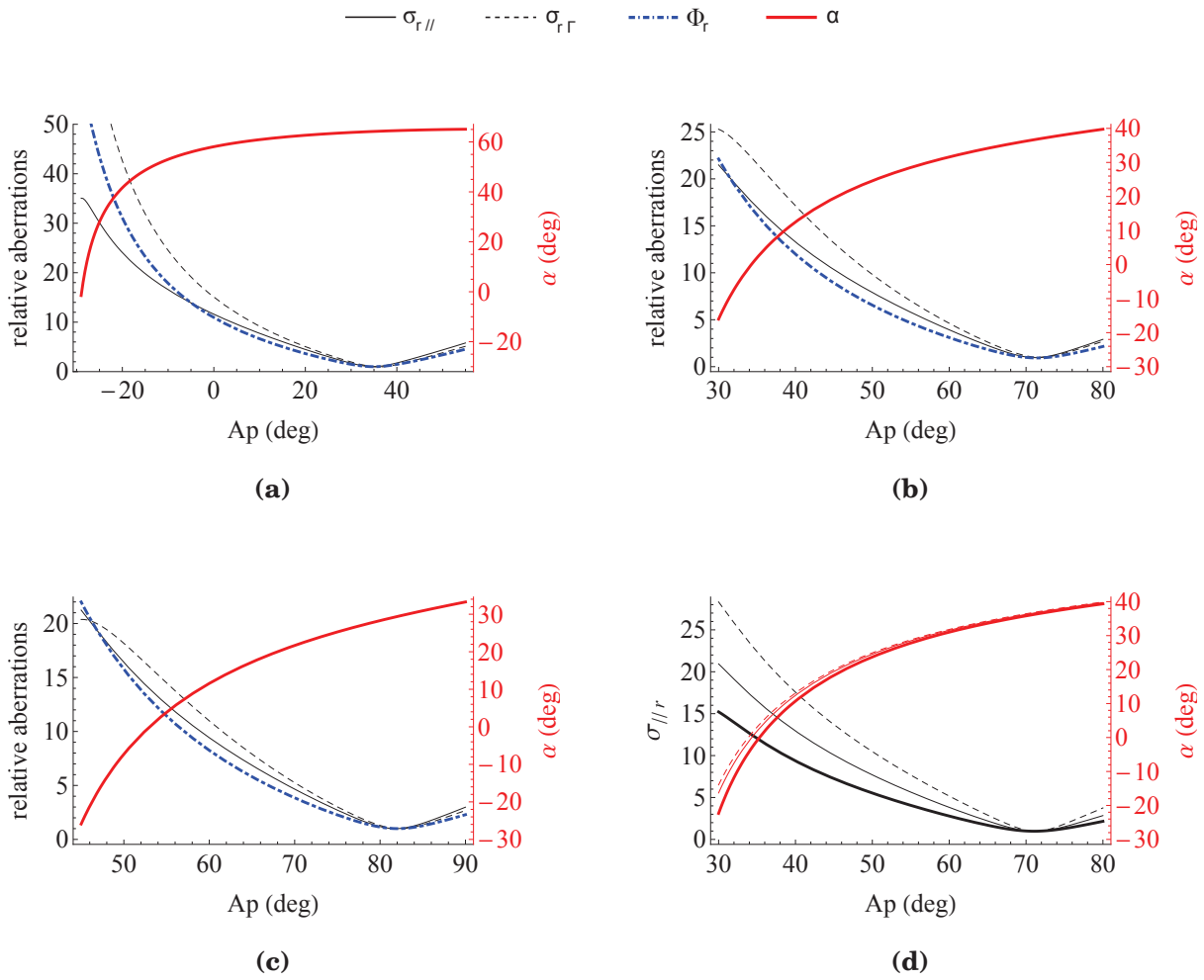

Figure A.9: Geometrical aberrations as a function of A_p. **(a)** N-BK7 prisms. **(b)** SF11 prisms. **(c)** N-SF66 prisms. **(d)** $\sigma_{r//}$ and α in SF11 prisms for $\Delta\theta_{int}$ = 10° (thick line), 7° (thin line), and 5° (thin dashed line).

A.3.2 | Aberrations with respect to the refractive index

Figure A.10 addresses the issue of optimal n_p. For VWFOV optimized prisms, increasing the refractive index from 1.5 to 2.0 leads to an improvement of a factor 3, while for resolution optimized prisms the decrease of $\sigma_{//}$ is less than ~25% regardless of $\Delta\theta_{int}$ (data not shown). Obviously, the second convention shows the same results for the VWFOV configuration since it is equal to the first one in that particular case. However, it inverses the tendency of $\sigma_{//}$ which increases by ~25% (**Figure A.11**). As a conclusion, using high refractive index prism could significantly improve the spatial resolution of VWFOW optimized prisms, but has low effect on resolution optimized prisms. In comparison with the wave aberration Φ, the standard deviation method shows a smaller decrease of aberrations for VWFOV optimized prism as n_p increases, especially at low n_p. For resolution optimized prisms, both models also slightly differ since Φ remains constant while both $\sigma_{//}$ and σ_{Γ} change by ~25 % over the n_p range. Nonetheless, these two different approaches lead to the same conclusions.

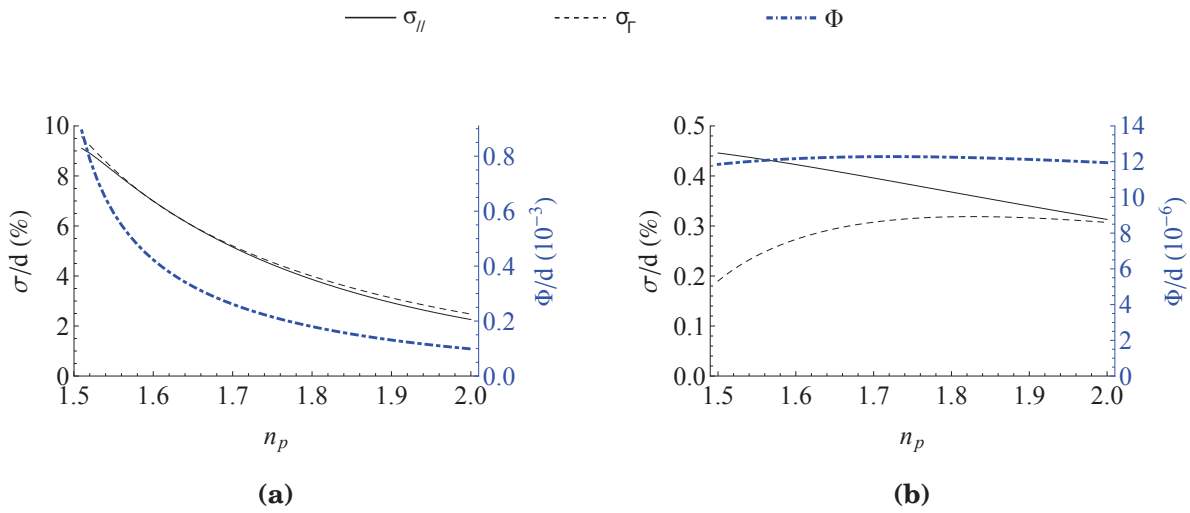

Figure A.10: Geometrical aberrations as a function of n_p for VWFOV and resolution optimized prisms. **(a)** VWFOV optimized prisms. **(b)** Resolution optimized prisms.

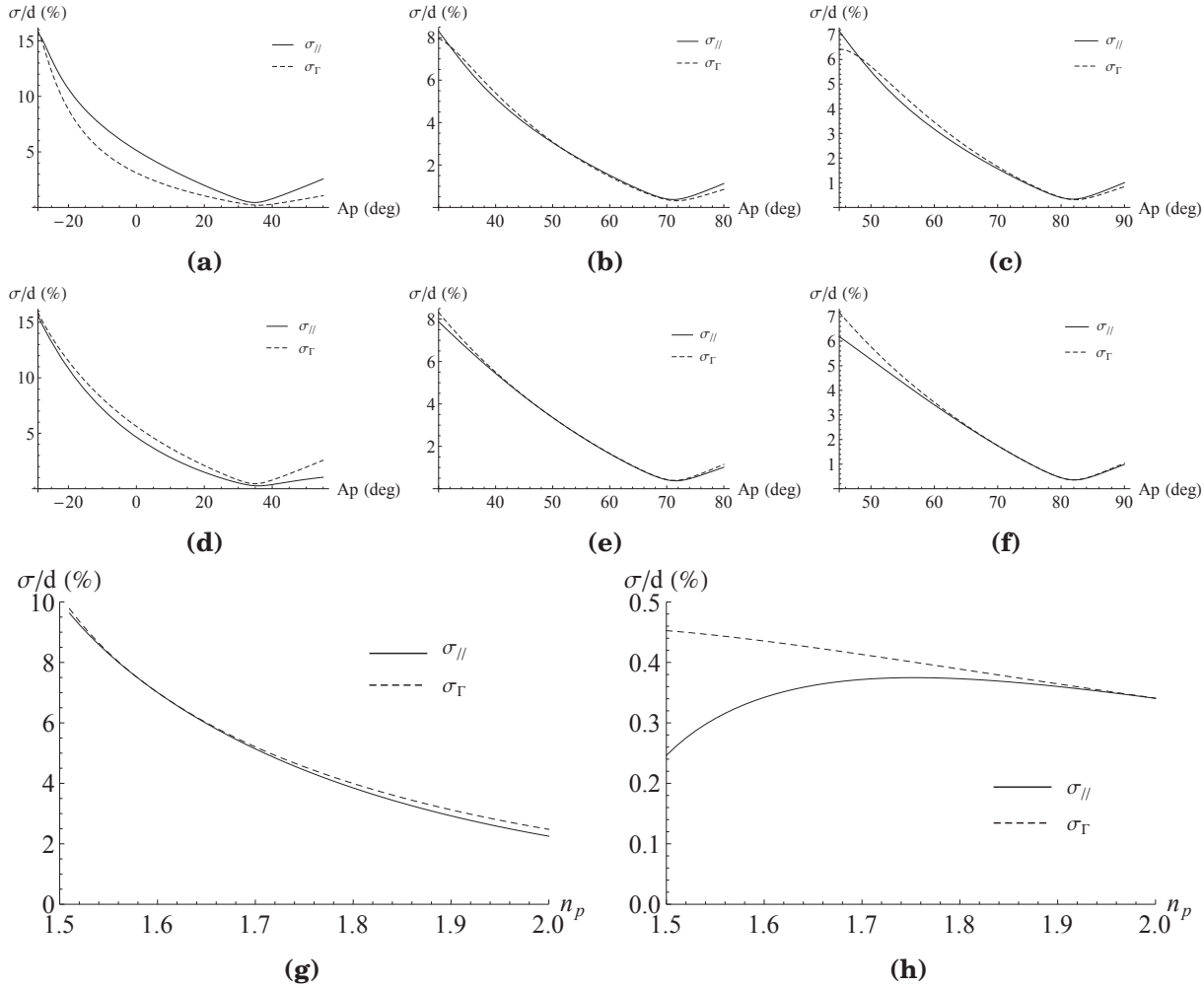

Figure A.11: Comparison between the convention of the virtual image plane and the perpendicular to the principal ray as reference in the estimation of geometrical aberrations. Aberration estimation as a function of A_p for N-BK7 **(a & d)**, SF11 **(b & e)** and N-SF66 prisms **(c & f)** for the two convention, respectively. Geometrical aberrations as a function of n_p for VWFOV optimized prisms **(g)** and resolution prisms **(h)** in the second convention.

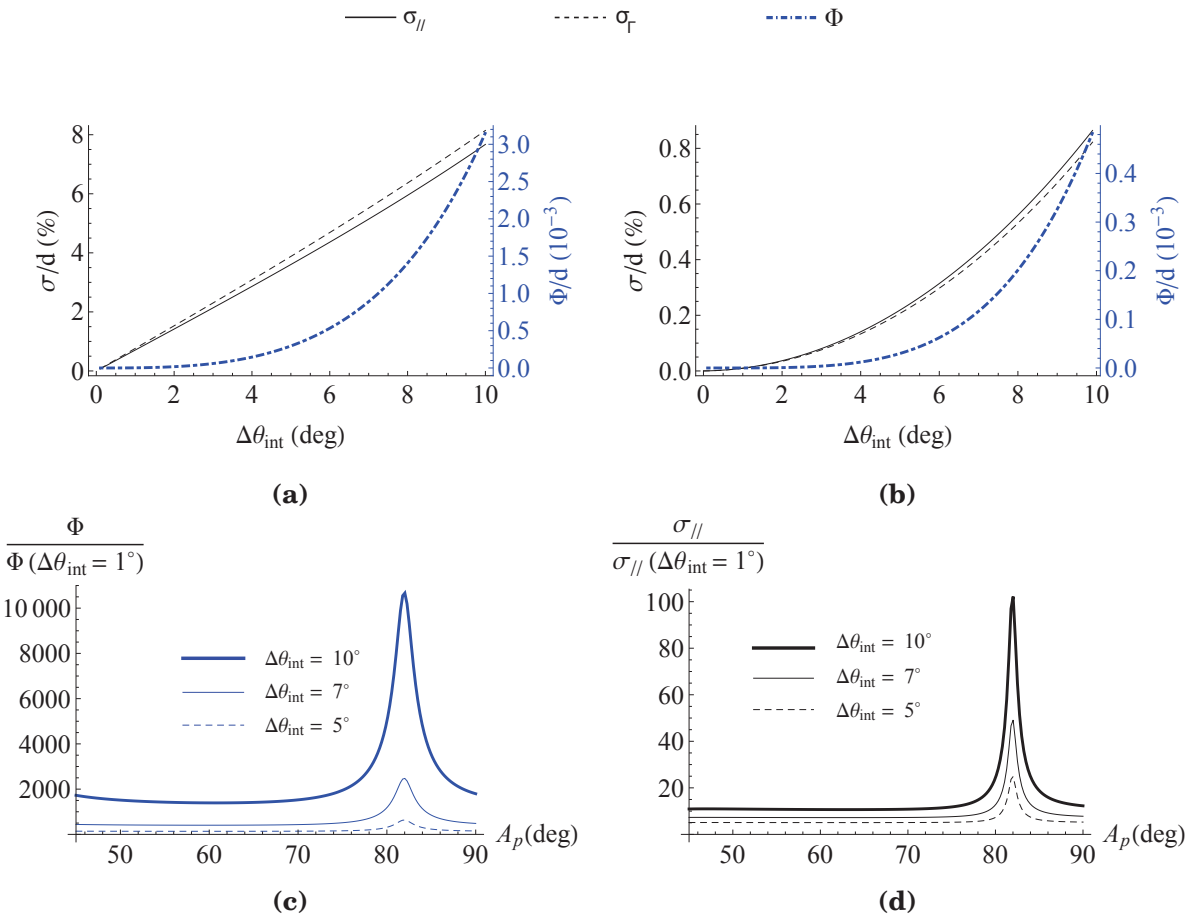

Figure A.12: Dependency of aberrations estimation on $\Delta\theta_{int}$. **(a)** VWFOV optimized N-SF66 prisms. **(b)** Resolution optimized N-SF66 prisms. **(c)** Ratio of Φ as a function of A_p for N-SF66 prisms. **(d)** Ratio of $\sigma_{//}$ as a function of A_p for N-SF66 prisms.

A.4 | Longitudinal and transverse spherical aberrations

The longitudinal and transverse spherical aberrations, LSA and TSA respectively, can be calculated for a given ray, as depicted in **Figure A.13b**.

$$LSA = O'_{lim}O' = OF \times \left[\frac{1}{n_p} - \frac{\tan(\Delta\theta_{int})}{\tan(\Delta\theta_{ext})}\right] \tag{A.4}$$

where O'_{lim} is the virtual image point for $\Delta\theta_{int} \to 0°$.

$$TSA = LSA \times \tan(\Delta\theta_{ext}) \tag{A.5}$$

with $\Delta\theta_{ext} = \arcsin[n_p \times \sin(\Delta\theta_{int})]$.

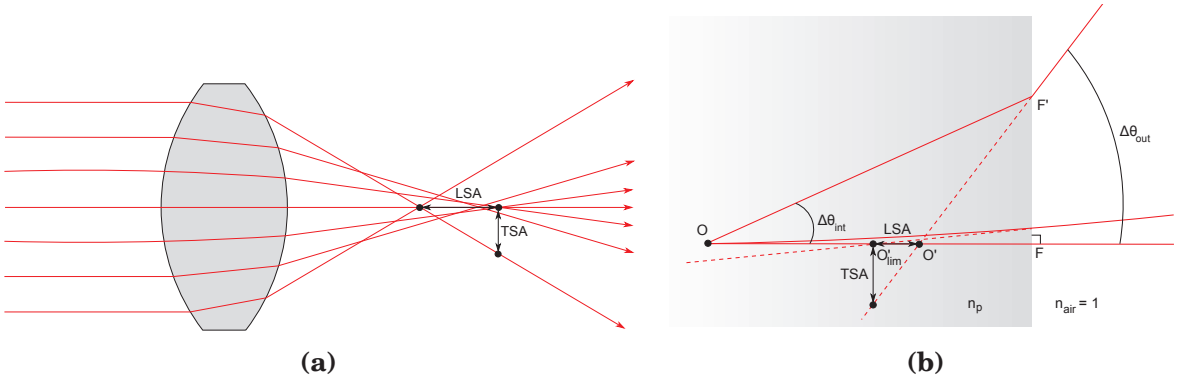

Figure A.13: Longitudinal and transverse spherical aberrations in a lens **(a)** and for a plane diopter **(b)**

A.5 | Optimisation process

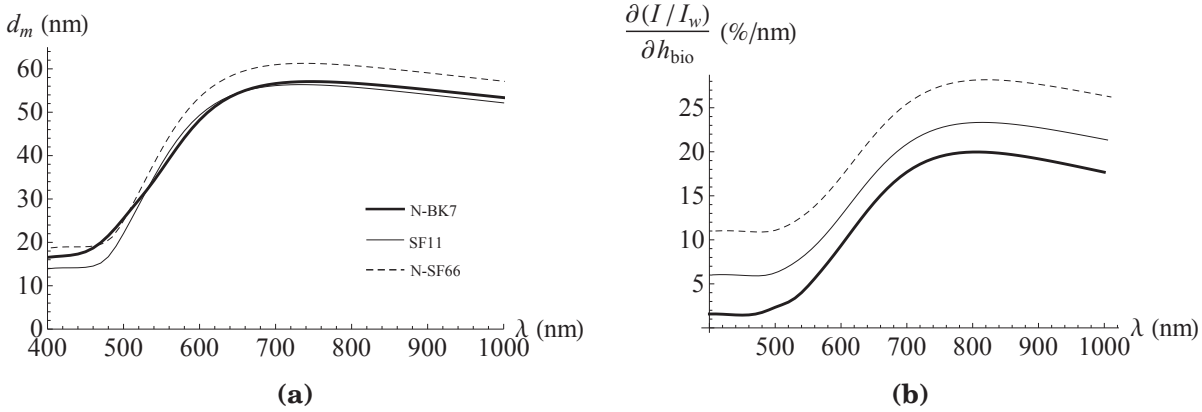

Figure A.14: Sensitivity comparison between different refractive index prisms for a gold/water interface. **(a)** Optimal gold thickness. The curve of N-SF66 is shifted by +5 nm for the sake of clarity, otherwise it is superimposed with the one of SF11. **(b)** Sensitivity in intensity. The curves of SF11 and N-SF66 are shifted by +5 and +10 % respectively for the sake of clarity, otherwise all the curves are superimposed.

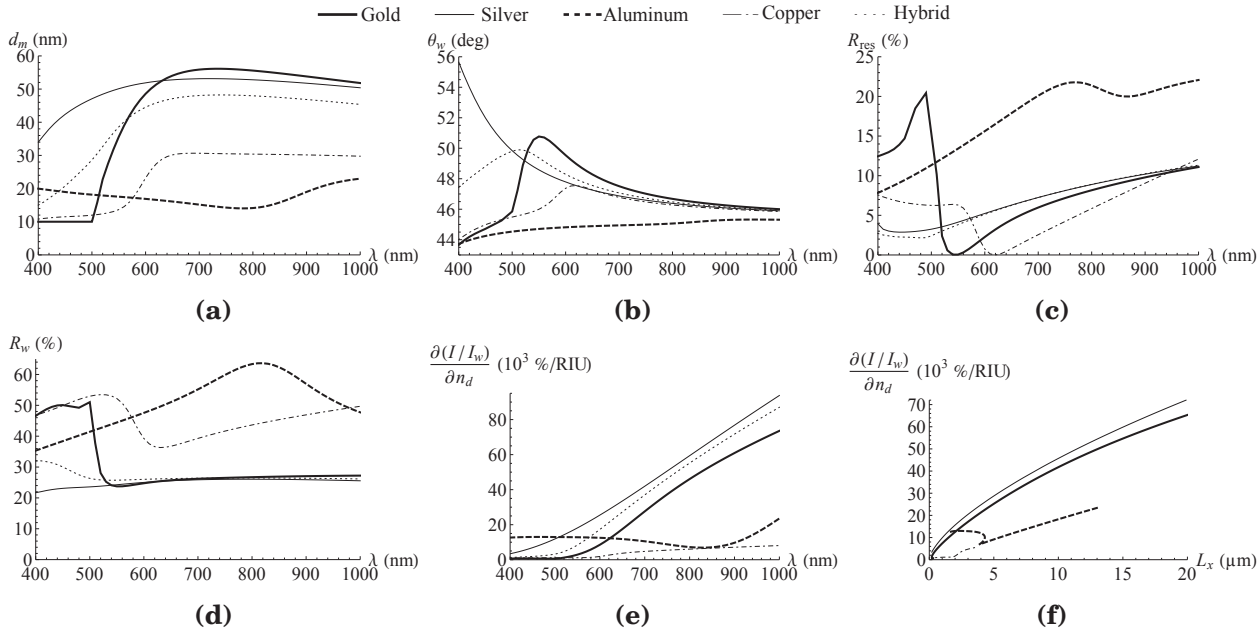

Figure A.15: Optimized sensitivities and trade-off in the dielectric refractive index shift convention. Note the similarity of sensibility with L_x (**Figure 1.4**) which explains the linearity of the trade-off curves.

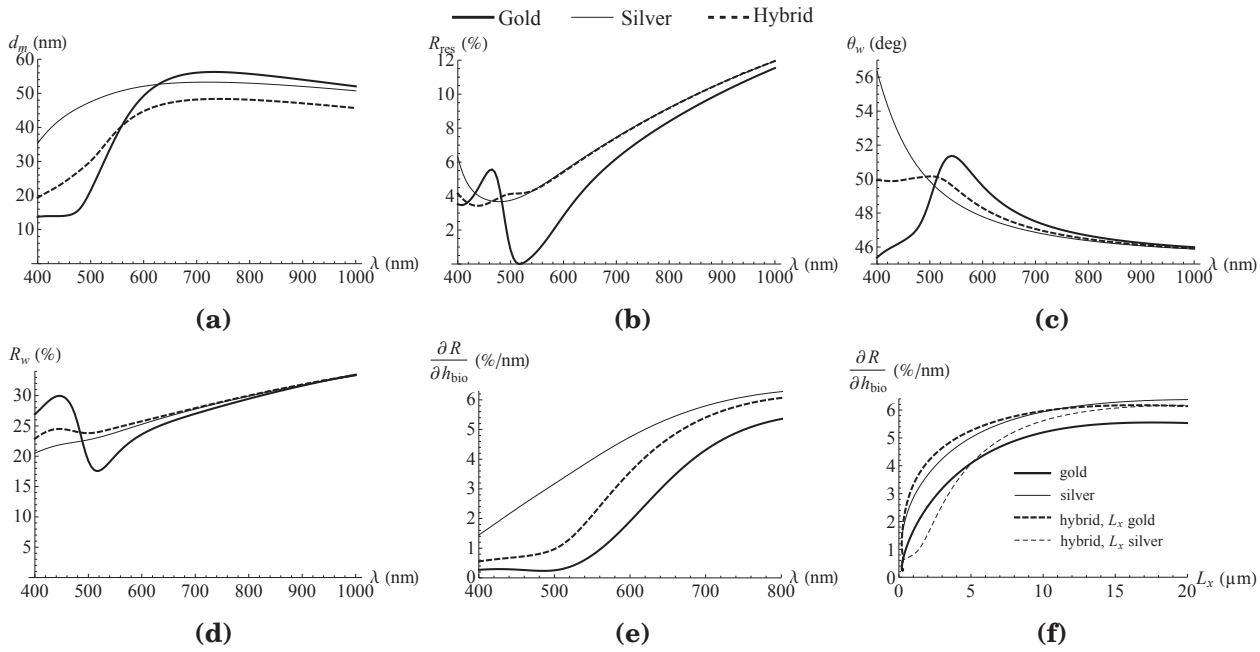

Figure A.16: Optimal metal thickness for sensitivity for a hybrid silver/5-nm-gold metal layer. **(a)** Optimal metal thickness d_m. **(b)** Reflectivity at θ_{res}. **(c)** Working angle. **(d)** Reflectivity at θ_w. **(e)** sensitivity in reflectivity. **(f)** trade-off between sensitivity and propagation length.

A.6 | Schematic view of the complete experimental set-up

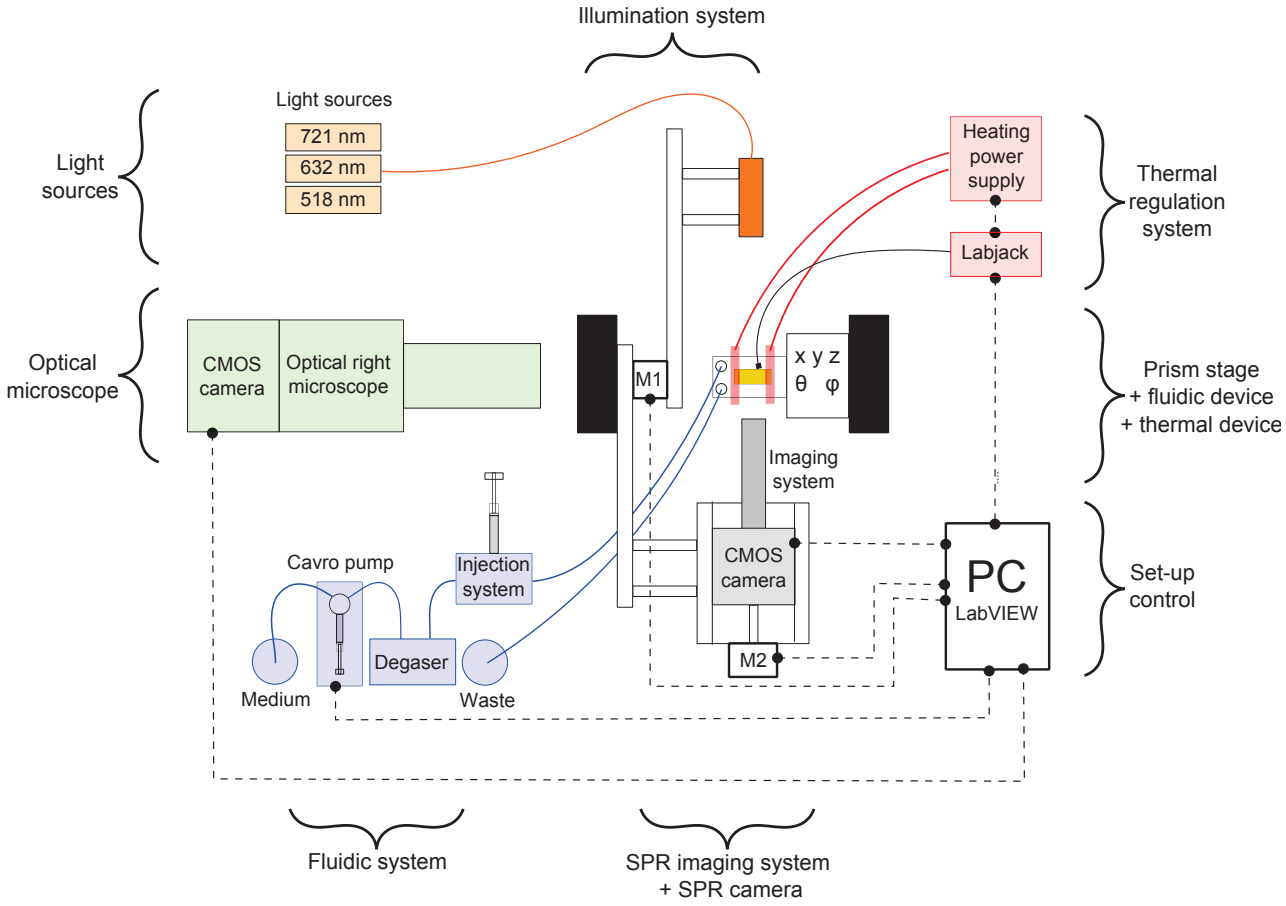

Figure A.17: Schematic view of the complete experimental set-up.

A.7 | Resolution parameters parallel to the SP

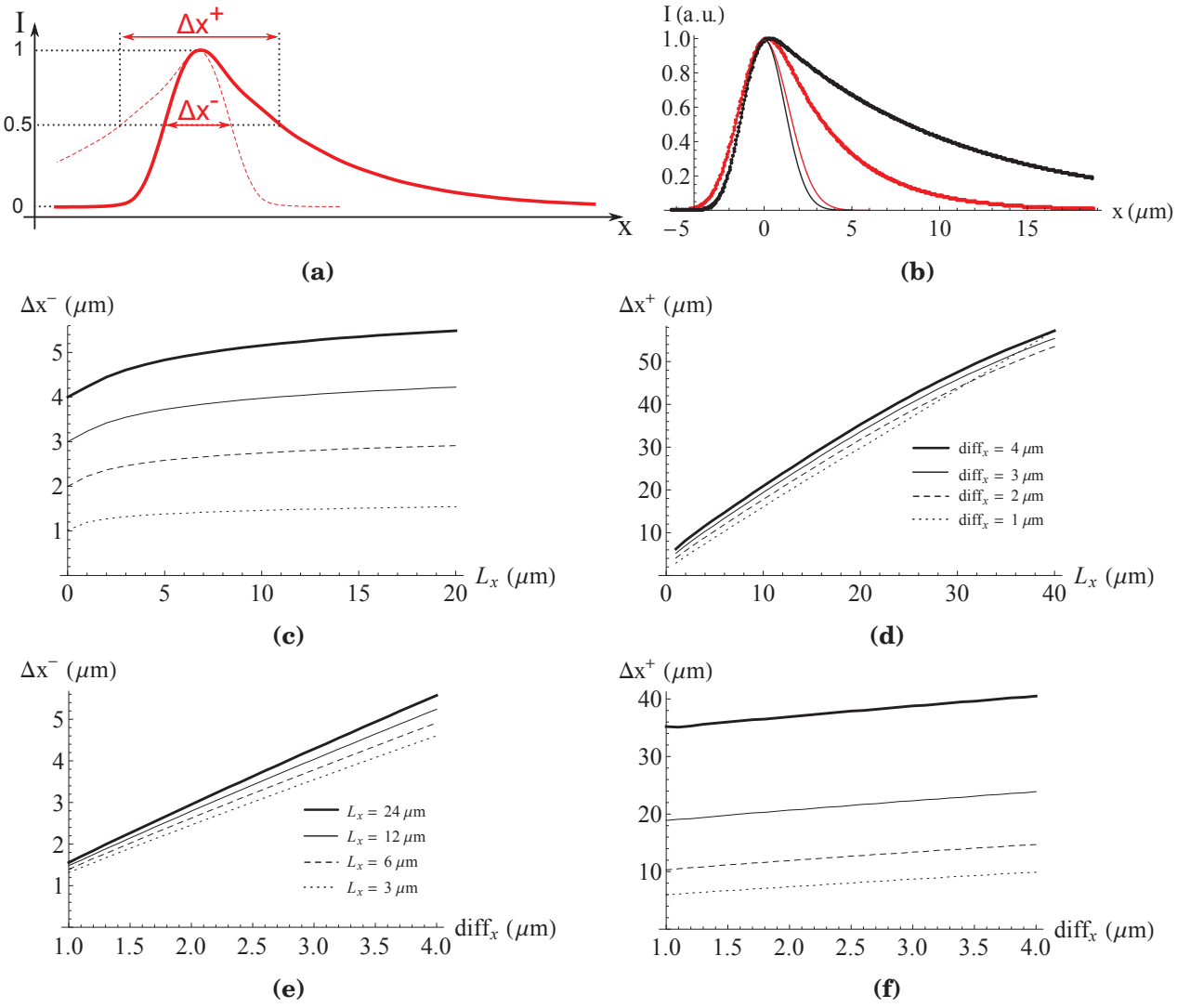

Figure A.18: Δx^- and Δx^+ as a function of L_x and $diff_x$. **(a)** Illustration of Δx^- and Δx^+ on the PSF. **(b)** Exemple of determination of Δx^- by a Gaussian fit of the left part of the theoretical PSF parallel to the SP at λ = 632 (red) and 721 nm (black). The value of $diff_x$ and L_x are the ones from the free fits of **Section 4.2.3**. **(c)** Δx^- as a function of L_x for different $diff_x$. **(d)** Δx^+ as a function of L_x for different $diff_x$. **(e)** Δx^- as a function of $diff_x$ for different L_x. **(f)** Δx^+ as a function of $diff_x$ for different L_x.

A.8 | Bookmark

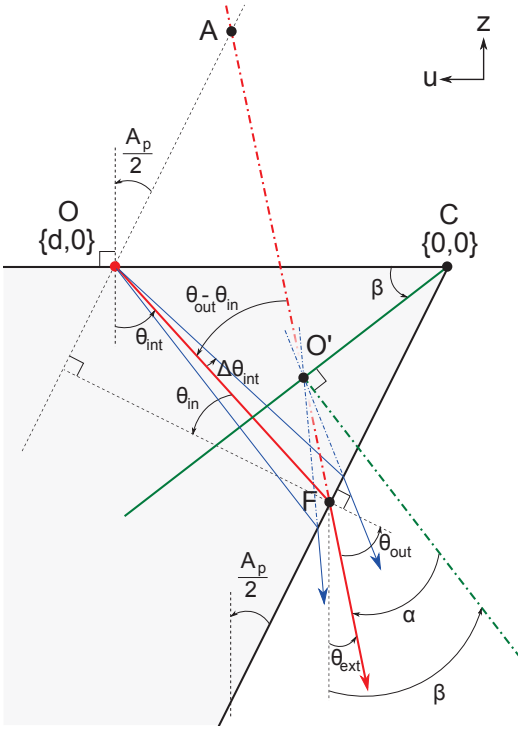

General optical scheme in prism-based imaging.

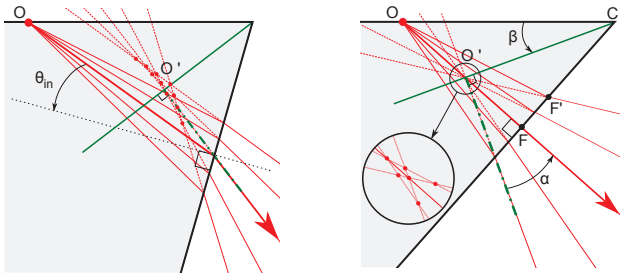

(a) VWFOV prism **(b)** resolution prism

Illustration of geometric aberrations.

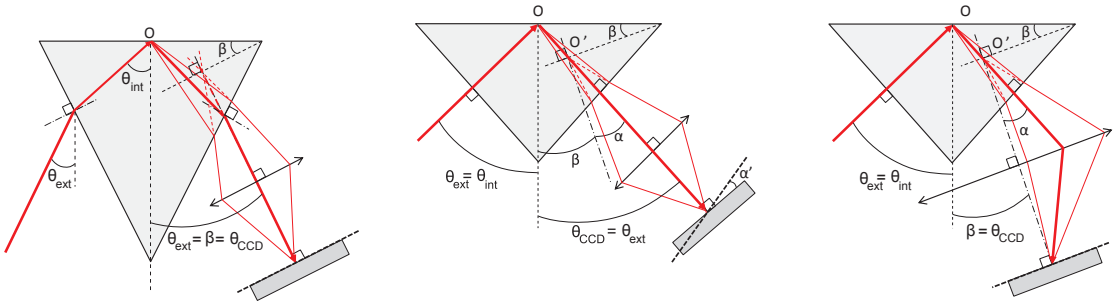

(a) VWFOV **(b)** line-scan **(c)** classic

Optimized prism-based SPRi configurations.

Bibliography

[1] R. W. WOOD, "On a remarkable case of uneven distribution of light in a diffraction grating spectrum", *Proceedings of the Physical Society of London*, vol. 18, no. 1, p. 269, 1902. (cited on pages 1 and 7)

[2] R. H. RITCHIE, "Plasma losses by fast electrons in thin films", *Physical Review*, vol. 106, no. 5, p. 874–881, 1957. (cited on pages 1 and 7)

[3] A. OTTO, "A new method for exciting non-radioactive surface plasma oscillations.", *Physica Status Soldi*, vol. 26, p. 99–101, 1968. (cited on pages 1 and 12)

[4] E. KRETSCHMANN and H. RAETHER, "Radiative decay of nonradiative surface plasmons excited by light", *Zeitschrift für Naturforschung A - A Journal of Physical Sciences*, vol. 23, p. 2135, 1968. (cited on pages 1 and 12)

[5] B. LIEDBERG, C. NYLANDER and I. LUNSTRÖM, "Surface plasmon resonance for gas detection and biosensing", *Sensors and Actuators*, vol. 4, no. 0, p. 299–304, 1983. (cited on pages 1 and 20)

[6] E. YEATMAN and E. A. ASH, "Surface-plasmon microscopy", *Electronics Letters*, vol. 23, no. 20, p. 1091–1092, 1987. (cited on pages 1 and 22)

[7] B. ROTHENHAUSLER and W. KNOLL, "Surface–plasmon microscopy", *Nature*, vol. 332, no. 6165, p. 615–617, 1988. (cited on pages 1 and 23)

[8] B. LIU, S. LI and J. HU, "Technological advances in high-throughput screening", *American Journal of PharmacoGenomics*, vol. 4, no. 4, p. 263–276, 2004. (cited on pages 1 and 24)

[9] S. RAY, G. MEHTA and S. SRIVASTAVA, "Label-free detection techniques for protein microarrays: Prospects, merits and challenges", *PROTEOMICS*, vol. 10, no. 4, p. 731–748, 2009. (cited on pages 1, 20 and 24)

[10] F. PILLET, C. THIBAULT, S. BELLON, E. MAILLART, E. TRÉVISIOL, C. VIEU, J. M. FRANÇOIS and V. A. LEBERRE, "Simple surface chemistry to immobilize dna probes that significantly increases sensitivity and spots density of surface plasmon resonance imaging based microarray systems", *Sensors and Actuators B: Chemical*, vol. 147, no. 1, p. 87–92, 2010. (cited on pages 1, 24 and 29)

[11] S. BOUGUELIA, Y. ROUPIOZ, S. SLIMANI, L. MONDANI, G. CASABONA, C. DURMORT, T. VERNET, R. CALEMCZUK and T. LIVACHE, "On-chip microbial culture for the specific detection of very low levels of bacteria", *Lab on a Chip*, vol. 13, no. 20, p. 4024–4032, 2013. (cited on pages 1, 24, 29 and 101)

[12] E. SURANITI, E. SOLLIER, R. CALEMCZUK, T. LIVACHE, P. N. MARCHE, M.-B. VILLIERS and Y. ROUPIOZ, "Real-time detection of lymphocytes binding on an antibody chip using spr imaging", *Lab on a Chip*, vol. 7, no. 9, p. 1206–1208, 2007. (cited on pages 1 and 27)

[13] R. BOMBERA, L. LEROY, T. LIVACHE and Y. ROUPIOZ, "Dna-directed capture of primary cells from a complex mixture and controlled orthogonal release monitored by spr imaging", *Biosensors and Bioelectronics*, vol. 33, no. 1, p. 10–16, 2012. (cited on pages 1, 27 and 81)

[14] Y. YANASE, T. HIRAGUN, S. KANEKO, H. J. GOULD, M. W. GREAVES and M. HIDE, "Detection of refractive index changes in individual living cells by means of surface plasmon resonance imaging", *Biosensors and Bioelectronics*, vol. 26, no. 2, p. 674–681, 2010. (cited on pages 1, 22, 24, 27, 29 and 98)

[15] H. E. de BRUIJN, R. P. H. KOOYMAN and J. GREVE, "Surface plasmon resonance microscopy: improvement of the resolution by rotation of the object", *Applied Optics*, vol. 32, no. 13, p. 2426–2430, 1993. (cited on pages 1, 8, 23, 35, 41 and 53)

[16] C. E. H. BERGER, R. P. H. KOOYMAN and J. GREVE, "Resolution in surface plasmon microscopy", *Review of Scientific Instruments*, vol. 65, no. 9, p. 2829–2836, 1994. (cited on pages 1, 8, 11, 23, 25, 26, 29, 35, 48, 49, 50 and 51)

[17] K. F. GIEBEL, C. BECHINGER, S. HERMINGHAUS, M. RIEDEL, P. LEIDERER, U. WEILAND and M. BASTMEYER, "Imaging of cell/substrate contacts of living cells with surface plasmon resonance microscopy", *Biophysical Journal*, vol. 76, no. 1, p. 509–516, 1999. (cited on pages 2, 8, 24, 26, 41, 49 and 51)

[18] A. PETERSON, M. HALTER, A. TONA, K. BHADRIRAJU and A. PLANT, "Surface plasmon resonance imaging of cells and surface-associated fibronectin", *BMC Cell Biology*, vol. 10, no. 1, p. 1–17, 2009. (cited on pages 2, 24, 26, 29, 35, 41, 51, 71 and 98)

[19] W. KONG, Z. ZHENG, Y. WAN, S. LI and J. LIU, "High-sensitivity sensing based on intensity-interrogated bloch surface wave sensors", *Sensors and Actuators B: Chemical*, vol. 193, no. 0, p. 467–471, 2014. (cited on pages 2 and 33)

[20] D. M. BRULS, T. H. EVERS, J. A. H. KAHLMAN, P. J. W. van LANKVELT, M. OVSYANKO, E. G. M. PELSSERS, J. J. H. B. SCHLEIPEN, F. K. de THEIJE, C. A. VERSCHUREN, T. van der WIJK, J. B. A. van ZON, W. U. DITTMER, A. H. J. IMMINK, J. H. NIEUWENHUIS and M. W. J. PRINS, "Rapid integrated biosensor for multiplexed immunoassays based on actuated magnetic nanoparticles", *Lab on a Chip*, vol. 9, no. 24, p. 3504–3510, 2009. (cited on pages 2, 33 and 34)

[21] J. HULME, C. MALINS, K. SINGH, P. R. FIELDEN and N. J. GODDARD, "Internally-referenced resonant mirror for chemical and biochemical sensing", *Analyst*, vol. 127, no. 9, p. 1233–1236, 2002. (cited on pages 2, 20 and 33)

[22] U. FANO, "The theory of anomalous diffraction gratings and of quasi-stationary waves on metallic surfaces (sommerfeld's waves)", *Journal of the Optical Society of America*, vol. 31, no. 3, p. 213–222, 1941. (cited on page 7)

[23] E. A. STERN and R. A. FERRELL, "Surface plasma oscillations of a degenerate electron gas", *Physical Review*, vol. 120, no. 1, p. 130–136, 1960. (cited on page 7)

[24] H. KANAZAWA, "On the plasma oscillations in metal foils", *Progress of Theoretical Physics*, vol. 26, no. 6, p. 851–860, 1961. (cited on page 7)

[25] P. MUYS, "Electromagnetic field equations of the volume plasmon", *Optics Letters*, vol. 37, no. 23, p. 4928–4930, 2012. (cited on page 7)

[26] B. SCHAFFER, U. HOHENESTER, A. TRUGLER and F. HOFER, "High-resolution surface plasmon imaging of gold nanoparticles by energy-filtered transmission electron microscopy", *Physical Review B*, vol. 79, no. 4, p. 041401, 2009. (cited on page 8)

[27] B. ROTHENHAUSLER and W. KNOLL, "Interferometric determination of the complex wave vector of plasmon surface-polaritons", *Journal of the Optical Society of America B*, vol. 5, no. 7, p. 1401–1405, 1988. (cited on pages 8 and 22)

[28] X. ZHANG and L. HU, "Estimating scattering of pure water from density fluctuation of the refractive index", *Optics Express*, vol. 17, no. 3, p. 1671–1678, 2009. (cited on page 8)

[29] A. VIAL and T. LAROCHE, "Description of dispersion properties of metals by means of the critical points model and application to the study of resonant structures using the fdtd method", *Journal of Physics D: Applied Physics*, vol. 40, no. 22, p. 7152, 2007. (cited on pages 8 and 110)

[30] Y. REN, J. K. CHEN and Y. ZHANG, "Optical properties and thermal response of copper films induced by ultrashort-pulsed lasers", *Journal of Applied Physics*, vol. 110, no. 11, 2011. (cited on pages 8 and 110)

[31] J. HOMOLA, "Electromagnetic theory of surface plasmons", *in Surface Plasmon Resonance Based Sensors*, vol. 4*in Springer Series on Chemical Sensors and Biosensors*, p. 3–44, Springer Berlin Heidelberg, 2006. (cited on pages 8, 12, 18 and 51)

[32] J. M. PITARKE, V. M. SILKIN, E. V. CHULKOV and P. M. ECHENIQUE, "Theory of surface plasmons and surface-plasmon polaritons", *Reports on Progress in Physics*, vol. 70, no. 1, p. 1, 2007. (cited on page 8)

[33] C. S. MOREIRA, A. M. N. LIMA, H. NEFF and C. THIRSTRUP, "Temperature-dependent sensitivity of surface plasmon resonance sensors at the gold-water interface", *Sensors and Actuators B: Chemical*, vol. 134, no. 2, p. 854–862, 2008. (cited on page 8)

[34] B. D. GUPTA and R. K. VERMA, "Surface plasmon resonance-based fiber optic sensors: Principle, probe designs, and some applications", *Journal of Sensors*, vol. 2009, 2009. (cited on pages 8, 13 and 15)

[35] R. TABASSUM, S. K. MISHRA and B. D. GUPTA, "Surface plasmon resonance-based fiber optic hydrogen sulphide gas sensor utilizing cu-zno thin films", *Physical Chemistry Chemical Physics*, vol. 15, no. 28, p. 11868–11874, 2013. (cited on page 8)

[36] J. VÖRÖS, "The density and refractive index of adsorbing protein layers", *Biophysical Journal*, vol. 87, no. 1, p. 553–561, 2004. (cited on page 9)

[37] L. S. JUNG, C. T. CAMPBELL, T. M. CHINOWSKY, M. N. MAR and S. S. YEE, "Quantitative interpretation of the response of surface plasmon resonance sensors to adsorbed films", *Langmuir*, vol. 14, no. 19, p. 5636–5648, 1998. (cited on pages 9 and 49)

[38] S. WANG, X. SHAN, U. PATEL, X. HUANG, J. LU, J. LI and N. TAO, "Label-free imaging, detection, and mass measurement of single viruses by surface plasmon resonance", *Proceedings of the National Academy of Sciences*, vol. 107, no. 37, p. 16028–16032, 2010. (cited on pages 11, 24, 83, 85 and 88)

[39] J. HOMOLA, I. KOUDELA and S. S. YEE, "Surface plasmon resonance sensors based on diffraction gratings and prism couplers: sensitivity comparison", *Sensors and Actuators B: Chemical*, vol. 54, no. 1-2, p. 16–24, 1999. (cited on page 11)

[40] M. NAKKACH, A. DUVAL, B. EA-KIM, J. MOREAU and M. CANVA, "Angulo-spectral surface plasmon resonance imaging of nanofabricated grating surfaces", *Optics Letters*, vol. 35, no. 13, p. 2209–2211, 2010. (cited on page 11)

[41] K. KATAYAMA, T. SAWADA, Q. SHEN and A. HARATA, "Detection of photoinduced electronic, thermal, and acoustic dynamics of gold film using a transient reflecting grating method under three types of surface plasmon resonance conditions", *Physical Review B*, vol. 58, no. 13, p. 8428–8436, 1998. (cited on page 12)

[42] L. LEROY, R. BOMBERA, E. ENGEL, R. CALEMCZUK, L. LAPLATINE, D.-d. R. BAGANIZI, P. N. MARCHE, Y. ROUPIOZ and T. LIVACHE, "Photo-thermal effect for localized desorption of primary lymphocytes arrayed on an antibody/dna-based biochip", *Lab on a Chip*, 2014. (cited on pages 12 and 108)

[43] J. HOMOLA and M. PILIARIK, "Spr sensor instrumentation", *in Surface Plasmon Resonance Based Sensors*, vol. 4*in Springer Series on Chemical Sensors and Biosensors*, p. 95–116, Springer Berlin Heidelberg, 2006. (cited on page 13)

[44] H. KANO, S. MIZUGUCHI and S. KAWATA, "Excitation of surface-plasmon polaritons by a focused laser beam", *Journal of the Optical Society of America B*, vol. 15, no. 4, p. 1381–1386, 1998. (cited on pages 13 and 23)

[45] R. C. JORGENSON and S. S. YEE, "A fiber-optic chemical sensor based on surface plasmon resonance", *Sensors and Actuators B: Chemical*, vol. 12, no. 3, p. 213–220, 1993. (cited on page 13)

[46] F. ABELES, "Recherche sur la propagation des ondes electromagnetiques sinusoidales dans les milieux stratifies. applications aux couches minces", *Annales de Physique*, vol. 5, p. 569–706, 1950. (cited on page 15)

[47] W. N. HANSEN, "Electric fields produced by the propagation of plane coherent electromagnetic radiation in a stratified medium", *Journal of the Optical Society of America*, vol. 58, no. 3, p. 380–388, 1968. (cited on page 15)

[48] T. TURBADAR, "Complete absorption of light by thin metal films", *Proceedings of the Physical Society*, vol. 73, no. 1, p. 40, 1959. (cited on page 16)

[49] E. M. YEATMAN, "Resolution and sensitivity in surface plasmon microscopy and sensing", *Biosensors and Bioelectronics*, vol. 11, no. 6-7, p. 635–649, 1996. (cited on pages 16 and 23)

[50] F. LONG, A. ZHU and H. SHI, "Recent advances in optical biosensors for environmental monitoring and early warning", *Sensors*, vol. 13, no. 10, p. 13928–13948, 2013. (cited on page 19)

[51] V. ESPINA, E. C. WOODHOUSE, J. WULFKUHLE, H. D. ASMUSSEN, E. F. PETRICOIN III and L. A. LIOTTA, "Protein microarray detection strategies: focus on direct detection technologies", *Journal of Immunological Methods*, vol. 290, no. 1-2, p. 121–133, 2004. (cited on page 20)

[52] X. LUO and J. J. DAVIS, "Electrical biosensors and the label free detection of protein disease biomarkers", *Chemical Society Reviews*, vol. 42, no. 13, p. 5944–5962, 2013. (cited on page 20)

[53] S. XU, "Electromechanical biosensors for pathogen detection", *Microchimica Acta*, vol. 178, no. 3-4, p. 245–260, 2012. (cited on page 20)

[54] A. M. c. EGEA, J. FONCY, J.-C. CAU, V. PAVEAU, J.-M. FRANCOIS and C. VIEU, "Optical label-free biodetection based on the diffraction of dna molecular gratings for in vitro diagnostic", *Biophysical Journal*, vol. 102, no. 3, p. 727a, 2012. (cited on page 20)

[55] A. C. EGEA, M. METIVIER, P. CROGUENNOC, M. REMAUD-SIMEON and C. VIEU, "Real-time monitoring of dextransucrase-based enzymatic reaction through surface-enhanced ellipsometric contrast (seec) microscopy in liquid environment", *BioNanoScience*, vol. 4, no. 1, p. 37–45, 2014. (cited on page 20)

[56] Y. FANG, "Label-free biosensors for cell biology", *International Journal of Electrochemistry*, vol. 2011, p. 16, 2011. (cited on page 20)

[57] D. EVANKO, "Label-free microscopy", *Nature Methods*, vol. 7, no. 1, p. 36, 2010. (cited on page 20)

[58] Y. YANASE, H. SUZUKI, T. TSUTSUI, T. HIRAGUN, Y. KAMEYOSHI and M. HIDE, "The spr signal in living cells reflects changes other than the area of adhesion and the formation of cell constructions", *Biosensors and Bioelectronics*, vol. 22, no. 6, p. 1081–1086, 2007. (cited on page 20)

[59] X. CHEN, M. C. DAVIES, C. J. ROBERTS, K. M. SHAKESHEFF, S. J. B. TENDLER and P. M. WILLIAMS, "Dynamic surface events measured by simultaneous probe microscopy and surface plasmon detection", *Analytical Chemistry*, vol. 68, no. 8, p. 1451–1455, 1996. (cited on page 20)

[60] A. BABA, W. KNOLL and R. ADVINCULA, "Simultaneous in situ electrochemical, surface plasmon optical, and atomic force microscopy measurements: Investigation of conjugated polymer electropolymerization", *Review of Scientific Instruments*, vol. 77, no. 6, 2006. (cited on page 20)

[61] R.-Y. HE, G.-L. CHANG, H.-L. WU, C.-H. LIN, K.-C. CHIU, Y.-D. SU and S.-J. CHEN, "Enhanced live cell membrane imaging using surface plasmon-enhanced total internal reflection fluorescence microscopy", *Optics Express*, vol. 14, no. 20, p. 9307–9316, 2006. (cited on page 20)

[62] V. CHABOT, Y. MIRON, P. G. CHARETTE and M. GRANDBOIS, "Identification of the molecular mechanisms in cellular processes that elicit a surface plasmon resonance (spr) response using simultaneous surface plasmon-enhanced fluorescence (spef) microscopy", *Biosensors and Bioelectronics*, vol. 50, no. 0, p. 125–131, 2013. (cited on pages 20 and 22)

[63] A. RENAUDIN, V. CHABOT, E. GRONDIN, V. AIMEZ and P. G. CHARETTE, "Integrated active mixing and biosensing using surface acoustic waves (saw) and surface plasmon resonance (spr) on a common substrate", *Lab on a Chip*, vol. 10, no. 1, p. 111–115, 2010. (cited on page 20)

[64] N. S. LYNN JR, J.-I. MARTINEZ-LOPEZ, M. BOCKOVA, P. ADAM, V. COELLO, H. R. SILLER and J. HOMOLA, "Biosensing enhancement using passive mixing structures for microarray-based sensors", *Biosensors and Bioelectronics*, vol. 54, no. 0, p. 506–514, 2014. (cited on page 20)

[65] A. BABA, P. TARANEKAR, R. R. PONNAPATI, W. KNOLL and R. C. ADVINCULA, "Electrochemical surface plasmon resonance and waveguide-enhanced glucose biosensing with n-alkylaminated polypyrrole/glucose oxidase multilayers", *ACS Applied Materials and Interfaces*, vol. 2, no. 8, p. 2347–2354, 2010. (cited on page 20)

[66] W. WANG, K. FOLEY, X. SHAN, S. WANG, S. EATON, V. J. NAGARAJ, P. WIKTOR, U. PATEL and N. TAO, "Single cells and intracellular processes studied by a plasmonic-based electrochemical impedance microscopy", *Nature Chemistry*, vol. 3, no. 3, p. 249–255, 2011. (cited on pages 20, 24 and 98)

[67] N. BASSIL, E. MAILLART, M. CANVA, Y. LÉVY, M.-C. MILLOT, S. PISSARD, R. NARWA and M. GOOSSENS, "One hundred spots parallel monitoring of dna interactions by spr imaging of polymer-functionalized surfaces applied to the detection of cystic fibrosis mutations", *Sensors and Actuators B: Chemical*, vol. 94, no. 3, p. 313–323, 2003. (cited on page 20)

[68] E. MERCEY, R. SADIR, E. MAILLART, A. ROGET, F. BALEUX, H. LORTAT-JACOB and T. LIVACHE, "Polypyrrole oligosaccharide array and surface plasmon resonance imaging for the measurement of glycosaminoglycan binding interaction", *Analytical Chemistry*, vol. 80, no. 9, p. 3476–3482, 2008. (cited on page 20)

[69] J. MITCHELL, "Small molecule immunosensing using surface plasmon resonance", *Sensors*, vol. 10, no. 8, p. 7323–7346, 2010. (cited on pages 20 and 95)

[70] P. N. ABADIAN, C. P. KELLEY and E. D. GOLUCH, "Cellular analysis and detection using surface plasmon resonance techniques", *Analytical Chemistry*, vol. 86, no. 6, p. 2799–2812, 2014. (cited on page 20)

[71] S. MILGRAM, R. BOMBERA, T. LIVACHE and Y. ROUPIOZ, "Antibody microarrays for label-free cell-based applications", *Methods*, vol. 56, no. 2, p. 326–333, 2012. (cited on pages 20, 22, 29, 61 and 74)

[72] J. HOMOLA, "Surface plasmon resonance sensors for detection of chemical and biological species", *Chemical Reviews*, vol. 108, no. 2, p. 462–493, 2008. (cited on pages 20 and 27)

[73] C. E. JORDAN, B. L. FREY, S. KORNGUTH and R. M. CORN, "Characterization of poly-l-lysine adsorption onto alkanethiol-modified gold surfaces with polarization-modulation fourier transform infrared spectroscopy and surface plasmon resonance measurements", *Langmuir*, vol. 10, no. 10, p. 3642–3648, 1994. (cited on page 20)

[74] MEYER, L. RIKKE, Z. XINGFEI, TANG, LONE, ARPANAEI, AYYOOB, KINGSHOTT, PETER, BESENBACHER and FLEMMING, "Immobilisation of living bacteria for afm imaging under physiological conditions", *Ultramicroscopy*, vol. 110, p. 9, 2010. (cited on page 20)

[75] R. G. NUZZO and D. L. ALLARA, "Adsorption of bifunctional organic disulfides on gold surfaces", *Journal of the American Chemical Society*, vol. 105, no. 13, p. 4481–4483, 1983. (cited on page 20)

[76] J. C. LOVE, L. A. ESTROFF, J. K. KRIEBEL, R. G. NUZZO and G. M. WHITESIDES, "Self-assembled monolayers of thiolates on metals as a form of nanotechnology", *Chemical Reviews*, vol. 105, no. 4, p. 1103–1170, 2005. doi: 10.1021/cr0300789. (cited on page 20)

[77] T. LIVACHE, A. ROGET, E. DEJEAN, C. BARTHET, G. BIDAN and R. TEOULE, "Preparation of a dna matrix via an electrochemically directed copolymerization of pyrrole and oligonucleotides bearing a pyrrole group", *Nucleic Acids Research*, vol. 22, no. 15, p. 2915–2921, 1994. (cited on pages 20 and 73)

[78] Y. L. JEYACHANDRAN, J. A. MIELCZARSKI, E. MIELCZARSKI and B. RAI, "Efficiency of blocking of non-specific interaction of different proteins by bsa adsorbed on hydrophobic and hydrophilic surfaces", *Journal of Colloid and Interface Science*, vol. 341, no. 1, p. 136–142, 2010. (cited on pages 21 and 75)

[79] E. WIJAYA, C. LENAERTS, S. MARICOT, J. HASTANIN, S. HABRAKEN, J.-P. VILCOT, R. BOUKHERROUB and S. SZUNERITS, "Surface plasmon resonance-based biosensors: From the development of different spr structures to novel surface functionalization strategies", *Current Opinion in Solid State and Materials Science*, vol. 15, no. 5, p. 208–224, 2011. (cited on pages 21 and 53)

[80] G. SCHREIBER, G. HARAN and H. X. ZHOU, "Fundamental aspects of protein-protein association kinetics", *Chemical Reviews*, vol. 109, no. 3, p. 839–860, 2009. (cited on pages 21 and 22)

[81] J. HOMOLA, J. STEPANEK, H. VAISOCHEROVÃ¡ and M. PILIARIK, "Molecular interactions in spr sensors", *in Surface Plasmon Resonance Based Sensors*, vol. 4*in Springer Series on Chemical Sensors and Biosensors*, p. 69–91, Springer Berlin Heidelberg, 2006. (cited on page 21)

[82] Q. HAN, E. M. BRADSHAW, B. NILSSON, D. A. HAFLER and J. C. LOVE, "Multidimensional analysis of the frequencies and rates of cytokine secretion from single cells by quantitative microengraving", *Lab on a Chip*, vol. 10, no. 11, p. 1391–1400, 2010. (cited on pages 22, 28, 94 and 95)

[83] N. P. GERRY, N. E. WITOWSKI, J. DAY, R. P. HAMMER, G. BARANY and F. BARANY, "Universal dna microarray method for multiplex detection of low abundance point mutations", *Journal of Molecular Biology*, vol. 292, no. 2, p. 251–262, 1999. (cited on page 22)

[84] A. W. PETERSON, M. HALTER, A. TONA, K. BHADRIRAJU and A. L. PLANT, "Using surface plasmon resonance imaging to probe dynamic interactions between cells and extracellular matrix", *Cytometry Part A*, vol. 77A, no. 9, p. 895–903, 2010. (cited on pages 22, 24 and 29)

[85] T. OKAMOTO and I. YAMAGUCHI, "Surface plasmon microscope", *in Optics in Complex Systems*, vol. 1319, p. 472–473, Proc. SPIE 1319, 1990. (cited on page 22)

[86] A. SEREDA, J. MOREAU, M. CANVA and E. MAILLART, "High performance multi-spectral interrogation for surface plasmon resonance imaging sensors", *Biosensors and Bioelectronics*, vol. 54, no. 0, p. 175–180, 2014. (cited on page 22)

[87] J. B. BEUSINK, A. M. C. LOKATE, G. A. J. BESSELINK, G. J. M. PRUIJN and R. B. M. SCHASFOORT, "Angle-scanning spr imaging for detection of biomolecular interactions on microarrays", *Biosensors and Bioelectronics*, vol. 23, no. 6, p. 839–844, 2008. (cited on page 22)

[88] E. MAILLART, *Surface plasmon resonance imaging for simultaneous analysis of multiple biomolecular interactions in real time*. PhD thesis, Université Paris Sud, 2004. (cited on pages 22, 34 and 38)

[89] P. GUEDON and Y. LEVY, "Procede de caracterisation d'une surface, et dispositif pour sa mise en oeuvre (wo 2002048689 a1)", 2003. (cited on page 22)

[90] T. M. CHINOWSKY, M. S. GROW, K. S. JOHNSTON, K. NELSON, T. EDWARDS, E. FU and P. YAGER, "Compact, high performance surface plasmon resonance imaging system", *Biosensors and Bioelectronics*, vol. 22, no. 9-10, p. 2208–2215, 2007. (cited on pages 22, 34, 45 and 71)

[91] C. E. H. BERGER, R. P. H. KOOYMAN and J. GREVE, "Surface plasmon propagation near an index step", *Optics Communications*, vol. 167, no. 1-6, p. 183–189, 1999. (cited on pages 23, 51 and 99)

[92] G. STABLER, M. G. SOMEKH and C. W. SEE, "High-resolution wide-field surface plasmon microscopy", *Journal of Microscopy*, vol. 214, no. 3, p. 328–333, 2004. (cited on pages 23 and 24)

[93] J. ELEZGARAY, T. ROLAND, L. BERGUIGA and F. ARGOUL, "Modeling of the scanning surface plasmon microscope", *Journal of the Optical Society of America A*, vol. 27, no. 3, p. 450–457, 2009. (cited on page 23)

[94] H. KANO and W. KNOLL, "A scanning microscope employing localized surface-plasmon-polaritons as a sensing probe", *Optics Communications*, vol. 182, no. 1-3, p. 11–15, 2000. (cited on page 23)

[95] E. BOYER-PROVERA, A. ROSSI, L. ORIOL, C. DUMONTET, A. PLESA, L. BERGUIGA, J. ELEZGARAY, A. ARNEODO and F. ARGOUL, "Wavelet-based decomposition of high resolution surface plasmon microscopy v (z) curves at visible and near infrared wavelengths", *Optics Express*, vol. 21, no. 6, p. 7456–7477, 2013. (cited on pages 23 and 24)

[96] L. BERGUIGA, S. ZHANG, F. ARGOUL and J. ELEZGARAY, "High-resolution surface-plasmon imaging in air and in water: V(z) curve and operating conditions", *Optics Letters*, vol. 32, no. 5, p. 509–511, 2007. (cited on page 23)

[97] M. M. A. JAMIL, M. YOUSEFFI, P. C. TWIGG, S. T. BRITLAND, S. LIU, C. W. SEE, J. ZHANG, M. G. SOMEKH and M. C. T. DENYER, "High resolution imaging of bio-molecular binding studies using a widefield surface plasmon microscope", *Sensors and Actuators B-Chemical*, vol. 129, no. 2, p. 566–574, 2008. (cited on pages 24 and 25)

[98] B. HUANG, F. YU and R. N. ZARE, "Surface plasmon resonance imaging using a high numerical aperture microscope objective", *Analytical Chemistry*, vol. 79, no. 7, p. 2979–2983, 2007. (cited on pages 24, 25, 49, 50, 51 and 71)

[99] E. HECHT, *Optics (4th Edition)*. Addison Wesley, 2001. (cited on pages 24 and 45)

[100] T. ZHANG, H. MORGAN, A. CURTIS and M. RIEHLE, "Measuring particle-substrate distance with surface plasmon resonance microscopy", *Journal of Optics A: Pure and Applied Optics*, vol. 3, no. 5, p. 333, 2001. (cited on page 25)

[101] A. JIN, T. OZAWA, K. TAJIRI, T. OBATA, S. KONDO, K. KINOSHITA, S. KADOWAKI, K. TAKAHASHI, T. SUGIYAMA, H. KISHI and A. MURAGUCHI, "A rapid and efficient single-cell manipulation method for screening antigen-specific antibody-secreting cells from human peripheral blood", *Nat Med*, vol. 15, no. 9, p. 1088–1092, 2009. (cited on pages 26, 28 and 29)

[102] J. L. SPUDICH and D. E. KOSHLAND, "Non-genetic individuality: chance in the single cell", *Nature*, vol. 262, no. 5568, p. 467–471, 1976. (cited on page 28)

[103] R. H. TEMPLER and O. CES, "New frontiers in single-cell analysis", *Journal of The Royal Society Interface*, vol. 5, no. Suppl 2, p. S111–S112, 2008. (cited on page 28)

[104] S. LINDSTROM and H. ANDERSSON-SVAHN, "Overview of single-cell analyses: microdevices and applications", *Lab on a Chip*, vol. 10, no. 24, p. 3363–3372, 2010. (cited on page 28)

[105] P. K. CHATTOPADHYAY, T. M. GIERAHN, M. ROEDERER and J. C. LOVE, "Single-cell technologies for monitoring immune systems", *Nature Immunology*, vol. 15, no. 2, p. 128–135, 2014. (cited on pages 28 and 74)

[106] R. T. CARSON and D. A. A. VIGNALI, "Simultaneous quantitation of 15 cytokines using a multiplexed flow cytometric assay", *Journal of Immunological Methods*, vol. 227, no. 1-2, p. 41–52, 1999. (cited on page 28)

[107] H. STREECK, N. FRAHM and B. D. WALKER, "The role of ifn-[gamma] elispot assay in hiv vaccine research", *Nat. Protocols*, vol. 4, no. 4, p. 461–469, 2009. (cited on page 28)

[108] R. A. SEDER, P. A. DARRAH and M. ROEDERER, "T-cell quality in memory and protection: implications for vaccine design", *Nat Rev Immunol*, vol. 8, no. 4, p. 247–258, 2008. (cited on page 28)

[109] C. MA, R. FAN, H. AHMAD, Q. H. SHI, B. COMIN-ANDUIX, T. CHODON, R. C. KOYA, C. C. LIU, G. A. KWONG, C. G. RADU, A. RIBAS and J. R. HEATH, "A clinical microchip for evaluation of single immune cells reveals high functional heterogeneity in phenotypically similar t cells", *Nature Medicine*, vol. 17, no. 6, p. 738–744, 2011. (cited on pages 28 and 95)

[110] S. WANG, S. OTA, B. GUO, J. RYU, C. RHODES, Y. XIONG, S. KALIM, L. ZENG, Y. CHEN, M. A. TEITELL and X. ZHANG, "Subcellular resolution mapping of endogenous cytokine secretion by nano-plasmonic-resonator sensor array", *Nano Letters*, vol. 11, no. 8, p. 3431–3434, 2011. (cited on pages 28, 72, 95 and 96)

[111] S. MILGRAM, S. CORTES, M.-B. VILLIERS, P. MARCHE, A. BUHOT, T. LIVACHE and Y. ROUPIOZ, "On chip real time monitoring of b-cells hybridoma secretion of immunoglobulin", *Biosensors and Bioelectronics*, vol. 26, no. 5, p. 2728–2732, 2011. (cited on page 29)

[112] H. SHINOHARA, Y. SAKAI and T. A. MIR, "Real-time monitoring of intracellular signal transduction in pc12 cells by two-dimensional surface plasmon resonance imager", *Analytical Biochemistry*, vol. 441, no. 2, p. 185–189, 2013. (cited on page 29)

[113] S.-H. KIM, W. CHEGAL, J. DOH, H. CHO and D. MOON, "Study of cell-matrix adhesion dynamics using surface plasmon resonance imaging ellipsometry", *Biophysical Journal*, vol. 100, no. 7, p. 1819–1828, 2011. (cited on pages 29, 92 and 98)

[114] L. MONDANI, Y. ROUPIOZ, S. DELANNOY, P. FACH and T. LIVACHE, "Simultaneous enrichment and optical detection of low levels of stressed escherichia coli o157:h7 in food matrices", *Journal of Applied Microbiology*, vol. 117, no. 2, p. 537–546, 2014. (cited on page 29)

[115] P. N. ABADIAN, N. TANDOGAN, J. J. JAMIESON and E. D. GOLUCH, "Using surface plasmon resonance imaging to study bacterial biofilms", *Biomicrofluidics*, vol. 8, no. 2, 2014. (cited on page 29)

[116] G. GOURY, *Recherches historico-monumentales : concernant les sciences, les arts de l'antiquité et leur émigration d'Orient en Occident*. Paris: Firmin Didot Frères, 1833. (cited on page 33)

[117] A. DEVILLE, *Histoire de l'art de la verrerie dans l'antiquité*. Paris: A. Morel et Cie, 1871. (cited on page 33)

[118] I. NEWTON, *Opticks*. 1704. (cited on page 33)

[119] R. DESCARTES, *Discours de la méthode*. 1637. (cited on page 33)

[120] F. M. MIRABELLA, *Internal Reflection Spectroscopy: Theory and Applications*. CRC Press, 1992. (cited on page 33)

[121] E. J. AMBROSE, "A surface contact microscope for the study of cell movements", *Nature*, vol. 178, no. 4543, p. 1194, 1956. (cited on page 33)

[122] C. E. SOTEROPULOS and H. K. HUNT, "Attaching biological probes to silica optical biosensors using silane coupling agents", *Journal of Visualized Experiments*, no. 63, p. e3866, 2012. (cited on page 34)

[123] R. CUSH, J. M. CRONIN, W. J. STEWART, C. H. MAULE, J. MOLLOY and N. J. GODDARD, "The resonant mirror: a novel optical biosensor for direct sensing of biomolecular interactions part i: Principle of operation and associated instrumentation", *Biosensors and Bioelectronics*, vol. 8, no. 7â€"8, p. 347–354, 1993. (cited on page 34)

[124] A. SINIBALDI, N. DANZ, E. DESCROVI, P. MUNZERT, U. SCHULZ, F. SONNTAG, L. DOMINICI and F. MICHELOTTI, "Direct comparison of the performance of bloch surface wave and surface plasmon polariton sensors", *Sensors and Actuators B: Chemical*, vol. 174, no. 0, p. 292–298, 2012. (cited on page 34)

[125] G. STEINER, V. SABLINSKAS, A. HÜBNER, C. KUHNE and R. SALZER, "Surface plasmon resonance imaging of microstructured monolayers", *Journal of Molecular Structure*, vol. 509, no. 1-3, p. 265–273, 1999. (cited on page 34)

[126] Y. YANASE, T. HIRAGUN, K. ISHII, T. KAWAGUCHI, T. YANASE, M. KAWAI, K. SAKAMOTO and M. HIDE, "Surface plasmon resonance for cell-based clinical diagnosis", *Sensors*, vol. 14, no. 3, p. 4948–4959, 2014. (cited on page 35)

[127] C. E. JORDAN, A. G. FRUTOS, A. J. THIEL and R. M. CORN, "Surface plasmon resonance imaging measurements of dna hybridization adsorption and streptavidin/dna multilayer formation at chemically modified gold surfaces", *Analytical Chemistry*, vol. 69, no. 24, p. 4939–4947, 1997. (cited on pages 35 and 75)

[128] S. B. IPPOLITO, B. B. GOLDBERG and M. S. ÜNLÜ, "Theoretical analysis of numerical aperture increasing lens microscopy", *Journal of Applied Physics*, vol. 97, no. 5, p. 053105, 2005. (cited on pages 40, 41, 45 and 46)

[129] K. YAMAMOTO, K. OSATO, I. ICHIMURA, F. MAEDA and T. WATANABE, "0.8-numerical-aperture two-element objective lens for the optical disk", *Japanese Journal of Applied Physics*, vol. 36, no. 1B, p. 456–459, 1997. (cited on page 41)

[130] T. SCHEIMPFLUG, "Improved method and apparatus for the systematic alteration or distortion of plane pictures and images by means of lenses and mirrors for photography and for other purposes (us 751347 a)", 1904. (cited on page 44)

[131] L. LAPLATINE, L. LEROY, R. CALEMCZUK, D.-d. R. BAGANIZI, P. N. MARCHE, Y. ROUPIOZ and T. LIVACHE, "Spatial resolution in prism-based surface plasmon resonance miscroscopy", *Optics Express*, vol. 22, p. 22771–22785, 2014. (cited on pages 45, 53, 87, 110 and 115)

[132] R. BARAKAT, "Rayleigh wavefront criterion", *Journal of the Optical Society of America*, vol. 55, no. 5, p. 572–573, 1965. J. Opt. Soc. Am. (cited on page 45)

[133] M. PILIARIK, L. PAROVA and J. HOMOLA, "High-throughput spr sensor for food safety", *Biosensors and Bioelectronics*, vol. 24, no. 5, p. 1399–1404, 2009. (cited on page 49)

[134] J. HOMOLA and M. PILIARIK, "Surface plasmon resonance (spr) sensors", *in Surface Plasmon Resonance Based Sensors*, vol. 4*in Springer Series on Chemical Sensors and Biosensors*, p. 45–67, Springer Berlin Heidelberg, 2006. (cited on page 49)

[135] B. H. ONG, X. YUAN, S. C. TJIN, J. ZHANG and H. M. NG, "Optimised film thickness for maximum evanescent field enhancement of a bimetallic film surface plasmon resonance biosensor", *Sensors and Actuators B: Chemical*, vol. 114, no. 2, p. 1028–1034, 2006. (cited on pages 51 and 53)

[136] S. SZUNERITS, X. CASTEL and R. BOUKHERROUB, "Preparation of electrochemical and surface plasmon resonance active interfaces: Deposition of indium tin oxide on silver thin films", *The Journal of Physical Chemistry C*, vol. 112, no. 29, p. 10883–10888, 2008. (cited on page 53)

[137] M. MANESSE, R. SANJINES, V. STAMBOULI, C. JOREL, B. PELISSIER, M. PISAREK, R. BOUKHERROUB and S. SZUNERITS, "Preparation and characterization of silver substrates coated with antimony-doped sno2 thin films for surface plasmon resonance studies", *Langmuir*, vol. 25, no. 14, p. 8036–8041, 2009. (cited on page 53)

[138] V. G. KRAVETS, R. JALIL, Y. J. KIM, D. ANSELL, D. E. AZNAKAYEVA, B. THACKRAY, L. BRITNELL, B. D. BELLE, F. WITHERS, I. P. RADKO, Z. HAN, S. I. BOZHEVOLNYI, K. S. NOVOSELOV, A. K. GEIM and A. N. GRIGORENKO, "Graphene-protected copper and silver plasmonics", *Sci. Rep.*, vol. 4, 2014. (cited on pages 53 and 107)

[139] N. C. LINDQUIST, A. LESUFFLEUR, H. IM and S.-H. OH, "Sub-micron resolution surface plasmon resonance imaging enabled by nanohole arrays with surrounding bragg mirrors for enhanced sensitivity and isolation", *Lab on a Chip*, vol. 9, no. 3, p. 382–387, 2009. (cited on page 53)

[140] T. WILKOP, Z. WANG and Q. CHENG, "Analysis of micro-contact printed protein patterns by spr imaging with a led light source", *Langmuir*, vol. 20, no. 25, p. 11141–11148, 2004. (cited on page 58)

[141] S. TANG and G. WHITESIDES, *Basic Microfluidic and Soft Lithographic Techniques*, vol. chapter 2*in Optofluidics: Fundamentals, Devices and Applications*. McGraw-Hill, 2010. (cited on pages 63 and 71)

[142] D. G. KROGER, "Convection heat transfer between a horizontal surface and the natural environment", *RandD Journal*, vol. 18, no. 3, p. 49–54, 2002. (cited on page 68)

[143] P. THEVENAZ, U. E. RUTTIMANN and M. UNSER, "A pyramid approach to subpixel registration based on intensity", *Image Processing, IEEE Transactions on*, vol. 7, no. 1, p. 27–41, 1998. (cited on page 70)

[144] U. SCHNEIDER, H.-U. SCHWENK and G. BORNKAMM, "Characterization of ebv-genome negative "null" and "t" cell lines derived from children with acute lymphoblastic leukemia and leukemic transformed non-hodgkin lymphoma", *International Journal of Cancer*, vol. 19, no. 5, p. 621–626, 1977. (cited on page 72)

[145] Y. SAMBUY, I. DE ANGELIS, G. RANALDI, M. L. SCARINO, A. STAMMATI and F. ZUCCO, "The caco-2 cell line as a model of the intestinal barrier: influence of cell and culture-related factors on caco-2 cell functional characteristics", *Cell Biology and Toxicology*, vol. 21, no. 1, p. 1–26, 2005. (cited on page 73)

[146] J. C. WYANT and K. CREATH, *Applied Optics and Optical Engineering, Volume XI*, vol. XI. New York: Academic Press, Inc., 1992. (cited on page 83)

[147] B. BAUMEIER, F. HUERKAMP, T. A. LESKOVA and A. A. MARADUDIN, "Scattering of surface-plasmon polaritons by a localized dielectric surface defect studied using an effective boundary condition", *Physical Review A*, vol. 84, no. 1, p. 013810, 2011. (cited on pages 83 and 88)

[148] X. FAN, W. ZHENG and D. J. SINGH, "Light scattering and surface plasmons on small spherical particles", *Light Sci Appl*, vol. 3, p. e179, 2014. Review. (cited on page 83)

[149] A. HEIFETZ, S.-C. KONG, A. V. SAHAKIAN, A. TAFLOVE and V. BACKMAN, "Photonic nanojets", *Journal of Computational and Theoretical Nanoscience*, vol. 6, no. 9, p. 1979–1992, 2009. (cited on page 83)

[150] A. DREZET, A. HOHENAU, J. R. KRENN, M. BRUN and S. HUANT, "Surface plasmon mediated near-field imaging and optical addressing in nanoscience", *Micron*, vol. 38, no. 4, p. 427–437, 2007. (cited on page 83)

[151] J. C. WEEBER, J. R. KRENN, A. DEREUX, B. LAMPRECHT, Y. LACROUTE and J. P. GOUDONNET, "Near-field observation of surface plasmon polariton propagation on thin metal stripes", *Physical Review B*, vol. 64, no. 4, p. 045411, 2001. (cited on page 83)

[152] L. DU, D. Y. LEI, G. YUAN, H. FANG, X. ZHANG, Q. WANG, D. TANG, C. MIN, S. A. MAIER and X. YUAN, "Mapping plasmonic near-field profiles and interferences by surface-enhanced raman scattering", *Sci. Rep.*, vol. 3, 2013. (cited on page 88)

[153] E. SIMON, B. BERGE, F. FILLIT, H. GATON, O. JACQUES-SERMET, M. GUILLET, F. LAUNE, J. LEGRAND, M. MAILLARD and T. N, "Optical design rules of a camera module with a liquid lens and principle of command for af and ois functions", *in SPIE*, vol. 7849, p. 784903, 2010. (cited on page 93)

[154] H. FISCHER, I. POLIKARPOV and A. F. CRAIEVICH, "Average protein density is a molecular-weight-dependent function", *Protein Science*, vol. 13, no. 10, p. 2825–2828, 2004. (cited on page 94)

[155] W. WANG, S. WANG, Q. LIU, J. WU and N. TAO, "Mapping single-cell-substrate interactions by surface plasmon resonance microscopy", *Langmuir*, vol. 28, no. 37, p. 13373–13379, 2012. (cited on page 98)

[156] M. ABRAMOWITZ and I. STEGUN, *Handbook of Mathematical Functions*. U.S. Department of Commerce, National Bureau of Standards, 1964. (cited on page 100)

[157] A. ABBAS, M. J. LINMAN and Q. CHENG, "New trends in instrumental design for surface plasmon resonance-based biosensors", *Biosensors and Bioelectronics*, vol. 26, no. 5, p. 1815–1824, 2011. (cited on page 107)

[158] J. A. DIONNE, E. VERHAGEN, A. POLMAN and H. A. ATWATER, "Are negative index materials achievable with surface plasmon waveguides? a case study of three plasmonic geometries", *Optics Express*, vol. 16, no. 23, p. 19001–19017, 2008. (cited on page 107)

[159] V. V. TEMNOV, "Ultrafast acousto-magneto-plasmonics", *Nat Photon*, vol. 6, no. 12, p. 872–872, 2012. (cited on page 107)

[160] N. BONOD, R. REINISCH, E. POPOV and M. NEVIÈRE, "Optimization of surface-plasmon-enhanced magneto-optical effects", *Journal of the Optical Society of America B*, vol. 21, no. 4, p. 791–797, 2004. (cited on page 107)

[161] J. LIN, J. P. B. MUELLER, Q. WANG, G. YUAN, N. ANTONIOU, X.-C. YUAN and F. CAPASSO, "Polarization-controlled tunable directional coupling of surface plasmon polaritons", *Science*, vol. 340, no. 6130, p. 331–334, 2013. (cited on page 107)

[162] A. PORS, M. G. NIELSEN, T. BERNARDIN, J.-C. WEEBER and S. I. BOZHEVOLNYI, "Efficient unidirectional polarization-controlled excitation of surface plasmon polaritons", *Light Sci Appl*, vol. 3, p. e197, 2014. (cited on page 108)

[163] H. DITLBACHER, J. R. KRENN, G. SCHIDER, A. LEITNER and F. R. AUSSENEGG, "Two-dimensional optics with surface plasmon polaritons", *Applied Physics Letters*, vol. 81, no. 10, p. 1762–1764, 2002. (cited on page 108)

[164] A. D. RAKIC, A. B. DJURISIC, J. M. ELAZAR and M. L. MAJEWSKI, "Optical properties of metallic films for vertical-cavity optoelectronic devices", *Applied Optics*, vol. 37, no. 22, p. 5271–5283, 1998. (cited on page 110)

[165] W. SELLMEIER, "Zur erklärung der abnormen farbenfolge im spectrum einiger substanzen", *Annual Review of Physical Chemistry*, vol. 143, 271, 1871. (cited on page 112)

[166] X. QUAN and E. S. FRY, "Empirical equation for the index of refraction of seawater", *Applied Optics*, vol. 34, no. 18, p. 3477–3480, 1995. (cited on page 112)

[167] P. D. T. HUIBERS, "Models for the wavelength dependence of the index of refraction ofwater", *Applied Optics*, vol. 36, no. 16, p. 3785–3787, 1997. (cited on page 112)

[168] A. V.-D. FUENSANTA and D. NATHAN, *The Human Eye and Adaptive Optics*. Topics in Adaptive Optics, 2012. (cited on page 114)

Acknowledgement

Voilà maintenant venu le temps de sortir du discours quelque peu impersonnel de l'écrit scientifique. La science est aussi une affaire d'hommes et de femmes, à qui je me propose ici de rendre honneur.

J'aimerais tout d'abord remercier les membres du jury, Benoit Boulanger pour avoir accepté d'en être le président, Emmanuel Maillart et Malcolm Buckle pour l'examination de mon travail et leurs remarques pertinentes, et tout particulièrement Christophe Vieu et Paul Charrette pour avoir accepté de rapporter le manuscrit. Merci à vous cinq pour votre temps et votre attention.

Cette aventure scientifique n'aurait pas vu le jour sans le travail de préparation et de suivi de ceux qui l'ont d'abord imaginée, puis mise en place, Roberto Calemczuk et Loïc Leroy. Roberto, merci pour ton encadrement et pour nos discussions, autant scientifiques que personnelles. J'ai été impressionné par la pertinence de tes remarques et questionnements qui soulèvent et révèlent souvent le fond du problème. Tu as aussi su faire preuve du détachement indispensable à la gestion d'une thèse alors que j'avais de la peine à m'extraire de mes émotions... Muchissimas gracias por todo ! Loïc, merci pour ta patience et pour tout ce temps que tu m'as consacré, que ce soit dans la paillasse en blouse blanche ou dans la pagaille de nos tableaux blancs. Ta capacité d'analyse et ton ingéniosité, mais surtout ta curiosité et ton intégrité, ont été un exemple pour moi, et j'espère que ces qualités continueront à l'être pour tes prochains doctorants. Chers encadrants, je vous remercie infiniment pour ces trois années de péripéties qui finissent dans la joie, avec l'agréable souvenir d'avoir formé un trio.

Cette thèse d'interface ne saurait s'être réalisée sans un second niveau d'encadrement où biologistes, chimistes et physiciens, s'entraident dans un but commun. Je tiens donc à remercier en premier lieu Yoann Roupioz qui a supervisé la partie biologie cellulaire et microbiologie de mon projet. Sans les deux ANR Cellestim et Mult-I-Cell-S dont il est le porteur, et dans lesquelles j'ai été impliqué, mes travaux n'auraient certainement pas pu être financés comme ils l'ont été. Merci également à toi Yoann pour ton implication dans la rédaction de notre article.

Je remercie chaleureusement Thierry Livache pour m'avoir accueilli au CREAB, et surtout d'avoir su y créer et y faire perdurer une ambiance aussi conviviale et professionnelle. Pour travailler correctement il faut évidemment des locaux et des moyens, mais aussi une équipe motivée dans laquelle on a envie de s'intégrer. Et sur tous ces points, je suis sacrément bien tombé ! Je tiens également à remercier Arnaud Buhot, l'actuel chef d'équipe, pour son aide en Mathematica ainsi que pour ses remarques et idées dans le traitement des données expérimentales.

Je remercie encore Jean-Pierre Travers et Fréderic Chamdezon de m'avoir accueilli au sein du SPrAM. Faire partie du conseil d'UMR a été une expérience très enrichissante. Ces moments d'échange indispensables à la vie (heureuse) des labos sont une bonne école de gestion de structure, que je conseille vivement aux doctorants.

N'étant pas biologiste de formation, j'ai eu la chance d'être bien entouré et je remercie vivement Radé, Sandrine, Stacie et Vincent pour m'avoir initié à la culture et l'entretien de lignées cellulaires et de souches bactériennes. Merci à vous pour votre aide.

Je remercie Philipe Montmayeul pour la grande qualité des pièces mecaniques qu'il a réalisées, ainsi que pour son aide au design de certaines structures. Tout mes remerciemments aussi à Seb, Raph et José pour leur précieuse aide aux manips, ainsi que pour la gestion du parc informatique

et de mes nombreuses commandes.

Un grand merci à Patrice Marche de l'Institut Albert Bonniot et son équipe pour leurs travaux sur le choix et la préparation des échantillons biologiques à qui j'en ai fait voir de toutes les couleurs (je parle des cellules...). Je remercie de même Thierry Leïchlé et l'équipe TEAM du LAAS-CNRS pour la fabrication du masque de photolithographie.

J'ai eu la chance de collaborer avec la start-up Prestodiag (Paris) à travers le "label création d'entreprise" de l'Université de Grenoble. Merci donc à Thibault Mercey de m'avoir reçu dans son équipe et à David Carrara pour le temps qu'il m'a consacré.

Merci à François Rieuthord et à Joël Eymery pour m'avoir laissé passer du temps sur Comsol. Même si ces résultats n'apparaissent pas ici, ils nous ont bien aidé à cerner la dynamique du chauffage localisé par SPR dans nos structures fluidiques, et m'ont donné l'occasion de m'initier aux simulations multi-physiques.

Merci à toi Franz pour m'avoir incité à enfin utiliser LaTeX, ainsi que pour ton aide et tes conseils avisés (et ton vin chaud...).

Sur son lieu de travail, on travaille, mais pas que, et heureusement ! Alors un immense merci à vous tous membres du CREAB pour tous ces moments partagés, que ce soit à la pause café (avec ces généreux gâteaux et mets exotiques...), autour d'un repas ou encore sur les pistes de ski. Nos conversations et autres élucubrations philosophiques nous ont parfois amenés loin !

J'aimerais enfin remercier tous ceux qui ont participé, de façon indispensable même si plus indirecte, à l'aboutissement de ces trois années pas toujours faciles... Papa et maman, des bancs de l'école aux bancs optiques, merci pour votre infaillible encouragement, soutien, sagesse et amour. Je me dois aussi de remercier individuellement tous ceux avec qui j'ai eu la chance de partager mon quotidien et qui m'ont soutenu, supporté, et, pendant la rédaction, nourri... Merci donc à vous mes chers colocs : Camille, Elodie, Pascal, Vincent, Laura, Ludo, Jim, Maïna, Charlotte, Camille, Carlos, Marion, Lucie, Nicolas, ainsi que tous les autres voisin-colocs ou habitants plus ou moins temporaires de ce lieu magique qu'est la colocation. Je n'ai pas la place de citer tous ceux a qui je pense ici, alors je me contenterai de vous embrasser ! Je me vois mûrir, doucement mais sûrement, et chacun de vous y a contribué à sa façon.

MERCI !

Abstract

Prism-based surface plasmon resonance microscopy is an optical imaging technique invented in the late 80s'. Its main advantage lies in its high sensitivity to optical index or thickness variations at a metal surface. Therefore, the monitoring of biological reactions can be performed in real-time without labeling agent such as fluorescence or enzymes. Over the last 25 years, SPR microscopy has become the major technique in label-free biodetection. The field of application range from the determination of affinity constant in biochemistry to the detection of pathogenic bacteria via cellular biology. Until now, the propagation length of the surface plasmons has been considered as the spatial resolution limit. However, many examples do not support this statement. In this PhD thesis, we demonstrate that the resolution is also limited by optical aberrations induced by the prism used to couple light and surface plasmons. Thus, we are able to explain why the experimental resolution was usually worse than the predicted one. The analysis of the image formation and the quantification of aberrations lead us to suggest two new optical configurations optimized for resolution. We also analyze which metal exhibits the better trade-off between propagation length and sensitivity. Experimentally, we obtain a resolution between 1.5 and 5 μm depending on the direction, on field-of-view up to several mm^2, and with a standard sensitivity for biodetection. We are then able to observe simultaneously several thousands of individual eukaryote and prokaryote cells. Finally, we develop a prototype dedicated to the real-time monitoring of protein secretion by immune cells. The limits of SPR microscopy and the solutions which could allow this kind of study are discussed. Preliminary results on adherent cells observation and improvement of bacterial detection are also presented.

Resumé

La microscopie par résonance de plasmons de surface à couplage par prisme a vu le jour à la fin des années 80. Le principal avantage de cette technique d'imagerie optique réside dans sa très grande sensibilité à de faibles variations d'indice optique ou d'épaisseurs à la surface d'un métal. De ce fait, le suivi d'interactions biologiques peut se faire en temps réel sans avoir recours à l'utilisation de marqueurs fluorescents ou enzymatiques. Depuis plus de 25 ans, la microscopie SPR s'est imposée comme la technique de référence de biodétection sans marquage. Ses champs d'application vont de la détermination de constantes d'affinité à la détection de bactéries pathogènes, en passant par la biologie cellulaire. Jusqu'à présent, on pensait la résolution spatiale limitée par la longueur de propagation des plasmons de surface. Or, de nombreux exemples ne corroborent pas cette hypothèse. Dans cette thèse, nous montrons qu'à ce phénomène de propagation se rajoute des aberrations optiques induites par l'utilisation d'un prisme pour coupler la lumière et les plasmons de surface. Nous expliquons ainsi pourquoi les résolutions expérimentales étaient souvent bien moins bonnes que celles attendues. Par l'analyse de la formation des images et la quantification des aberrations, nous aboutissons à deux nouvelles configurations optiques optimisées pour la résolution. Nous analysons ensuite quel métal offre le meilleur compromis entre longueur de propagation et sensibilité. Expérimentalement, nous obtenons une résolution comprise entre 1.5 et 5 μm suivant la direction, sur des champs de vision de plusieurs mm^2, et ce, avec une sensibilité standard en biodétection. Nous sommes ainsi en mesure d'observer simultanément plusieurs milliers de cellules individuelles, eucaryotes et procaryotes. Finalement, nous développons un prototype dédié au suivi en temps réel de sécrétions de protéines par des cellules immunitaires. Les limites de la microscopie SPR et les solutions qui permettraient de faire aboutir ce type d'étude sont examinées. Des études préliminaires sont aussi menées sur l'observation de cellules adhérentes ainsi que sur l'amélioration de la détection de bactéries.